

**Tool Wear and Workpiece Surface
Integrity during Ni-Based Superalloy
Machining with Multi-layer CVD
Alumina Coated Carbides**

Henry Boyle

A thesis presented for the degree of
Doctor of Philosophy
2025



**University of
Sheffield**

School of Chemical, Materials and Biological Engineering
The University of Sheffield

Abstract

Ni-based superalloys are used in the most hostile engineering environments, including the hottest stages of aeroengines. The exceptional high-temperature performance of these alloys presents significant challenges during machining; substantial heat and high stresses are generated that impact the integrity of both the tool and the workpiece. Alumina coatings are known for their excellent chemical stability and low thermal conductivity. Therefore, they are considered well-suited for cutting hard-to-machine alloys.

In the following work, an in-depth study of alumina degradation during a series of turning experiments on wrought and powder metallurgy (PM) alloys. During axial turning experiments involving a wrought alloy (IN718), high levels of coating pull-out and delamination were observed. In contrast, when turning a PM superalloy (RR1000), a lower propensity for adhesive wear and alumina grain pull-out was observed; however, a faster wear rate and a higher concentration of Hf-rich reaction products formed across the contact zone, indicating chemical wear. It is hypothesised that thermally driven wear phenomena are more significant when turning RR1000.

Both fine and coarse grained RR1000 were machined, with the latter causing faster overall wear and significant notching during tool engagement. A higher wear rate was also detected at the higher cutting speed tested. Larger fluctuations in the machining force response were measured when turning the less homogeneous CG material. The deformation characteristics of the CG material were also observed to be more diffuse and more inhomogeneous, which was accompanied by irregular shear band formation in the produced chips.

Additional dry orthogonal experiments were performed on as-HIP RR1000. Significant adhesion and Hf-rich reaction product formation were again detected, supporting previous observations regarding the significant chemical affinity between alumina and RR1000. The results presented demonstrate the limitations of state-of-the-art textured alumina coatings in terms of Ni-based superalloy turning, highlighting the need for further research in this area.

Dedication

This work is dedicated to all my grandparents; you are with me always.

Preface

This thesis is submitted for the Degree of Doctor of Philosophy at the University of Sheffield. The research described was carried out at the University of Sheffield under the supervision of Prof. Martin Jackson and Prof. Katerina Christofidou, at the Advanced Manufacturing Centre (AMRC) under the supervision of Pete Crawforth, and at Sandvik Coromant under the supervision of Prof. Susanne Norgren and Alex Graves.

The following published paper utilised works that have been presented in:

Insights in α -Al₂O₃ degradation in multilayer CVD coated carbide tools when turning IN718
(Chapter 5)

Two chapters have been submitted for publication, and are currently under review:

Effect of workpiece grain size and cutting speed on multi-layer CVD α -Al₂O₃ coating degradation and workpiece surface integrity when turning an advanced Ni-based superalloy for aeroengine disk applications
(Chapter 6)

Orthogonal dry turning of an advanced Ni-based superalloy for aeroengine disk applications in the as-HIP condition using multi-layer CVD α -Al₂O₃ coatings
(Chapter 7)

Acknowledgements

I have been lucky to have been supervised by some incredible individuals: Martin Jackson, Susanne Norgren, Alex Graves, Pete Crawforth, and Kathy Christofidou. It simply would not have been possible without them, for this, I am truly grateful. I would also like to thank Ru Peng, and Mattias Calmunger at Linköping University, for their patience and willingness to give me the time to complete my thesis during the start of my Postdoc position.

I have been lucky to share this journey with my Advanced Metallics CDT colleagues, as well as those in the STAR research group and Modern AIChEME. A special mention is necessary for my fellow Nickel metallurgists: Jonah Shrive, and Miguel Espadero Sanchez-Crespo, as well as Martin Tse, and Axel Bjerke for their assistance with Thermo-Calc modelling. I would also like to thank Zhiyu Quan for his help in obtaining such wonderful EBSD images.

I'd like to thank the technical staff from the AMRC: Joel Fisher, Kevin Flanagan, and Harry Perks, for assisting me during machining trials. I'd also like to thank the technicians and engineers from the University labs, as well as the staff at the Sorby center: Ian Ross, Le Ma, Stuart Creasey-Gray, Cheryl Shaw, Sylwester Mikula, Tesoro Monaghan, Neil Hind, Holger Krain, and Dean Haylock. My deep appreciation goes out to Sharon Brown, Joan Kelly, and Rae Helm for organising the Advanced Metallics CDT.

From what I have gathered by talking to other PhD students, the level of support I have received from Sandvik Coromant is truly unprecedented. A massive thank you to Steve Weston, Justin Davies, and Ryan Smith, for helping me with the more hands on aspects of a machining PhD, I have learned so much from our conversations. I'd also like to thank those over in Sweden who have assisted in a wide range of different technical aspects of the project: Changhong Xiao, Christer Fahlgren, Wei Wan, and Jonas Östby.

My thanks to the project sponsors: the Engineering and Physical Sciences Research Council (EPSRC) and Sandvik Coromant. I would also like to thank Rolls-Royce for providing research materials.

Last but not least, I would like to thank my friends and family for their support.

"You don't get to the forefront of materials engineering without breaking a few diamond blades."

-Martin Jackson, 2021

Contents

1	Introduction	1
2	Literature Review	6
2.1	Metallurgy and Processing of Nickel Based Superalloys	6
2.2	Computer Numeric Controlled Machines	13
2.3	Fundamentals of Machining	13
2.3.1	Orthogonal Cutting	14
2.3.2	Turning Methods for Machining Research	17
2.4	Design of Cutting Tools	20
2.4.1	Tool Materials	20
2.4.2	PVD Coatings	21
2.4.3	CVD Coatings	22
2.4.4	Tool Geometry	26
2.5	Tool Wear	28
2.5.1	Wear Mechanisms	29
2.5.2	Wear Types	32
2.6	Machinability	35
2.6.1	Ni-based Superalloys	36
2.6.2	Influence of Coolant	43
2.7	Alumina Degradation during Machining	44

2.7.1	Wear of Textured CVD Alumina Coatings during Steel Turning	45
2.8	Conclusion	47
3	Experimental Materials	49
3.1	Cutting Inserts	49
3.1.1	Coating	49
3.1.2	Geometry	49
3.2	Workpiece Materials	50
3.2.1	Processing	50
3.2.2	Composition	51
4	Experimental Methods	52
4.1	Scanning Electron Microscopy SEM	52
4.1.1	Types of Electron Emitters	52
4.1.2	Interaction of Electron Beam with Sample	53
4.1.3	Types of Detectors	54
4.2	Scanning Transmission electron Microscopy (STEM)	56
4.3	X-ray Diffraction	57
4.4	Optical Measurement System	59
4.4.1	Conventional Light Optical Microscopy	59
4.4.2	3D Optical Measurement Systems	59
4.5	Hardness Testing	60
4.6	Metallographic Preparation	60
4.6.1	Insert Cleaning	61
4.7	Machining Force Measurement	61

4.7.1	Machining Force Response	62
4.8	Machining Strategies	63
4.9	Chemical Etching	64
4.9.1	Phosphoric Acid Electrolytic Etch for Inspection of Machining Induced Damage	64
4.9.2	Glyceregia Etch for Removal of Adhered material on Cutting Tools	64
4.10	Modelling	64
4.10.1	Thermo-Calc	65
4.10.2	Mean-field Model	65
4.10.3	3D FEM Modelling	65
5	Insights in alumina degradation in multilayer CVD coated carbide tools when turning IN718	66
5.1	Introduction	66
5.2	Materials and method	66
5.2.1	Experimental Materials	67
5.2.2	Test Methods	67
5.2.3	Characterisation techniques	67
5.3	Results and Discussion	68
5.4	Conclusions	78
6	Effect of workpiece grain size and cutting speed on tool wear and workpiece microstructural damage when turning RR1000 with multi-layer CVD alumina coated carbides	79
6.1	Introduction	79
6.2	Materials and Methods	80
6.2.1	Experimental Materials	80

6.2.2	Test methods	81
6.2.3	Characterisation Techniques	82
6.2.4	Modelling techniques	82
6.3	Results and Discussion	83
6.3.1	Surface Integrity of Turned CG and FG RR1000	83
6.3.2	Tool Wear	99
6.4	Conclusion	121
7	Orthogonal dry turning of RR1000 in the as-HIP condition using multi-layer CVD alumina coated carbide tools	124
7.1	Introduction	124
7.2	Materials and Methods	125
7.2.1	Experimental Materials	125
7.2.2	Test methods	125
7.2.3	Characterisation Techniques	126
7.3	Results and Discussion	127
7.4	Machining Forces and Tool Wear	127
7.5	Conclusion	137
8	Conclusions and Future Work	139
8.1	Conclusions	139
8.2	Future Work	141
	Appendices	162

List of Figures

1.1	Superalloy market share of different manufacturing sectors as of 2022 by volume and revenue [6].	2
1.2	Damage caused by failure of alloy IN718 high pressure turbine stage two disk as result of low cycle fatigue cracks initiated from internal subsurface [8]. N.B. Annotations are from original report.	3
1.3	Comparison of tool coating technologies.	5
2.1	Crystal structures of γ and γ' phases.	8
2.2	Crystal structures of γ'' phases [31].	9
2.3	Variation in flow strength against temperature for Ni-Al-Cr alloys with varying γ' fraction [31].	10
2.4	Effect of γ' particle diameter on theoretical critical resolve shear stress [33].	11
2.5	ECCI analysis using the $g = \bar{1}\bar{1}1$ diffracting vector for fine-grain precipitate condition: (a) and (c); coarse-grain precipitate condition: (b) and (d). Key: SB = slip band; SF = stacking fault; SC = strongly coupled dislocations [35].	12
2.6	Single-crystal microstructure (CMSX-4 alloy), after second stage of ageing fine cubic γ' precipitates can be observed [25].	13
2.7	Diagram demonstrating a standard OD turning turning setup, alongside the relevant processing parameters (courtesy of Sandvik Coromant.)	14
2.8	Diagram showing comparison of orthogonal and oblique cutting (adapted from [41]).	15
2.9	Diagram showing geometric features of orthogonal cutting, and construction of Merchant circle (adapted from [43]).	16
2.10	Diagram showing approximate positions of primary (I), secondary (II), and tertiary (III) shear zones during orthogonal cutting.	17

2.11	Diagram demonstrating the difference between different tube type and fin type orthogonal lathe setups commonly used in research settings.	18
2.12	Diagram demonstrating the difference between OD turning and facing operations in terms of feed direction, and the position of primary and auxiliary cutting edges.	19
2.13	Tool material selection graph, showing hardness against toughness for different tool materials [52].	20
2.14	PVD coating process to produce multilayer TiCN coatings (courtesy of Sandvik Coromant).	22
2.15	CVD coating process to produce multilayer alumina coatings (courtesy of Sandvik Coromant).	23
2.16	Thermal transformation sequence of alumina hydroxides. Hydroxides are in square boxes, and transition aluminas are in epileptical ones (adapted from [63]).	24
2.17	The α -alumina unit cell; made using VESTA 3.	25
2.18	Diagram showing the ploughing effect during orthogonal cutting (adapted from [68]).	27
2.19	Diagram showing influence of tool nose radius (courtesy of Sandvik Coromant)	27
2.20	Diagram showing the difference between an insert featuring a chip breaker, and one that does not (courtesy of Sandvik Coromant).	28
2.21	Diagram showing typical flank wear variation against spiral-cut-length (SCL).	29
2.22	Diagram showing the difference between two-body and three-body abrasive wear.	30
2.23	Diagram showing types of two-body abrasive wear (adapted from [75]). . . .	30
2.24	Diagram showing influence of temperatures on active wear mechanisms [78].	32
2.25	Diagram showing typical features of a worn cutting insert (adapted from [79]).	33
2.26	Diagram showing steps for progressive material loss via discreet plastic deformation mechanism (adapted from [82]).	34
2.27	Diagram showing plastic deformation under compressive stress schematics for: depression, and impression.	34

2.28	Schematic of metal surface [86].	36
2.29	IR thermal camera image taken normal to cutting direction, showing temperature gradients during orthogonal turning of advanced Ni-based superalloy using uncoated carbide inserts at a cutting speed of $30 \text{ m} \cdot \text{min}^{-1}$, and a feed rate of $0.1 \text{ mm} \cdot \text{rev}^{-1}$ [15].	37
2.30	Scanning transmission x-ray microscopy (STEM) micrograph and x-ray energy dispersive spectroscopy (X-EDS) scans of machining effected layers after orthogonal turning of advanced Ni-based superalloy using a heavily worn tool ($VB = 0.3 \text{ mm}$); $V_c = 80 \text{ m} \cdot \text{min}^{-1}$, $f_n = 0.1 \text{ mm} \cdot \text{rev}^{-1}$ [16].	40
2.31	Influence of feed rate and workpiece material grain size on flank and rake face tool wear when turning IN718 with uncoated carbide inserts with a 0° rake angle [105].	41
2.32	White light interferometry of worn tool with TiAlN + MoST coating after orthogonal turning of IN718; $V_c = 60 \text{ m} \cdot \text{min}^{-1}$, $f_n = 0.1 \text{ mm} \cdot \text{rev}^{-1}$ [45].	43
2.33	Proposed plastic deformation driven wear mechanism for alumina coatings during steel machining (adapted from [117]).	45
2.34	Sliding zone alumina wear during steel machining for different alumina growth textures: (001), (012), (110) (adapted from [125]).	47
3.1	SF edge geometry utilised for OD turning trials.	50
3.2	Comparison of the two different tool geometries employed.	50
4.1	Diagram of interaction volume produced SEM [131].	54
4.2	Diagram showing the formation of characteristic Kikuchi bands on the phosphorous screen on an EBSD detector, and the position of the X-EDS detector (adapted from [132]).	56
4.3	Diagram showing x-ray interaction with material [133].	58
4.4	Diagram showing x-ray diffraction acquisition, from 3D cone, to 2D and 1D detectors (adapted from [140]).	59
4.5	Example 3D scan of cutting insert, produced using Alicona system, displaying characteristic BUE formed after Ni-based superalloy machining.	60

4.6	Dynamometry setup used in OD turning trials, alongside digram showing machining force components acting on a cutting insert.	62
4.7	Diagram showing simplified machining strategy employed during OD turning trials.	63
5.1	Machining forces measured: Cutting force (F_c), Feed force (F_f) and Passive Force (F_p), using Kistler piezoelectric plate dynamometer during 32 m machined length test.	69
5.2	BSE SEM micrographs of tool wear developed during turning trial at each SCL (a) 2 m (b) 32 m (c) 128 m.	70
5.3	X-EDS of adhered material on worn inserts for Al, Ti and Ni at different SCLs: (a) 2 m (b) 32 m (c) 128 m.	71
5.4	SEM micrographs of worn unetched insert showing sticking (zone A), sliding zone (zone B), and end-of-contact (zone C) after a SCL of 128 m: (a) BSE imaging mode (b) SE imaging mode. Delamination and TiCN exposure is observed in zone C.	72
5.5	SE SEM micrograph showing worn surface of etched alumina after 128m SCL in the sliding zone (zone B).	73
5.6	BSE SEM micrograph of post-etched surface for insert ran to 32 m SCL in the sliding zone (zone B) displaying potential reaction products adhered to alumina.	74
5.7	Cross-section of adhered material within the sliding zone (zone B), showing region 1; used for compositional analysis.	74
5.8	EPMA performed on adhered IN718 material in sliding zone (zone B) after a SCL of 128 m.	75
5.9	SEM BS micrographs showing alumina wear unetched (BSE imaging) and etched (SE imaging) sister inserts compared at different SCLs (a) region 1 at 2 m (b) region 2 at 2 m (c) region 1 at 32 m (d) region 2 at 32 m (e) region 1 at 128 m (f) region 2 at 128 m.	76
5.10	Cross sections of inserts taken from zones B and C at different SCLs: (a) 2 m (b) 32 m (c) 128 m.	78
6.1	BSE SEM micrograph of electro-etched subsurface deformation when turning the (a) CG material (b) FG material at $100 \text{ m} \cdot \text{min}^{-1}$	84

6.2	Subsurface deformation generated when turning the CG material at a surface speed of $100 \text{ m} \cdot \text{min}^{-1}$. Image shows evidence for dependency of slip band formation on grain orientation.	84
6.3	SE SEM micrograph of electro-etched subsurface, showing SPD layer produced when turning (a) CG material at $70 \text{ m} \cdot \text{min}^{-1}$ (b) CG material at $100 \text{ m} \cdot \text{min}^{-1}$ for FG material (c) FG material at $70 \text{ m} \cdot \text{min}^{-1}$ (d) FG material at $100 \text{ m} \cdot \text{min}^{-1}$	85
6.4	Bar chart showing influence of workpiece material condition and cutting speed on severely deformed layer thickness.	86
6.5	TEM X-EDS map of FG material turned at $100 \text{ m} \cdot \text{min}^{-1}$, prepared using FIB lift-out technique, showing secondary and tertiary γ' dissolution variation across the machined surface, viewed normal to the cutting direction, alongside corresponding estimated temperature distribution.	87
6.6	EBSD data showing z-IPF maps of machined surfaces viewed normal to the cutting direction: (a) CG $70 \text{ m} \cdot \text{min}^{-1}$ (b) CG $100 \text{ m} \cdot \text{min}^{-1}$, (c) FG $70 \text{ m} \cdot \text{min}^{-1}$ (d) FG $100 \text{ m} \cdot \text{min}^{-1}$. A strong deformation gradient is observed, with highly deformed, non-indexed regions (white) occurring near the surface.	89
6.7	EBSD data showing KAM maps of machined surfaces (colourbar misorientation is in $^\circ$): (a) CG $70 \text{ m} \cdot \text{min}^{-1}$ (b) CG $100 \text{ m} \cdot \text{min}^{-1}$ (c) FG $70 \text{ m} \cdot \text{min}^{-1}$ (d) FG $100 \text{ m} \cdot \text{min}^{-1}$	90
6.8	KAM against depth for each condition tested; note different x-axis and y-axis scales.	91
6.9	Estimated damage depth based on XRD FWHM measurement for FG RR1000 at varying SCLs.	91
6.10	Comparison of average machining force response values for all cuts performed during initial tool wear trials; measurements were averaged over the first second of tool engagement; error bars demonstrate range of values measured.	93
6.11	Comparison of contact zone area measured over 2 m and 32 m SCL for different machining conditions tested.	94
6.12	Force feedback plot at $100 \text{ m} \cdot \text{min}^{-1}$, sampled at 400 Hz for (a) CG material (b) FG material.	95

6.13	Force response maps for CG and FG materials, demonstrating variations in machining forces that has been attributed to microstructural variation and tool wear.	95
6.14	Medium magnification SEM SE micrograph of chips produced when turning CG and FG material at 100 m · min ⁻¹	96
6.15	Low magnification SEM SE micrograph of chips produced when tuning CG and FG material at 100 m · min ⁻¹	96
6.16	Simulated dissolution at different temperatures using mean field model for FG RR1000 (a) secondary γ' (b) tertiary γ'	97
6.17	AdvantEdge simulation of machining process using IN718 for material model at 70 and 100 m · min ⁻¹	99
6.18	BSE SEM micrograph of tool nose after a SCL of 2 m when turning (a) CG RR1000 at 70 m · min ⁻¹ (b) CG RR1000 at 100 m · min ⁻¹ (c) FG material at 70 m · min ⁻¹ (d) FG material at 100 m · min ⁻¹	101
6.19	BSE SEM micrograph of rake face after a SCL of 2 m when turning (a) CG material at 70 m · min ⁻¹ (b) FG material at 70 m · min ⁻¹ for FG material (c) CG material at 100 m · min ⁻¹ (d) FG material at 100 m · min ⁻¹	103
6.20	SE SEM micrograph of BCB formed on rake face after 2 m SCL, at 100 m · min ⁻¹ when turning the CG material.	104
6.21	X-EDS scan of BCB to rear of rake face formed when turning CG material for 2 m SCL at 100 m · min ⁻¹	104
6.22	BS SEM micrograph of insert BCB formed when turning the FG material 16 m SCL at 100 m · min ⁻¹ ; corresponding compositions for each region is given in Table 6.3.	105
6.23	Close-up BS SEM micrograph of Figure 6.22, showing rake face BCB formed when turning the FG material 16 m SCL at 100 m · min ⁻¹	106
6.24	EPMA scans and accompanying BSE image of BCB on insert formed when turning the FG RR1000 16 m SCL at 100 m · min ⁻¹	107
6.25	BSE SEM micrograph of etched rake face after a SCL of 2 m when turning (a) CG material at 70 m · min ⁻¹ (b) FG material at 70 m · min ⁻¹ for FG material (c) CG material at 100 m · min ⁻¹ (d) FG material at 100 m · min ⁻¹	108

6.26	BSE SEM micrograph of tool face post etching for tool used to turn CG RR1000 for 2 m SCL at $100 \text{ m} \cdot \text{min}^{-1}$	109
6.27	SEM micrographs of sliding region on tool rake face after turning CG material 32 m SCL at $70 \text{ m} \cdot \text{min}^{-1}$, viewed using (a) SE imaging mode (b) BSE imaging mode.	110
6.28	BSE SEM micrograph of rake face after turning the FG material after a SCL of 600 m, turned at a speed of $70 \text{ m} \cdot \text{min}^{-1}$	110
6.29	Graphs showing alumina wear across rake and flank, measured from cross-sections taken parallel to chip flow, at SCLs of 2 m, 16 m and 32 m.	113
6.30	Graphs showing alumina wear rate on tool rake, measured from cross-sections taken parallel to chip flow.	113
6.31	Cross-section SE SEM micrograph showing crack formation around BUE after turning FG RR1000 for 2 m.	114
6.32	Diagram showing general features of alumina wear behaviour, adapted from SEM cross section micrograph taken after a SCL of 32 m when tuning the CG RR1000.	115
6.33	Schematic demonstrating generalised alumina wear variation against time for CG and FG RR1000.	116
6.34	Graph showing calculated volume fraction against O_2 partial pressure for O_2 partial pressures ranging from 1×10^{-27} to 1, corresponding phase compositions are give in Figure 6.36.	118
6.35	Graph showing calculated volume fraction against O_2 partial pressure for O_2 partial pressure ranging from 1×10^{-27} to 1, corresponding phase compositions are give in Figure 6.36.	119
6.37	Summary schematic demonstrating relationship between workpiece surface integrity, chip formation, machining force response, and alumina wear rate for CG and FG RR1000	123
7.1	Diagram of experimental setup used in orthogonal turning trial, and relevant machining force components.	126
7.2	Diagram showing top down view of cutting inserts used in trial, and approximate position of sectioning line used to produce cross-sectional samples. . .	127

7.3	BS SEM micrographs showing rake face wear during RR1000 turning trial after varying SCLs: 12 m, 17 m and 57 m.	128
7.4	Influence of kV on the amount of adhered material observed during BS SEM imaging; micrographs show rake face adhesion on a test insert ran at surface speed of $80 \text{ m} \cdot \text{min}^{-1}$ for 11 m, at a feed rate of $0.5 \text{ mm} \cdot \text{rev}^{-1}$	129
7.5	X-EDS scan and accompanying BS SEM micrograph of BCB after a turning a SCL of 12 m.	131
7.6	X-EDS scan and accompanying BS SEM micrograph of BCB after a turning a SCL of 57 m.	132
7.7	BS SEM micrographs of cross sections taken parallel to chip flow after varying SCLs: 12 m, 17 m and 57 m.	133
7.8	Cross sectional BS SEM micrograph of BCB formed after turning a SCL of 57 m; the crack observed was likely formed during metallographical preparation.	134
7.9	X-EDS scan and accompanying BS SEM micrograph of region displayed in Figure 7.8.	135
7.10	Simplified schematic showing characteristic wear behaviour during orthogonal turning in RR1000.	136
7.11	BS SEM micrograph of adhered chip on tool rake face after a SCL of 17 m.	137
A1	Modelled stresses experienced by tool during AdvantEdge FE machining simulations.	163
A2	Average grain diameter histograms for (a) CG RR1000 (b) FG RR1000.	164
A3	Thermal profiles used for mean field modelling of precipitate dissolution for FG RR1000.	164
A4	Approximate sectioning line taken parallel to chip flow for all inserts examined.	165
A6	Variation in corundum composition in mole fraction with temperature when combined with RR1000; simulation was performed in Thermo-Calc by mixing 1 mol of RR1000 with 0.005 mol of alumina in the Poly 3 module using the TCNi12 database (all phases except corundum and L12 phases (γ , γ' , MC carbide) were suppressed).	167

List of Tables

3.1	Composition in wt.% for IN718 and RR1000.	51
4.1	SEM models and their electron sources.	53
4.2	SEM operational parameters.	54
4.3	Sample preparation method used for Ni-based Superalloys and WC cutting inserts. N.B. Final polishing step was not used on cutting inserts.	61
5.1	Composition in Wt.% for nominal, and measured values for adhered IN718 in region 1 (see Figure 5.7).	75
6.1	γ' precipitate radius and volume fraction for CG and FG RR1000 material conditions.	81
6.2	Hardness measurements and average grain size for CG and FG RR1000. . . .	81
6.3	Normalised composition in Wt.% for major elements in RR1000 found within regions of BCB (see Figure 6.22).	106

Nomenclature

- FCC: Face-centred cubic
- BCC: Body-centred cubic
- CG: Coarse grain
- FG: Fine grain
- YSA: Yield strength anomaly
- APB: Antiphase boundary
- ECCI: Electron channel contrast imaging
- PM: Powder metallurgy
- HIP: Hot isostatic pressing
- CNC: Computer numerical control
- CAD: Computer-aided design
- CAM: Computer-aided manufacture
- MRR: Material removal rate
- FEM: Finite element method
- DOC: Depth-of-cut
- CFD: Chip flow direction
- OD: Outer diameter
- ER: Edge radius
- PVD: Physical vapour deposition
- CVD: Chemical vapour deposition
- BUE: Built-up edge
- PPB: Primary particle boundaries

- STEM: Scanning transmission electron microscopy
- X-EDS: X-ray energy dispersive spectroscopy
- VB: Flank wear
- APT: Atom probe tomography
- HPC: High-pressure coolant
- SEM: Scanning electron microscopy
- FEG: Field-emission gun
- EBSD: Electron backscattered diffraction
- EBSP: Electron backscattered pattern
- SE: Secondary electron
- BSE: Backscattered electron
- EPMA: Electron probe microanalysis
- WDS: Wavelength dispersive spectroscopy
- XRD: X-ray diffraction
- FWHM: Full width half maximum
- SCL: Spiral cut length
- TiCN: Titanium carbonitride
- IN718: Inconel 718
- CALPHAD: Computer Coupling of Phase Diagrams and Thermochemistry
- SPD: Severe plastic deformation
- IPF: Inverse pole figure
- KAM: Kernel average misorientation
- BCB: Bright contrast band
- Wt.%: Weight percent
- Vf: Volume fraction
- V_c : Cutting speed

- a_p : Depth-of-cut
- f_n : Feed rate
- D_m : Turned diameter
- n : Number of turns
- ρ : Mean value
- t_c : Cut chip thickness
- t : Uncut chip thickness
- h_o : Height of ploughed material
- t_a : Actual uncut chip thickness
- h_p : Machining affected layer thickness
- λ_s : Inclination angle
- η : Chip flow angle
- r : Precipitate radius
- F_p : Passive force
- F_c : Cutting force
- F_f : Feed force
- R : Resultant force
- λ : Wavelength
- d : Interplanar spacing
- α -alumina: Alpha alumina
- κ -alumina: Kappa alumina
- μ : Mu phase
- σ : Sigma phase
- γ : Gamma phase
- γ' : Gamma prime
- γ'' : Gamma double prime
- ϕ : Shear plane angle

Chapter 1

Introduction

By 2052, it is anticipated that global passenger traffic for air travel will approach 25 billion, approximately 2.5 times the levels projected in 2024 [1]. Simultaneously, the aerospace sector aims to reach net-zero by 2050. This ambitious target requires the rapid development of new technologies, as well as significant improvements to be made in the existing manufacturing infrastructure. A combination of complementary propulsion methods (e.g., sustainable aviation fuels, hydrogen turbines, battery powered electric motors) are anticipated to be adopted to facilitate carbon neutral transport over a wide range of transport distances [2]. Both sustainable aviation fuels and hydrogen propulsion require high temperature materials, such as Ni-based superalloys, to be employed in the hottest regions of the gas-turbine. Hydrogen gas turbines burn even hotter than traditional gas turbines, meaning that future developments will require innovations in terms of materials, coatings, and cooling systems [3].

The global superalloy market has been valued at approximately £5.4 billion in 2021, and is projected to grow at a rate of over 8.5% annually from 2022 to 2029 [4]. Ni-based superalloys make up approximately 80% of the overall market [5], with the majority being utilised in aerospace applications (Figure 1.1). In terms of metallic systems, these materials exhibit exceptional properties, such as high strength, creep, and oxidation resistance, as well as the ability to withstand extreme high temperatures. Said properties make them suitable for the most challenging operating conditions found within gas turbine systems. The machining of Ni-based superalloys is crucial for producing functional components with tight dimensional tolerances, however, the creation of more sophisticated alloys has generally led to decreased machinability. This in turn has driven the development of new tools and tool coatings, capable of delivering increased productivity. The following introductory chapter will discuss the industrial importance of machining Ni-based superalloys to the UK economy, and discuss the role of coatings in the context of cutting tools.

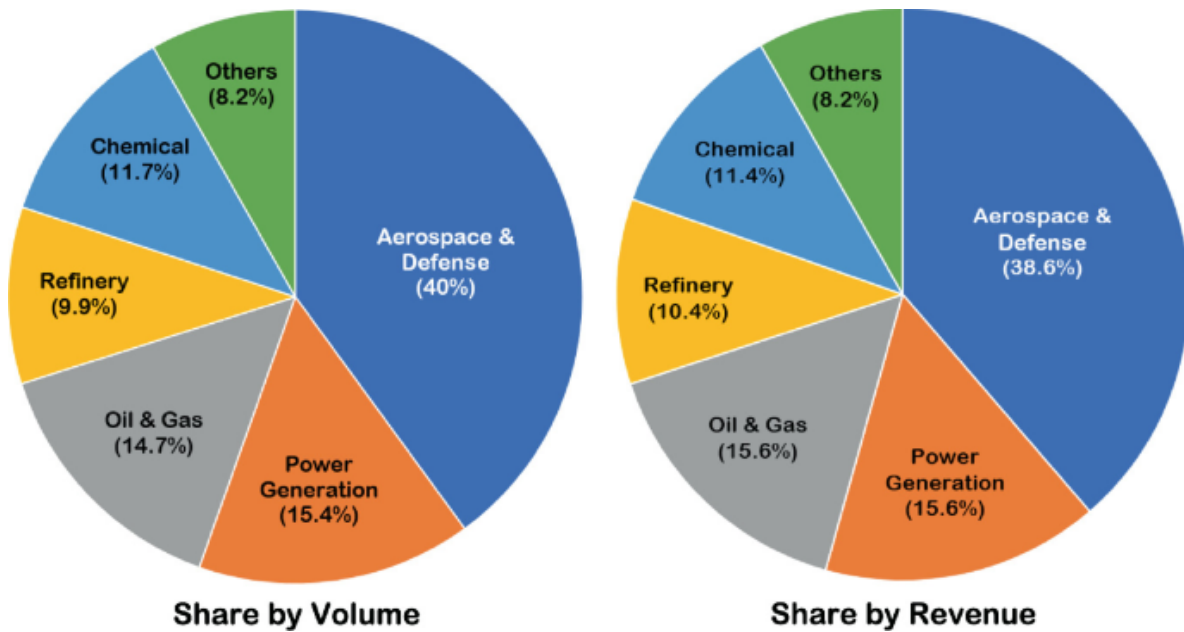


Figure 1.1: Superalloy market share of different manufacturing sectors as of 2022 by volume and revenue [6].

The UK aerospace industry is the second largest in the world, with 70% of all domestic aerospace production being exported [7]. The total turnover within civil aerospace, as of 2022, was over £27 billion [7]. In total there are over 3000 different aerospace companies of varying size within the UK, with BAE, Airbus, and Rolls-Royce being the largest [7]. Rolls-Royce boasts a fleet of over 13000 engines worldwide [7], many of which contain Ni-based superalloy components. Such components are typically utilised in turbine blades, high-pressure disks, and combustion chambers. Rotative parts such as blades and disks, must endure extreme rotational speeds, and high temperatures, resulting in high stresses. It is of paramount importance that the failure of these parts be avoided, as this can result in catastrophic engine failures, which will jeopardise passenger safety. An example of an uncontained turbine rotor failure due to low cycle fatigue cracking of a Ni-based alloy is shown in Figure 1.2.

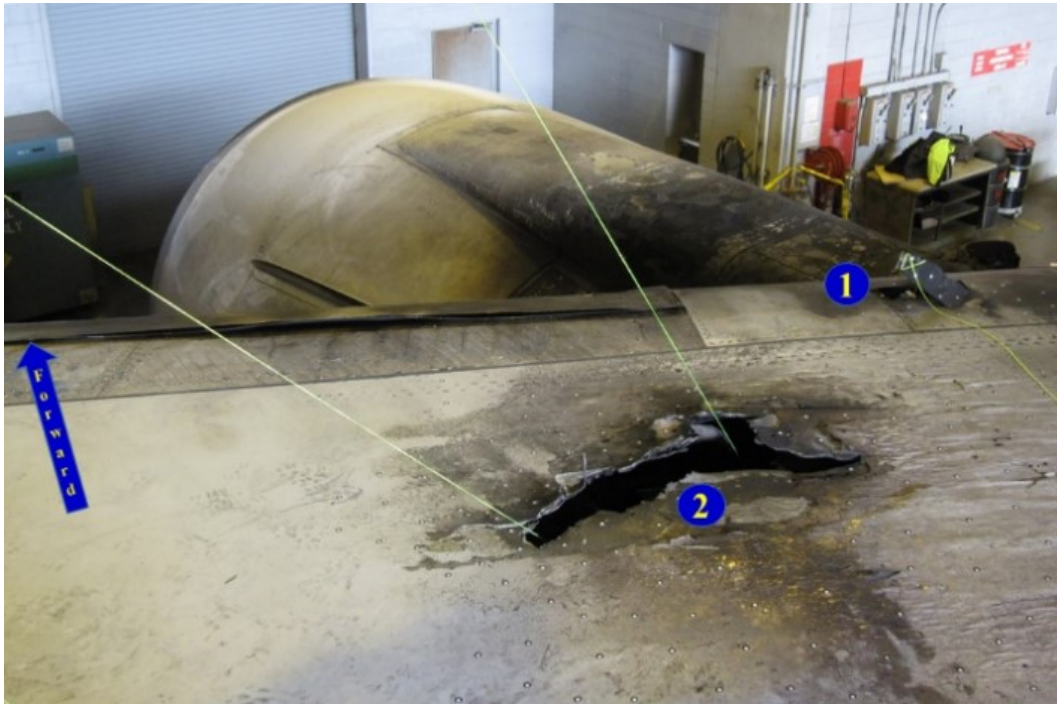


Figure 1.2: Damage caused by failure of alloy IN718 high pressure turbine stage two disk as result of low cycle fatigue cracks initiated from internal subsurface [8]. N.B. Annotations are from original report.

The same properties that give Ni-based alloys excellent in-service performance, lead to challenging machining conditions. During the machining of aerospace forgings, as much as 95% of the total weight can be removed, in addition, frequent tool changes due to rapid wear, significantly limit production rates. These factors mean that machining aerospace forgings can account for 60% of the overall manufacturing cost of a finished component [9]. Hence, there is a strong impetus within aerospace manufacturing to reduce the overall amount of material that needs to be machined by moving towards near-net type operations, such as Wire Arc Additive Manufacturing [10, 11], in order to reduce buy-to-flight ratios.

It is clear from instances like those seen in Figure 1.2, that any advances increasing manufacturing efficiency for critical aerospace components, can only be permitted if functional performance is maintained. In machining terms, this imposes strict limitations on achievable material removal rates during finishing operations, due to the damage that is induced at the surface and sub-surface. Surface condition heavily influences crack initiation and fatigue life in Nickel-based alloys, which is related not only to processing conditions, but also on the level of tool wear [12, 13, 14]. For this reason, aerospace manufacturers are typically highly conservative when selecting tool wear limits prior to tool change.

The term "white layer" is used within aerospace manufacturing to describe the heavily deformed, nanocrystalline layer, which forms as a result of intense thermomechanical loading

at the surface during machining processes. Its name comes from its white appearance when viewed using an optical microscope after chemical etching. The presence of white layer has been shown to be detrimental to low cycle fatigue life when machining Ni-based superalloys [12], as such, aerospace manufacturers have tight controls surrounding the maximum permissible depths of white layer, especially for critical components. Tool condition, and the accompanied change in microgeometry, influences the condition of the surface produced in the final component. Worn tools generate more heat as a result of increased contact area, which promotes dissolution of the γ' strengthening precipitates, and therefore, a deterioration in mechanical properties [15, 16]. To avoid this, the original tool geometry must be maintained by limiting overall wear. Hence, prolonging tool life has three main benefits: saving consumable costs associated with cutting tools, increasing the efficiency of material removal by reducing the amount of tool changes and permitting faster rates of material removal, and producing a higher quality end product with reduced chance for tool failure and part scrapage. It should be noted that in this context, the term "tool life" is somewhat misleading, since certain tools will only show improved performance at higher cutting speeds. As such, the amount of material removed in a given time is a more meaningful performance indicator than simply the lifetime of the tool. To this end, over the last 50 years, one approach that has facilitated dramatic advancement, is the development of hard coatings and ceramics [17, 18].

Within aerospace, coated carbide and ceramic tools are commonly employed to machine Ni-based superalloys, due to their ability to maintain hardness at high temperatures. Coated carbides tend to be preferred for finishing operations with lower cutting speeds, where surface condition is of paramount importance. Ceramic tools are typically more brittle, and so require higher cutting speeds, which facilitate increased levels of workpiece softening; they are more suited to roughing operations. Although machining at higher cutting speeds permits higher material removal rates, they tend to promote the formation of white layer in the machined surface [19]. Several techniques have been developed to reduce cutting forces and prolong the lives of cutting tools during machining, including laser assisted machining [20], cryogenic cooling [21], and high pressure coolant (HPC) [22, 23]. Of all these techniques, only HPC has found widespread industrial adoption.

Physical vapour deposition (PVD) and chemical vapour deposition (CVD) are two common methods of producing hard coatings for machining applications, a comparison of some key features is shown in Figure 1.3. CVD coatings are generally, thicker, more wear resistant, and more heat resistant. Texture controlled oxide coatings can also be deposited using the CVD process, and can be optimised to have preferred crystallographic orientations that are optimised to reduce wear during machining [24]. Within steel machining, this has led to massive gains in productivity. These same coatings are also employed at lower material removal rates for machining Ni-based superalloys. This leads to the formation of the following research questions that have dictated the direction of this thesis:

- What are the dominant wear mechanisms acting on alumina coated tools during Ni-based machining, and how do these compare with the published research on steel ma-

chining? (Chapters 5, 6, and 7)

- How does alloy chemistry, and grain size impact these wear mechanisms? (Chapters 5, 6, and 7)
- What is the relationship between surface damage and tool wear when machining Ni-based alloys? (Chapters 6, and 7)
- Can methods be developed to study the tool-workpiece interaction in machining using alternatively processed, lower cost workpiece materials? (Chapter 7)

	Deposition Temp. (°C)	Thickness (µm)	Sharpness	Toughness	Coverage	Wear resistance
PVD	< 500	2 - 6	Excellent	Excellent	Line-of-sight	Good
CVD	> 1000	2 -20	Good	Good	Complete	Excellent

Figure 1.3: Comparison of tool coating technologies.

In summation, current trends in air travel, coupled with the demands of achieving net-zero by 2050, mean that there is a significant driving force for continued research on the processing of high temperature materials. Ni-based superalloy machining is an integral component aerospace manufacturing, both nationally and internationally. A wide range of tooling solutions are currently employed to machine Ni-based superalloys. Generally Ni-based superalloys exhibit poor machinability in terms of tool life and workpiece surface integrity. Alumina coated carbides, originally developed for steel machining, are widely employed when machining Ni-based superalloys, however, little is currently understood about the mechanisms behind alumina degradation during these types of operations. To this end, the following thesis aims to provide insight, in order to assist the development of the next generation of cutting tool solutions, tailored at Ni-based superalloy machining.

The structure of the thesis is as follows: Chapter 2 provides relevant background information and a comprehensive review of the existing literature. Chapters 3 and 4 outline the experimental methods and materials, respectively. Chapter 5, the first of three experimental results chapters, examines the wear of alumina-coated carbides during single-point turning of a typical wrought alloy (IN718). Chapter 6 employs a similar methodology to investigate how observed wear varies when turning a powder metallurgy Ni-based superalloy used in aeroengine disc applications (RR1000); the influence of workpiece grain size and turning cutting speed is also explored. Chapter 7 presents orthogonal turning as a means of assessing alumina coating wear when machining as-HIP RR1000, further exploring the chemical interactions identified in Chapter 6. Finally, Chapter 8 summarises the findings and discusses future research directions.

Chapter 2

Literature Review

Much has been published in the field of machining science in the last century. In this time period there have been dramatic advancements in machine tools, control systems, cutting tools, and machining strategies, which has facilitated the manufacture of progressively more geometrically complex components from a wide range of workpiece materials. Despite these advancements, very little is known about the interaction between tool and workpiece at a fundamental level, since chip formation tends to obscure the region of interest. Within the contact zone high temperatures, pressures, and strain rates cause microstructural changes to both tool and workpiece at a range of length scales. The following chapter will discuss the relevant background information in terms of workpiece material, general machining, tool coatings, and tool wear; the state-of-the-art in terms of Ni-based superalloy machining and alumina coating wear behaviour is then presented, before some concluding remarks regarding the research gap that will be addressed in the following thesis work.

2.1 Metallurgy and Processing of Nickel Based Superalloys

Superalloys are metallic materials classified based on their ability to perform at high temperature, typically more than 0.7 times their absolute melting temperatures. They are typically composed of either Ni, Fe-Ni, or Co. In general, superalloys have a low thermal expansion, and are designed to maintain strength and corrosion resistance at high temperatures. These properties make them the material of choice for use in aeroengines, as well as other structural applications including marine equipment, nuclear reactors, chemical processing, and pollution control [25].

Ni-based superalloys are the most abundant class of superalloy, and are used predominantly for components that function within the hottest sections of aeroengines, where temperatures can reach as high as 1200°C [25]. Their unique combination of high strength, long fatigue life, oxidation resistance, and resistance to stress rupture and creep, make them ideally suited to this application [26]. High operating temperatures in gas turbines are essential for increased efficiency and reduced emissions, making it desirable to continually increase compressor discharge, and turbine entry temperatures. This fundamental relationship has been the

main driving force behind the development of improved Ni-based superalloys that can safely operate at these higher temperatures. Nevertheless, the high density of Ni-based superalloys means that there remains a desire to limit their use in aeroengines, and to replace them with lighter alternatives (e.g., intermetallics) where possible [27].

The chemistry of Ni-based superalloys is complex, typically there are upwards of 10 alloying elements, each added in specific amounts to optimise certain properties. The resulting microstructures are therefore extremely complex, and are also heavily dependent on the processing route and parameters. The most important kind of Ni-based superalloy are those strengthened by an ordered γ' phase, that coherently precipitates within a disordered matrix of γ . The matrix phase γ is face-centred cubic (FCC) Ni, whereas γ' is an ordered primitive cubic $L1_2$ structure, containing Ni and Al atoms (Figure 2.1). Since both phases have similar lattice parameters (0-1%), the precipitation of the γ' phase occurs homogeneously throughout the matrix, ensuring long-term temperature stability. A small misfit between the two lattices is essential in minimising the interfacial energy, which lowers the driving force behind precipitation at grain boundaries. The topography of the γ' phase is also impacted by the degree of lattice mismatch, and as the coherency is decreased the precipitated γ' will turn from cubic to plate-like [25]. A low mismatch is beneficial to improve stress rupture, which can also be increased by increasing the γ' volume fraction. During a standard heat treatment, peak hardness is associated with specific a precipitate size, and as they coarsen the γ/γ' mismatch will increase [28].

Typically there are three different sizes of γ' particles, from largest to smallest these are: primary, secondary, and tertiary. The standard heat treatment process entails a high temperature solution treatment, this can be either above or below the solvus depending on the preferred properties, followed by a lower temperature precipitation heat treatment, which is necessary to produce the correct size distribution of secondary and tertiary precipitates. Heating above the solvus will cause dissolution of all γ' , including the largest primary particles, facilitating grain growth; material in this condition is referred to as coarse grain (CG). Heat treating below the solvus, means that the largest primary precipitates are maintained, which restricts grain growth, resulting in a fine grain (FG) material condition. Larger grained CG material offers superior creep resistance, and slower crack propagation, however, smaller grained FG will exhibit higher strength, as per the Hall-Petch relationship. In some instances, dual microstructure disks are produced in an attempt to have optimised, location-specific properties, such that the rim, which operates at higher temperatures, has a CG microstructure, whilst the bore, which operates at lower temperatures and is subjected to higher stresses, has a FG microstructure [29, 30].

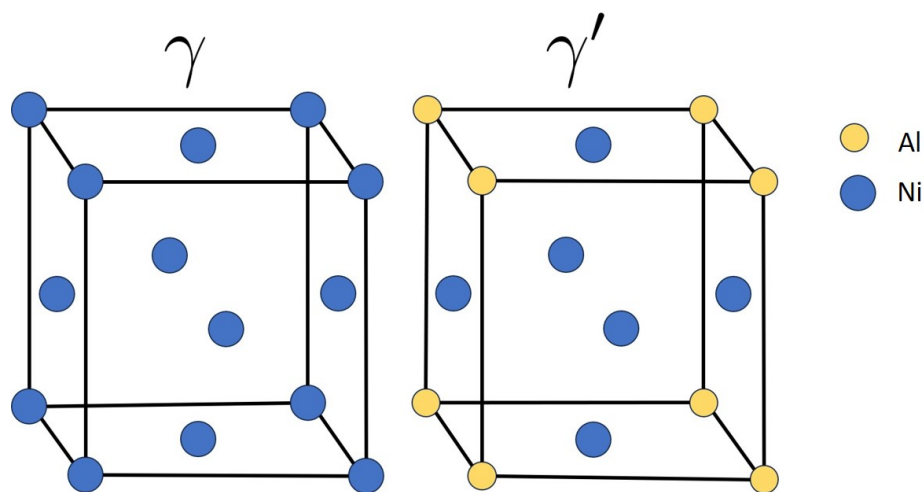


Figure 2.1: Crystal structures of γ and γ' phases.

There are many other phases that form in Ni-based superalloys that improve in-service performance, such as carbides and borides. MX type inclusions typically contain reactive elements such as Ti, Ta, and Hf. In alloys rich in Fe and Nb, the primary strengthening precipitate is in fact γ'' and not γ' . γ'' has an ordered body-centred cubic (BCC) $D0_{22}$ type crystal structure, which has a composition that can be approximated as Ni_3Nb (Figure 2.2). There are also unwanted phases that can form in Ni-based superalloys, especially after in-service ageing, which include the topologically closed-packed phases: μ , σ , Laves etc. Different alloy additions will impact different phases, depending on where they partition, and can, broadly speaking, be divided into three groups: Cr, Co, Fe, and Mo are solid solution strengtheners that strengthen the γ phase; Al, Ti, Ta, Nb, and Hf influence the formation and strengthening of the γ' precipitates; finally, C, B, and Zr provide grain boundary strengthening.

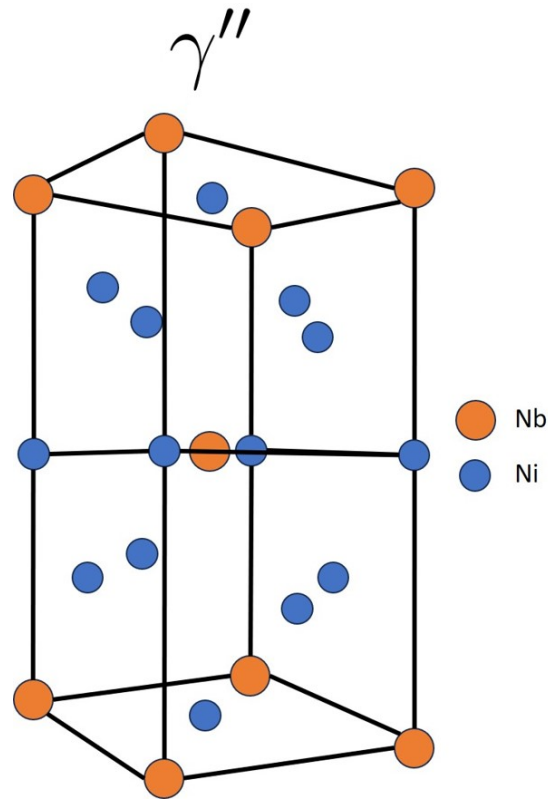


Figure 2.2: Crystal structures of γ'' phases [31].

Perhaps the most unique and advantageous feature of Ni-based superalloy materials containing γ' is that they exhibit a so-called yield strength anomaly (YSA), whereby the yield strength of the material increases with temperature, as opposed to decreasing, as is the case with most metallic systems. This effect does not continue indefinitely, and typically the peak occurs around 800°C [32]. This trend is shown clearly in Figure 2.3, which shows the influence of γ' fraction on flow stress at different temperatures. To understand the mechanisms that lead to this behaviour, it is necessary to take a step back and consider the deformation of both phases and the crystallographic relationships between them.

When dislocations move through the γ phase, it is energetically favourable for pairs of partial dislocations to form that are bound by the energy of the stacking fault produced. Due to the coherent nature of the γ' precipitates, dislocations can travel between the two phases. When a pair of partial dislocations travelling through the γ phase arrives at the interface with γ' , they will recombine to form a perfect dislocation. However, since the γ' phase has a BCC $D0_{22}$ type crystal structure, the perfect dislocation will become a pair of superpartial dislocations. As with partial dislocations moving through the γ , superpartial dislocation movement will cause a stacking fault to form. When superpartial dislocations move through γ' , they cause both structural and chemical discontinuities (due to the ordered nature of the phase), referred to as an antiphase boundary (APB). Although this provides substantial strengthening, there

is another mechanism that is primarily responsible for the YSA behaviour. During high-temperature deformation, cross-slip is enabled in FCC from the close-packed $\{111\}$ planes to the $\{100\}$ planes. When this occurs in the γ' structure, and a superpartial dislocation slips onto the $\{100\}$ planes, a segment of the APB is left behind, locking the dislocation in place. This is referred to as a Kear-Wilks mechanism. As temperature increases further, typically in excess of 800°C , additional slip systems are activated, allowing the pinned dislocations to be "unlocked." In reality, there are additional mechanisms also involved in the unique YSA behaviour; these are discussed at length in [31].

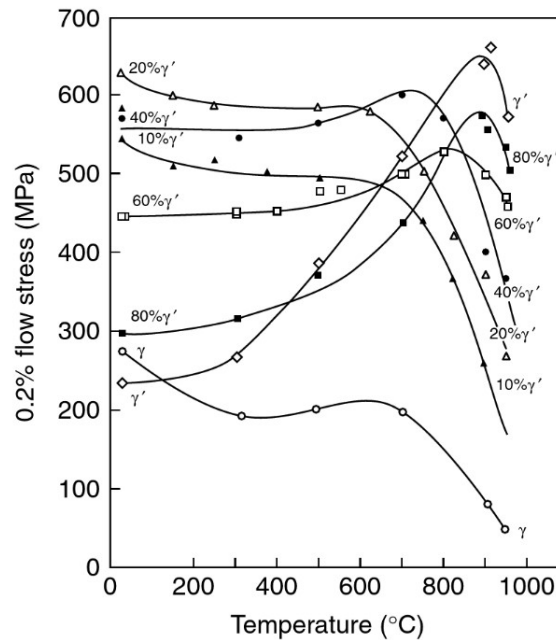


Figure 2.3: Variation in flow strength against temperature for Ni-Al-Cr alloys with varying γ' fraction [31].

The deformation mechanics of γ' strengthened Ni-based superalloys depends heavily on the size distribution of the γ' precipitates [33, 34, 35, 36, 37]. Figure 2.4a shows diagrammatically the transition in precipitate cutting mode from weakly coupled pairs (small precipitate diameters), to strongly coupled pairs (large precipitate size). Figure 2.4b demonstrates the influence this effect has on the critically resolved shear stress, whereby there is optimum γ' precipitate size found at the point of transition. For bimodal alloys it is the tertiary precipitate radius (r) and volume fraction V_f that is most important for achieving optimal yield stress; for the alloy RR1000, commonly used in aeroengine disk applications, it has been shown that an optimum yield strength is achieved when $r = 15$ nm, and $V_f \geq 10\%$ [38]. The larger γ' precipitates, i.e., primary and secondary, are less important in terms of yield strength, and influence the fatigue and creep life [36, 37].

Since γ' -containing Ni-based superalloys are two-phase materials, load transfer can occur

such that the soft phase, which deforms mostly plastically, transfers load onto the harder phase, which deforms mostly elastically. In these alloys, weakly coupled dislocations will yield no load transfer, whereas dislocation bowing and Orowan looping, which involves dislocations moving around the precipitate particle, will lead to deformation in only the γ phase, and therefore contribute to load transfer [34]. As such, load transfer is detected in alloys containing larger γ' precipitates [34], where looping is more common.

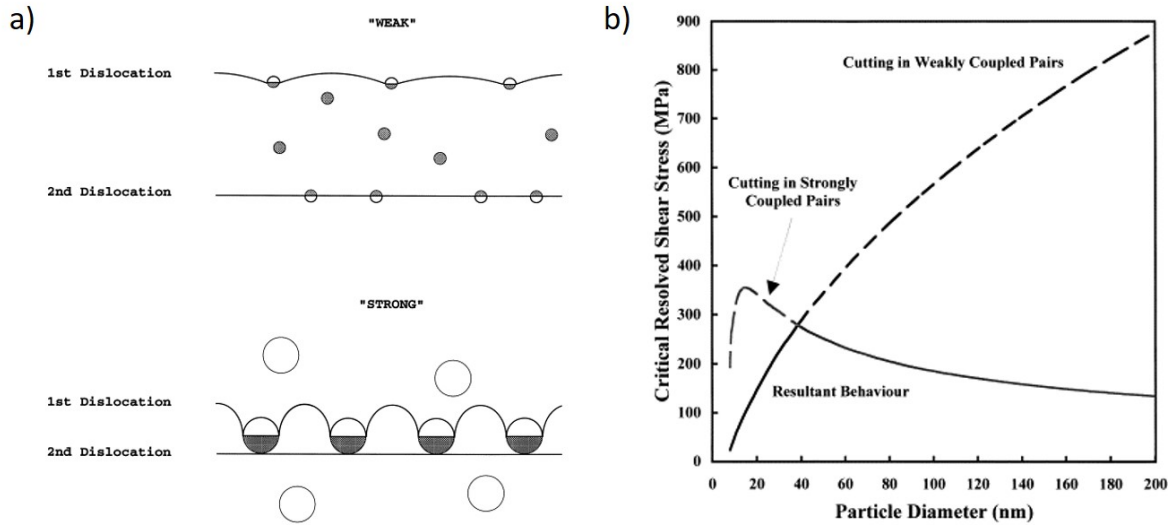


Figure 2.4: Effect of γ' particle diameter on theoretical critical resolved shear stress [33].

Harte et al. [35] investigated the effect of γ' particle size on deformation in terms of slip and misorientation for RR1000. They reported that the fine- γ' variant had a higher yield strength, as the primary deformation mode was shearing in the strongly coupled regime, whereas the coarse- γ' variant has a more significant contribution from Orowan looping, which causes the strengthening precipitates to be bypassed. The authors also reported that reducing the precipitate size can increase the yield strength as the gaps between precipitates become smaller; In addition, the authors observed that the coarse- γ' variant showed greater early stage strain hardening; when viewed at a finer scale using electron channelling contrast imaging (ECCI), they observed more dislocation interactions and pileups at the γ/γ' interfaces Figure 2.5. In contrast, in the fine- γ' variant, there was additional deformation between slip bands in the form of coupled dislocations and bowing around γ' particles Figure 2.5c). Variations in slip characteristics were also observed, whereby cross slip and diffuse slip were more common in the coarse- γ' variant but were less evident in the fine- γ' variant.

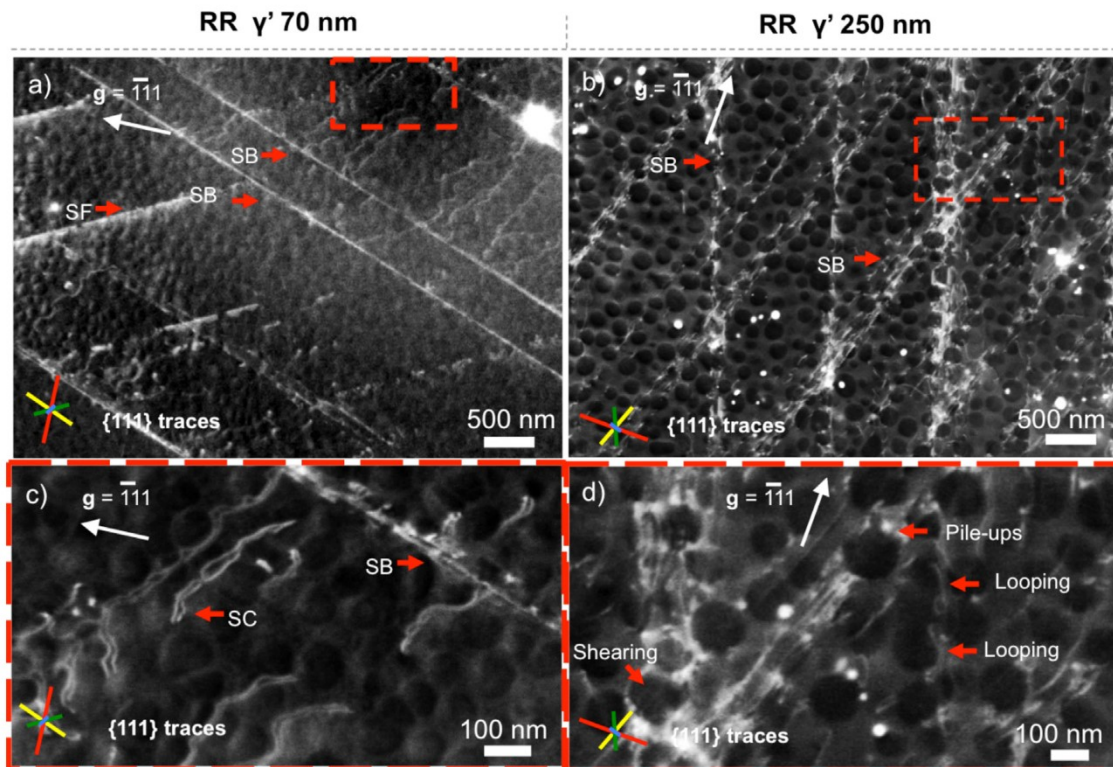


Figure 2.5: ECCI analysis using the $g = \bar{1}11$ diffracting vector for fine-grain precipitate condition: (a) and (c); coarse-grain precipitate condition: (b) and (d). Key: SB = slip band; SF = stacking fault; SC = strongly coupled dislocations [35].

Alloy chemistries are tailored for specific processing routes, which are used to control microstructure and material properties for specific applications. Single crystals are cast using directional solidification to increase creep resistance of turbine blades (Figure 2.6), fine equiaxed structures are also produced to increase fatigue resistance of turbine disks [25]. Historically, the relationship between alloy chemistry and processing has been problematic, since higher Wt.% alloy additions, leads to an increased risk of segregation, especially in large castings [39]. To circumvent this issue, powder metallurgy (PM) processes have been developed to produce fully dense parts without melting, resulting in a superplastic, uniform, fine grained microstructure [39]. Hot isostatic pressing (HIP) and extrusion, or a combination of both, can be used to consolidate the powder, due to the application of heat and pressure [39]. The produced material exhibits a low alloy flow stress, which readily permits further processing via isothermal forging. The HIP process allows the production of near-net forging preforms, as well as near-net machining preforms, which require no additional hot work. This can help reduce buy-to-flight ratios during aerospace manufacturing, and reduce the cost associated with non-critical components [40].

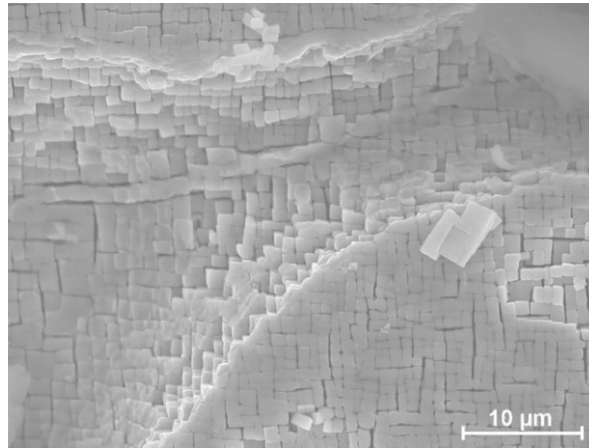


Figure 2.6: Single-crystal microstructure (CMSX-4 alloy), after second stage of ageing fine cubic γ' precipitates can be observed [25].

2.2 Computer Numeric Controlled Machines

The adoption of computer numeric controlled (CNC) machines within industrial manufacturing, has facilitated massive advancements in productivity. If correctly implemented, it allows parts to be manufactured in an automated fashion, with a high degree of control and repeatability. This is particularly useful within research settings, as it allows parameters to be systematically varied with relative ease. Another distinct advantage compared to traditional, manual machining, is that it can be coupled with computer-aided design (CAD), and computer-aided manufacture (CAM), such that processes can be simulated prior to implementation, reducing development time and cost.

2.3 Fundamentals of Machining

Machining defines the act of material removal via subtractive cutting type processes. The umbrella term “machining”, entails a multitude of different cutting operations. Some operations, such as grinding, are abrasive in nature, and material removal occurs due to the interaction of many sharp particles with the workpiece. Other operations, such as turning, milling, and drilling, rely on a sharp edge, or a number of edges, to shear the workpiece material.

Machining operations can broadly be sub-divided into roughing or finishing operations, depending on how much material is to be removed. Roughing is the most aggressive operation, and is generally used further upstream in manufacturing processes, where there is significant material to be removed, and surface quality is lower priority. For this reason, high material removal rates (MRRs) can be employed. In turning type processes, MRR can be calculated

using Equation (2.1), where V_c is the cutting speed measured in $\text{m} \cdot \text{min}^{-1}$, f_n is the feed rate measured in $\text{mm} \cdot \text{rev}^{-1}$, and the depth-of-cut (DOC) is a_p , measured in mm, as such, the resulting units for MRR are $\text{cm}^3 \cdot \text{min}^{-1}$. A typical outer diameter turning process is displayed in Figure 2.7.

$$\text{MRR} = a_p \times V_c \times f_n \quad (2.1)$$

Finishing operations occur at the end of production, and therefore, the surface condition is of paramount concern. In a machining context, surface integrity is a term broadly used to refer to the condition of both surface and subsurface structures that are affected during workpiece deformation. The quality of said structures can be assessed in numerous ways depending on the requirements of the component; some commonly used metrics include: surface roughness, residual stress state (often measured as a profile from surface to bulk), and maximum depth of strain induced by the machining process. Limited accessibility, high cost, and the sometimes destructive nature of these analysis techniques, mean that sampling is typically employed in manufacturing settings to ensure conformance with predefined specifications that have been found experimentally to relate to functional performance, such as fatigue life.

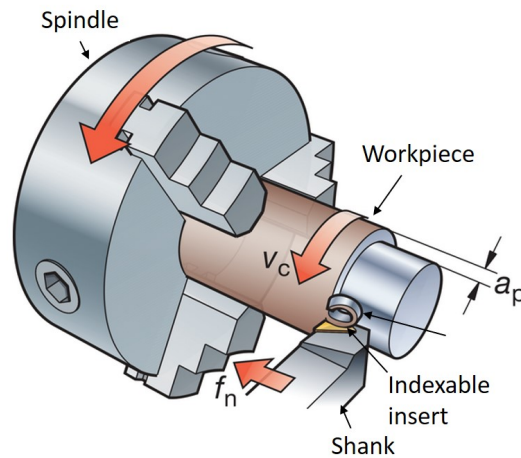


Figure 2.7: Diagram demonstrating a standard OD turning turning setup, alongside the relevant processing parameters (courtesy of Sandvik Coromant.)

2.3.1 Orthogonal Cutting

Orthogonal cutting is a mode of cutting that employs only one cutting edge, allowing a 2D simplification of the cutting process to be performed. It is therefore used extensively to study material deformation characteristics, and to produce finite element method (FEM) models.

True orthogonal cutting will be a planing type operation, whereby the cutting edge is perpendicular to a workpiece, that has a completely straight wall-like profile (Figure 2.8). As long as the workpiece is sufficiently thick, then the plane strain condition is assumed, and side flow of material is neglected. In oblique cutting, the cutting edge is held at an inclination angle λ_s . The chip produced is therefore wider, and flows at a chip flow angle η . A comparison between orthogonal and oblique cutting is presented in Figure 2.8.

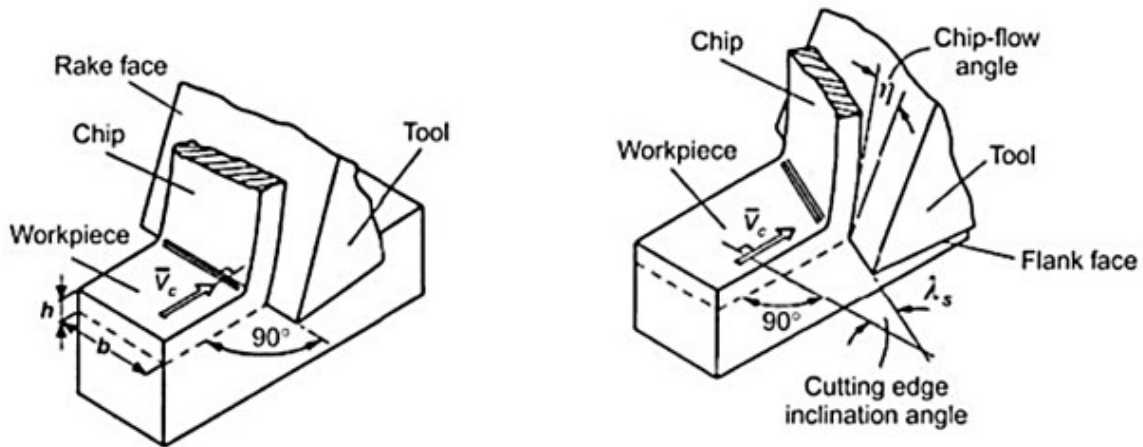


Figure 2.8: Diagram showing comparison of orthogonal and oblique cutting (adapted from [41]).

Merchant Model

The simplification offered by the orthogonal case, gives rise to the 2D Merchant model [42]. First published in 1945, this marked a significant breakthrough in machining science, as it represented the first step in predicting material behaviour during cutting processes. Several key assumptions must be made to facilitate the analysis, these are: the tool is considered to be infinitely sharp, the process is a "true" orthogonal one, and the shear deformation is confined to an infinitely thin shear plane. Within the Merchant force circle (Figure 2.9), the relationship between machining forces, and relevant angles is presented. Of key importance is the shear angle ϕ , which determines whether a thin fast moving chip is formed, or a thicker, slow moving one. During cutting, ϕ will vary in order to minimise energy, and is related to the cutting ratio, which is given by Equation (2.2), in which the theoretical uncut chip thickness is t , and cut chip thickness is t_c .

$$r = \frac{t}{t_c} \quad (2.2)$$

In reality, the Merchant model has been found to be of limited usefulness in terms of predictive machining forces. This is largely due to it's over simplification of the frictional interface

on the tool rake, in which sliding friction is assumed. Extensive experimental study has revealed that during most metal cutting, conditions of seizure are far more common than sliding ones, resulting in significant changes to the chip formation mechanisms [43].

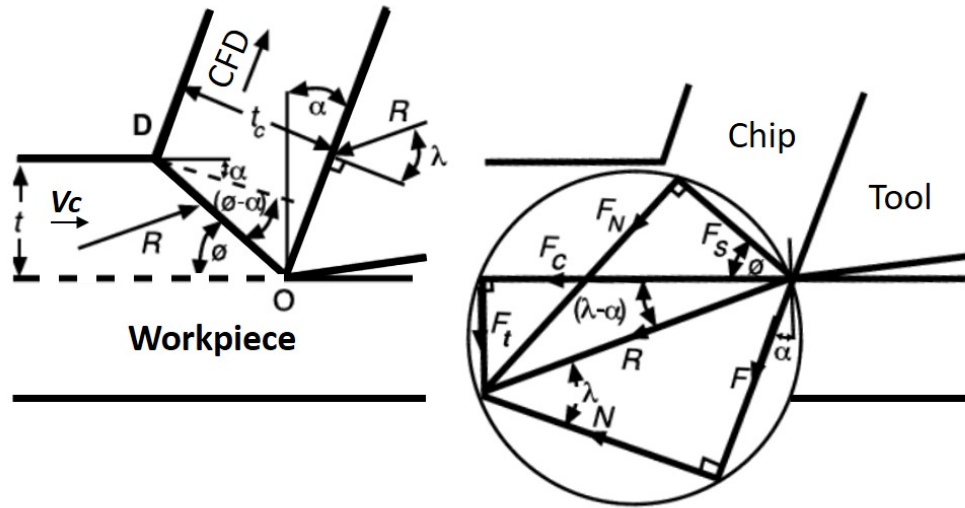


Figure 2.9: Diagram showing geometric features of orthogonal cutting, and construction of Merchant circle (adapted from [43]).

Shear Zones

Plastic deformation of the workpiece material occurs along the shear plane and the surrounding area, referred to as the primary shear zone (I), as seen in Figure 2.10. The energy required is related, according to minimum energy theory, to ϕ , and V_c [43]. In addition to this, there is a rubbing contact in the secondary shear zone (II), as the chip moves in the chip-flow-direction (CFD) along the the tool rake face. Similarly, in the tertiary shear zone (III), there is an interaction between the tool flank and workpiece (Figure 2.10). The tertiary shear zone is of particular importance, since it relates to the residual stress distribution of the generated surface, which will impact it's in service performance [12, 44]. Deformation in all three shear zones also leads to heat generation, which relates to a multitude of different phenomena, including workpiece softening, tool wear, and workpiece residual stresses.

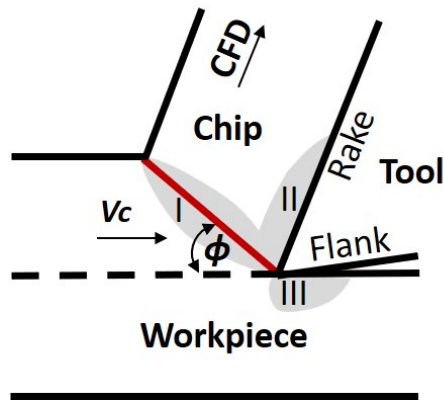


Figure 2.10: Diagram showing approximate positions of primary (I), secondary (II), and tertiary (III) shear zones during orthogonal cutting.

2.3.2 Turning Methods for Machining Research

In turning operations, the workpiece rotates, and the tool remains stationary relative to said rotation, producing parts with a circular cross-section when viewed from the plane normal to the axis of rotation. To machine the required part geometry, the tool can traverse in different directions.

Orthogonal Turning

So-called "orthogonal" turning involves a single cutting edge. Due to the curved nature of the workpiece it is not truly orthogonal, however, if the the workpiece radius is sufficiently large, it is an adequate, and convenient approximation, facilitating longer times in cut compared to planing operations. To achieve this on a regular lathe, a thin-walled tube type, or fin type workpiece can be employed. If a thin-walled workpiece is utilised, then the tool will move along an axial vector that is parallel to the axis of rotation; if a fin type workpiece is used, then the vector traversed by the tool will be radial. Cutting speed in turning, also called surface speed, is calculated as the product of the spindle speed, and the machined part circumference.

If the spindle speed, and the machined part circumference is known, then the cutting speed (V_c) can be calculated using the following equation:

$$V_c = \frac{\pi \times D_m \times n}{1000}$$

where V_c is the cutting speed in $\text{m} \cdot \text{min}^{-1}$, D_m is the turned diameter in mm, and n is the

spindle speed in RPM.

Comparing these two methods, a distinct advantage of the tube type approach, is that since the circumference remains consistent, a constant cutting speed will be maintained. Conversely, when using a fin type setup, if the RPM remains constant, then the effective surface speed will drop as the tool moves towards the centre. To combat this, n can be increased as the machined circumference reduces, as a result, the consistency of the cutting speed will depend on the effectiveness of the lathe controller, which will vary on different systems. Considering the efficiency of material usage, if the starting material is a cylindrical billet, then the fin type approach will involve less material waste. In either case, using a lathe is often preferable to a planing setup, since it facilitates longer times in cut, and utilises relatively compact workpieces. One issue with this kind of approach is the accumulation of heat, which is less easily dissipated, due to the lower thermal mass of a thin workpiece. Nevertheless, this technique is frequently used within research settings, in order to measure material properties, thermal behaviour, and tool wear [45, 46, 47, 48]. Additionally, it can also be employed during operando machining experiments, when using transmission x-ray diffraction techniques, allowing the strain evolution in tool coatings, and the deformed workpiece to be measured [49, 50, 51].

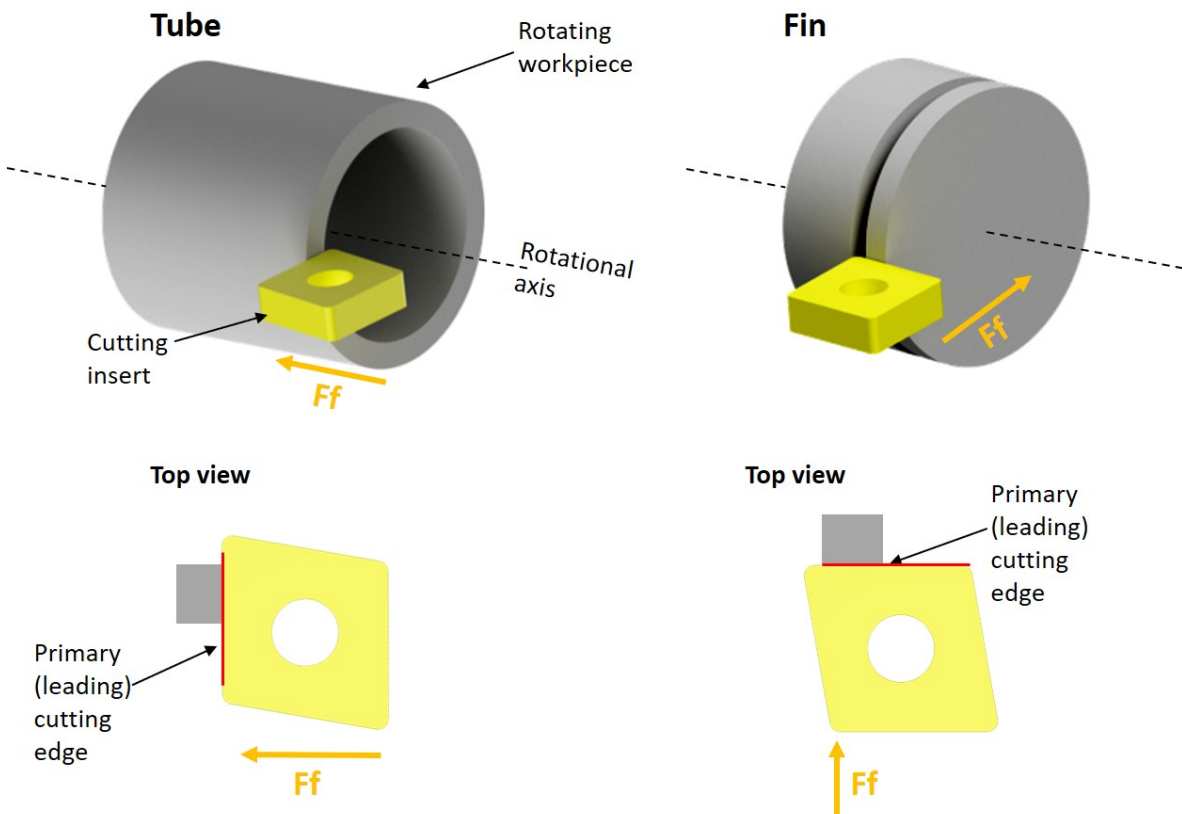


Figure 2.11: Diagram demonstrating the difference between different tube type and fin type orthogonal lathe setups commonly used in research settings.

Conventional Turning

In conventional turning (i.e. involving a primary and an auxiliary cutting edge), when the tool moves axially whilst contacting the spinning workpiece, this is referred to as outer diameter (OD) turning, conversely, when the tool moves radially, then this is called facing. This is shown diagrammatically in Figure 2.12. OD turning and facing, are analogous to orthogonal turning of tube type, and fin type workpieces, respectively, exhibiting the same behaviours in terms of cutting speed variation. Unlike orthogonal turning setups previously discussed, this mode of turning is commonplace within industrial, and does not require a simple cylindrical workpiece. These factors, coupled with minimal material waste, make conventional turning the preferred choice for tool wear studies in research settings.

During conventional turning, the cutting conditions can be controlled by changing 3 main parameters: (V_c , f_n , and a_p). To calculate V_c , Section 2.3.2 can be used. f_n describes the length the tool will traverse in the feed direction, during one workpiece rotation. The DOC, measured in mm, can be defined as the difference between the uncut and cut diameters, divided by two. The product of these parameters gives the MRR, as per Equation (2.1).

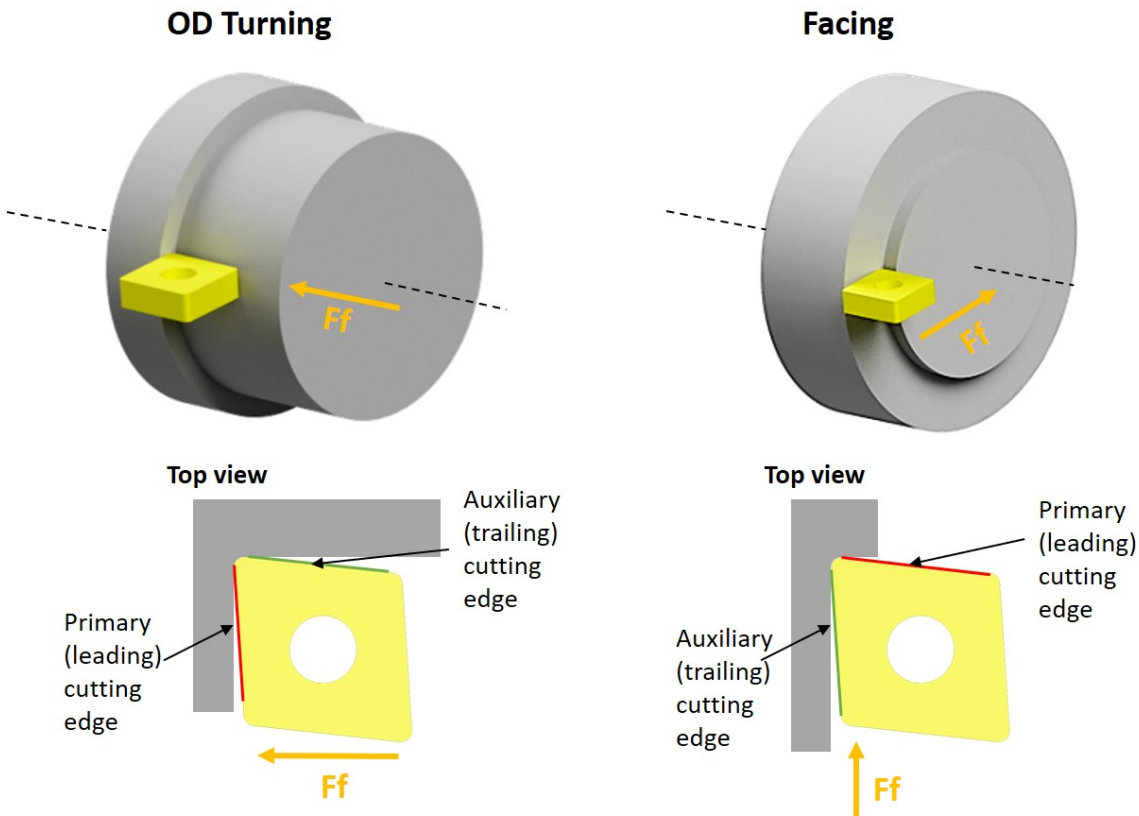


Figure 2.12: Diagram demonstrating the difference between OD turning and facing operations in terms of feed direction, and the position of primary and auxiliary cutting edges.

2.4 Design of Cutting Tools

Cutting tools can be tailored to suit the demands of specific machining conditions, which is related to the process and material being machined. Said tailoring is commonly achieved by altering the geometry, substrate material, and coating. As a result, cutting tool manufacturers produce thousands of different variants to help optimise machining operations and improve efficiency.

2.4.1 Tool Materials

Tool material selection is a key component of implementing effective industrial machining. The two key characteristics that dictate a tool's machining performance are hardness and toughness. It is often the case that when one is increased, the other decreases, hence, there is often a compromise to be made, which will depend on the specifics of the workpiece material, and the machined part geometry. Figure 2.13 shows the relationship between hardness and toughness for different tool materials; we can imagine that the perfect tool material would sit in the top right of this graph. It is interesting to note that cemented carbides sit more or less in the middle of the graph. It is for this reason that they find such widespread use in machining applications, as they provide a good balance in properties.

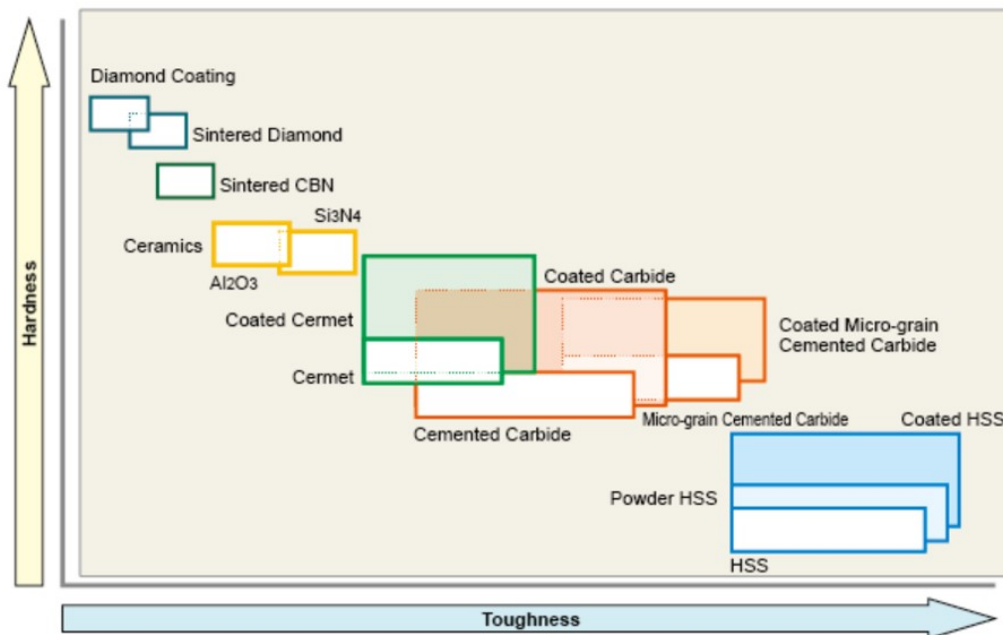


Figure 2.13: Tool material selection graph, showing hardness against toughness for different tool materials [52].

The use of coatings allows the performance of many engineering materials to be greatly increased, this is especially true with regard to processes that occur at the surface, such as corrosion, and wear. Coating technology has rapidly advanced over the last 60 years, and there is a significant body of academic work aimed at developing superior coatings, by better understanding coating deposition, and degradation in-service [53, 24, 54, 55]. Within machining, coatings are commonly used to protect an underlying substrate from abrasive, chemical, diffusive, and adhesive wear mechanisms, and to enhance the tool performance due to degradation resistance of the coating itself. They may also help to reduce machining forces by lowering friction in regions where the tool and workpiece material interact [56].

2.4.2 PVD Coatings

Physical vapour deposition (PVD) is a vacuum coating process in which the source material is vaporised, and then condensed onto a solid substrate. This must be performed in the presence of reactive gases such as nitrogen (N_2), or oxygen (O_2). Said gases will interact with the vaporized particles, which results in the deposition of nitrides, oxides, or carbo-nitrides on the substrate surface. Compared to chemical vapour deposition (CVD), PVD processes offer several advantages, including the ability to be processed at much lower temperatures. This can be advantageous for a number of reasons, such as: lower thermal stresses, compatibility with a broader range of materials, better energy efficiency, and reduced risk of unwanted chemical interactions promoted by higher deposition temperatures.

In PVD processes, different energy sources can be used to evaporate the source material to produce thin films: focused electron beams, high-energy lasers, and high-density arcs. The process is effectively controlled by altering key processing parameters: substrate temperature, operating pressure, and the types of reactive gases. This in turn influence the thickness, structure, internal stresses, substrate, and adhesion of the deposited coating, which will alter the mechanical properties, and its in service performance.

The earliest commercialised PVD coatings utilised in machining were TiN. This was later followed by TiCN, TiAlN, and many other similar compounds. Electron beam evaporation is often used for Ti coatings, as it offers good adhesion, whilst minimising interfacial stress. This is performed in a Ni atmosphere. To produce multilayer coatings, sputtering methods are typically used to improve adhesion, and to limit interfacial stresses [57, 58].

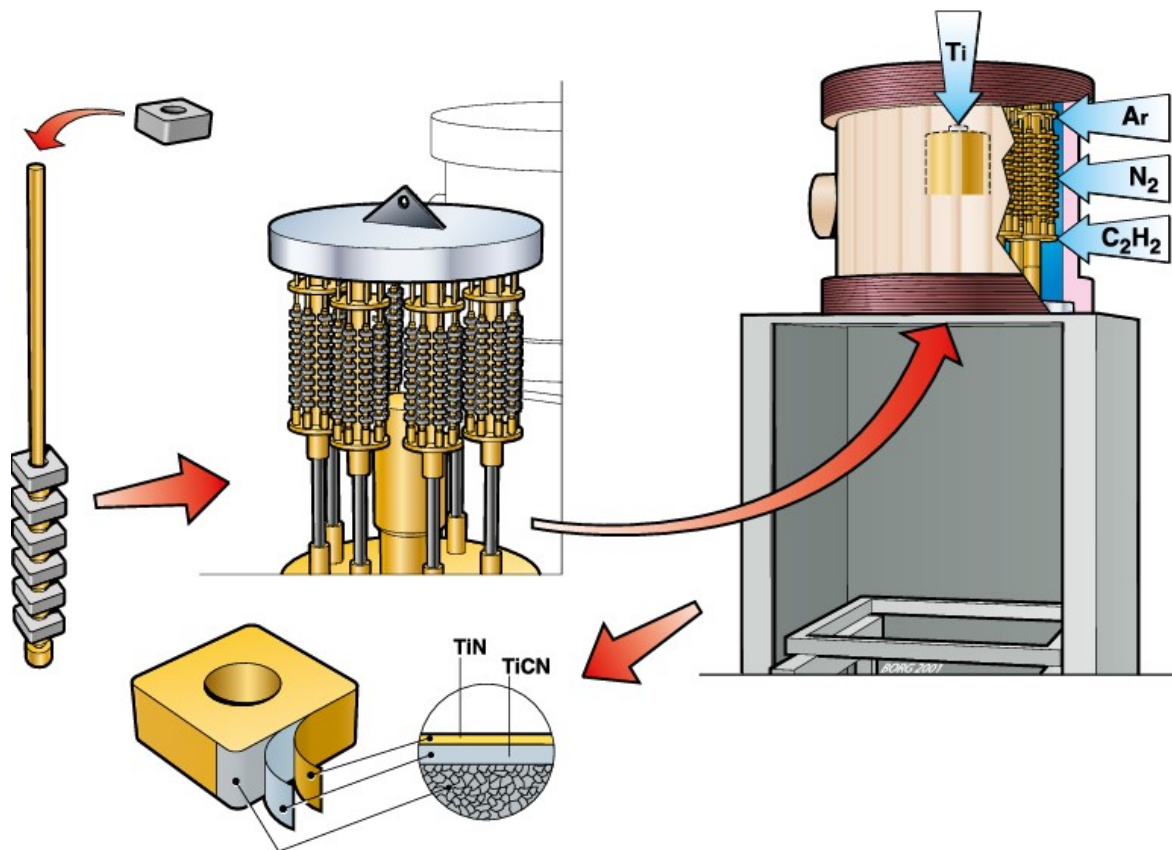


Figure 2.14: PVD coating process to produce multilayer TiCN coatings (courtesy of Sandvik Coromant).

2.4.3 CVD Coatings

Chemical vapour deposition (CVD) is a coating method that can be employed for a variety of different applications, these include: wear-resistant coating for machining, thin-film semiconductors, and biocompatible coatings [53, 59, 60].

CVD is widely used for cutting tool applications, due to its ability to produce thick (5-40 μm), chemically stable coatings, with a high level of control. During the CVD process solid material is deposited onto a solid substrate surface from a gas mixture, which occurs through chemical reactions between the gas reactants, and interactions with the substrate surface. Typically, said reactions, can be initiated and sustained by either heat (thermal CVD), or ions and electrons (plasma activated CVD).

Compared to PVD, CVD offers several advantages, including its ability to cover irregularly shaped surfaces. In addition, CVD technology facilitates the rapid deposition of pure mate-

rial, without the need for the high vacuum levels. α -alumina, κ -alumina, TiC, TiN, and TiCN, are some of the most widely used CVD coatings [61]. During cutting tool manufacture, cutting inserts are typically coated using thermally activated processes in hot-wall CVD reactor. This allows many cutting inserts to be coated in a single process cycle.

To be effective in cutting tool applications, coatings must endure high pressures, in the GPa region, and high temperatures, around 1000°C. The later is of particular importance, as many wear related phenomena, such as chemical wear, are accelerated by it. Other considerations for coating selection include high hot-hardness, to limit abrasion wear, and limited affinity with the workpiece, to limit adhesive wear.

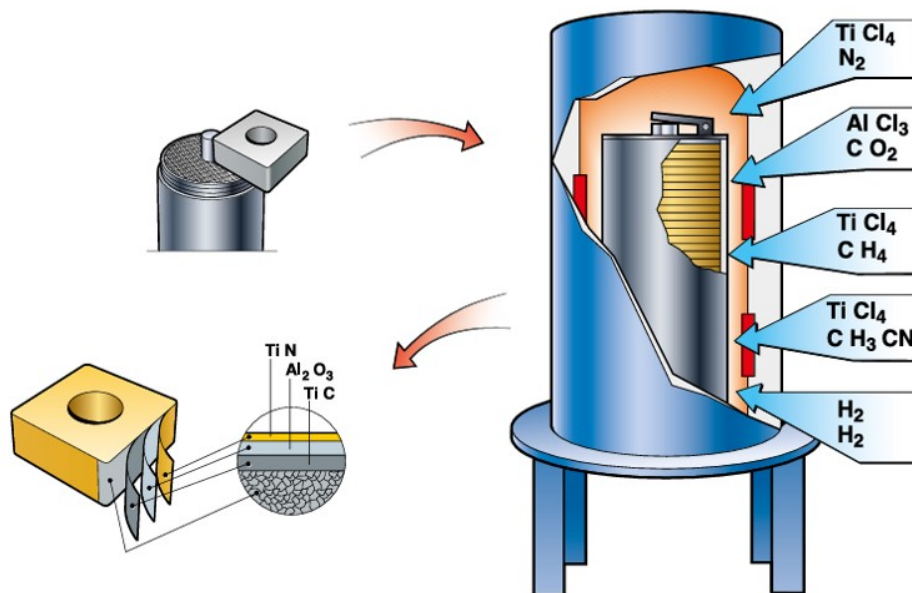


Figure 2.15: CVD coating process to produce multilayer alumina coatings (courtesy of Sandvik Coromant).

Alumina phases

Aluminium oxide, also known as Alumina, can exist in multiple polymorphic forms, all with the same chemical formula Al_2O_3 , which can be obtained by heating a precursor Al hydroxide (Figure 2.16). Each polymorph exhibits subtly different crystallographic configurations. There is ongoing debate regarding whether these are genuinely new phases, or if they result from absorbed inter-lamellar water and impurities. In applications requiring wear-resistant coatings, such as machining, only stable alpha-alumina (α -alumina), and metastable kappa-alumina (κ -alumina) are employed; the later is generally inferior as it will decompose during machining into the stable α -alumina form, which is accompanied by a volume decrease,

and subsequent cracking [62]. It has only been in the last two decades that pure α -alumina coatings could be manufactured [53], prior to this, only mixed coatings consisting of both κ -alumina and α -alumina were achievable. Given its chemical stability, hot corrosion resistance, high hot hardness, high melting point, and low thermal conductivity, α -alumina is ideally suited to conditions at the tool-chip, and tool-workpiece interfaces.

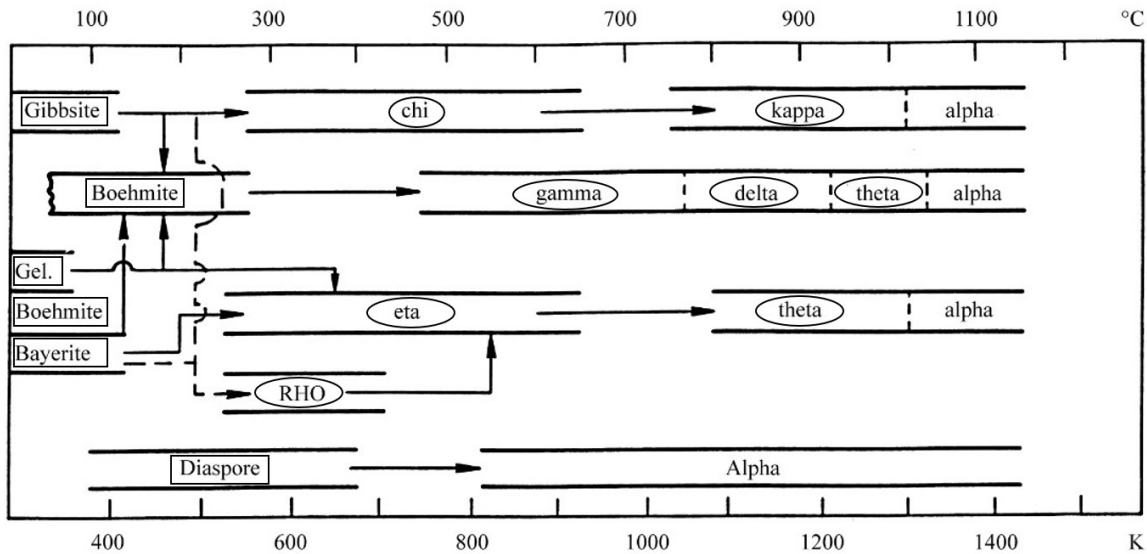


Figure 2.16: Thermal transformation sequence of alumina hydroxides. Hydroxides are in square boxes, and transition aluminas are in epileptical ones (adapted from [63]).

α -Alumina

The crystallographic structure of α -alumina is referred to as the corundum structure, the unit cell is shown in Figure 2.17. Six parallel (0001) planes of oxygen ions are stacked in a $\alpha A\beta B\gamma B\alpha A\beta B\gamma$ sequence. In each layer of oxygen ions, there are octahedral voids where Al^{3+} ions can reside; in the corundum structure, two-thirds of these voids will be filled.

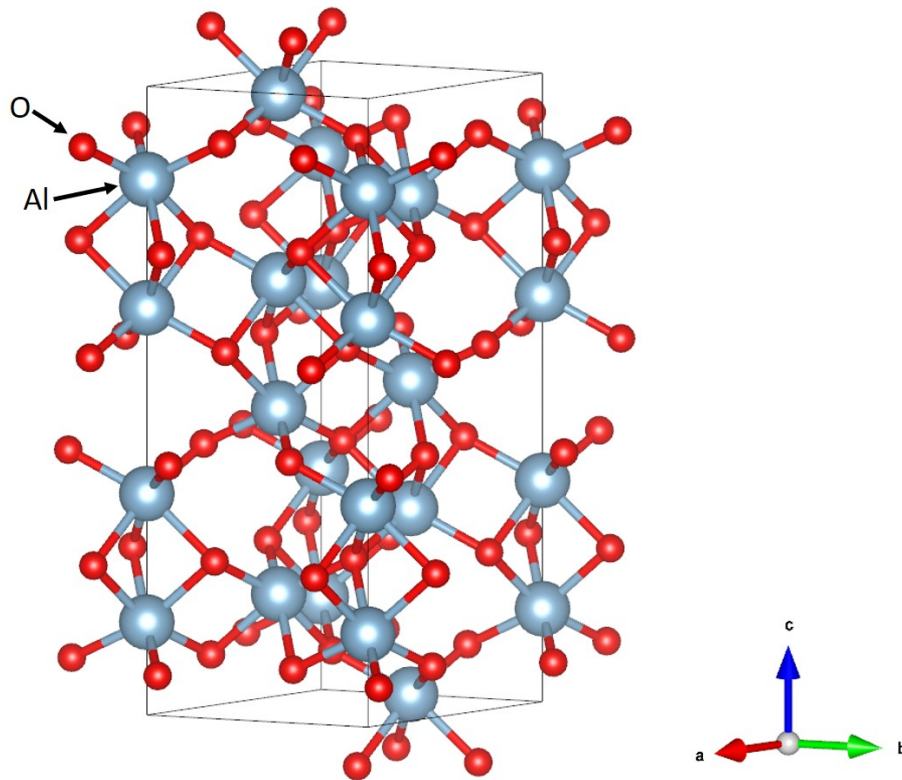
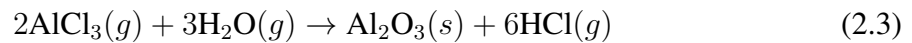


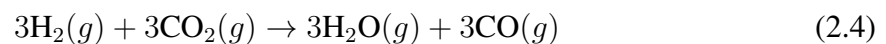
Figure 2.17: The α -alumina unit cell; made using VESTA 3.

CVD Alumina Coatings

CVD alumina coatings can be obtained via the $\text{AlCl}_3\text{-H}_2\text{-CO}_2$ system, and there is substantial body of research concerning their deposition dating back 50 years [64, 65, 66]. The formation of solid Al_2O_3 from the gas mixture is based on the hydrolysis of AlCl_3 by water, and is shown below:



The water is produced from the high-temperature reduction of CO_2 by H_2 , which controls the deposition rate:



Combining Equation (2.3) and Equation (2.4), the overall reaction can be expressed as follows:



One limitation of this technique, is that the growth of alumina is highly sensitive to impurities, such as Co, which can lead to irregular crystal growth, and poor coating adhesion. Since Co is present in the binder phase of cemented carbide substrates, an intermediate layer between the substrate and the alumina layer is typically applied.

Modern pure α -alumina CVD coatings exhibit a large grained microstructure, ranging from approximately 1–5 μm . To form highly textured coatings, temperatures above 1000°C are required.

2.4.4 Tool Geometry

In reality tools are not infinitely sharp as presented in Figures 2.9 and 2.10, and even if they could be manufactured to have this geometry, in many instances they would not be optimal, and may lack adequate toughness to handle fluctuations in the machining force response. Therefore, edge geometries are tailored by cutting tool manufacturers to suit specific applications, which will effect not only the tool wear, but also the surface of the machined part. The term Edge rounding (ER), describes the sharpness of a cutting edge in terms of the inscribed circle that can be drawn between the tool rake and flank, which influences the magnitude of machining forces [67].

The shape of the cutting edge is linked to the residual profile of the machined surface [68, 69, 70, 71]. This occurs as a result of the ploughing effect, which describes the "ironing" of workpiece material that flows underneath the cutting tool. The ER of a tool influences the formation of a "stagnation zone" in front of the progressing tool (see Figure 2.18). In the stagnation zone, no material flows, as such, its presence will influence how much material will flow under the tool. In essence, stagnated material will perform as if it is part of the tool itself. The shape of this zone is also influenced by other geometric characteristics of the tool, such as chamfering [68]. The height of the material that is ploughed by the tool is shown in Figure 2.18 as h_o . This can be subtracted from theoretical uncut chip thickness t to give the actual uncut chip thickness t_a . The amount of material that flows beneath the tool, impacts the stress distribution, and the thickness of the machining affected layer thickness h_p . This behaviour can be modelled effectively using the finite element method, in order to tailor surface properties and performance, via edge geometry selection [68].

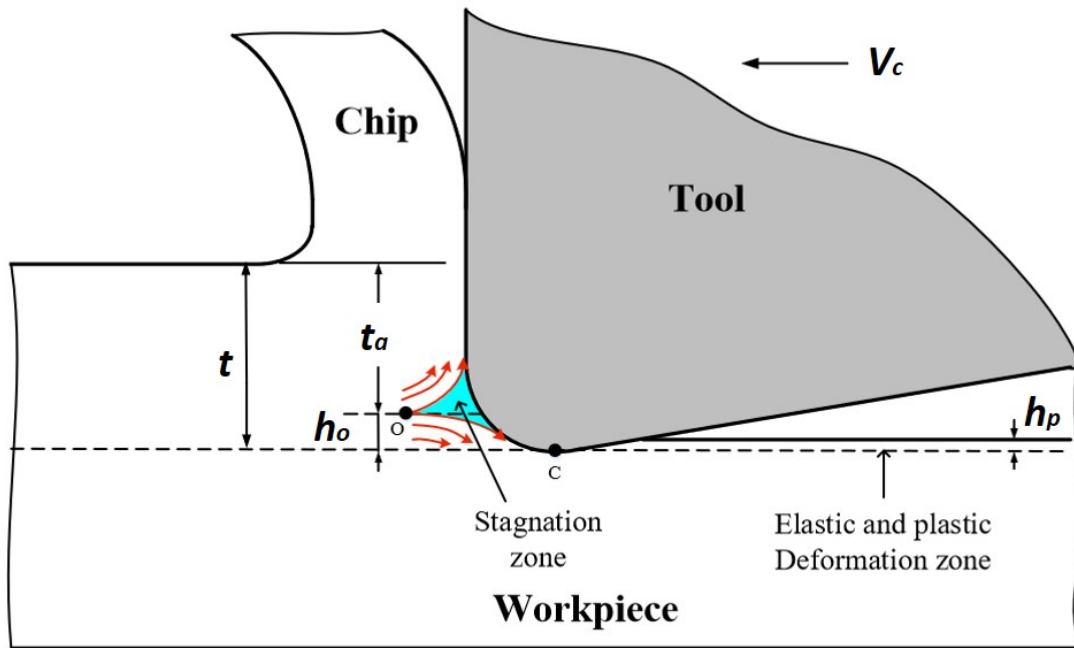


Figure 2.18: Diagram showing the ploughing effect during orthogonal cutting (adapted from [68]).

Figure 2.19 displays the relationship between nose radius and feed rate during turning, whereby larger feed rates can be achieved for tools with larger nose radii (r_ϵ). A larger nose radius results in a stronger edge, meaning that it will be more suited to operations involving interrupted cuts, or machining inhomogenous material. However, a larger nose will also increase the contact area, leading to higher machining forces and cutting temperatures, and therefore, increased tensile residual stresses in the machined surface [72], which are detrimental to fatigue life.

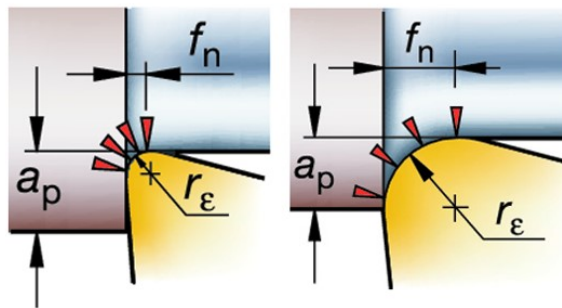


Figure 2.19: Diagram showing influence of tool nose radius (courtesy of Sandvik Coromant)

Another consideration that can influence the integrity of the machined surface, is the micro-

geometry of the rake face. To assist chip control, many inserts feature rake face geometry that increases the curvature of the formed chip. This is achieved by locally changing the effective rake angle from positive to negative, as seen in Figure 2.20. The presence of a chip breaker will impact the cutting mechanics, and alter the stress state of the machined surface produced [72].

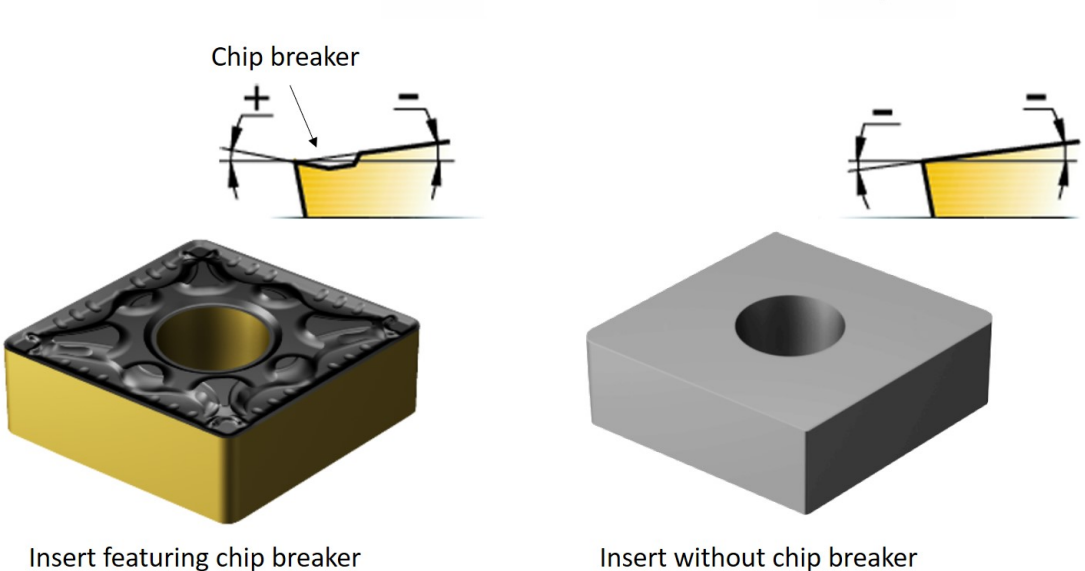


Figure 2.20: Diagram showing the difference between an insert featuring a chip breaker, and one that does not (courtesy of Sandvik Coromant).

2.5 Tool Wear

During a cutting tools life, the wear rate varies depending on the condition of the cutting edge, which in turn is related to the amount of material that has been machined. The early work on the subject was performed by Taylor [73], giving rise to the famous Taylor equation, which relates cutting speed to tool life. Taylor identified three distinct regions of flank wear rate over a cutting tools lifetime, as shown in Figure 2.21: a rapid initial wear regime (I), a steady state wear regime (II), and finally a rapid, fatal wear regime (III). It should be noted that recent development in high speed machining, and new tool materials, have shown that increasing cutting speed can in many instances increase tool life [74].

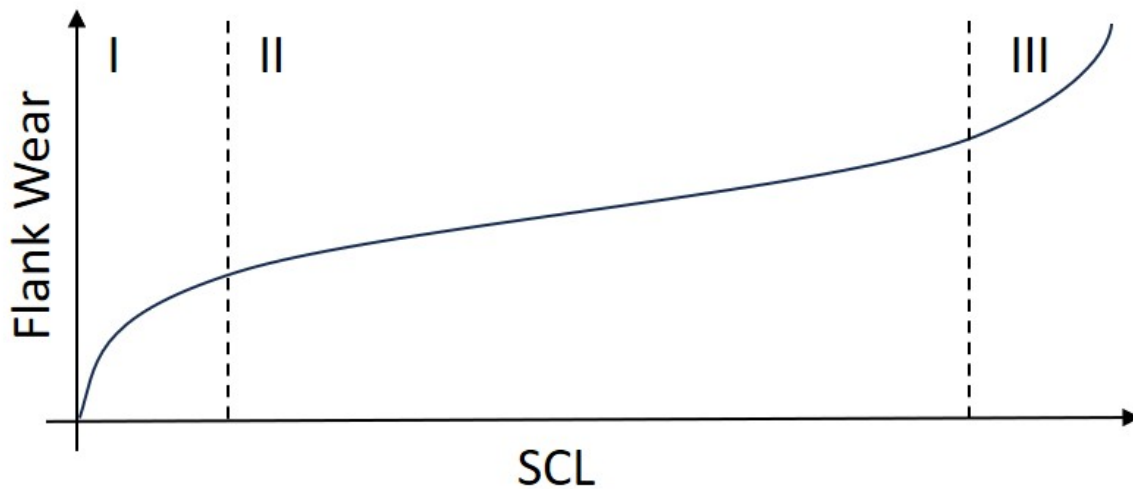


Figure 2.21: Diagram showing typical flank wear variation against spiral-cut-length (SCL).

2.5.1 Wear Mechanisms

Regardless of tool selection, the extreme conditions present at the tool-chip and tool-workpiece interfaces, lead to a combination of different wear mechanisms, often acting simultaneously. This inherent complexity, makes the study of worn surfaces challenging, and careful observation is required to separate the contribution of different effects.

Abrasive

Abrasive wear occurs as a result of a hard material, or material of equal hardness, interacting with a softer one. In metal cutting, these hard particles may be inclusions or precipitates, originating from the workpiece material, they can also originate from regions of the worn tool that have been dislodged. Abrasive wear can be subdivided into two-body, and three-body abrasion Figure 2.22. Two-body abrasion involves the wearing of asperities as two surfaces move against one another in opposite directions. Three-body abrasion involves additional free moving particle that lie between the two surfaces. Two-body wear can be divided further based on the damage that is caused to the workpiece material, these are: cutting, fracture, ploughing, and grain pull-out. This is shown diagrammatically in Figure 2.23.

Cutting typically occurs when sharp, hard asperities move across a soft, ductile material. This results in the loss of displaced material in front of the advancing abrasive particle. On the other hand, fracture occurs when the abraded surface is brittle, and material loss occurs as a result of crack convergence. If the abrasive asperities are blunter, and the abraded material is

soft, then cutting is less likely, and repeated plastic deformation can lead to local fatigue at either side of the formed groove, due to side-flow. Finally, if the abraded material is brittle, and has weak intergranular bonds, then grain pull-out may also occur.

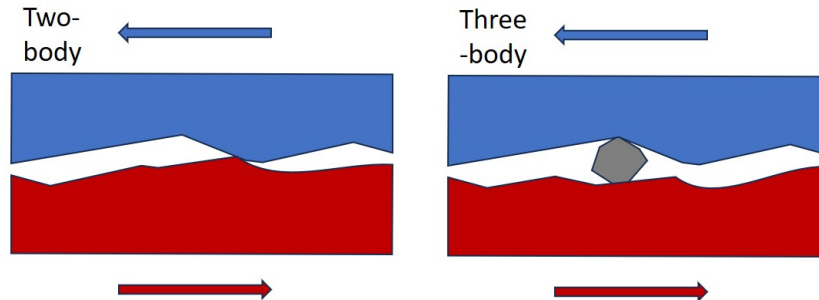


Figure 2.22: Diagram showing the difference between two-body and three-body abrasive wear.

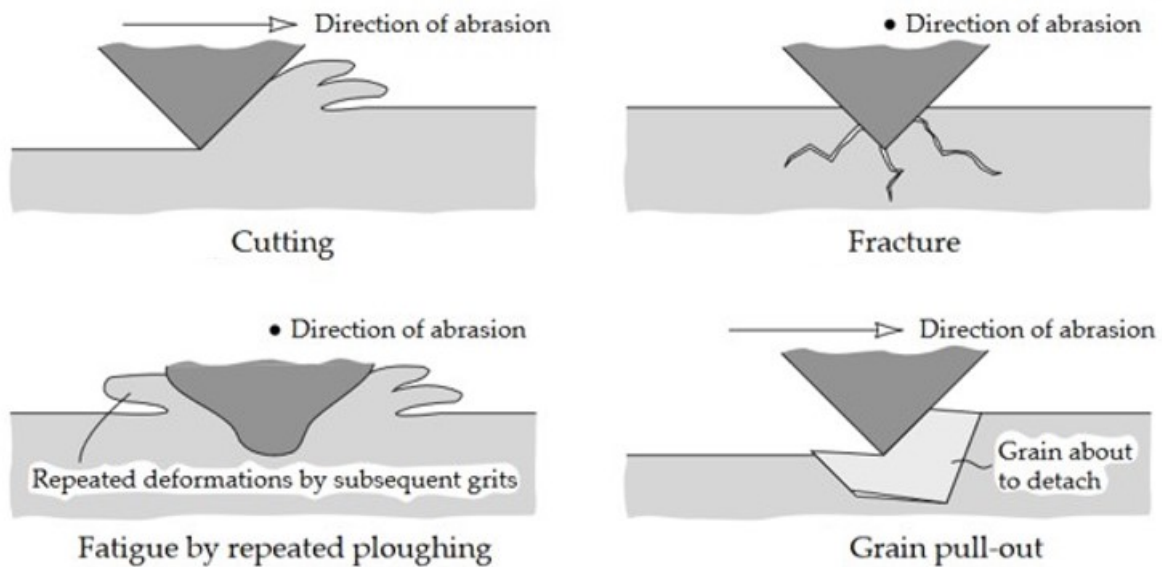


Figure 2.23: Diagram showing types of two-body abrasive wear (adapted from [75]).

Adhesion and Attrition

Adhesive wear occurs via localised welding at the tool-chip, and tool-workpiece interfaces, due to a combination of high pressure, and a chemical affinity that exists between tool and workpiece material. This behaviour will likely be promoted by higher cutting temperatures, and increased workpiece softening. The amount of tool material loss is often related to the strength of the new bond that forms at the interface. If this bond is stronger than the bonds

within the tool, then the shearing action of the workpiece material moving across the tool surface, will result in fracture of the tool material, and subsequent material loss. Conversely, if the adhered material remains in place, then it provides a site for chemical reactions to occur (see chemical and diffusion below).

Attrition wear describes material loss as a result of stick-slip contact conditions, whereby there is a cyclical transition from adhesion to sliding. The irregular flow of material necessary for this mechanism of wear, often occurs when machining inhomogeneous, ductile materials, where there is a tendency to produce discontinuous chips. This results in a rough surface topography of the worn tool, due to localised coating pull-out and intergranular fracture.

Chemical and Diffusion

Chemical wear refers to chemical interactions that occur during machining, which culminate in the loss of tool material. This can include the formation of new reaction products, or the diffusion of elements into a particular phase. In some regions of the tool, where pressures are lower, oxidation of the tool material can also occur. In the machining case, there is a continual refreshment of workpiece material, that has no protective oxide, and is heavily deformed (meaning there are more diffusion pathways); in contrast, the tool has only a fixed amount of material. These boundary conditions mean that the concentration of minor alloy additions in the workpiece, can become enriched on the tool surface. New phases may then form that can be easily removed by high shear stresses, resulting in loss of tool material.

Diffusion, or diffusive wear, can occur in both directions of an interface, i.e., tool material can diffuse into the workpiece, or workpiece material can diffuse into the tool. The later, can cause the tool to be weakened, and promote material loss in this manner [76]. In some instances, protective layers called tribolayers can also be formed by reactions at the tool-workpiece and tool-chip interfaces, which can prevent diffusive wear [77]. As such, these interactions are not considered chemical wear mechanisms, as they will extend tool life.

Temperature Effects on Wear Balance

The active wear mechanisms are dependant on processing parameters, especially cutting speed, since this has the greatest impact with regards to local temperatures in the contact zone [15]. Figure 2.24 shows how cutting temperature is related to different wear mechanisms. It can be observed that abrasion is relatively consistent throughout, whereas chemical wear (diffusive wear and high temperature oxidation) begins at an intermediate temperature, after which point, it increases expectationally. Conversely, adhesive wear starts at lower temperatures, increases to a maximum, and then begins to decrease as chemical wear starts to dominate. In reality the size and shape of these curves will be dependant on both tool and workpiece materials, as well as other factors, such as lubrication.

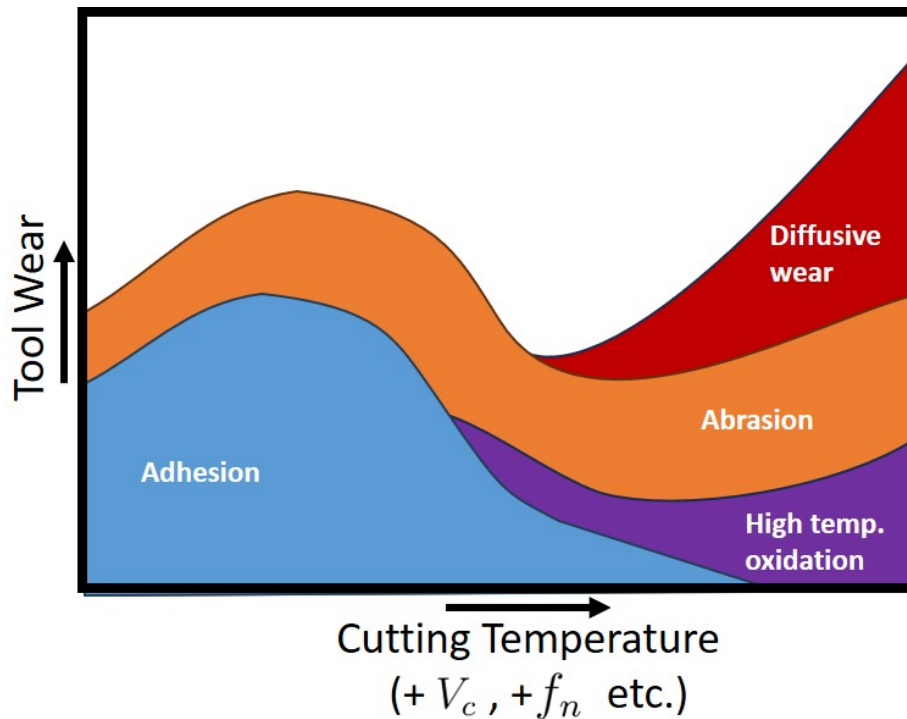


Figure 2.24: Diagram showing influence of temperatures on active wear mechanisms [78].

2.5.2 Wear Types

The wear mechanisms described in previous section culminate in visible wear types on worn cutting tools, as seen in Figure 2.25. These wear types often involve several different wear mechanisms working simultaneously. They are also related to the processing parameters employed. For example, machining at higher speeds will lead to higher cutting temperatures and accelerate crater wear, as such, crater wear will tend to be the life-limiting wear type. Conversely, at lower cutting speeds, the crater wear rate is reduced and flank wear will tend to be the life-limiting wear type. In practical terms, this means machinists can use wear types to identify whether or not the optimum parameters are being employed i.e. if inserts are failing due to cratering, then the process may need to be slowed down, whereas, if inserts fail due to reaching flank wear limit, then the cutting speed could be increased. In terms of the machined part, flank wear has a greater influence on surface quality, as it effects the frictional interaction in the tertiary shear zone. Crater wear can also influence this, although the greater risk is total failure of the cutting edge, as cratering leads to a progressively weaker cutting edge.

Considering industrial machining practises, certain features, especially for critical aerospace parts, must be machined in a single pass. To increase efficiency, it is common practise for

cutting speeds to be increased well outside of their recommended parameters, so that the tool is fully worn in a single pass; therefore, the study of thermally accelerated wear phenomena is of paramount importance when developing tooling solutions.

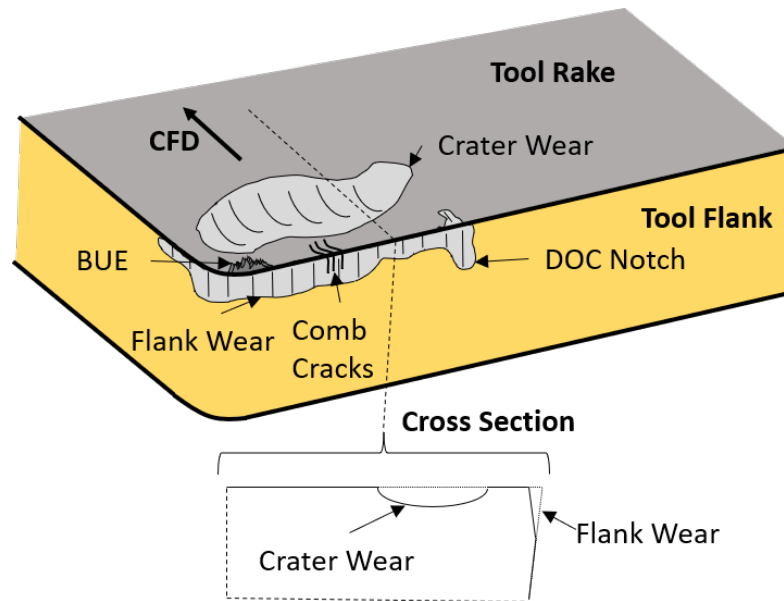


Figure 2.25: Diagram showing typical features of a worn cutting insert (adapted from [79]).

Flank Wear

Flank wear occurs on the tool flank (Figure 2.25), and is often used as a measure of wear limit during machining processes. Generally speaking, it is considered the preferred wear type, due to its predictable nature. It is often attributed primarily to abrasive type wear phenomena, caused by hard particle in the workpiece material. Flank wear does not tend to occur consistently across a cutting edge, hence an average is typically taken, as well as the maximum. If either of these values exceed a certain threshold, commonly referred to as VB, then the worn tool will be replaced by a new one.

Crater Wear and Discrete Plastic Deformation

Crater wear occurs on the tool rake (see Figure 2.25), where temperatures are highest, and where there are significant shear stresses acting on the tool [43]. In many cases, it is caused primarily by chemical wear, however, it can also involve abrasive mechanisms [80]. In the case of alumina coated tools, local plastic deformation of the tool surface due to shear also contributes, which occurs as a result of temperature dependant slip [81]. For alumina coated

tools the mechanism was first presented by Dearnley [82], and is shown diagrammatically in Figure 2.26.

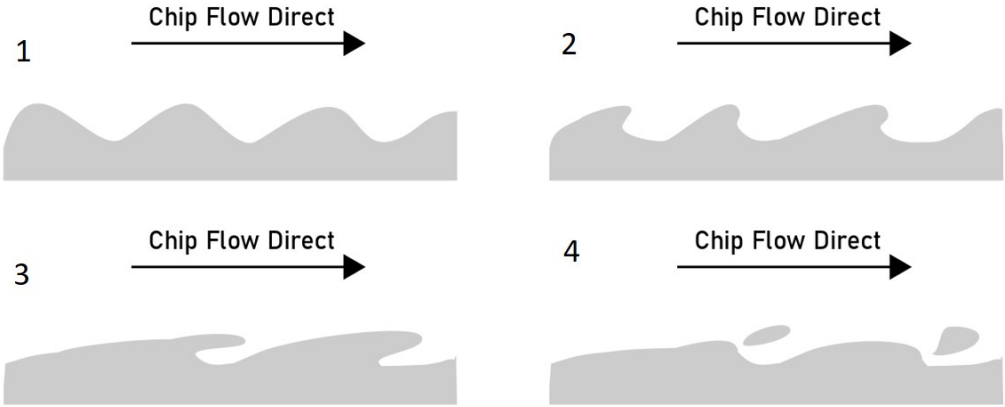


Figure 2.26: Diagram showing steps for progressive material loss via discrete plastic deformation mechanism (adapted from [82]).

Bulk Plastic Deformation

The term "Plastic deformation", is typically used by machinists when referring to plastic deformation of the underlying substrate material, as a result of high temperature and compressive stresses. Depending on the specifics of the process and local temperatures, this can either result in an impression, or a depression of the cutting edge (Figure 2.27). This behaviour is often detrimental to performance, as it alters the geometry of the cutting edge.

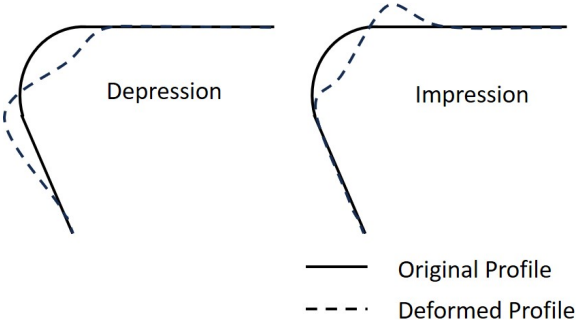


Figure 2.27: Diagram showing plastic deformation under compressive stress schematics for: depression, and impression.

Coating Delamination (Flaking)

Tensile forces can develop during machining due to the formation of a strong interface between the tool and workpiece material (adhesion). In the case of coated inserts, this can lead to coating removal (attrition and adhesion).

Notch Wear

Notch wear occurs around the DOC (see Figure 2.25), as a result of a combination of high stresses caused by work hardening at the machined surface; other factors such as oxidisation, abrasion, and adhesion are also influential. It's formation can be prevented by using appropriate machining strategies, these include: varying the DOC, "rolling" in and out of cut i.e. using an arcing tool path during engagement/disengagement, and chamfering edges prior to tool engagement.

Cracks

The high temperatures that occur during machining can cause cracks to form in coatings and substrates. Comb cracks, as shown in Figure 2.25, run perpendicular to the primary cutting edge, and occur as a result of thermal fatigue; these often occur during intermittent cutting type operations. Cracks that run parallel to the primary cutting edge are more likely caused by mechanical fatigue.

Built-up-edge (BUE)

BUE is a form of adhesive wear localised to the cutting edge, where workpiece material accumulates (see Figure 2.25). It could be argued that BUE is not always a true wear type, since it can even prevent wear to the tool material [83]. However, if the BUE is unstable, it can lead to adhesive wear as it breaks off. It can also serve to increase the machining forces, due to the accompanied change to the tool microgeometry, which can have detrimental effects on the surface quality.

2.6 Machinability

Machinability is often defined as the ease in which a material can be removed during machining. Mills and Redford [84] point out that the actual definition is far more subjective, and that

the term can be used to refer to a multitude of different features related to a machining operation. The importance of each feature will depend on the context of the operation. Common features include: the quality of the machined surface produced, chip control, tool wear rate and the machining force response.

The two central material properties that influence a material's machinability, are the material strength, and the strain at fracture [85]. The combination of these two factors can be used to predict the energy requirements of creating a fracture in the material volume. Most of the energy is converted to heat, which is generated via a combination of plastic deformation, and friction between the tool-chip and tool-workpiece interface. These high temperatures will lead to microstructural changes in the workpiece, that will result in a graded structure, whereby the properties of the sub-surface and surface can be entirely different to the bulk material (Figure 2.28) [86].

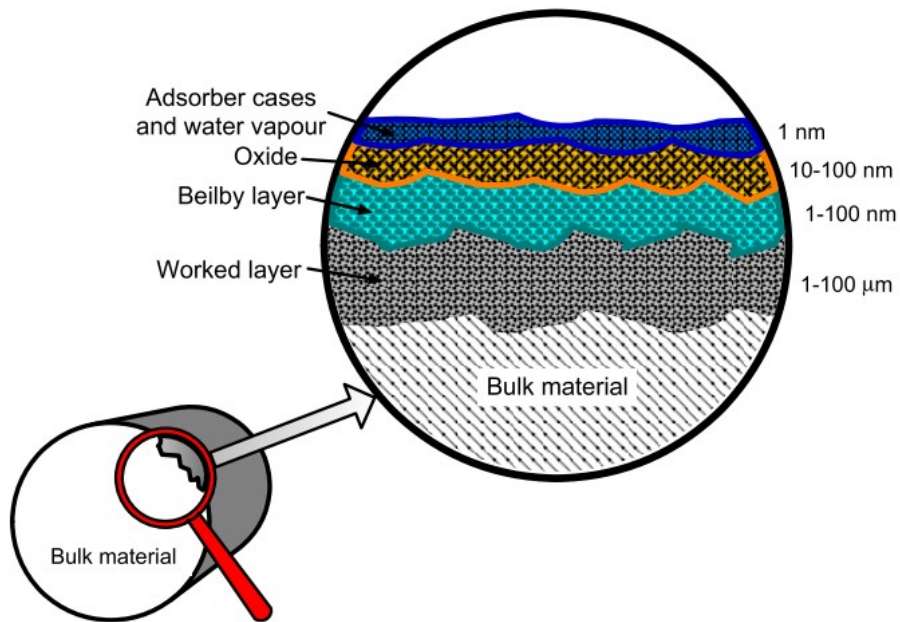


Figure 2.28: Schematic of metal surface [86].

2.6.1 Ni-based Superalloys

Nickel-based superalloy microstructures are tailored to exhibit exceptional performance at high temperature in terms of strength and creep resistance. The same properties that are beneficial in-service lead to challenging machining conditions. Ni-based superalloys are classified as hard-to-machine materials. When machining Ni-based Superalloys, segmented chips tend to form, which leads to cyclic loading of the tool; chip control also tends to be poor, especially at lower cutting speeds. Tool wear occurs via a combination adhesive, attritional, chemical,

diffusive, and abrasive wear mechanisms. The elevated temperatures generated at the tool-chip and tool-workpiece interfaces, accelerate specific wear phenomena (Figure 2.24). Due to these factors, Ni-based superalloys are machined at relatively low material removal rates when compared to other materials, such as steels.

Ni-based superalloys exhibit low thermal conductivities, which leads to high thermal gradients in the cutting zone [15, 87], contributing to the acceleration of thermally driven tool wear phenomena. Workpiece adhesion and work hardening are also especially severe, contributes to depth-of-cut (DOC) notch wear [88, 17]. In addition, the presence of hard abrasive particles within the microstructure are also thought to contribute to the occurrence of abrasive wear when using certain tool materials [89, 17].

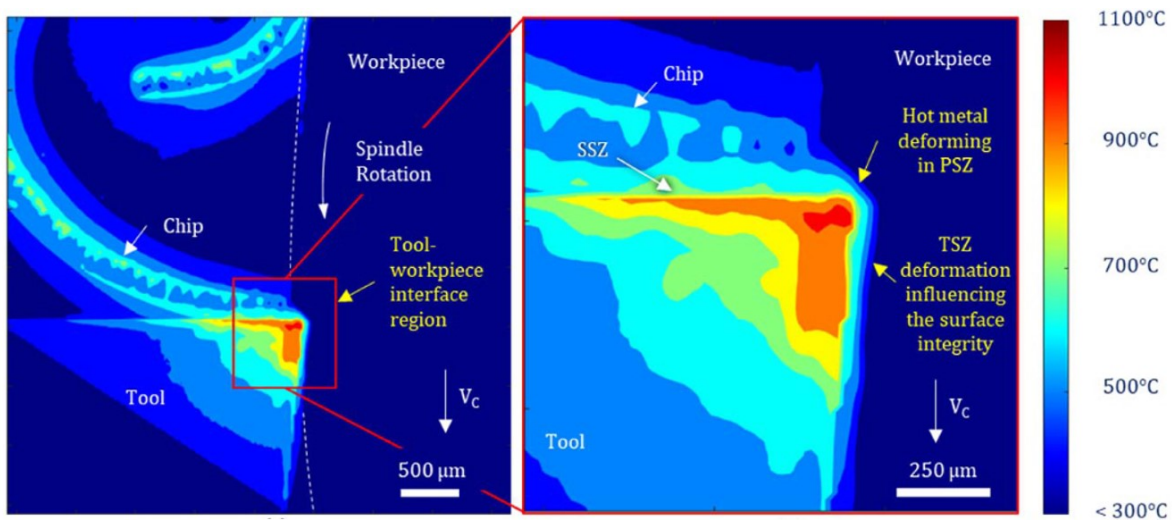


Figure 2.29: IR thermal camera image taken normal to cutting direction, showing temperature gradients during orthogonal turning of advanced Ni-based superalloy using uncoated carbide inserts at a cutting speed of $30 \text{ m} \cdot \text{min}^{-1}$, and a feed rate of $0.1 \text{ mm} \cdot \text{rev}^{-1}$ [15].

Various tool materials have been explored for machining Ni-based superalloys. Ceramic tools are commonly used for continuous roughing operations requiring a high material removal rate and high cutting speeds, permitted by their high melting temperatures and hot hardness [90]. For semi-finishing and finishing operations, coated carbides (PVD [91] and CVD [92]) as well as cBN [91, 93] tools are generally preferred.

Workpiece Surface Integrity

Generally, Ni-based superalloys will exhibit poor surface integrity characteristics [94, 95]. Although alloy additions can be used to improve machinability [96], these materials are de-

signed to operate at extreme temperatures and so large cutting forces, and severe plastic deformation (SPD) layers, are often inevitable. In addition, surface defects such as pickup, swept grains and white layer formation are prevalent, which can be detrimental to component functional performance, especially in terms of fatigue life [12]. It has also been observed that modern PM alloys with improved high temperature performance exhibit a reduced tolerance to machining induced damage when compared to wrought alloys [97]. Sub-surface damage is particularly concerning during the manufacture of critical parts, as it is harder to rectify and detect. As such, careful consideration of permissible tool wear limits is imperative, to ensure the quality, and in-service performance of machined components.

As previously discussed Section 2.1, Ni-based superalloys exhibit a YSA at elevated temperatures. Although this behaviour is highly advantageous in-service during high temperature applications, it is often detrimental to machining operations. La Monaca et al. [98] utilised a unique experimental orthogonal cutting setup, whereby tool and workpiece can be heated independently to investigate the role that temperature alone has on the cutting process. The authors discovered that the YSA effect can become advantageous if the temperature in the tertiary shear zone is increased to match the temperature range that exhibits the YSA, as this will reduce deformation in the machined surface. In addition, by increasing the temperature in the primary shear zone, so that it exceeds the YSA temperature range, lower cutting forces and energies could be obtained.

In their subsequent work using the same apparatus [99], the influence of cutting temperature on shear localisation, and the transition from continuous to discontinuous chip formation was explored. The authors found that increasing the temperature of the workpiece and tool will promote nanoscale shear localisation in chips. Within these nanocrystalline regions, misorientation is low due to recrystallisation, which occurs after the formation strain induced intra-granular dislocation networks, and is assisted by increased thermal energy at higher temperatures. In contrast, the neighbouring large grain regions of the chip exhibit high levels of misorientation, since there is less energy for recrystallisation to occur. At lower cutting temperatures the deformation is more consistent across the chip, leading to continuous chip formation. Although deformation is more severe when higher cutting temperatures are used, the deformation is more localised, leading to a reduction in cutting forces (25–30%). In spite of lower cutting forces, more damage to the workpiece subsurface will occur, due to thermal softening in this region. This highlights that cutting forces alone do not provide a suitable means of assessing machining induced damage.

Powder metallurgy PM Nickel-based superalloys utilised in aeroengine application are typically consolidated using hot isostatic pressing HIP, followed by extrusion and isothermal forging. Extrusion is necessary to break down prior-particle boundaries (PPBs) that are detrimental to functional performance and influence the subsequent forging steps [100]. As-HIP material can exhibit yield strength, ultimate tensile strength, and ductility comparable to extruded/forged material after heat treatment, hence it has the potential to be used in non-critical applications [40].

Liao et al. [101] investigated the influence of γ' distribution on machining induced damage by comparing two similar PM alloys produced using HIP, with a varying volume fraction of γ' (43% and 57%). They found that a lower volume fraction of γ' would result in a slightly higher level of strain in the machined surface during normal cutting conditions. Under aggressive cutting conditions they found that the lower γ' volume fraction alloy exhibited enhanced thermal softening, and a corresponding high level of subsurface damage. Despite exhibiting a reduction in machining induced damage, a higher volume of γ' will result in reduced machinability due to the increase in force required to deform the material at high temperatures. A temperature of 950°C was recorded at the tool-workpiece/tool-chip interface using a thermal camera. The authors made no comment regarding the influence this may have on the tool wear generated; however, it can generally be assumed that higher cutting energies will generate higher levels of tool wear when machining comparable materials.

In a subsequent study, Liao et al. [16] investigated the formation of white layer in PM Ni-based superalloys using an orthogonal turning setup and aggressive cutting parameters. The authors hypothesise that given the potential measurement error in the previous study, the actual temperature could be as high as 1150 - 1200°C; the high levels of dissolution they observed within the machined surface would indicate that this is indeed likely. Cyclic uniaxial micro compression tests later performed, demonstrated that white layer in Ni-based superalloys exhibits almost no elastic recovery, which results in a significant deterioration in the mechanical properties and functional performance of manufactured components. In contrast, Ding et al. [102] found the yield strength of the white layer to be nearly twice that of the bulk when using micro compression tests on machined 720Li, which was attributed to grain nano-sized refinement. Comparing the two studies, it becomes clear that Ding et al. utilised less aggressive machining conditions, which caused less thermally driven dissolution and recrystallisation to occur. As such, when they extracted the micro-compression samples, only a small area of the sample contained regions with fully dissolved precipitates, in contrast, the samples extracted by Liao et al. consisted of approximately 50% dissolved precipitates.

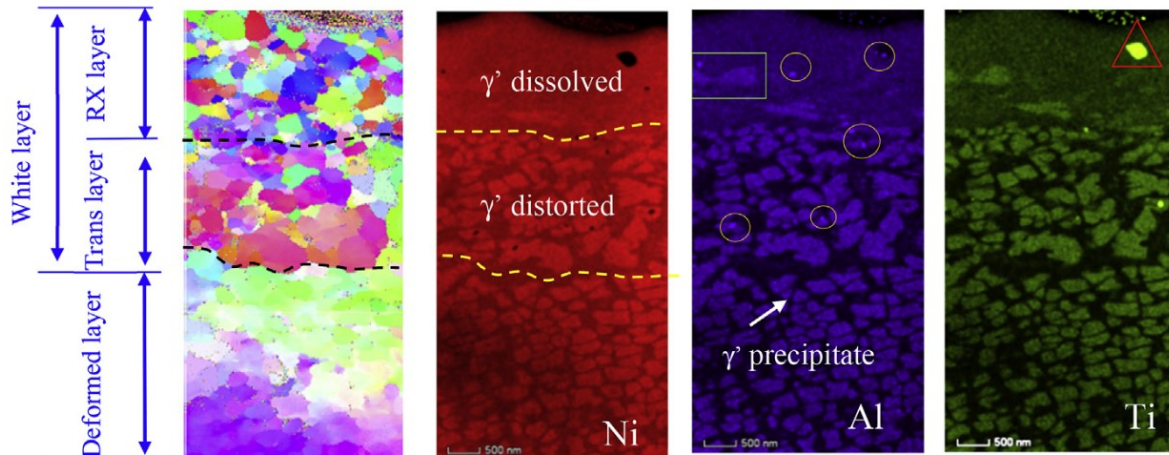


Figure 2.30: Scanning transmission x-ray microscopy (STEM) micrograph and x-ray energy dispersive spectroscopy (X-EDS) scans of machining effected layers after orthogonal turning of advanced Ni-based superalloy using a heavily worn tool ($V_B = 0.3 \text{ mm}$); $V_c = 80 \text{ m} \cdot \text{min}^{-1}$, $f_n = 0.1 \text{ mm} \cdot \text{rev}^{-1}$ [16].

Experimental drilling and end milling trials were carried out on RR1000 by Soo et al. [103] revealed re-deposited material on the hole surfaces occurred during drilling operations. In addition, white layer and material drag was observed on cross-sectional micrographs of the machined surface. During the end milling trial minimal subsurface damage was observed when using new tools, however, when using worn tools burring, increased microhardness, and white layer were observed to occur.

Hood et al. [104] utilised multilayer TiCN/alumina coated carbide tooling during an experimental turning trial to investigate surface integrity when machining RR1000. Upon examination of the machined surface, redeposited material, side flow and laps (material folded onto itself) were evident at a range of surface speeds. Cross-sectional micrographs of the machined surface revealed no evidence of white layer in either the feed or radial directions, although material drag was observed. When turning under more aggressive conditions using round ceramic inserts, Axinte et al. [19] found that a comparable disk alloy would exhibit a discontinuous white layer with a maximum thickness of 2-3 μm . Material drag, laps and surface plucking (small particles removed from the machined surface) were also observed.

Workpiece Grain Size Effects

Controlling grain size of Ni-based Superalloy materials, allows aeroengine manufacturers to optimise material properties for specific loading conditions [30]; this invariably affects the machinability characteristics. Cedergren et al. [105] used a single point turning experiment to investigate the influence of workpiece material, grain size, and feed rate on chip formation

and tool wear when machining IN718 with uncoated carbide inserts. They found that grain size has a larger impact on notch wear than feed rate, as shown in Figure 2.31. It was also observed that workpiece material deformation and chip formation is more inhomogeneous with large grain material. Singh et al. [106] performed a turning study to investigate the influence of heat treatment on the machinability of IN718. It was observed that the cutting and feed forces are dependent on the material hardness and not grain size, since hardness is determined by the distribution, shape and size of the strengthening precipitates (γ' and γ''). When cutting softer material, there was less machining induced damage in the form of micro cracks, grain refinement and strain localisation, as a result of the lower cutting forces. In contrast, the softer materials also experienced deeper levels of intragranular strain.

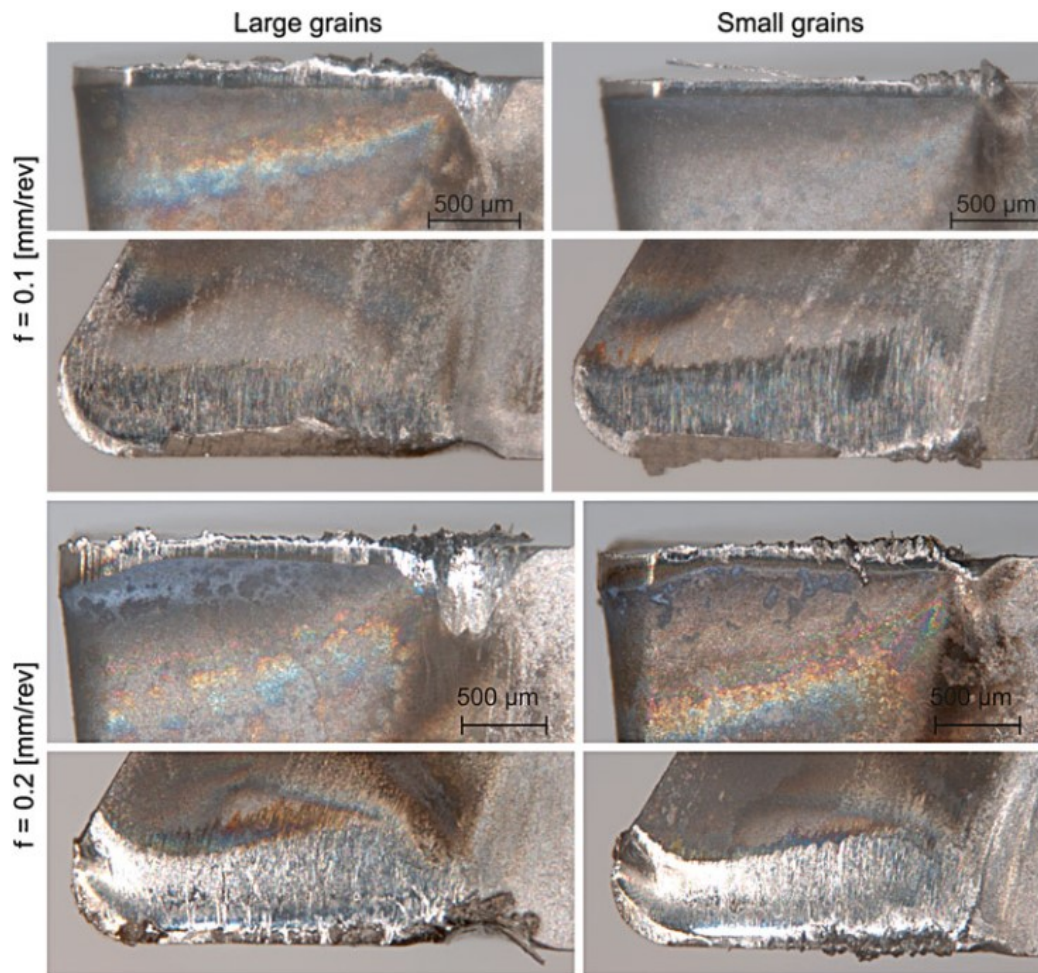


Figure 2.31: Influence of feed rate and workpiece material grain size on flank and rake face tool wear when turning IN718 with uncoated carbide inserts with a 0° rake angle [105].

In an OD turning study performed by Olovsjö et al. [107] on Waspaloy, it was found that increasing the grain size leads to more inhomogeneous deformation and more pronounced chip

segmentation, which corresponds to higher levels of notch wear and burr formation. In a similar turning study, Olovsjö and Nyborg [108] compared the wear behaviour of uncoated tools when machining IN718 and Waspaloy. They observed that finer grained IN718 deformed isotropically, with very little chip segmentation, or notch wear on used cutting inserts. These same trends were less pronounced when comparing fine and coarse grained Waspaloy, however, it was hypothesised this was due to a smaller difference in average grain size between the two material conditions as opposed to differences in the alloy chemistries. The authors discovered that in spite of the lower cutting forces generated when machining IN718, that the flank wear rate was greater. IN718 contains hard abrasive NbC carbide particles, and it is not clear from the results presented whether the scaring observed on the flank face had a similar width to these particles, if so, it would suggest that said particles may be responsible for differences in the flank wear rate detected. No difference in propensity for notch formation was observed in the two materials, although tighter control of alloy grain size would be required to confirm this.

Wear of Coated Carbide Tools

Coated carbides are widely used for Ni-based machining to extend tool life by providing protection to the underlying hardmetal substrate. The dominant wear mechanisms for CVD TiCN/alumina coated carbides when turning Inconel 825 have been reported to be abrasion and adhesion, leading to edge chipping and nose wear during dry machining [109]. Compared to PVD coated tools, such as TiAlN and TiN, the CVD coating was found to produce higher temperatures, greater dynamic fluctuation in machining force signals and increased BUE formation [109]. During turning of IN718, it has been shown that CVD TiCN/alumina coated carbide can outperform single-layer (TiAlN) PVD coated carbides at high cutting speeds ($100 \text{ m} \cdot \text{min}^{-1}$) but not at medium speeds ($50 \text{ m} \cdot \text{min}^{-1}$) [17]. It was also found that the majority of abrasive wear occurs on the tool flank, which the authors claimed was due to hard abrasive particles from the workpiece material. As the abrasive wear was concentrated on the tool flank, it is possible that dislodged sections of the hard tool material (substrate and/or coating), caused by adhesive wear, may also contribute. Kadirgama et al. [110] found that during milling of Hastelloy C-22HS with CVD TiCN/alumina coated carbides, that adhesion, and chemical wear (oxidation of the underlying substrate) were the dominant wear mechanisms; the tool wear types were reported as flank wear, chipping, BUE formation, plastic deformation, and notching. Ezugwu et al. [88] reported that flank wear and notching were the dominant failure mechanisms of CVD TiCN/alumina coated carbides when turning IN718, compared to flank wear, excessive chipping and flaking for multilayer and single layer PVD tools.

Song et al. [83] investigated the initial wear behaviour of coated and uncoated carbides during dry turning of IN718 when using CVD TiCN/alumina tooling, adhesive wear was identified as the primary wear mechanism. In a similar study on IN718 turning by Rakesh et al. [111], again adhesion, and additionally abrasion, were identified as the dominant wear mechanisms,

culminating coating delamination and abrasion driven crater wear. The authors claim abrasive wear occurred due to the presents of hard abrasive particles in the workpiece but provided no evidence to support this. Diffusive wear is also alleged to have occurred; however, it is not clear how this could be distinguished from adhesive wear given the evidence provided as no cross sectioning of worn cutting insert was carried out in order to reveal the level of chemical interaction between tool and workpiece material. Devillez et al. [45] observed notch formation at either side of the contact zone during orthogonal turning experiments on both coated and uncoated carbide tools when turning IN718. During the early stages of cut, the dominant wear mechanisms were found to be adhesive wear resulting from adhesion of the workpiece to the tool material. When turning with coated tools this led to crater wear and notch formation (see Figure 2.32).

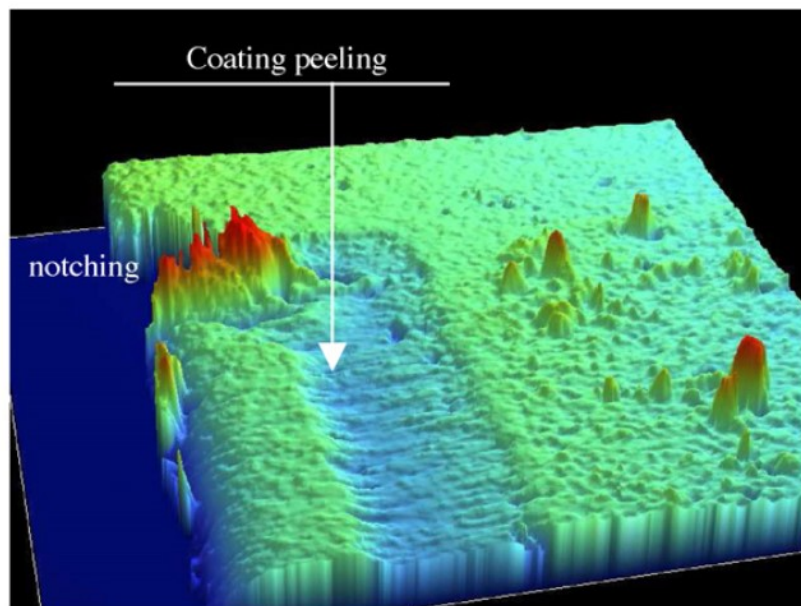


Figure 2.32: White light interferometry of worn tool with TiAlN + MoST coating after orthogonal turning of IN718; $V_c = 60 \text{ m} \cdot \text{min}^{-1}$, $f_n = 0.1 \text{ mm} \cdot \text{rev}^{-1}$ [45].

2.6.2 Influence of Coolant

Coolant, also referred to as cutting fluid, is frequently used when machining hard-to-machine materials like Ni-based superalloys to dissipate heat, preventing premature tool failure. It has been observed that utilising a directed high-pressure coolant (HPC) jet on the rake face reduces the tool contact length; however, due to the high pressures within the contact zone, coolant has relatively little impact on the friction coefficient as it is unable to penetrate the interface between tool and workpiece [112]. Alagan et al. [113] investigated the impact of simultaneous rake and flank high-pressure cooling on chip formation mechanics when turning IN718 with uncoated carbide tools. They found that increasing the rake cooling reduced the

chip width and curvature. Flank cooling was found to mainly affect the shear instability and chip breaking. When increasing the cutting speed, the chip thickness and shear angle were observed to increase.

Polvorosa et al. [114] investigated the influence of HPC on tool wear of uncoated carbide cutting inserts when turning fine grain and coarse grain variants of two Ni-based superalloys: IN718 and Waspaloy. They found that, compared to conventional low-pressure coolant application, HPC reduced cutting and feed forces significantly, as well as notch wear formation. Ezugwu and Bonney [22] investigated the influence of varying HPC on tool wear and cutting forces when turning IN718. The effectiveness of HPC in increasing tool life was observed to be dependent on cutting speed, as it was found to be more effective at higher speeds. Additionally, cutting forces only decreased with increased coolant pressure at specific speeds and feeds. These findings highlight that the relationship between cutting force and HPC pressure is complex and dependent on both material and processing conditions.

In some instances, however, coolant application can promote tool wear mechanisms. Sosa et al. [115] used a cyclic contact fatigue test to investigate the role of coolant on crack propagation in textured α -alumina coatings during milling operations. It was shown that under wet conditions, there is a faster widening of the CVD cooling cracks, which leads to the development of large comb-cracks and ultimately coating failure. In continuous turning-type operations, this kind of thermal cycling does not occur, and the application of coolant is unlikely to promote coating crack propagation in this manner.

2.7 Alumina Degradation during Machining

CVD alumina coatings are thought to be well suited to the conditions that develop during Ni-based superalloy machining, and are commonly used in combination with other wear resistant coatings such as TiCN in multi-layer coating systems. Since these coatings were developed for steel machining, and are most effective for this application, the majority of the published work focused on alumina degradation mechanisms have utilised steel as the workpiece material.

Dearnley and Trent [116] first reported on the rake face crater wear of CVD alumina coatings during steel turning, and observed plastic deformation to the asperities of early-stage mixed alumina coatings (which were partially textured, containing both α -alumina and κ -alumina). This resulted in the formation of characteristic ridges parallel to the cutting direction, concentrated in the location of the maximum rake face temperature. These ridges were observed to form most notably when turning at high speeds. Dearnley [117] later suggested that these ridges form via the plastic deformation of coating asperities, which culminates in ductile fracture and material loss of the coating (see Figure 2.33). Goh et al. [118] reported that plastic deformation by single glide of individually spalled grains was responsible for the formation

of these long ridges during medium carbon steel turning when using alumina-based ceramic inserts. The authors also claimed plastic deformation induced necking resulted in the formation of short spikes in the surface nearer to the cutting edge, indicating that multiple slip conditions were present in the surface layer of the tool. Furthermore, they suggest the spiked appearance may be caused by partially dislodged or damage grains that are fused onto the tool material before being deformed. Fallqvist et al. [119] used a pin-on-disk tribometer to study wear behaviour of textured α -alumina coatings with different growth textures at high and low temperatures. When using a cast iron pin, they found plastic deformation was the dominant wear type for the (001) growth texture and that micro-chipping occurred when the other growth textures were tested.

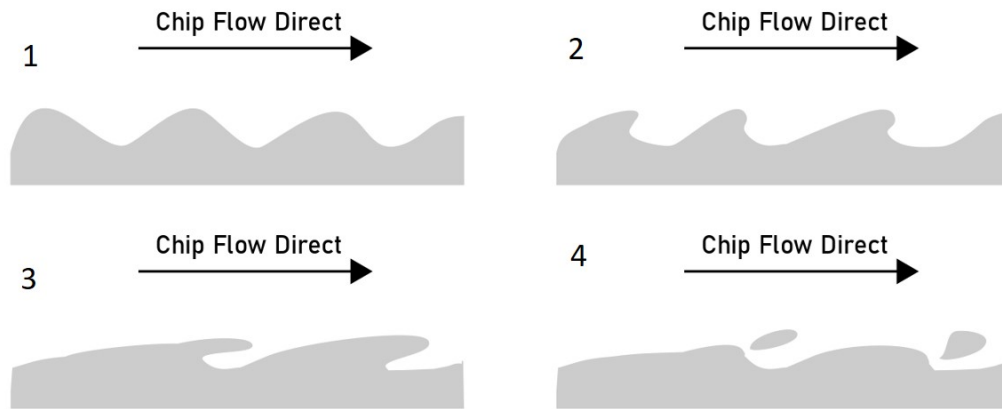


Figure 2.33: Proposed plastic deformation driven wear mechanism for alumina coatings during steel machining (adapted from [117]).

2.7.1 Wear of Textured CVD Alumina Coatings during Steel Turning

During steel turning it has been demonstrated that the wear resistance of pure α -alumina coatings can be controlled by varying the growth texture. It has been hypothesised when machining steels, that the optimum wear resistance of α -alumina coatings is achieved when the basal plane (001) lies parallel to the substrate surface [24]. M'Saoubi et al. [120] observed that during steel turning, textured α -alumina coatings exhibited three distinct types of wear in the sticking, transition, and sliding zones, when machined at high speeds ($300 \text{ m} \cdot \text{min}^{-1}$). When machined at intermediate speeds ($100 \text{ m} \cdot \text{min}^{-1}$), no evidence of characteristic ridges indicative of plastic deformation was observed in the transition or sliding zones. Using energy-dispersive X-ray spectroscopy (X-EDS) to investigate the chemistry of the plastically deformed alumina in the transition zone, it was discovered that Mg containing oxide deposits were formed, possibly originating from non-metallic inclusions in the work-

piece material. Bejjani et al. [121] demonstrated that when turning different types of steel workpiece materials with α -alumina coated carbides, that the positions and sizes of each wear zone would vary, as would the topography and wear rate in the transition zone.

Bjerke et al. [122] investigated the performance of CVD α -alumina when turning Ca-treated steels. The authors were able to explain the anomalous wear behaviour, in which a reduction in tool life was seen when using CVD α -alumina tools despite Ca-treatment leading to a tool life increase when turned using other tool materials, such as uncoated carbides [123]. Although commonly regarded as inert, via a combination of microstructural investigations, thermodynamic calculations, and temperature measurement, it was demonstrated that the alumina will react at the conditions experienced during machining, and that the degradation was driven by non-metallic inclusion and oxides within the workpiece material. In a subsequent investigation [124], it was shown using high pressure diffusion couples that these kinds of reactions are dependent on oxygen. The authors suggested that non-metallic inclusions in engineered steels should be saturated with Al to prevent this kind of chemically driven wear.

Shoja et al. [125] performed an extensive analysis of the crater wear mechanisms that occur during steel turning when using CVD TiCN/ α -alumina coated carbide tools with differing alumina growth textures. Chemical wear, plastic deformation, micro-rupture, and abrasion were all found to occur during turning operations. An estimated temperature range of between 950-1000°C was stated by the authors. Nano-scale terraces were observed to form depending on the growth texture used for the coating. Contrary to previous claims surrounding micron-size grooves caused by abrasive wear from the workpiece material [24], no such grooves were observed on the (001) sample, demonstrating that the abrasive particles causing this wear could not originate from the workpiece, as seen in Figure 2.34. Micron-sized groove formation within the sliding zone only occurred in instances where non-optimal growth textures such as (012) and (110) are utilised, which is caused by heterogeneous deformation that occurs in the earlier part of the contact (sticking and transition zones), causing coating fragments to be generated which can in turn abrade the coating. In contrast basal (001) coatings deform more homogeneously and only display nano-sized groove formation in the sliding zone.

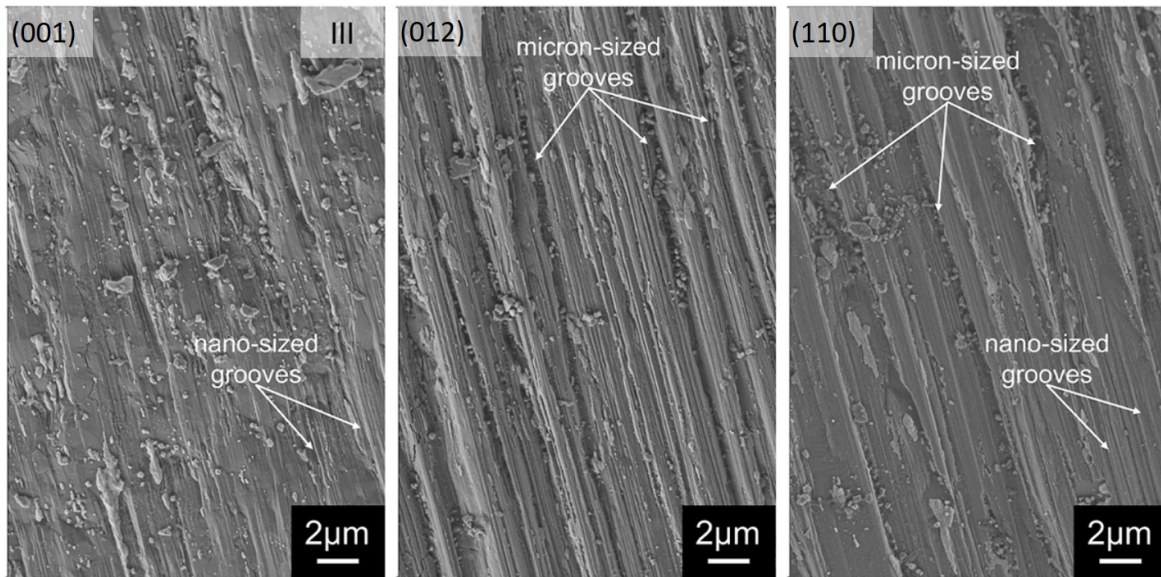


Figure 2.34: Sliding zone alumina wear during steel machining for different alumina growth textures: (001), (012), (110) (adapted from [125]).

In their later work [81], it was hypothesised that the sliding of hard coating fragments within the contact zone can lead to sub-micron scale plastic deformation due to stress concentrations (ploughing). The authors also found new evidence that micro-terrace formation, on the edge of the sticking zone, is caused by crystallographic dependent chemical etching [81]. In addition, they hypothesised that when machining steels the $(Al,Fe)_3O_4$ spinel phase can form, or, if Si is present, a phase mixture with a low melting point could also form [126]. Both of these reaction products should be easily removed by workpiece flow, culminating in tool wear. Atom probe tomography (APT) was utilised in the study and revealed suspected diffusion of oxygen from the alumina into the adhered material. Conversely, no diffusion of workpiece material into the tool was detected. These findings suggest that chemical wear may play a pivotal role in the degradation of alumina, and that further investigations are required to reveal the nature of these reactions.

2.8 Conclusion

In summation, the literature review presented demonstrates that significant recent advancements have been made with respect to Ni-based superalloy surface integrity during machining processes, and alumina wear mechanisms during steel turning. In spite of this, there appears to be a clear gap in the current state-of-the-art understanding of alumina deformation during Ni-based superalloy machining, and how this relates to alloy chemistry and microstructure. To date, much of the work in this area has utilised non-textured and mixed (α and κ)-alumina

coatings and not strongly textured α -alumina, thus they degrade in a different manner. Furthermore, wear tests have tended to focus on the entire cutting tool system, i.e., coating and substrate, and there has yet to be any targeted research on the degradation of the outermost alumina layer of multilayer alumina-coated carbides. In the case of steels, it has been shown that many misconceptions surrounding the role of chemical and abrasive wear behaviour of alumina have persisted for many years. This poses the question: how do these new discoveries relate to Ni-based superalloys, which are more heavily alloyed, and exhibit higher levels of work hardening, lower thermal conductivities, and superior high-temperature strength?

In the following work, an in-depth exploration into the degradation mechanisms of the textured alumina layer of CVD TiCN/ α -alumina coated carbides, and its relation to workpiece surface integrity, is presented when turning a range of Ni-based materials. This has revealed the dramatic impact of workpiece chemistry and microstructure on alumina wear, and demonstrates the fundamental limitations of alumina coatings utilised in these applications. Looking to the future, questions must now be raised over the suitability of alumina coatings for Ni-based machining, if the demand from industry is geared towards higher rates of material removal, and hence, improved manufacturing efficiency.

Chapter 3

Experimental Materials

As with all practical materials science research, the materials used are of paramount importance. For machining studies, both the tool and the workpiece must be compatible and suitable for the chosen process. Furthermore, the quality of these materials must be high to ensure repeatability, and to minimise the risk of damage to the CNC machines performing the cutting.

3.1 Cutting Inserts

State-of-the-art Sandvik Coromant cutting inserts were utilised throughout the work presented. These inserts have been specifically tailored for optimal performance during Ni-based machining.

3.1.1 Coating

The Sandvik Coromant S205 coating was used in all experimental turning trials performed. This multilayered coating is composed of an inner TiN layer, followed by a TiCN layer, then a bonding layer of Ti(C,N,O), and finally, a α -alumina layer. The α -alumina layer of the coating is textured in (0001) direction. There is also an additional TiN layer on the flank face, which is added primarily for wear detection. This layer is not present on the rake face, since it is removed via an abrasive blasting process. All coatings were deposited onto a WC-Co hardmetal substrate.

3.1.2 Geometry

Two different insert geometries, were employed: one for OD turning (CNMG120408-SF), and one for orthogonal turning (TCMW110304). The SF in CNMG120408-SF refers to the specific edge geometry, as shown in Figure 3.1. These CNMG inserts feature a chip breaker

to assist chip control (see Section 2.4.4). In contrast, the TCMW110304, is a flat insert that features no chip breaker. A comparison is shown in Figure 3.2.

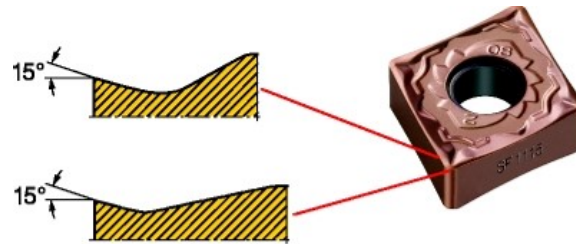


Figure 3.1: SF edge geometry utilised for OD turning trials.

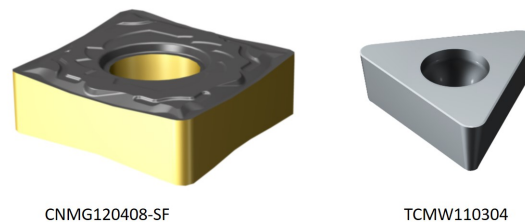


Figure 3.2: Comparison of the two different tool geometries employed.

3.2 Workpiece Materials

Two Ni-based Superalloy materials were machined during the experimental turning trials presented, namely, IN718 and RR1000.

3.2.1 Processing

Comparing the two alloys, IN718 is a wrought alloy, which means it is typically manufactured using an ingot metallurgy processing route. The billet material utilised in this study was processed by Vacuum Induction Melting, followed by Electroslag Remelting. Several heat treatments were then employed by the material supplier to produce a favourable microstructure in terms of mechanical properties: solution annealed, heat to 980° C, hold for 90 min, water quench, aged, heat to 718° C, hold for 480 , furnace cool 50° C/hr, heat to 621° C, hold for 480 min, air cool.

In contrast, RR1000 is a proprietary PM superalloy used by Rolls-Royce for high pressure turbine disks in modern aeroengine applications, which is capable of operating at high operating temperatures in excess of 650 ° C [127]. The material used in this study was produced by consolidating atomised powder using HIP, which was then isothermally forged. The two received billets were cores from disk forgings, commonly referred to as "centre slugs". Two separate heat treatments were then performed to produce CG RR1000 and FG RR1000. Further details of the full heat treatments can be found in Chapter 6.

3.2.2 Composition

The composition for IN718 was provided by the material supplier and the composition for RR1000 was taken from literature [128]. Observing the two alloy compositions in Table 3.1, some clear differences can be noted. IN718 contains significant amounts Fe and Nb, which means γ'' is the primary strengthening precipitate. Conversely, RR1000 is primarily strengthened by γ' , and contains Co, a solid solution strengthener, as well as greater amounts of reactive MC formers such as Hf, Ti, and Ta, which is permitted by PM processing routes.

Table 3.1: Composition in wt.% for IN718 and RR1000.

Element	Ni	Fe	Cr	Co	Nb	Mo	Ti	Al	Hf	Ta	Zr	Trace
IN718	Bal.	17.8	18.5	–	5.3	3.0	1.1	0.5	–	–	–	0.2
RR1000 [128]	Bal.	–	15.0	18.5	–	5.0	3.6	3.0	0.5	2.0	0.06	0.04

Chapter 4

Experimental Methods

In order to perform this thesis work, a wide range of experimental and modelling techniques were employed. In many cases, optimisation required a significant degree of trial and error. As such, it is hoped that some of this information will provide useful insights, especially for those in the early stages of their study.

4.1 Scanning Electron Microscopy SEM

Scanning electron microscopy (SEM) is widely used within the field of materials science for examining features at scales ranging from millimetres to nanometres. It can be used alongside various different detectors, to analyse topography, chemistry, and crystallographic information, such as grain orientation. This versatility, coupled with its impressive depth-of-field, has led to its widespread popularity. Within the field of machining science, there is now a drive to develop in-situ mechanical SEM experiments, that can capture material deformation behaviour in real time [129, 130].

4.1.1 Types of Electron Emitters

There are two main types of electron guns, these are: thermionic-emission, and field-emission. In thermionic-emission guns, electrons are produced by heating a filament that is typically composed of either W or (LaB₆); this filament acts as the cathode (emitter). They can produce a stable electric current of up to 1 μ A, without the need for an ultra-high vacuum. Cold-cathode field emission guns (FEGs), utilise a sharp (radius of curvature \approx 100 nm), single crystal, W tip, to serve as the cathode. A strong electric field is applied in a high vacuum environment, which causes electrons to be emitted due to the field-emission phenomenon. This method allows for higher resolution images to be obtained, with a narrow energy spread, although, the cost is higher when compared to thermionic-emission guns. The Schottky-emission FEGs are another variant of FEG, in which the work function of the tip is lowered. This is achieved by the addition of a thin coating layer of Zirconium Oxide, which is

also heated to a temperature of around 1800K. These types of emitters have a similar brightness to cold-cathode FEGs, but are more stable because there is less absorption of residual gas molecules when operating at high temperatures, in addition, they can also produce higher probe currents. In the following work, a range of different SEMs were utilised, these are summarised in Table 4.1.

Table 4.1: SEM models and their electron sources.

SEM	Electron Source
JEOL JSM-7900F	Cold-cathode FEG
FEI Inspect f50	Cold-cathode FEG
JEOL JXA 8530F PLUS	Schottky-emission FEG
Zeiss EVO LS25-1204	Thermionic (LaB ₆)
Hitachi TM3030	Thermionic (W)

4.1.2 Interaction of Electron Beam with Sample

The strength of the acceleration voltage and the type of material influence the interaction volume, which in turn affects the emission of all types of energy from the sample. This is illustrated diagrammatically in Figure 4.1. Therefore, acceleration voltage is a key parameter when observing thin layers from above, which may start to disappear as the acceleration voltage is increased. The spot size influences the spatial resolution of the SEM, whereby a smaller spot size generally results in a clearer image, though this may also impact the signal-to-noise ratio, as the beam current is reduced. The SEM parameters used within the work presented is given below in Table 4.2.

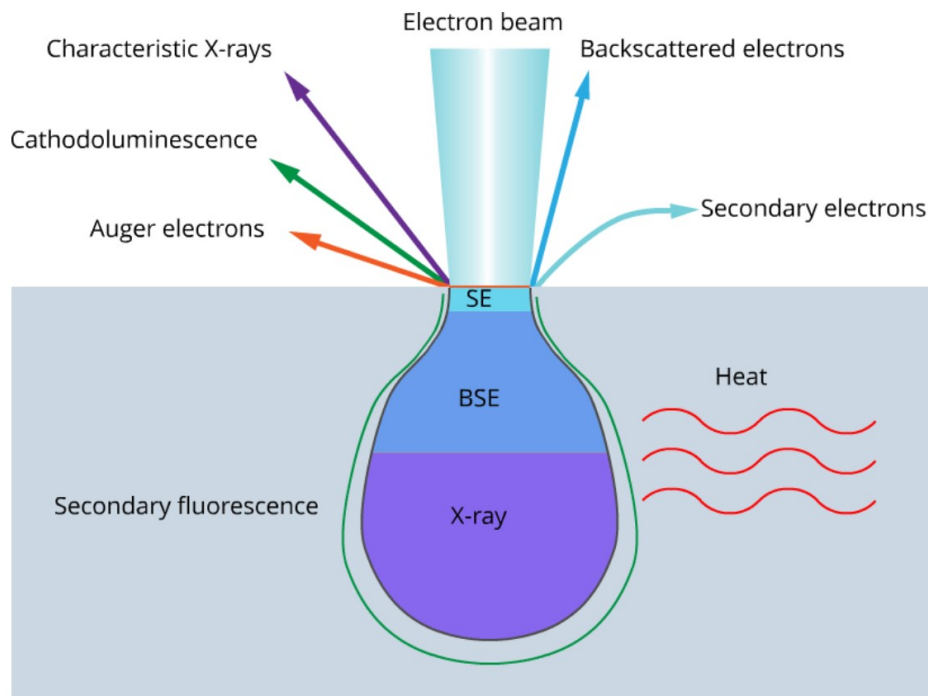


Figure 4.1: Diagram of interaction volume produced SEM [131].

Table 4.2: SEM operational parameters.

Parameter	Value
Voltage	10 – 20 keV
Spot Size	3 – 4
Working Distance	7.5 – 10.5 mm

4.1.3 Types of Detectors

There are four main types of SEM detectors that have been used for imaging and analysis within this thesis: backscattered electron (BSE), secondary electron (SE), electron backscatter diffraction (EBSD), and X-ray energy dispersive spectroscopy (X-EDS). A brief description of each imaging technique they provide is given below.

Backscattered Electron (BSE) Imaging

Backscattered electrons (BSE) are higher energy electrons formed via elastic scattering of electrons from the primary incident beam that are ejected from the sample being imaged. The

contrast in BSE images can be used to observe changes in chemistry, as elements with higher atomic numbers appear brighter. Since BSEs are produced from deeper within the interaction volume (see Figure 4.1), they provide less spatial resolution than secondary electrons (SEs).

Secondary Electron (SE) Imaging

Secondary electrons (SE) are low-energy electrons formed via inelastic scattering close to the surface of the imaged sample (see Figure 4.1). SEs can then be detected by a secondary electron detector, typically an Everhart-Thornley type, which uses a positively charged grid to attract the negatively charged electrons. This detector converts the captured SEs into a signal used to form the image. Topographical information can be obtained from SE imaging, as edges and surface features tend to emit more SEs and thus appear brighter in the image.

Electron Backscatter Diffraction (EBSD)

Electron backscatter diffraction (EBSD) is a technique used to analyse texture, grain orientation, phase, and strain in crystalline materials. An EBSD map is constructed by scanning over a tilted sample and recording electron backscatter patterns (EBSPs) at many points. EBSPs are produced when backscattered electrons are diffracted by the crystallographic planes of the material, producing Kikuchi bands. The width and orientation of these bands are related to Bragg's Law and the distance to the detector, typically a phosphor screen, and can be used to identify features of the crystal structure. The equation for Bragg's Law is given in Equation (4.1), where λ is the wavelength of the backscattered electrons, d is the spacing between the crystal planes, θ is the angle of incident rays, and n is an integer. Electrons can either constructively or destructively interfere with each other based on this relationship.

$$n\lambda = 2d \sin \theta \quad (4.1)$$

X-ray Energy Dispersive Spectroscopy (X-EDS)

X-ray Energy Dispersive Spectroscopy (X-EDS) can be used to form composition analysis of materials. In X-EDS, the high energy of an electron beam can displace inner-shell electrons. When an outer-shell electron drops down to fill this vacancy, energy is emitted in the form of a characteristic X-ray (Figure 4.1). An energy spectrum is produced based on the energy gap between these two electron positions. Each element has a unique "fingerprint" corresponding to its emitted X-ray energy, which can then be used to determine the elements present in a sample. Care must be taken when analysing the results from X-EDS, as peaks from different elements' energy spectra may overlap. Therefore, effective analysis often requires prior

knowledge of the likely elements in the sample. The X-ray count rate, i.e., how many X-rays are detected by the detector, can be optimised by adjusting the spot size and acceleration voltage. All results were collected on an 80 mm Oxford X-EDS system.

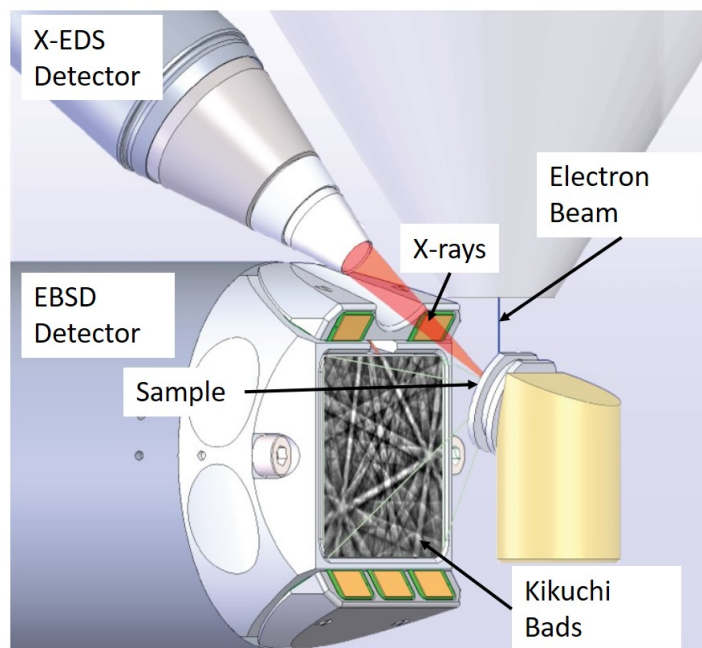


Figure 4.2: Diagram showing the formation of characteristic Kikuchi bands on the phosphorous screen on an EBSD detector, and the position of the X-EDS detector (adapted from [132]).

4.2 Scanning Transmission electron Microscopy (STEM)

Scanning Transmission Electron Microscopy (STEM) works by firing a powerful electron gun (100 – 300 keV) at an ultra-thin electron transparent sample (20 – 200 nm), which is typically created by milling the sample with a focused ion beam (FIB). As electrons pass through the sample, some are scattered while the remaining electrons are transmitted through. The electrons that are transmitted will then hit a detector, creating an image. The main benefit of this technique compared to SEM is its higher resolution. It can also be paired with X-EDS to study nanoscale changes in composition.

The TEM system employed within the following thesis was a Titan G2 60-300, equipped with a monochromator, an image and a probe corrector, operated at 300 kV. The STEM EDS maps were collected with a SuperX EDS detector.

Electron Probe Microanalysis (EPMA)

Electron Probe Microanalysis (EPMA) is a type of electron microscopy that is optimised for quantitative chemical analysis. EPMA often employs wavelength dispersive spectroscopy (WDS) rather than X-EDS. WDS spectrometers consist of a crystal and a detector; the diffraction of X-rays by the crystal depends on the X-ray's wavelength and the orientation of the crystal, allowing only X-rays of a specific wavelength to be detected at any one time. Because of this feature, EPMA systems are typically equipped with multiple spectrometers for the simultaneous detection of different elements. The main advantage of WDS over EDS is its improved energy resolution, which makes it easier to differentiate between closely spaced spectrum peaks. This feature is particularly useful for measuring light elements, such as O, although the quantification tends to be less reliable than is the case with heavier elements that emit higher energy x-rays. WDS also has a lower detection limit, allowing for the detection of trace elements, as well as better repeatability, and a higher count rate than is found on X-EDS systems. In the following work a JEOL JXA 8530F PLUS microscope was utilised.

4.3 X-ray Diffraction

X-ray diffraction (XRD), can be used to ascertain information about the structure of crystalline materials such as lattice parameters, phase, and strain. In XRD, an x-ray tube is used to produce monochromatic x-rays that interact with a the target sample, producing a range of different interactions; this is shown diagrammatically in Figure 4.3. The scattered diffracted x-rays will diffract as per the Bragg Equation (Equation (4.1)), however in this case, λ will be equal to the wavelength of diffracted x-rays, not electrons.

INTERACTION OF X-RAYS WITH MATTER

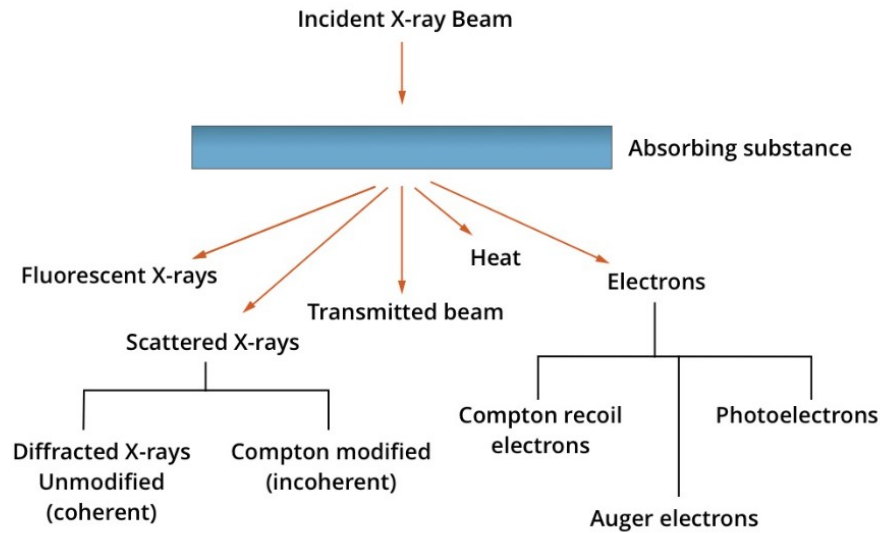


Figure 4.3: Diagram showing x-ray interaction with material [133].

The scattering of x-rays occurs in all directions, and so the constructive interference that satisfies the Bragg Law will produce a cone shape (see Figure 4.4). If a 2D section of this cone is examined, normal to the cones axis, an arc, or circle will be produced. Conversely, if a 1D slither is taken, as is the case for most lab based systems, a 1D XRD pattern will be produced with the 2θ angle on the x-axis, and intensity on the y-axis (observe Figure 4.4). For crystalline materials, these peaks will occur at specific angles according to the lattice spacings. In addition, other features of spectra, such as peak width, which can be quantified using full-width at half maxima (FWHM) intensity, can be utilised to assess the degree of damage in machined surfaces [134, 135, 136, 137]. In the following work, the methodology presented in [137] was utilised for all on-machine XRD measurements performed, whereby a Proto iXRD portable residual stress diffractometer, mounted on wheels, was brought to the workpiece to perform measurements. Since the effect of curvature is known to influence XRD via asymmetric broadening [138], and any inconsistency introduced due variation in workpiece diameter were mitigated by randomising all cuts performed. In addition, the curvature of the billet was relatively large relative to the beam size and well within limits recommended for measurement of hoop residual stress using XRD to within an accuracy of 10% [139].

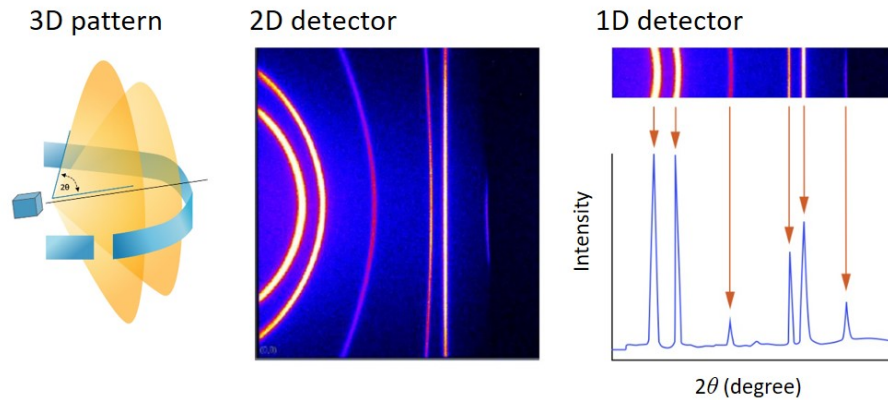


Figure 4.4: Diagram showing x-ray diffraction acquisition, from 3D cone, to 2D and 1D detectors (adapted from [140]).

4.4 Optical Measurement System

Compared with SEMs, optical systems often provide far quicker image acquisition, and generally require less sample preparation, due in part to the lower magnifications that they can achieve. Optical systems were used throughout the following work for a range of tasks. A description of some of the systems utilised is provided below.

4.4.1 Conventional Light Optical Microscopy

A Nikon Eclipse LV150 light optical microscope was utilised during metallographic preparation to inspect ground and polished surfaces after each step, in order to check that they had worked effectively. This system features darkfield microscopy, which was used to observe surface scratches. The same microscope was also used for inspecting etched samples to check if they had been etched to the correct level, prior to examination using SEM.

4.4.2 3D Optical Measurement Systems

The Alicona InfiniteFocusSL is an optical microscope, designed for surface characterisation, that is capable of rapidly capturing multiple images and then stacking them to create a digital, 3D representation. This system was used to measure ER values of tools prior to machining trials, to ensure consistency. Attempts were also made to measure cutting insert wear levels post machining, however, it was found that the reflective surfaces led to significant artifact generation. The propensity for BUE formation during Ni-based Superalloy machining also

caused overhangs to form that limited the systems line-of-sight, resulting in regions where no data was recorded. An example of this behaviour is shown in Figure 4.5.

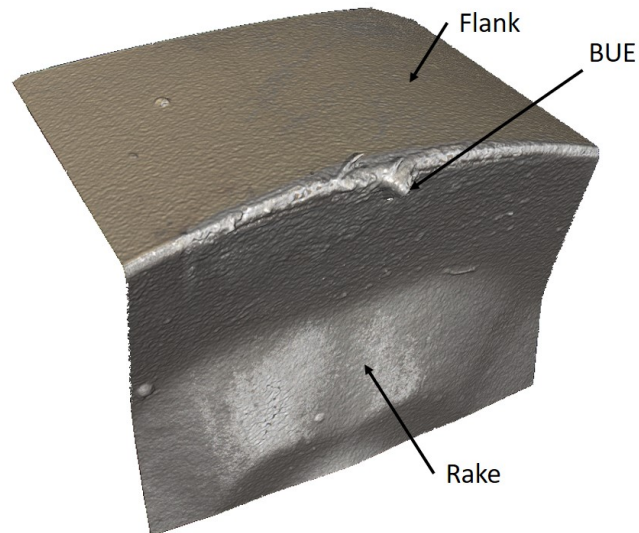


Figure 4.5: Example 3D scan of cutting insert, produced using Alicona system, displaying characteristic BUE formed after Ni-based superalloy machining.

4.5 Hardness Testing

Hardness testing allows rapid examination of material deformation behaviour. Measurements are taken by applying a known load to an indenter that has a specific geometry. The width of the indent is then measured, which can be converted to a hardness value using conversion tables. If a small indenter is used, as in the case in micro and nano hardness measurements, then an array of indents can be employed to examine changes in hardness, e.g., when moving from surface to bulk.

In this work microhardness testing was performed to examine bulk material properties, and multiple measurements were made to examine material homogeneity. All microhardness testing was performed using a Mitutoyo HM-101. Indents were spaced 3 times that of the indent diagonal to ensure consistent results were obtained.

4.6 Metallographic Preparation

Both workpiece material and cutting inserts were metallographically prepared in order to perform microscopy, or etching of cross-sectional samples. Samples were sectioned using a

Struers Secotom-50; a 10S20 cut-off wheel was employed to perform all cuts. Feed rates were varied between 0.05–0.25 mm·rev⁻¹ depending on the sample thickness. The rotational speed (RPM) was set 2200. After sectioning samples were mounted in conductive Bakelite using a Buehler Simplimet Mounting Press. They were then ground and polished using the method shown in Table 4.3. The time required for the final polishing step was altered depending on material grain size. For large grained materials, longer times were required, due to the relief of the polished surface.

Table 4.3: Sample preparation method used for Ni-based Superalloys and WC cutting inserts. N.B. Final polishing step was not used on cutting inserts.

Stage	Surface	Application	Force (N)	Time (s)	Rotation
Grinding	SiC Grinding Paper (P400)	Water	25	60	Corotate
Grinding	SiC Grinding Paper (P800)	Water	25	60	Corotate
Grinding	SiC Grinding Paper (P1200)	Water	25	60	Corotate
Grinding	Struers MD Largo	9 µm Diamond Suspension	25	240 – 480	Corotate
Grinding	Struers MD Dur	3 µm Diamond Suspension	25	240 – 480	Corotate
Grinding	Struers MD Dur	1 µm Diamond Suspension	25	240 – 480	Corotate
Polishing	Struers MD Chem	9:1 Colloidal Silica (0.05 µm) to H ₂ O ₂ (and water drip)	15	600 – 1200	Counter

4.6.1 Insert Cleaning

Cutting inserts were examined in an as-machined state, and a post-etch state (see Section 4.9.2), without any additional sectioning or polishing. This required debris, which tended to accumulate on the edges, to be removed. This was achieved by submerging inserts in acetone, before placing in an ultrasonic bath for 10 minutes. After the inserts were removed, compressed air was then immediately directed at the cutting edge, such that any residual acetone would be pushed away from the region of interest.

During cutting insert imaging using SEM, and Alicona (see Section 4.1 and Section 4.4.2), adhesive tack was lightly dabbed on the inspection surface to remove dust, or residue left from the cleaning process previously described.

4.7 Machining Force Measurement

A Kistler plate piezoelectric force dynamometer, Type 9129AA model, was utilised for machining force measurement during all turning trials. This setup was employed to measure the

machining force components along three axes: passive (F_p), cutting (F_c), and feed (F_f) directions, as shown in Figure 4.6. The resultant force (R) can be calculated using Equation (4.2). This setup allows forces to be measured in real-time, so the quality of a cut can be assessed. Practically, this means that incorrect parameter selection, i.e., incorrect DOC, can be identified immediately, since it will be accompanied by a change in machining forces. Similarly, tool engagement and disengagement can be assessed and optimised to reduce force spikes that may lead to tool damage. Inspecting machining force data can also reveal information about the edge condition, such as overall wear, or sudden changes to tool geometry (e.g., chipping, BUE removal). Furthermore, it can also be used to reveal changes in the workpiece material (e.g., grain size, composition). Sampling was typically carried out at 20,000 Hz.

$$R = \sqrt{(F_c)^2 + (F_p)^2 + (F_f)^2} \tag{4.2}$$

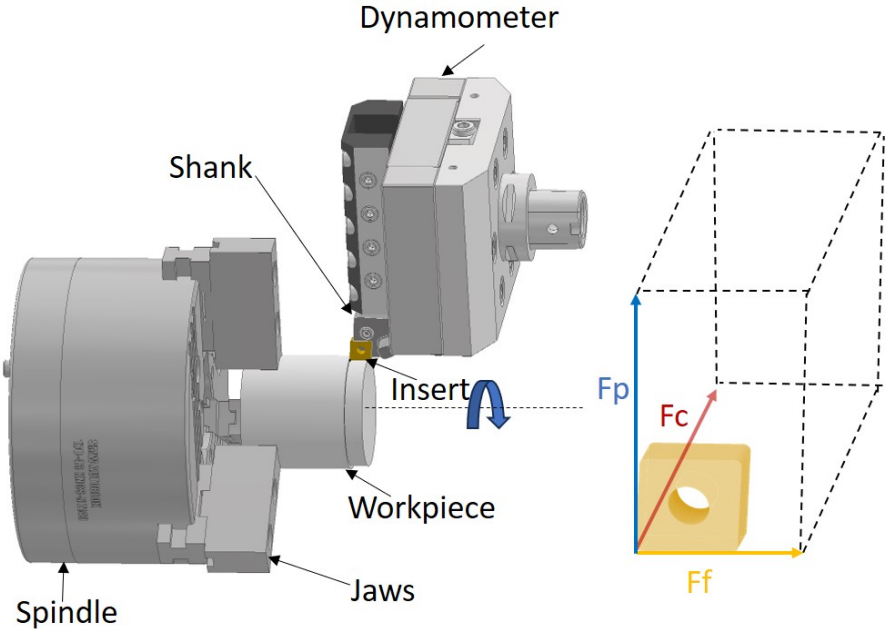


Figure 4.6: Dynamometry setup used in OD turning trials, alongside digram showing machining force components acting on a cutting insert.

4.7.1 Machining Force Response

It has been demonstrated that dynamometry data measuring the machining force response of a material, can be used to reconstruct microstructural features of Ti alloys, such as grain size [141, 142]. This technique has also been performed on functionally graded Ni-based Superalloys [143], however, the same degree of resolution has not yet been realised. The

technique works by plotting the variations in the z force component, i.e., the axial force (F_f as shown in Figure 4.6), as the tool moves from edge to centre during a facing pass at a low feed rate that is similar in magnitude to the insert ER; DOC and speed can then be varied accordingly to optimise the reconstructed microstructural maps. A full description of the technique used within this work is provided in [144].

4.8 Machining Strategies

When machining hard materials with hard coatings, care must be taken to protect the cutting tool during tool engagement and disengagement. Figure 4.7 demonstrates the machining strategy employed during the experimental OD turning trials, in a simplified diagrammatic form. Here we can see a chamfer has been added to reduce machining forces during the first tool engagement of the pass (cut 1), which arcs in, cuts the workpiece, and then exits at 45° . The next cut, cut 2, then arcs in, picks up the same tool path as cut 1, i.e., cutting air, then proceeds to cut additional material, before finally exiting at 45° . Since the DOC employed was significantly less than the nose radius, this disengagement strategy could be used, otherwise the tool path would need to arc out as well as arc in. Each subsequent pass is stepped back to avoid hitting a shoulder, which would cause the machining forces to spike, potentially damaging the tool.

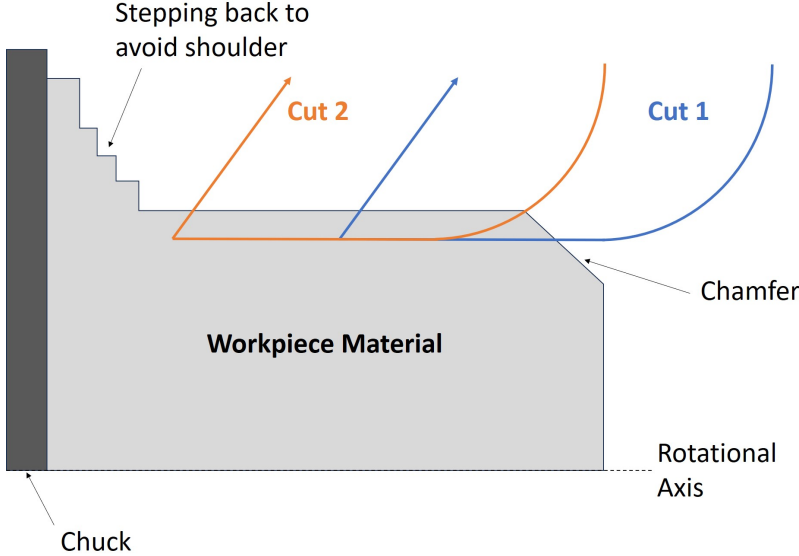


Figure 4.7: Diagram showing simplified machining strategy employed during OD turning trials.

4.9 Chemical Etching

Chemical etching can be used in materials analysis to remove a specific phase or group of materials, allowing another part of the system to be observed more clearly. In this work, etching was carried on both tools and workpiece materials, these are described below.

4.9.1 Phosphoric Acid Electrolytic Etch for Inspection of Machining Induced Damage

Phosphoric acid electrolytic etching was utilised to observe γ' precipitates in Ni-based Superalloy machined surfaces. This involved placing samples in a 10% phosphoric acid solution, before placing an electrode in the solution. A voltage is then applied (5 V at 50 mA), and the other electrode is quickly touched onto the samples' surface. The sample is then cleaned in water, followed by isopropyl. Inspection can then be carried out using optical microscopy. If the surface is under-etched the process is repeated, however, if it is over-etched, then the sample must first be repolished before re-etching.

4.9.2 Glyceregia Etch for Removal of Adhered material on Cutting Tools

During Ni-based Superalloy machining, adhesion of workpiece material on cutting tools is prevalent. Etching was performed in order to investigate the worn tool surface below the adhered material. To this end, a standard Glyceregia solution (Glycerol, HCl, and HNO₃, in a 3:2:1 ratio) was used to submerge inserts. Inserts were submerged for 15 minutes at a time, before being inspected, and then flipped over. This was repeated 3 – 6 times, depending on the workpiece material.

4.10 Modelling

A range of modelling techniques were performed to support the experimental work presented in Chapter 6. These are described in the following subsections.

4.10.1 Thermo-Calc

The commercial modelling software Thermo-Calc (version 2024b) was used to perform thermodynamic simulations of phase equilibria, using the TCNi12 database.

4.10.2 Mean-field Model

Mean field modelling as presented by Anderson [145] was carried using the M2i2 digital platform, which was in development at the time of implementation. The influence of temperature on γ' dissolution and coarsening for RR1000 was investigated, neglecting the influence of any additional mechanical effects that occur during machining (e.g., precipitate shearing, adiabatic band formation etc.), to support temperature estimation during the ex-situ analysis of the machining induced white layer.

4.10.3 3D FEM Modelling

FEM modelling of the OD turning process was carried out using the commercial FEM cutting simulation software AdvantEdge (Third Wave AdvantEdge v7.3014) in 3D, in order to explore the influence of cutting speed on maximum cutting temperatures during OD turning of RR1000. The insert was modelled using the in-built Carbide General material model; the coating was not considered. The element edge length for mesh creation was varied at different points on the tool: 8 μm at the nose, 20 μm on the near-edge rake face region, 50 μm on the chip breaker and adjacent rake-face region. Since no material data was available for RR1000, a standard workpiece using the in-built IN718 material model was employed. The workpiece was configured to be a 20 mm long cuboid. The mesh was refined by setting the Adaptive Remeshing Parameters, whereby the minimum element edge length was 9.8 μm for the chip bulk, and 7.5 μm for cutter edge. A cut of 8 mm length was modelled, and loads from the cutting contact on the insert were calculated using a steady state analysis, averaging results over the last 25% of the cut. Temperature plots were made using Tecplot 360.

Chapter 5

Insights in alumina degradation in multilayer CVD coated carbide tools when turning IN718

IN718 is a wrought alloy, widely used across a broad range of applications, and accounts for over half the overall market share [146], as such, alumina coated carbides are routinely used to machine this specific alloy. Although there has been significant published research regarding general tool wear, there have been no studies focused on the alumina layer degradation, as with steel machining. The aim of this chapter is to introduce a methodology that limits wear to the outermost alumina coating layer, and to explore the characteristic rake face wear when turning IN718.

5.1 Introduction

In the study that follows, the rake face degradation mechanisms of textured alumina layer of CVD TiCN/ α -alumina coated carbides was investigated when performing single point turning on IN718. Short SCLs were employed to limit wear to the outermost alumina coating layer; SCL was incrementally increased in order observe the wear progression. SEM in both SE and BSE imaging modes was used to study the worn surfaces on tools in both etched and unetched states. X-EDS was also utilised alongside EPMA to investigate chemical wear phenomena. Finally, cross-sections of worn tools were made to investigate the overall thickness reduction in the alumina over time.

5.2 Materials and method

The following section details the materials and methodology utilised in the machining experiment presented.

5.2.1 Experimental Materials

The workpiece material was aged IN718 (composition given in Table 3.1), which was solution annealed at 980°C for 1.5 hours, water quenched, and then aged at 718°C for 4 hours before being furnace-cooled at 50°C · h⁻¹. Finally, it was aged at 621°C for 4 hours, then air-cooled. IN718 (composition given in Table 3.1), with a hardness of 411 HBW and an average grain diameter of 38.5 μm. The billet had an initial diameter of 120 mm and a length of 202 mm. A QS-PCLNL 2020-12C shank and Sandvik Coromant commercial grade inserts with a CNMG 12 04 08-SF geometry were used for the experiments (see Section 3.1.2). The inserts feature the S205 coating, which has been tailored for optimal performance when machining Ni-based superalloys (see Section 3.1.1). Prior to the trials, edge rounding measurements were taken of 40 insert cutting edges, 25 inserts within a $\rho = 40 \pm 1 \mu\text{m}$ range were down selected for the trial. The cutting fluid used was Blaser Vasco 7000, a commercial coolant with a pH of 8.5/9 and a concentration of 11.7%.

5.2.2 Test Methods

The experimental machining trials were conducted on an DMG Mori NLX 2500 lathe, the experimental setup is shown in Figure 4.6. Longitudinal turning operations were performed over different machined SCLs: 2 m, 32 m and 128 m. A Kistler plate piezoelectric force dynamometer (Type 9129AA) was used to measure the machining force components during cutting in the passive (F_p), cutting (F_f) and feed (F_c) directions; this was done primarily to monitor the edge condition and ensure consistent tool engagements; a sample rate of 20 kHz was selected (see Section 4.7). Parameters used were chosen to be representative of a standard industrial process. Machining strategies were configured to reduce spikes in machining forces (see Section 4.8). High pressure through tool coolant with a pressure of 65 bar was used for all cuts made. Since coolant properties heavily influence tool wear, pH levels were measured using litmus paper and concentration levels were monitored using a refractometer to ensure they remained consistent throughout the trial. As per the tooling manufacturers recommendations, DOC used for all cuts was 0.25 mm and the feed rate 0.1 mm · rev⁻¹. A cutting speed of 100 m · min⁻¹ was employed. Machined lengths of 2 m, 32 m and 128 m were selected for the initial wear trial, which represent 0.2%, 2.7% and 11.7% of tool life respectively (verified by previous tool life trial). Three repeats were conducted for each length.

5.2.3 Characterisation techniques

Scanning electron microscopy (SEM) was carried out on a Zeiss EVO LS25-1204 and a Hitachi TM3030; imaging was conducted using a combination of backscattered electron (BSE)

and secondary electron (SE) detectors (see Section 4.1). A 45° holder was used for imaging tool nose wear. An 80 mm Oxford X-EDS system was used to perform compositional analysis (see Section 4.1). Etched inserts were etched in Glyceregia for approx. 1 hour (see Section 4.9). Average thickness measurements were taken cross sectional micrographs from five separate measurements spaced 10 μm apart across 50 μm sample sections; three repeats were taken of each measurement.

5.3 Results and Discussion

An example of the machining forces measured during the experiment is shown in Figure 5.1. In all experiments performed the F_c was found to be the largest of all force components, followed by the passing force F_p , and then the feed force F_f . The resultant, R , was calculated as ≈ 170 N. The smooth gradient during the initial engagement indicates a stable entrance of the tool with no unexpected failure or abrupt wear, similarly there are no large variations during the cut either. The wear observed during the trials is shown after 2 m, 32 m and 128 m SCL in Figure 5.2. After 2 m SCL, the workpiece material is adhered to the tool (Figure 5.2a). By 32 m, the region covered by adhered material has increased significantly in thickness, a DOC notch and chip adhesion can also be observed (Figure 5.2b). After 128 m (Figure 5.2c) SCL, the thickness of the adhered material on the cutting edge has increased further. In addition, the DOC notch has continued to expand and a small trailing edge notch has started to develop (Figure 5.2c).

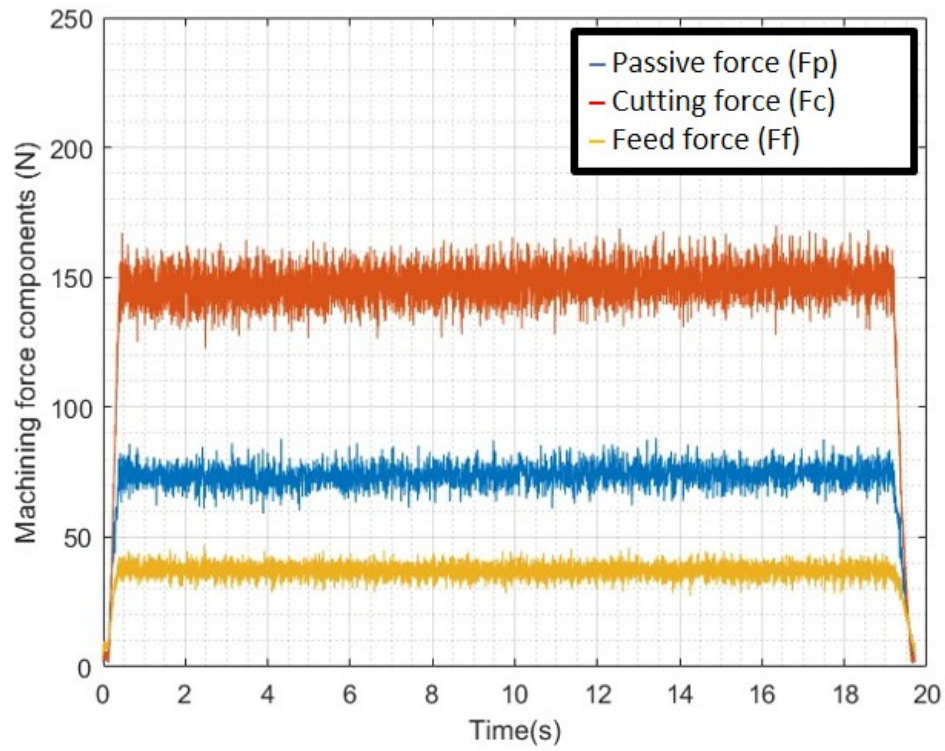


Figure 5.1: Machining forces measured: Cutting force (F_c), Feed force (F_f) and Passive Force (F_p), using Kistler piezoelectric plate dynamometer during 32 m machined length test.

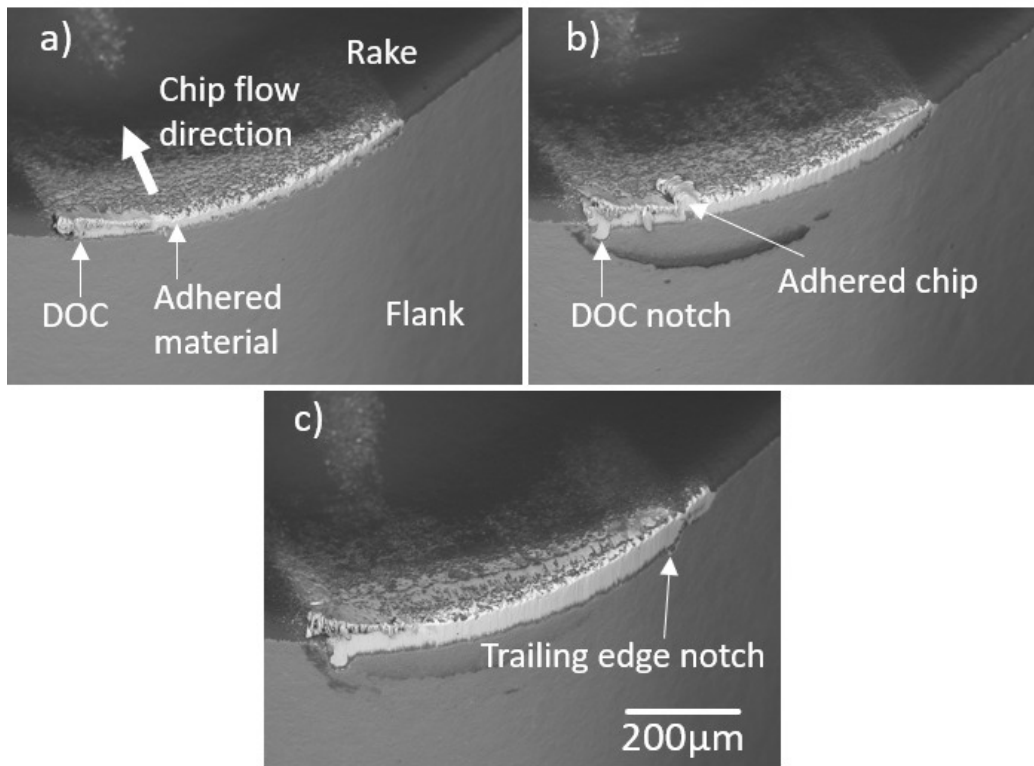


Figure 5.2: BSE SEM micrographs of tool wear developed during turning trial at each SCL (a) 2 m (b) 32 m (c) 128 m.

Figure 5.3 shows X-EDS mapping of the elements Al, Ti, and Ni on the damaged tools after each SCL. The Al signal indicates the alumina coating and so is the majority of the signal seen on the rake of the tool. Ni indicates adhered workpiece material, which has formed or adhered in the tool-chip contact zone. The Ti signal indicates that the TiCN layer of the coating has now been exposed as the alumina coating has been removed. Figure 5.3a shows a small notch/chipping or failure of the alumina coating already after 2 m of turning, towards the trailing edge of the tool. The wear may be concentrated in this region as the chip is at its thinnest, meaning the chip compression ratio is higher, and so more work hardening and grain refinement of the workpiece material can be expected. After 32 m (Figure 5.3b), the wear in this region continues to expand as the alumina layer is removed, there is also exposure of the TiCN layer around the DOC notch. By 128 m, (Figure 5.3c), the alumina layer has worn further in the regions previously displaying wear. Furthermore, the alumina coating wear around the DOC has become significantly enlarged and elongated. Several additional areas of alumina coating failure have also appeared towards the rear of the contact zone as the chip begins to deflect.

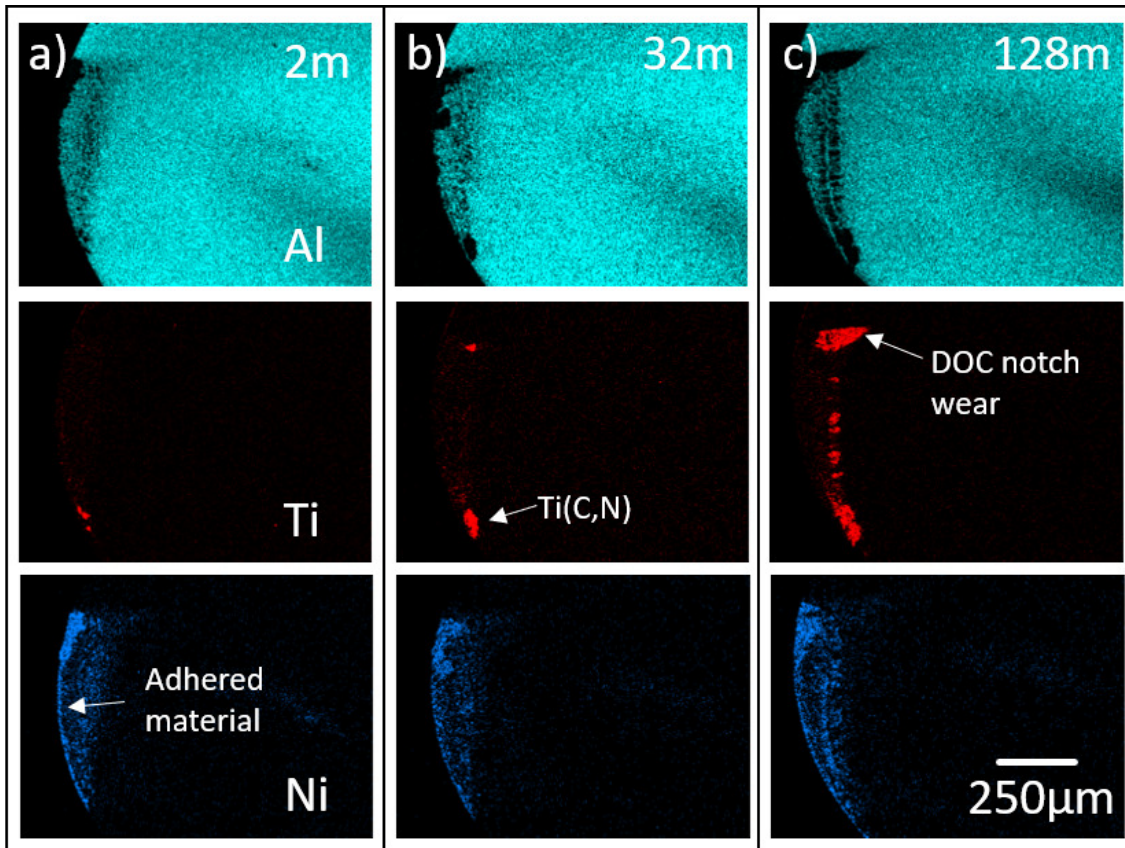


Figure 5.3: X-EDS of adhered material on worn inserts for Al, Ti and Ni at different SCLs: (a) 2 m (b) 32 m (c) 128 m.

In Figure 5.4a it can be seen that the strong signals of Ti are areas where the alumina coating has delaminated; Figure 5.4b shows the rough topography of the fractured surface that remains. Three distinct wear zones can be seen in the worn surface. Zone A is the sticking zone, an area that appears to correspond to the edge radius of the tool. Zone B is the sliding zone, distinguished by the smeared adhered workpiece material. There is no clear transition zone observed between zones A and B, potentially due to the small DOC employed. Zone C is the end of contact zone, an area in which there is a transition from the sliding contact of zone B as the chip begins to separate from the tool. In this zone, delamination events occur most frequently (except for the DOC and trailing edge notches), which occurs as a result of an adhesively driven tearing force [147]. Crater wear tends to occur some distance behind the cutting edge [116]. The exact position is dependent on the contact pressure, sliding velocity and temperature distribution [148]. In zone C the high pressure coolant jet on the rake side of the tool forms a hydrodynamic wedge which changes the stress distribution, reducing the size of the contact zone, lowering frictional forces and temperatures. The reduction in pressure in this region may permit the occurrence of coolant driven wear phenomena and oxidation to occur. This behaviour has not been seen during steel turning investigations regarding alumina

layer degradation [24, 120, 121, 125]. This may be attributed primarily to the high degree of adhesive wear associated with machining IN718: in combination with the effect of HPC and a very reactive workpiece material with low thermal conductivity.

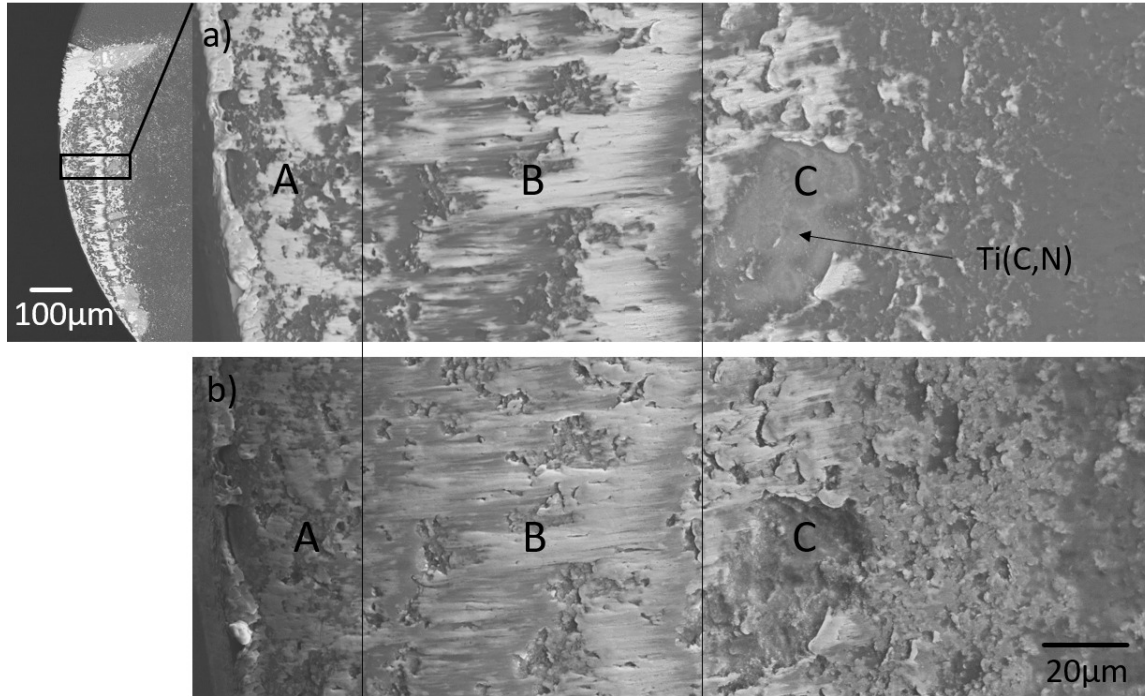


Figure 5.4: SEM micrographs of worn unetched insert showing sticking (zone A), sliding zone (zone B), and end-of-contact (zone C) after a SCL of 128 m: (a) BSE imaging mode (b) SE imaging mode. Delamination and TiCN exposure is observed in zone C.

In order to explore the wear mechanisms that alumina is subjected to it is necessary to remove the adhered material using etching techniques. The worn alumina surface of the etched sister insert in zone B, after 128 m SCL, is presented in Figure 5.5. The worn surface exhibits two characteristic distinct wear types: the first type is identified by ridges that have formed, indicative of plastic deformation in the alumina due to slip, which appears to correspond to the smeared material observed in Figure 5.4. Plastic deformation of alumina has been widely reported during dry steel turning [24, 120, 121, 125]. Although no temperature measurements were made during this experiment, since longitudinal turning operations do not permit the use of a thermal camera, maximum rake face temperatures in orthogonal dry Ni-based superalloy turning have been reported to be in the region of 1000°C [15], which is comparable to those achieved during dry steel turning [55]. Therefore, the likelihood for activation of different slip systems in the alumina coating is expected to be similar. The effect of coolant on the maximum temperature remains disputed as an exact measurement of surface temperatures at the tool-chip contact is often not feasible. Thermal modelling suggests that a temperature decrease of between 31–38°C could be expected when using an 80 bar coolant pressure supply

when turning IN718 using similar processing parameters to those used in the study [149]. As such, the impact of coolant on maximum temperatures in the contact zone is considered to be minimal.

The second observable wear type shown in Figure 5.5 is grain pull-out of the alumina coating. It is hypothesised that coating pull-out is largely controlled by an adhesive wear dominated mechanism that occurs when the bond formed between tool and workpiece material has a stronger bonding energy than the intergranular bonding energy of the alumina grains. This in contrast to the observations made during steel turning experiments in which no grain pull-out is observed in zone B [24, 120, 121, 125].

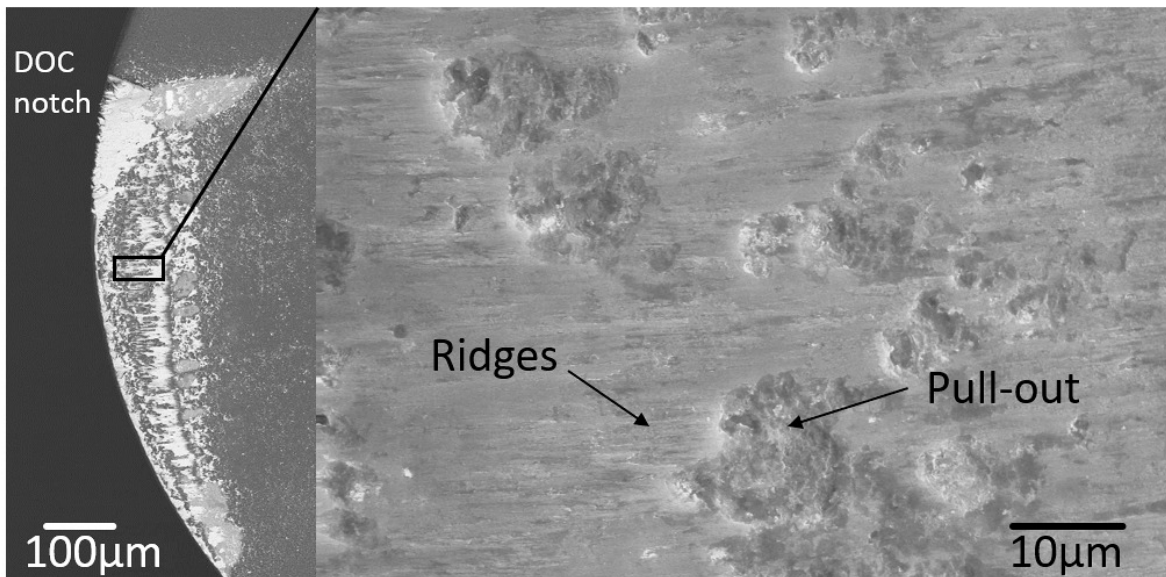


Figure 5.5: SE SEM micrograph showing worn surface of etched alumina after 128m SCL in the sliding zone (zone B).

Etching worn tools also allows non-metallic bonds to be observed created by reaction products; these appear as areas of brighter contrast when using BSE imaging. The presence of these kind of chemical interactions seen in Figure 5.6, indicate that chemical wear could be an additional active wear mechanism. The majority of these reaction products are too fine to be easily identified using X-EDS, however some instances of Nb-rich inclusion bonding was identified.

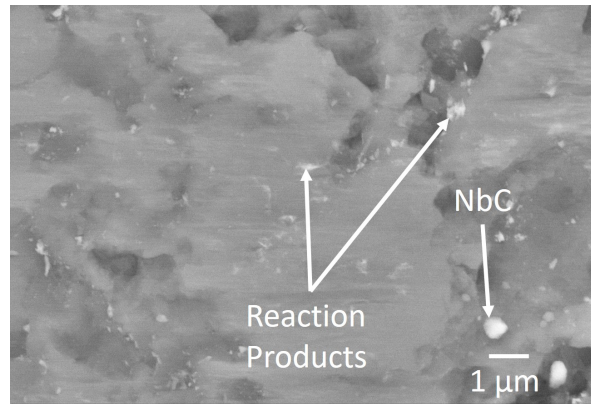


Figure 5.6: BSE SEM micrograph of post-etched surface for insert ran to 32 m SCL in the sliding zone (zone B) displaying potential reaction products adhered to alumina.

EPMA was later employed to investigate if any diffusion from tool to workpiece could be observed in the sliding zone of an unetched tool after 128 m SCL; the area examined is shown in Figure 5.7. Figure 5.8 displays the corresponding EPMA maps for the different elements examined; the composition is generally homogeneous except for a single Nb-rich region, which is due to the presence of an adhered Nb-rich inclusion Table 5.1 presents the composition of region 1 shown in Figure 5.7. It can be observed there is an enrichment of Ti and Al, however, the Al enrichment is likely as a result of the additional signal from the neighbouring alumina coating. The Ti enrichment indicates that this element may react with the alumina, resulting in potential chemical wear.

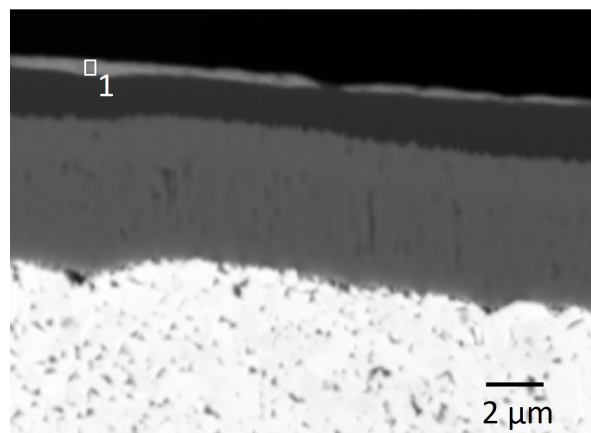


Figure 5.7: Cross-section of adhered material within the sliding zone (zone B), showing region 1; used for compositional analysis.

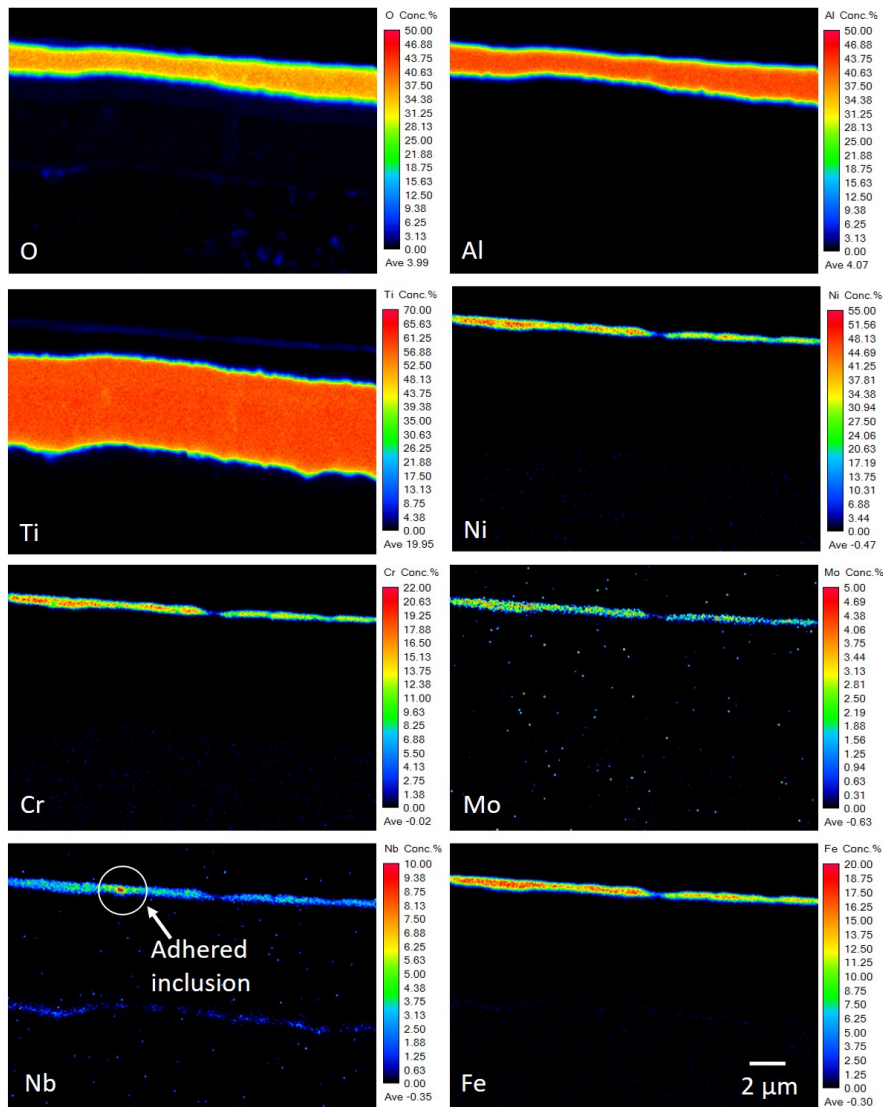


Figure 5.8: EPMA performed on adhered IN718 material in sliding zone (zone B) after a SCL of 128 m.

Table 5.1: Composition in Wt.% for nominal, and measured values for adhered IN718 in region 1 (see Figure 5.7).

	Ni	Fe	Cr	Nb	Mo	Ti	Al
Nom.	53.6	17.8	18.5	5.3	3.0	1.1	0.5
1	48.5	17.8	23.3	4.1	3.0	2.2	1.0

To study the wear progression during machining, SEM micrographs were taken in both BSE and SE imaging modes of the etched sister inserts at each SCL tested. BSE images were

used to indicate when the alumina layer had worn through, as changes in composition will be shown as changes in contrast. SE images were taken to obtain topographical information, in order to determine if grains of the alumina had been pulled out. The etched sister inserts were imaged in two regions: 1 and 2 (see Figure 5.9). Region 1 is positioned near middle of the tool, near the average chip thickness. Region 2 is located towards the trailing edge, and so the surface speed is slower than at region 1 as it is closer to the centre of rotation. In addition, the chip is thinner, and therefore the chip compression rate is higher.

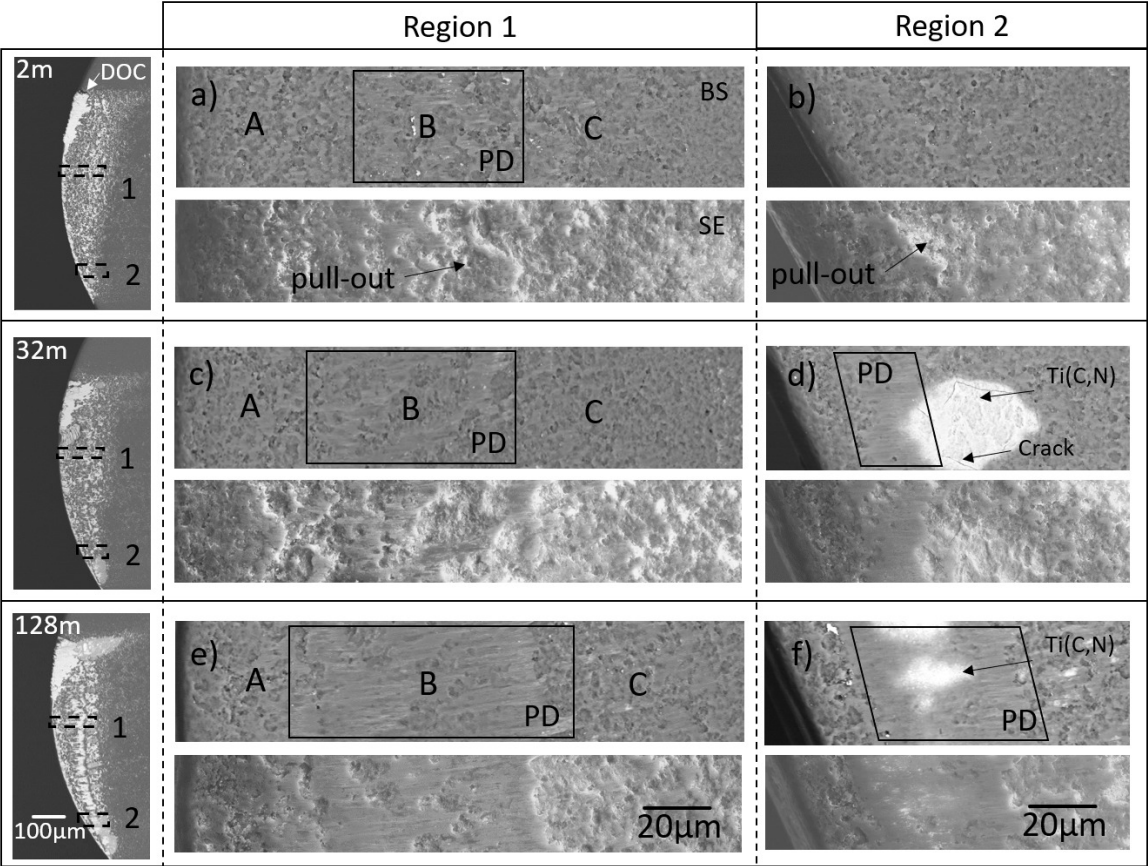


Figure 5.9: SEM BS micrographs showing alumina wear unetched (BSE imaging) and etched (SE imaging) sister inserts compared at different SCLs (a) region 1 at 2 m (b) region 2 at 2 m (c) region 1 at 32 m (d) region 2 at 32 m (e) region 1 at 128 m (f) region 2 at 128 m.

Despite the short time in cut, Figure 5.9a demonstrates there is evidence of plastic deformation in region 1 (shown as PD) after a SCL of 2 m, which corresponds to the sliding contact present in zone B. In the area displaying plastic deformation there are also indications of coating pull-out; to the left of this region there is an area characterised solely by coating pull-out. This area corresponds to workpiece seizure in zone A. Towards the right of the plastically deformed region there are areas displaying coating pull-out, which lie within zone C. In region 2, there appears to be less evidence of plastic deformation (Figure 5.9b), although some

coating pull-out has occurred.

After 32 m of cutting (Figure 5.9c), the plastically deformed area has expanded towards the zone A, potentially due to the temperature increase caused by the longer time in cut. Significant grain pull-out is also observed within the plastically deformed area, as well as to the right in zone C. In region 2 after 32 m SCL (Figure 5.9d), there is a large delaminated region to the right of the plastically deformed area. The change in contrast across these two regions appears gradual, demonstrating further plastic deformation of the alumina layer occurred after the delamination event.

After a SCL of 128 m (Figure 5.9e), the plastically deformed regions of alumina have increased both towards and away from the cutting edge. It appears as if this wear behaviour has resulted in a smoother topography. Areas exhibiting coating pull-out can be observed within the plastically deformed region, as well as in zone A and zone C. In region 2 (Figure 5.9f), it appears as if the continued alumina wear via plastic deformation has in part led to the TiCN layer becoming partly exposed. This appears to be as a result of a more gradual wear than was observed in Figure 5.9d, since the revealed TiCN is contained entirely within the plastically deformed area. This highlights the fact that there is significant variability when observing the wear behaviour, as this gradual wear regime may not be observed if a sudden delamination has already occurred.

Cross sections of the worn tools were metallographically prepared to investigate variations in alumina coating thickness. This was done by polishing away approximately 0.15 mm of material (as shown in Figure 5.10). Two separate 50 μm sample regions were chosen to be representative of zone B, 100-150 μm from the tool edge, and zone C, 200-250 μm from the tool edge; the average coating thickness (x_{av}) is shown for each sample region. After 2 m of cutting (Figure 5.10a) it can be observed that both sample regions have a similar appearance in terms of both topography and thickness. A similar observation is made after 32 m of cutting (Figure 5.10b), although in zone B, a dislodged section (labelled DS) is observed whereby both the alumina and TiCN layer have been removed. This could suggest the coating contained cracks that resulted in fracture during polishing or machining. After 128 m (Figure 5.10c), a noticeable difference in the two regions is revealed, with a large section of alumina ($\approx 20 \mu\text{m}$) in zone C being completely removed and the underlying TiCN layer exposed.

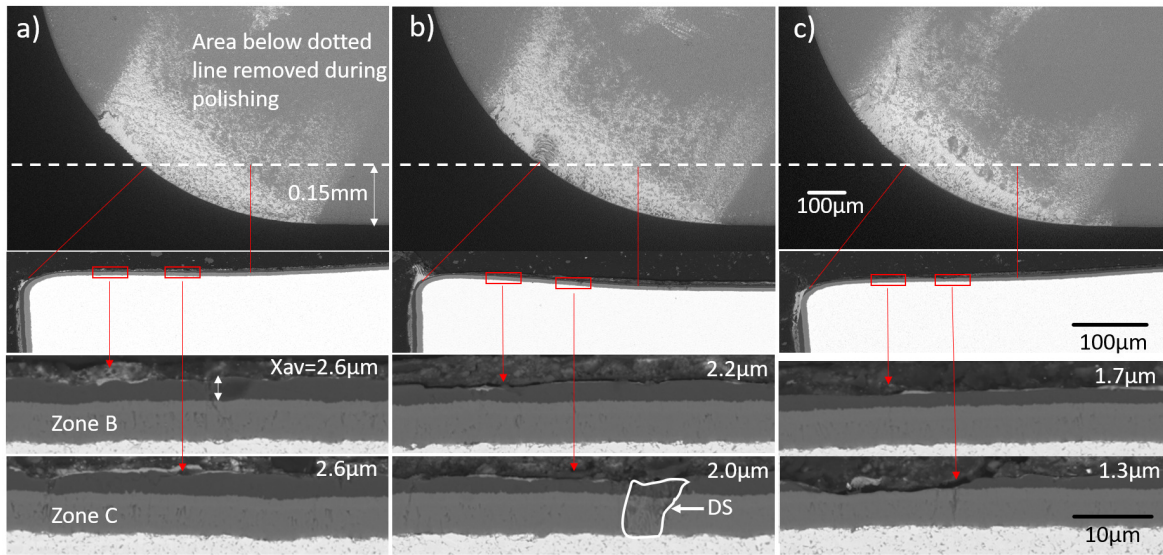


Figure 5.10: Cross sections of inserts taken from zones B and C at different SCLs: (a) 2 m (b) 32 m (c) 128 m.

5.4 Conclusions

In the chapter presented, OD turning using HPC was performed on IN718 using industry relevant parameters. SCL was varied in order to explore the degradation of the outermost textured alumina layer of a multi-layered CVD TiCN/ α -alumina coating deposited on a carbide substrate. It was found that turning IN718 leads to significant adhesive wear and coating loss due to attrition, which initiates upon tool engagement with the workpiece. Significant coating loss occurred at the end-of-contact zone due to the tensile forces that develop as the chip begins to deflect, further emphasising the adhesive nature of the workpiece material. Evidence of plastic deformation of the worn alumina surface was detected in the sliding zone, indicating high temperatures present in this region of the contact. Reaction products in the sliding zone were also detected that appear to be rich in the reactive refractory element Nb, suggesting chemical wear may also occur within this region. The alumina coating on the rake face nearest to the cutting edge remained intact suggesting that the coating offers adequate protection over the initial turned meters to protect the edge from premature failure.

Chapter 6

Effect of workpiece grain size and cutting speed on tool wear and workpiece microstructural damage when turning RR1000 with multi-layer CVD alumina coated carbides

In Chapter 5, significant coating pull-out and plastic deformation of alumina asperities were observed during single-point turning of a typical wrought superalloy (IN718) after relatively short SCLs, demonstrating the limited protection offered by alumina in certain regions of the rake face contact. PM Ni-based Superalloys are broadly considered harder-to-machine than wrought alloys, exhibiting improved high temperature performance as a result of a higher concentration of γ' forming elements. It is currently unclear how these variations in workpiece chemistry will impact alumina coating degradation during turning, and whether other factors such as turning cutting speed and workpiece grain size are also influential. The proceeding chapter aims to answer these questions.

6.1 Introduction

In the following study RR1000 was heat treated to produce two material conditions with differing grain sizes (CG, FG), at two different cutting speeds, which represent the upper and lower bounds typically recommended by the tool manufacturer (Sandvik Coromant). Machining forces were recorded using dynamometry during tool wear trials. This was done to assess the effectiveness of the machining strategies employed, to monitor the tool wear progression, and to compare the deformation characteristics of different machining conditions. Analysis was then carried out on worn tools at varying SCLs to observe the wear progression of the outermost alumina layer, this involved utilising a range of analytical techniques: SEM, EPMA, and X-EDS. In addition, machined surfaces were also examined using electrolytic etching to reveal precipitate deformation, TEM was also utilised to examine as-polished sur-

faces, in addition to EBSD. Modelling was performed using a range of software packages: AdvantEdge (FEM), Thermo-Calc (CALPHAD), and a M2i2 Digital Platform (mean field model).

6.2 Materials and Methods

The following section details the materials and methodology utilised in the machining experiment presented.

6.2.1 Experimental Materials

In the following work RR1000 was selected to be the workpiece material for the experimental machining trials (see Section 3.2). The billets utilised were two "centre slugs" taken from aero-engine disk forgings. Billet dimensions were approximately $\varnothing = 65$ mm, length = 140 mm. Both billets were then heat treated to produce two distinct material conditions. The first billet was solution heat treated above the γ' solvus at 1160°C for 1.5 hrs. Processing at this temperature dissolves the primary γ' precipitates that limit grain growth, allowing for a coarse grain (CG) material to be obtained; it should be noted that this experimental CG material has a broader distribution of grain size than material typically refereed to as "CG RR1000" within industry (see Figure A2 of appendix A). The second billet was solution heat treated below the γ' solvus at 1120°C for 1.5 hrs., hence, grain growth of γ is suppressed by the retention of primary γ' precipitates, in order to produce a fine grain (FG) material condition. After air cooling, a second precipitation heat treated was carried on both billets for 8 hrs. at 760°C. The grain size distribution for the FG material is representative of material refereed to as "FG RR1000" within industry (see Figure A2 of appendix A).

Average γ' precipitate sizes and volume fractions (Vf) are given in Table 6.1; average grain sizes and bulk hardnesses for both material conditions are shown in Table 6.2. The data presented in Table 6.1 was measured using SE SEM images of electrolytically etched samples that were taken of the bulk material ≈ 25 mm from the billet centre. Vf values for the primary and secondary γ' precipitates were measured, and were estimated for the tertiary γ' precipitates by calculating the theoretical equilibrium total γ' Vf (0.44), before subtracting the summation of the measured primary and secondary γ' Vf. Equilibrium calculations were performed using Thermo-Calc and the TCNi12 database. Av. r measurements for tertiary γ' presented in Table 6.1 should be treated with some caution, since the smallest precipitates are towards the limit of the resolution practically achievable on the SEM system employed.

Table 6.1: γ' precipitate radius and volume fraction for CG and FG RR1000 material conditions.

	Tertiary		Secondary		Primary	
	Av. r (nm)	Vf	Av. r (nm)	Vf	Av. r (nm)	Vf
CG	10	0.06	90	0.38	N/A	N/A
FG	11	0.04	60	0.28	340	0.12

Table 6.2: Hardness measurements and average grain size for CG and FG RR1000.

	Hardness (Hv0.5)			Av. Grain
	Min.	Max.	Av.	Size (μm)
CG	446	459	453.2	30
FG	461	472	467.4	4

Sandvik Coromant S205 CNMG120408-SF cutting inserts were utilised during the experiments (see Section 3.1.2), featuring the S205 coating described in Section 3.1.1. Inserts with ER of $\rho = 42 \pm 3.2 \mu\text{m}$ were used in the trial. The coolant utilised was Blaser Vasco 7000 with a concentration of 8.1 %, which was applied through a QS-PCLNL 2020-12C shank at a pressure of 40 bar, delivering cooling to both the rake and flank faces.

6.2.2 Test methods

Single point outer-diameter turning was carried out on a DMG Mori NLX 2500 lathe using the following machining parameters: DOC = 0.25 mm, feed = $0.1 \text{ mm} \cdot \text{rev}^{-1}$, surface speed = 70 and $100 \text{ m} \cdot \text{min}^{-1}$. Continuous outer diameter turning operations were conducted at various SCL values: 2, 16, 32, 64, and 128 m; these were performed in a single cut. In addition, conventional wear testing was conducted using the FG material up to a SCL of 700 m, which was reached in increments 100 m, as such, said cutting inserts were subjected to successive engagements and disengagements. To ensure material homogeneity in terms of grain size and precipitate morphology, cuts were performed only on the first 15 mm of the diameter (i.e. $\varnothing = 50\text{-}65 \text{ mm}$), and were fully randomised. Engagements and disengagements were configured to prevent the tool coming into contact with corners or edges that may cause accelerated damage to the cutting inserts (see Section 4.8). A Kistler plate piezoelectric force dynamometer, Type 9129AA model, was employed as per the method described in Section 4.7.

An additional face turning experiment was then performed on the remaining workpiece ma-

terial to investigate if machining force response data could be used to produce digital fingerprints, in order to assess material homogeneity in terms of centre to edge grain size variation (see for Section 4.7.1). To enable this, different cutting parameters were employed: DOC = 0.1 mm, feed = 0.05 mm · rev⁻¹, surface speed = 60 m · min⁻¹.

6.2.3 Characterisation Techniques

Post-machined samples, that had been turned a SCL between 6–9 m, were sectioned, and then ground and polished to reveal surfaces normal to the feed direction, such that deformation in the cutting direction could be observed (see Section 4.7 for description of force components with respect to workpiece orientation). The full metallographic preparation method is given in Section 4.6.

SEM microscopy was performed using a Zeiss EVO LS25-1204, a Hitachi TM3030, and a JEOL JSM-7900F, using a combination of BSE and SE detectors; a JEOL JSM-7900F was used to obtain orientation mapping via EBSD; X-EDS was performed on a 80 mm Oxford X-EDS system (see Section 4.1). EPMA was performed using a JEOL JXA 8530F PLUS (see Section 4.2).

Etched inserts were submerged in Glyceregia for one hour to observe wear obscured by adhered workpiece material; machined surfaces were electrolytically etched in phosphoric acid to reveal precipitates (see Section 4.9). An Alicona infinite focus SL was used to measure ER values (see Section 2.4.4 and Section 4.4.2). Cuttings inserts with ER values within a $\rho = (42 \pm 2 \mu\text{m})$ range were then down selected for the cutting trial. All microhardness measurements were performed on a DuraScan microhardness tester (see Section 4.5).

XRD was performed using a Proto iXRD portable residual stress diffractometer (see Section 4.3). Measurement of FWHM using XRD was implemented as a non-destructive method for assessing the degree of machining induced damage, as per the method presented by Brown et al. [137], further details are provided in Section 4.3. Measurements were performed at the midpoint of the machined length, i.e., half the total SCL for each cut, to eliminate the chance for interference from neighbouring cuts, or corners created during tool disengagement.

6.2.4 Modelling techniques

3D FEM cutting simulations were carried out using the commercial software AdvantEdge (see Section 4.10.3) to understand the influence of cutting speed on cutting temperatures. Simulations were performed using the same parameters (i.e., DOC, feed, cutting speed) as in the machining experiments performed.

Simulations of γ' dissolution and coarsening for FG and CG RR1000 due to thermal effects

was performed using the method presented in [145] (see Section 4.10.2). This was done to assist in temperature estimation during inspection of the machined surface post machining.

Thermo-Calc thermodynamic simulations of workpiece oxidation were performed for RR1000 to explore the preferential congregation of specific reaction products towards the rear of the contact zone during OD turning (see Section 4.10.1).

6.3 Results and Discussion

6.3.1 Surface Integrity of Turned CG and FG RR1000

Inspecting the machined surfaces after electrolytic etching in Figure 6.1, the bulk precipitate morphology is revealed for both CG and FG material conditions. As shown in Table 6.1, Figure 6.1 demonstrates that secondary γ' precipitates are finer in the FG material than in the CG material. The absence of primary γ' precipitates in the CG is also apparent, resulting in higher volume fraction of secondary γ' precipitates. It has been shown that the FG heat treatment will result in a $\approx 13\%$ higher yield stress at a temperature of 750°C , primarily due to the Hall-Petch effect [38]. It should be noted that the difference becomes less significant as temperature is increased [38], and as temperatures approach the γ' solvus ($\approx 1150^\circ\text{C}$ [145]), secondary γ' particles are anticipated to dissolve more readily in the FG material condition on account of their smaller radius.

It can be observed in Figure 6.1 that higher depths of machining induced damage occur when turning the CG material, as indicated by the swept grain structure and high density of slip bands, in which precipitate shearing is observed. Cross-slip was also observed in certain grains of the GG material, where the local microstructure was orientated favourably for this deformation mode to occur (see Figure 6.2). Figure 6.1 demonstrates that both CG and FG material conditions exhibit a severe plastic deformation (SPD) layer in the topmost layer of their respective surfaces.

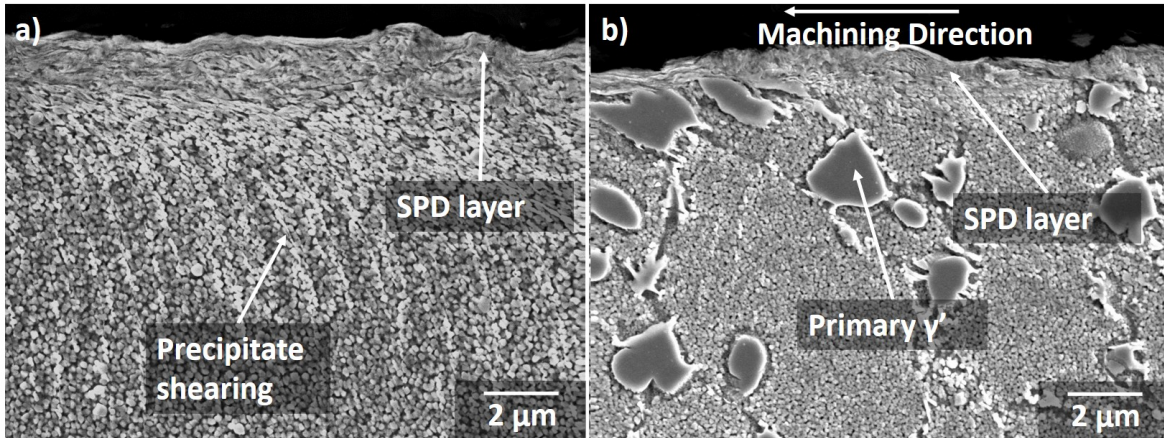


Figure 6.1: BSE SEM micrograph of electro-etched subsurface deformation when turning the (a) CG material (b) FG material at $100 \text{ m} \cdot \text{min}^{-1}$.

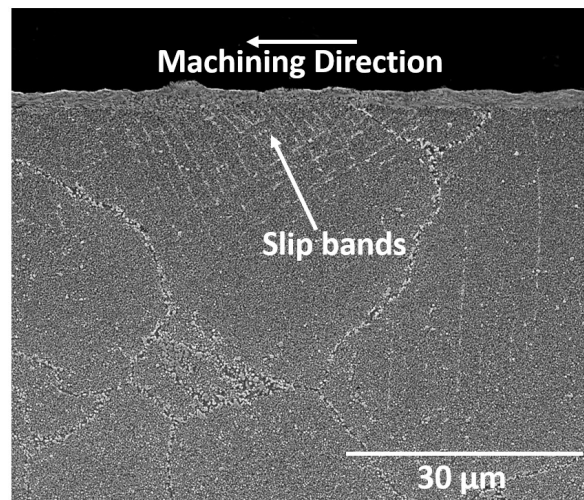


Figure 6.2: Subsurface deformation generated when turning the CG material at a surface speed of $100 \text{ m} \cdot \text{min}^{-1}$. Image shows evidence for dependency of slip band formation on grain orientation.

Figure 6.3 displays the SPD layer at higher magnification. The thickness and characteristics of the SPD layer are observed to vary significantly depending on the local microstructural texture and γ' morphology. In addition, varying levels of γ' dissolution within the SPD layer were observed, ranging from partial dissolution (Figure 6.3a), whereby the outlines of the secondary precipitates can still be distinguished, to total dissolution (Figure 6.3b), in which no visible structure can be observed. Figure 6.3b also displays inclusions, near to the surface that appear to be undeformed, on account of their high temperature stability and high hardness; this is likely to be a boride or carbide [150]. When machining the FG material,

primary γ' was observed in some instances to "shield" the secondary γ' , limiting the deformation if near surface precipitates (Figure 6.3c). Below the SPD layer precipitate shearing was observed when turning both material conditions (Figure 6.3b and Figure 6.3d), although was more common when turning the CG material; this subsurface region is subjected to high strain but lower temperatures that do not facilitate precipitate dissolution.

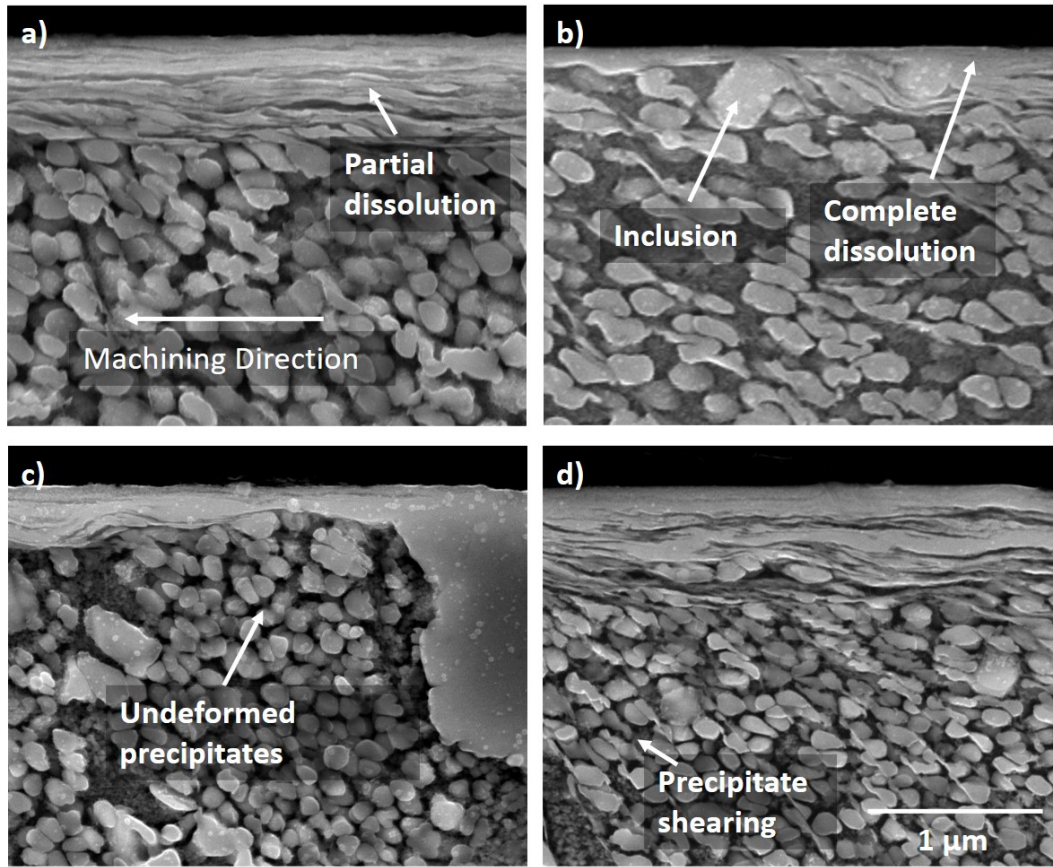


Figure 6.3: SE SEM micrograph of electro-etched subsurface, showing SPD layer produced when turning (a) CG material at $70 \text{ m} \cdot \text{min}^{-1}$ (b) CG material at $100 \text{ m} \cdot \text{min}^{-1}$ for FG material (c) FG material at $70 \text{ m} \cdot \text{min}^{-1}$ (d) FG material at $100 \text{ m} \cdot \text{min}^{-1}$.

Visually estimated measurements of the heavily deformed layer thickness over all conditions tested are presented in Figure 6.4. The boundary for this region was defined as regions displaying partial or complete dissolution. Although no significant difference was observed when comparing average values, higher ranges were measured when turning the CG material. Furthermore, larger variations were also measured when turning both materials at the higher speed of $100 \text{ m} \cdot \text{min}^{-1}$. Typically, during aeroengine manufacture, this kind of localised surface damage is inspected using optical microscopy, after the surface is etched with an etchant that targets the γ' phase; it is generally referred to as "white layer" in the aerospace industry if no visible grain structure can be observed. This kind of damage has been frequently observed

when machining RR1000 [103, 151, 12].

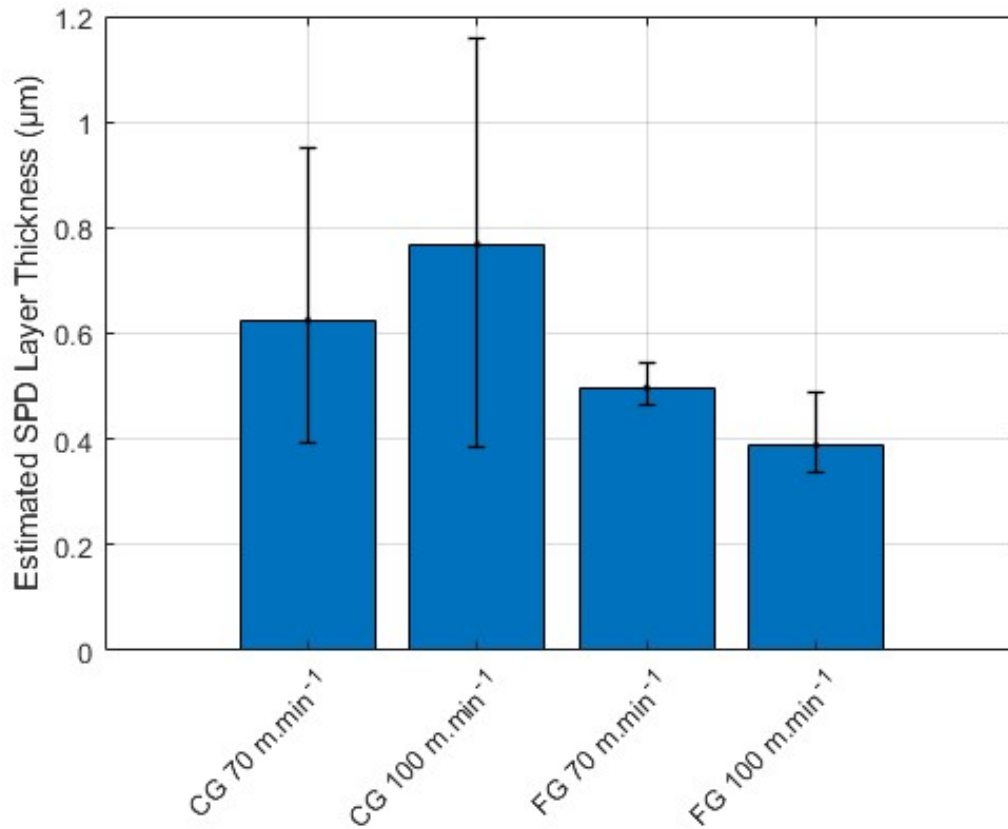


Figure 6.4: Bar chart showing influence of workpiece material condition and cutting speed on severely deformed layer thickness.

To explore the characteristics of the SPD layer at higher resolution, TEM was employed. Figure 6.5 shows TEM X-EDS performed on a FG sample machined at $100 \text{ m} \cdot \text{min}^{-1}$, and indicates that dissolution of tertiary γ' in the given region begins to occur approximately $1.8 \text{ } \mu\text{m}$ below the machined surface. Dissolution of secondary γ' precipitates can be observed to occur at depths less than $0.2 \text{ } \mu\text{m}$. Clearly local temperatures at the workpiece surface are approaching the γ' solvus temperature, however, this temperature may effectively be lowered by the high strain and defect density at the machined surface, which leads to precipitate shearing, effectively reducing the particle radius and lowering the amount of energy required for their dissolution. Other considerations such as slip band formation can also lead to higher local temperatures due to adiabatic heating. Furthermore, the swept grain behaviour leads to a higher concentration of slip bands near to the surface. Temperatures approaching the γ' solvus have been measured by IR thermography during orthogonal turning of an advanced Ni-based alloys by Liao et al. [16] under aggressive cutting conditions with worn tools. It

would therefore seem reasonable that similar local temperatures can occur under conventional machining conditions with new tools at high cutting speeds.

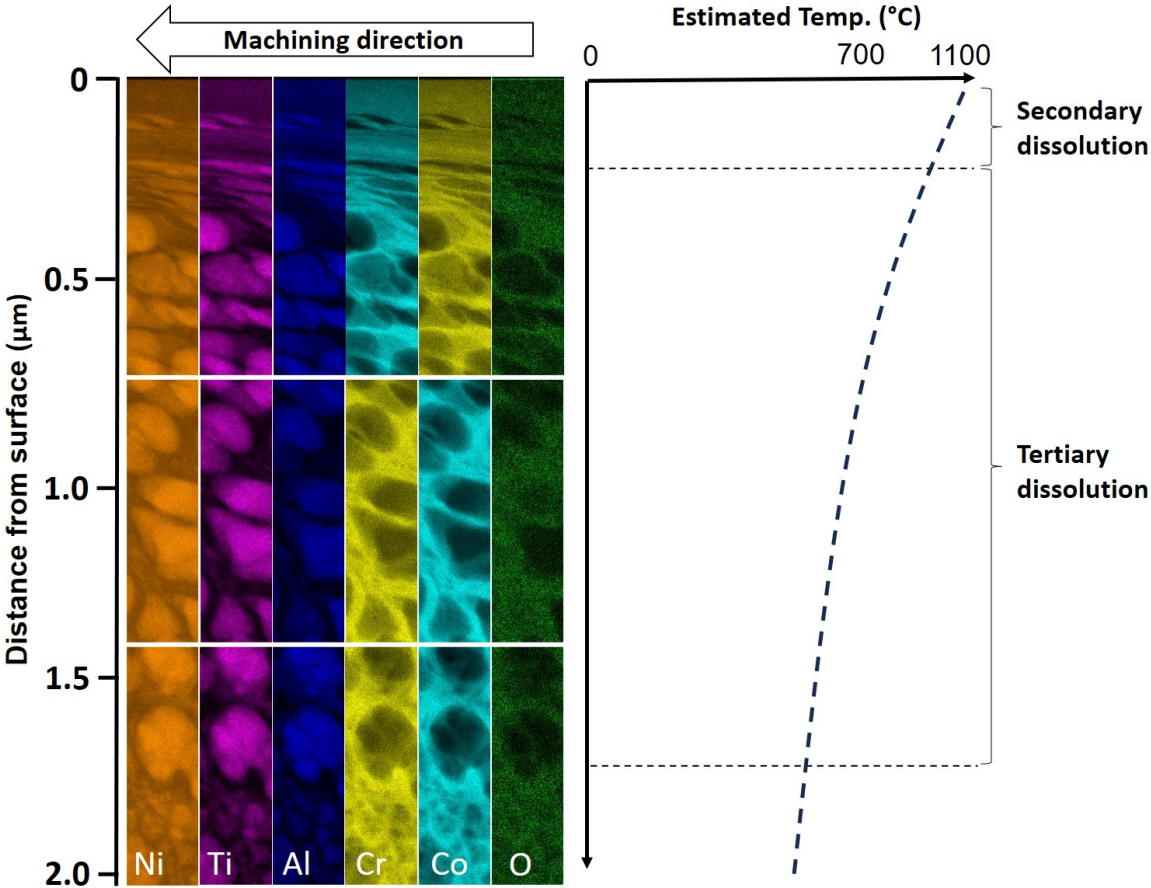


Figure 6.5: TEM X-EDS map of FG material turned at $100 \text{ m} \cdot \text{min}^{-1}$, prepared using FIB lift-out technique, showing secondary and tertiary γ' dissolution variation across the machined surface, viewed normal to the cutting direction, alongside corresponding estimated temperature distribution.

Figure 6.6 shows EBSD data for each machining condition. Inverse pole figures (IPF) are presented for the z-direction. Due to the highly strained nature of the SPD layer, there are non-indexed regions along the surface. This is seen most clearly in the FG condition, due to the higher magnification used. Below the SPD layer, intragranular strain due to lattice rotation, and subgrain formation are shown by variations in misorientation contrast. Observing both surfaces, at the higher speed of $100 \text{ m} \cdot \text{min}^{-1}$, the depth of damage in terms of both non-indexed regions at the surface, and subsurface misorientation contrast appears greater. As shown in Figure 6.1, local variations in grain orientation are also observed to have a large influence on the degree of deformation that occurs when turning both CG and FG conditions.

Typically, to help identify surface damage, kernel average misorientation (KAM) mapping was employed. This is effectively achieved by comparing the misorientation of each pixel with respect to its neighbours; regions with high misorientation will correspond to those that have a high defect density. Figure 6.7 displays KAM maps for all machining condition tested. For the CG condition at $100 \text{ m} \cdot \text{min}^{-1}$, it can clearly be seen from the stronger signal near surface that there are higher levels of damage induced by the faster strain rate deformation. In contrast, the FG material appears to have a higher level of damage at the slower cutting speed of $70 \text{ m} \cdot \text{min}^{-1}$, however this is likely due to the large amount of non-indexed regions that occur at the higher speed of $100 \text{ m} \cdot \text{min}^{-1}$. Artifacts of the KAM image analysis can also be observed across the surface for the FG material in the form of straight lines, due to over-extrapolation.

To quantify the diffusivity of the observed deformation, line scans were performed on the KAM maps using the commercial Aztec software (see Figure 6.8); these were taken below the surface artifacts previously described, at 20 equidistant locations across the machined surface. Comparing the two material conditions, larger depths of damage are seen in the CG material, due to the reduction in grain size strengthening. Figure 6.8 also confirmed that higher levels of surface deformation occur when the CG material is turned at higher speeds. In addition, it appears as though turning at the slower cutting speed of $70 \text{ m} \cdot \text{min}^{-1}$ induces more subsurface deformation into the bulk, which may occur due to reduced material softening at the lower speed, which has previously been reported during Ni-based superalloy machining [98, 152]. For the FG material condition, similar maximum levels of misorientation are detected at the surface for both speeds, however, unlike the CG material, the subsurface deformation is higher for a cutting speed of $100 \text{ m} \cdot \text{min}^{-1}$. This is likely because when turning the FG material the majority of the deformation is confined to the first $20 \mu\text{m}$, in contrast, when turning the CG material, the deformation is more diffuse, extending 3 times further to around $60 \mu\text{m}$. As such, the increased thermal softening that occurs during higher strain rate deformation has a greater influence on the subsurface deformation when machining the FG material.

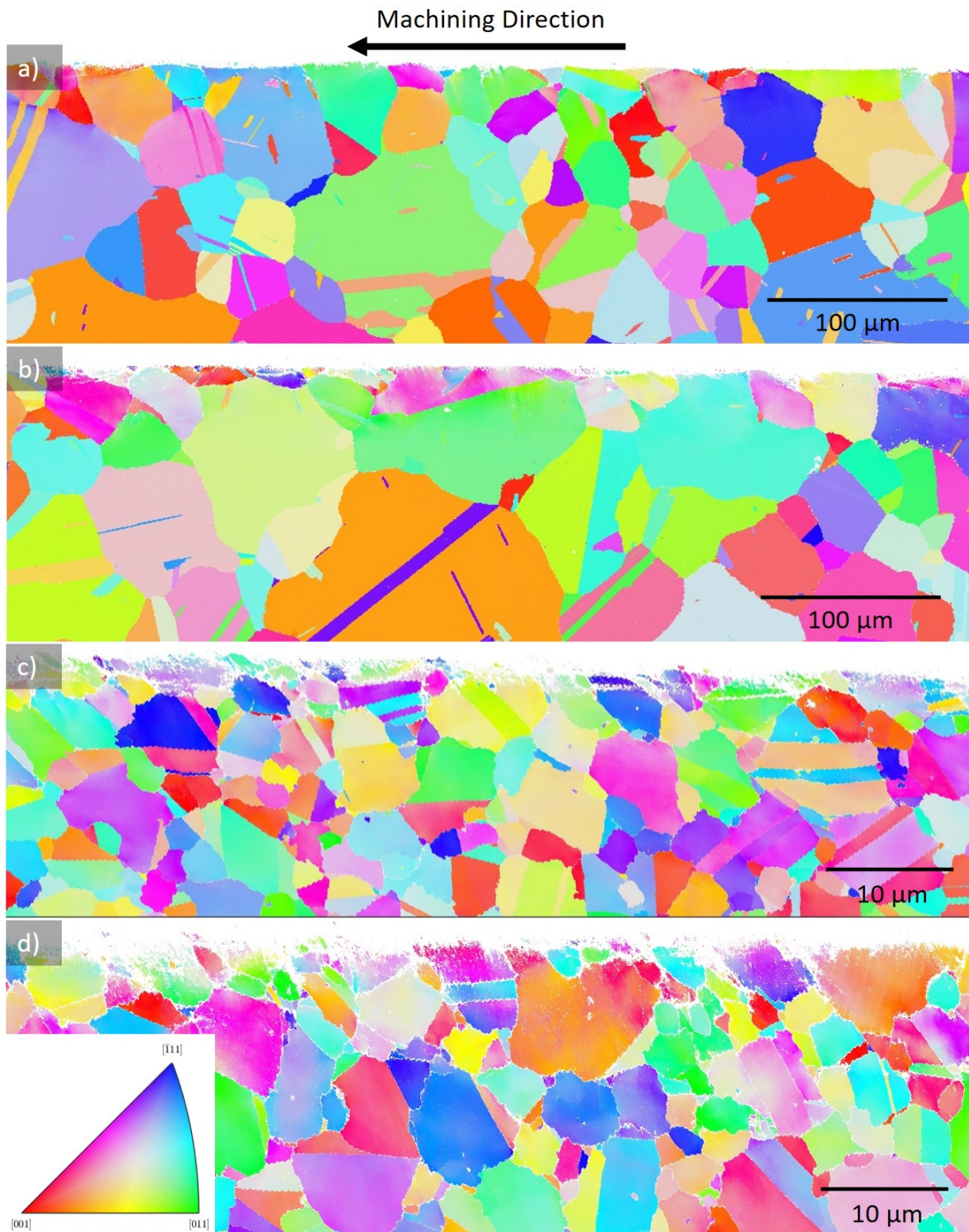


Figure 6.6: EBSD data showing z-IPF maps of machined surfaces viewed normal to the cutting direction: (a) CG $70 \text{ m} \cdot \text{min}^{-1}$ (b) CG $100 \text{ m} \cdot \text{min}^{-1}$, (c) FG $70 \text{ m} \cdot \text{min}^{-1}$ (d) FG $100 \text{ m} \cdot \text{min}^{-1}$. A strong deformation gradient is observed, with highly deformed, non-indexed regions (white) occurring near the surface.

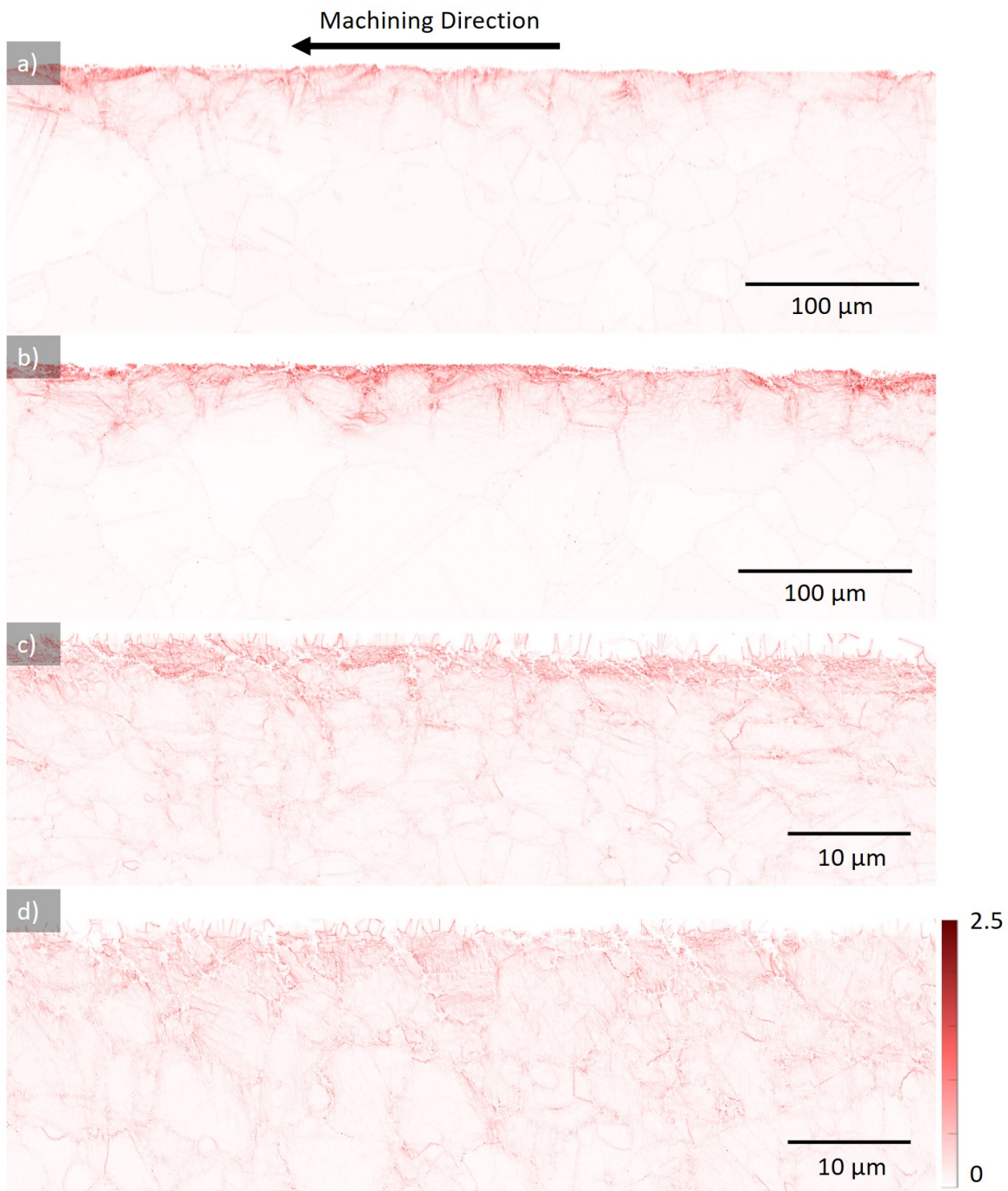


Figure 6.7: EBSD data showing KAM maps of machined surfaces (colourbar misorientation is in $^{\circ}$): (a) CG $70 \text{ m} \cdot \text{min}^{-1}$ (b) CG $100 \text{ m} \cdot \text{min}^{-1}$ (c) FG $70 \text{ m} \cdot \text{min}^{-1}$ (d) FG $100 \text{ m} \cdot \text{min}^{-1}$.

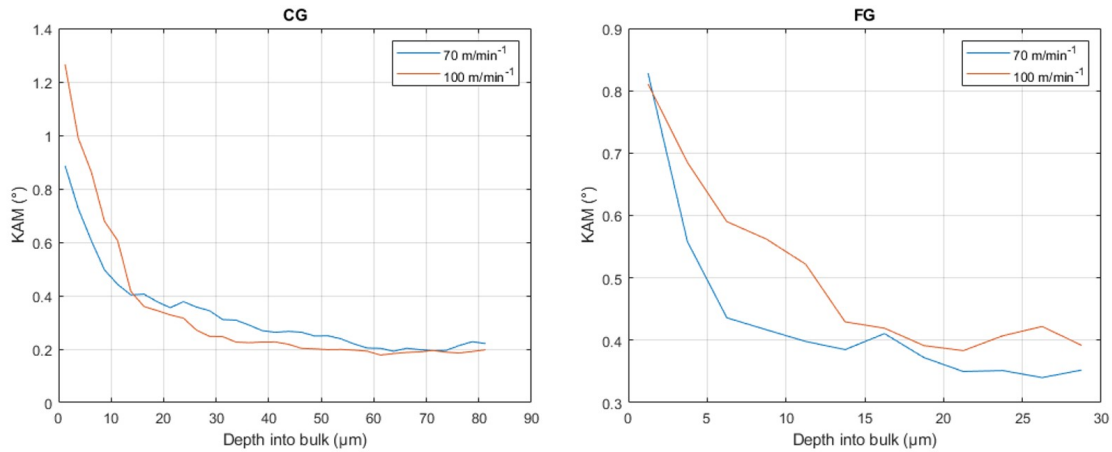


Figure 6.8: KAM against depth for each condition tested; note different x-axis and y-axis scales.

FWHM measurement can be used to access the degree of deformation in the machined surface (see Section 4.3). This was performed at varying SCLs for the FG material (see Figure 6.9). The results appear to support Figure 6.8, whereby more deformation occurs at the higher cutting speed of $100 \text{ m} \cdot \text{min}^{-1}$. It is also apparent that the depth of damage, which in this case is calibrated based on what a typical aerospace visual assessment would consider damage (i.e., swept grains), increases with SCL and stabilises after 32 m.

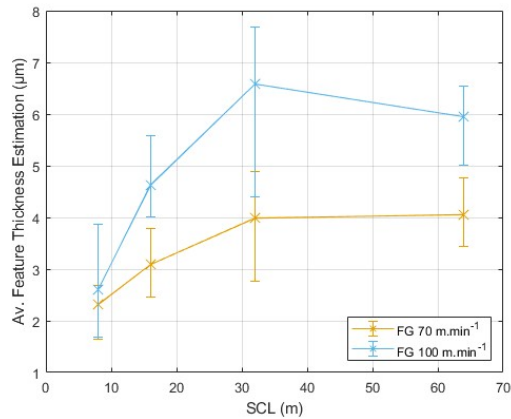


Figure 6.9: Estimated damage depth based on XRD FWHM measurement for FG RR1000 at varying SCLs.

Machining Force Response and Chip Formation During CG and FG RR1000 Turning

Figure 6.10 demonstrates that the average machining forces across all 3 force components are comparable for both material conditions, in addition, cutting speed is observed to have a negligible impact on average machining forces. When comparing these results with those obtained in Chapter 5, the balance of force components is observed to shift: F_p (+36%), F_c (-30%), and F_f (+32%). Due to the significant reduction in the largest force component F_c , the overall the average resultant force, R , is observed to decrease by 10%. This could be related to higher cutting temperatures that occur when turning CG and FG RR1000, as a result of a higher V_f of γ' , which promotes localised workpiece softening.

Close examination of the tool contact zone reveals that this finding could also be related to an increased contact area when turning IN718, which is softer and has less resistance to deformation at high temperature. This effect is shown in Figure 6.11; there also seems to be a marginally higher contact area when turning the CG material, suggesting additional deformation occurs ahead of the advancing tool, as a result of more diffuse deformation characteristics. It should be noted that the HPC pressure was different in the RR1000 and IN718 experiments performed (40 bar and 65 bar, respectively), suggesting that difference between the two contact areas could have been even higher, since higher pressure HPC will contribute to chip deflection, lowering the contact area [113].

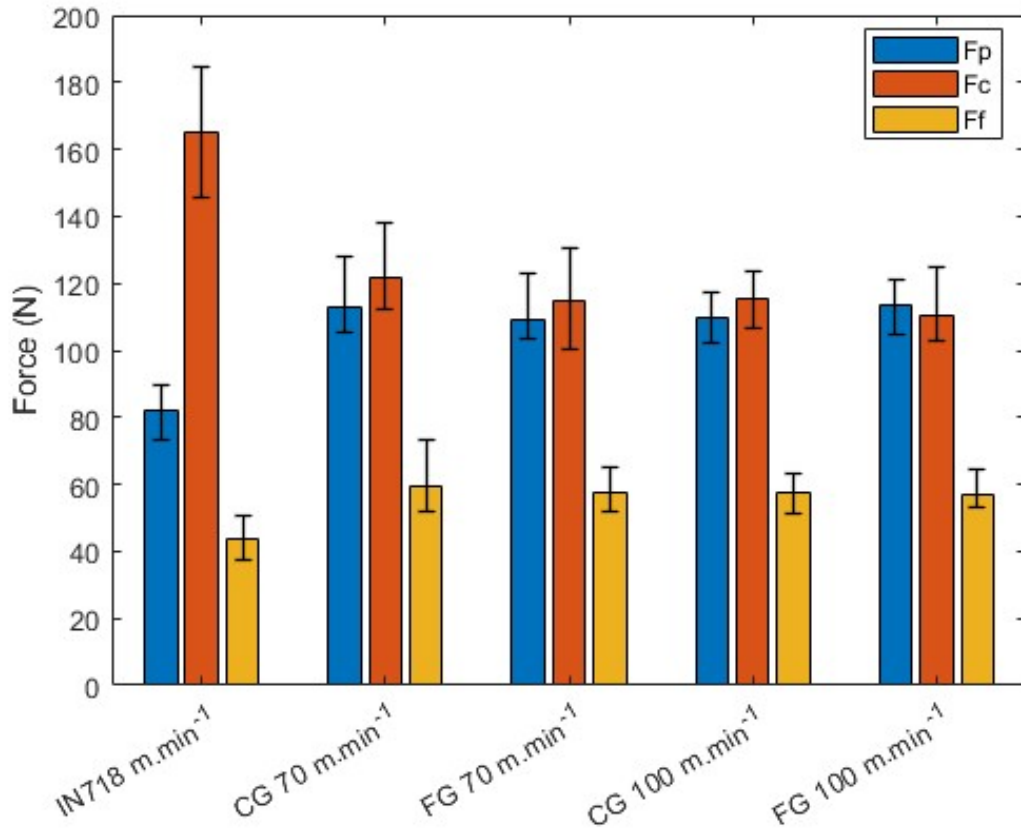


Figure 6.10: Comparison of average machining force response values for all cuts performed during initial tool wear trials; measurements were averaged over the first second of tool engagement; error bars demonstrate range of values measured.

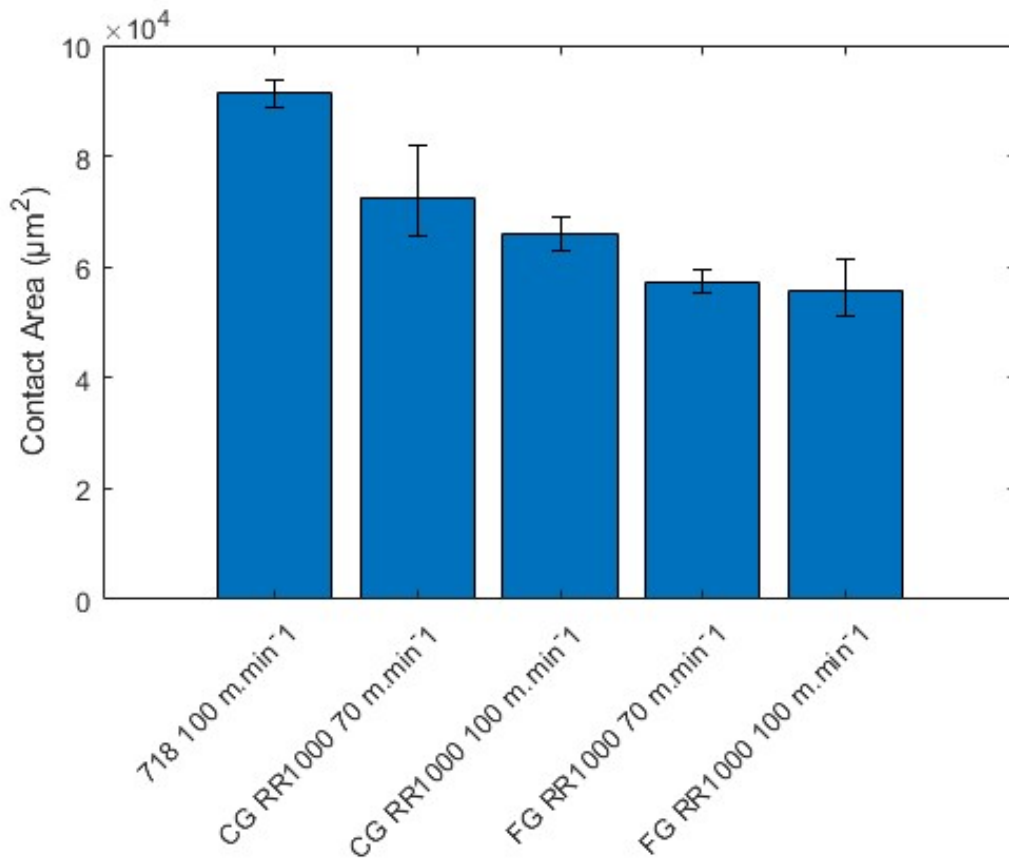


Figure 6.11: Comparison of contact zone area measured over 2 m and 32 m SCL for different machining conditions tested.

Observing Figure 6.12, it is apparent that the different deformation characteristics observed in Section 6.3.1 have a dramatic influence on the machining force response, whereby the range of force values produced in one singular cut is approximately 4 times greater when turning the CG material compared to the FG material. Fluctuations in machining force are heavily influenced by variations in deformation behaviour as the tool moves across the workpiece. The influence of these variations are reduced when turning the FG material, since it is more homogeneous, meaning the stress distribution surrounding the tool will interact with a larger sample of randomly orientated grains. In contrast, as seen in Figure 6.2, when machining the CG material the mode of deformation can alternate dramatically over a large area, especially when slip occurs in a single large grain with a "soft" orientation.

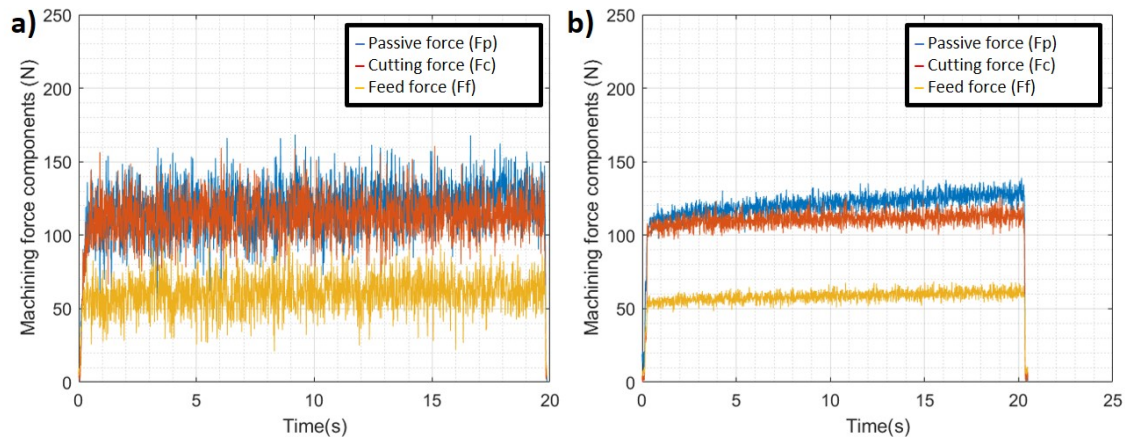


Figure 6.12: Force feedback plot at $100 \text{ m} \cdot \text{min}^{-1}$, sampled at 400 Hz for (a) CG material (b) FG material.

Machining force data can also be plotted spatially, as per the method presented in Section 4.7.1. Figure 6.13 in Appendix A shows a digital reconstruction of the F_z force component, measured during facing passes performed approximately 10 mm from the end of each billet, highlighting the larger fluctuations in machining force that occur when turning the CG material compared to the FG material. In addition, an increase in the average cutting force for both material conditions can be observed as the tool moves towards the billet centre, due to tool wear and the corresponding increase in contact area.

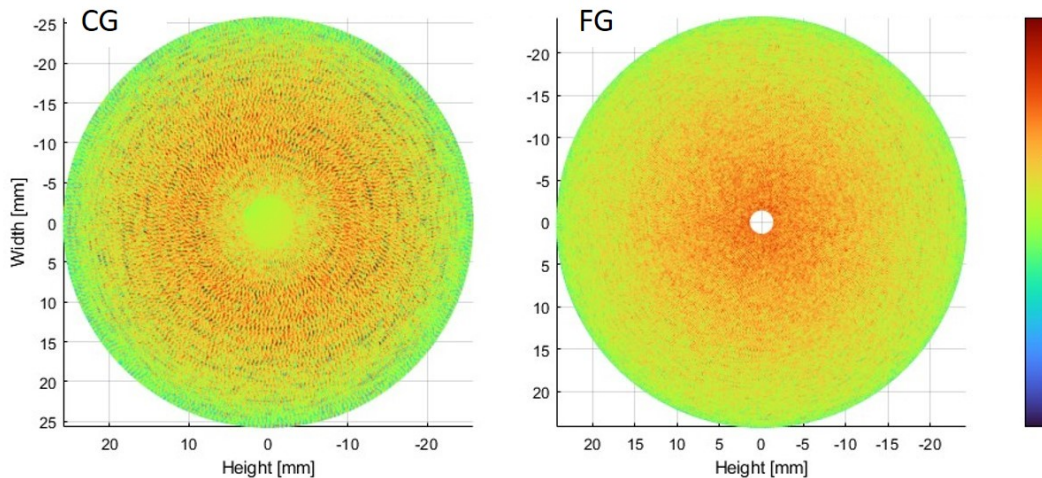


Figure 6.13: Force response maps for CG and FG materials, demonstrating variations in machining forces that has been attributed to microstructural variation and tool wear.

The deformation mechanics of the cutting process are reflected in the generated chip, observing the generated chip post-machining is therefore a convenient means of inferring informa-

tion regarding how material condition influences deformation. Figure 6.14 demonstrates that spiral chips are produced when turning both material conditions, however, it can be seen that the periodic fracture that occurs along the side of the chip that runs along the tools trailing edge is more consistent when turning the more homogenous FG material. Viewing the front of the chips in Figure 6.15, the shear localisation and segmentation is also seen to have a more regular periodicity, culminating in reduced fluctuations in machining force.

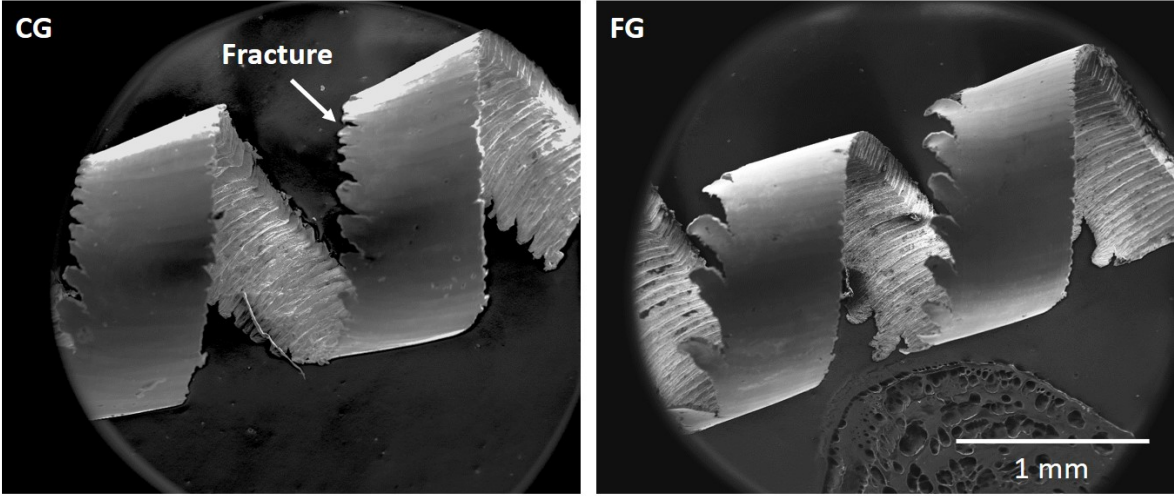


Figure 6.14: Medium magnification SEM SE micrograph of chips produced when turning CG and FG material at $100 \text{ m} \cdot \text{min}^{-1}$.

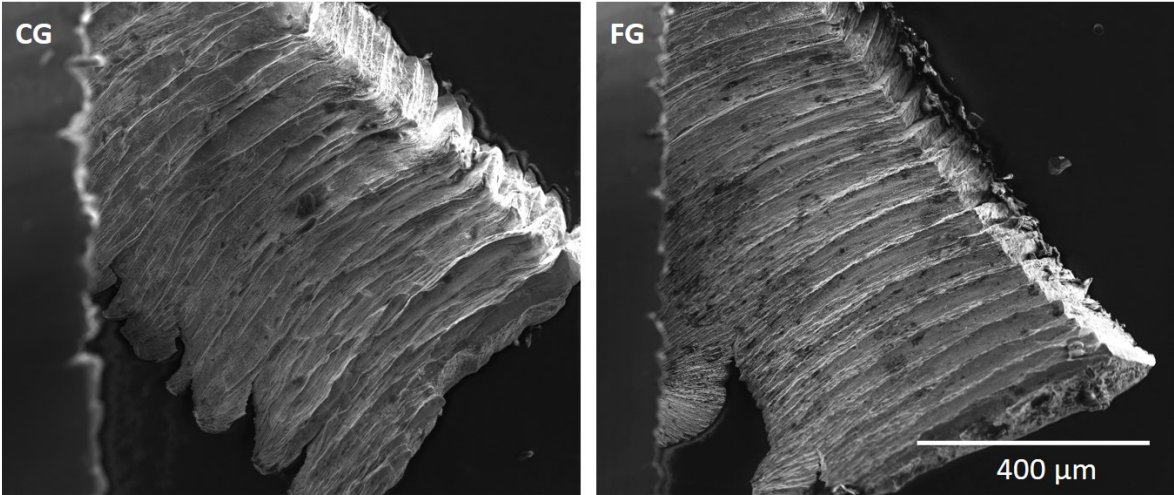


Figure 6.15: Low magnification SEM SE micrograph of chips produced when turning CG and FG material at $100 \text{ m} \cdot \text{min}^{-1}$.

Mean field Modelling of γ' Dissolution

In order to better understand the relationship between cutting temperature and γ' dissolution observed in the secondary shear zone (see Figure 6.5), thermal modelling was performed using the mean field method (see Section 4.10.2). This approach allows the change in the γ' distribution for FG RR1000 to be estimated for different heat treatments. Since the actual heating and cooling rates were not recorded, an estimated thermal profile was employed (see Figure A3 of Appendix A), as such, only relative differences between temperatures can be inferred. It should be noted that the model neglects the influence of mechanical effects, such as precipitate shearing, that will occur in the machining case.

Figure 6.16 demonstrates that increasing cutting temperature during machining will lead to increased γ' dissolution, suggesting the secondary γ' observed in Figure 6.5 will require local temperatures within the secondary shear zone in the region of 1120°C. At temperatures $\leq 1000^\circ\text{C}$, the driving force for dissolution is greatly reduced, and at 900°C no significant secondary γ' dissolution can be observed. Since tertiaries are smaller ($r = 11$ nm, compared to $r = 60$ nm for secondaries), some dissolution is predicted to occur at 900°C, and at 1000°C there is complete dissolution. Another interesting observation is that the dissolved secondary γ' is predicted to reprecipitate upon cooling as tertiary γ' . Observing Figure 6.5, it is unclear if reprecipitation can be observed in the top 1.8 nm, due to the nanoscale nature of said precipitates.

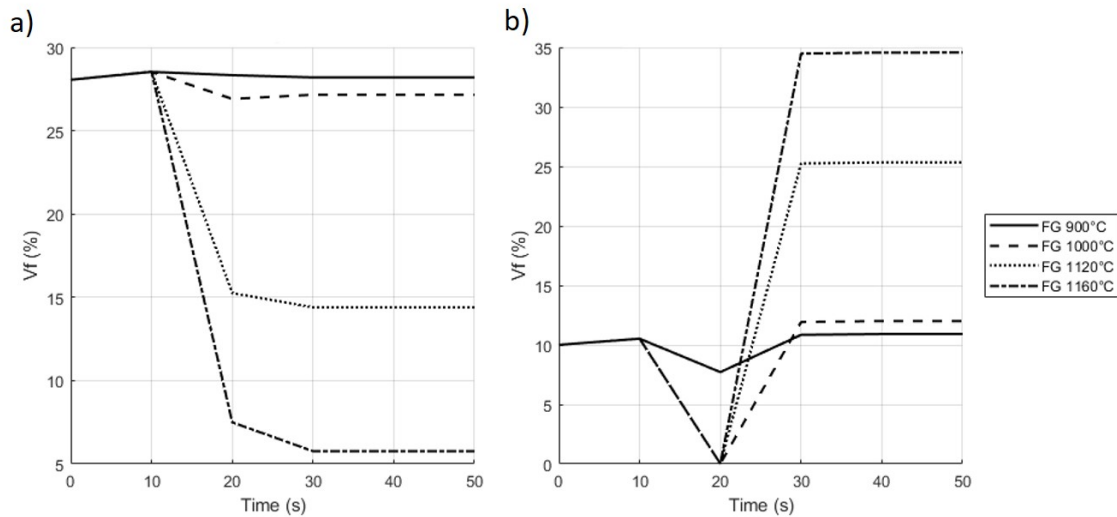


Figure 6.16: Simulated dissolution at different temperatures using mean field model for FG RR1000 (a) secondary γ' (b) tertiary γ' .

3D FEM Model of Turning Process

To further investigate the effect of cutting speed on temperature at the tool-workpiece interface, modelling of the OD turning operation was performed using the commercial FEM cutting simulation software AdvantEdge by Third Wave Systems (see Section 4.10.3). Since no material data was available for RR1000, the in-built IN718 material model was used instead. The simulation was run at the two speeds tested (70 and $100 \text{ m} \cdot \text{min}^{-1}$). A 9% higher temperature was measured when running at $100 \text{ m} \cdot \text{min}^{-1}$ compared to $70 \text{ m} \cdot \text{min}^{-1}$. As such, this would indicate that a slightly higher level of dissolution should be observed in the machined surface at the higher speed. In both cases, maximum temperatures in the region of 700°C (639°C at $70 \text{ m} \cdot \text{min}^{-1}$, and 739°C at $100 \text{ m} \cdot \text{min}^{-1}$) were observed, however, Figure 6.5 and Figure 6.16 suggest that local temperatures in the tertiary shear zone are $\approx 1100^\circ\text{C}$.

This major discrepancy is hypothesised to be due to several factors: different material properties between RR1000 and IN718, utilisation of an inaccurate friction model, no consideration of evolving tool geometry (i.e., tool wear, BUE), no inclusion of the tool coating, and improper boundary conditions. Of all these factors, the first is thought to be the most significant, since RR1000 has higher volume fraction of the strengthening γ' phase compared to IN718, which gives the material improved resistance to deformation at high temperature.

The stress distributions (normal and maximum shear) for the tool contact zones are displayed in Figure A1. These plots were made using the software GNU Octave 5.1.0. Very little variation can be observed between the calculated stresses from the two speeds tested. It can be noted that the calculated stress loads shown in the figure are very high. In the real physical situation, there will be plastic deformation of the cutting edge, which will relax the stresses.

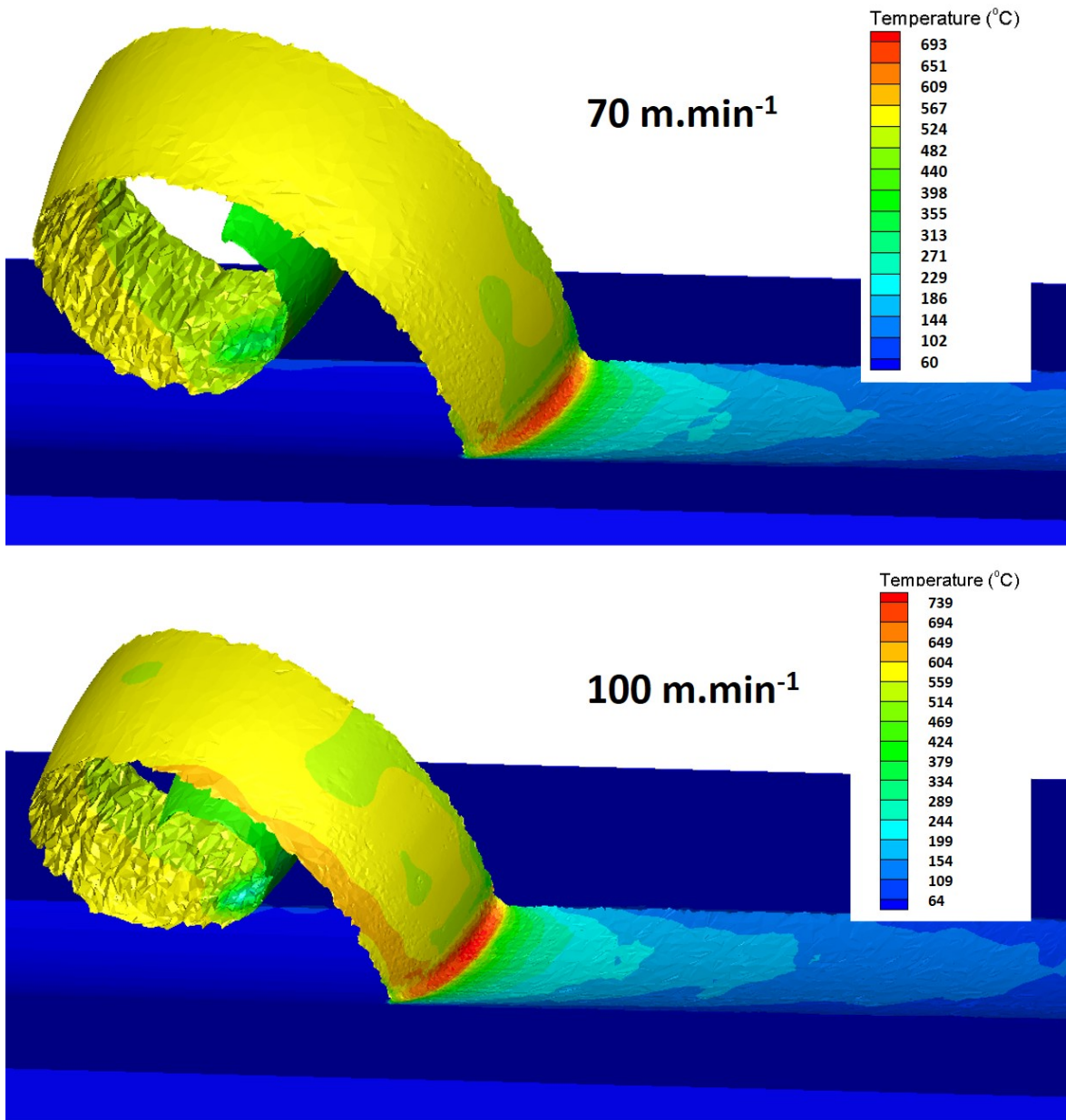


Figure 6.17: AdvantEdge simulation of machining process using IN718 for material model at 70 and 100 m · min⁻¹.

6.3.2 Tool Wear

In Figure 6.18 it can be observed that when turning both CG and FG materials, workpiece adhesion occurs rapidly across the contact zone within the first 2 m of tool engagement. Adhered material is observed to be concentrated on the cutting edge, which can form via

the ploughing of workpiece material as the tool is brought out of cut as the feed rate is progressively reduced. A band of adhered RR1000 towards the rear of the contact as the chip deflects can also be observed, which is typical in most turning operations. When turning the CG material, significant notching and exposure of the WC substrate was observed at the DOC, and was more severe at the higher cutting speed of $100 \text{ m} \cdot \text{min}^{-1}$. No DOC notch wear was observed at the lower speed of $70 \text{ m} \cdot \text{min}^{-1}$ when turning the FG material, and only slight notching was detected at the higher cutting speed.

It has previously been reported that notch formation is typically worse when turning larger grained Ni-based superalloy material [105, 107]. This behaviour is attributed in part to the formation of a work hardened layer on the surface [153]. Hence, the increased subsurface damage presented in Section 6.3.1 may correlate to increased strain hardening, and therefore, to increased notch wear. In addition, the large fluctuations in machining force that occur when turning the CG material will contribute to coating fatigue. This effect is especially important during the initial engagement, when no workpiece softening has begun to occur. When turning both materials, increased notching occurred at the higher cutting speed, this may be attributed to higher levels of strain hardening at higher strain rates. At this stage of the wear progression there is also a slight indication of notch formation towards the trailing edge. It should be noted that higher rates of notch wear during Ni-based superalloy machining can be exacerbated by the application of HPC [154].

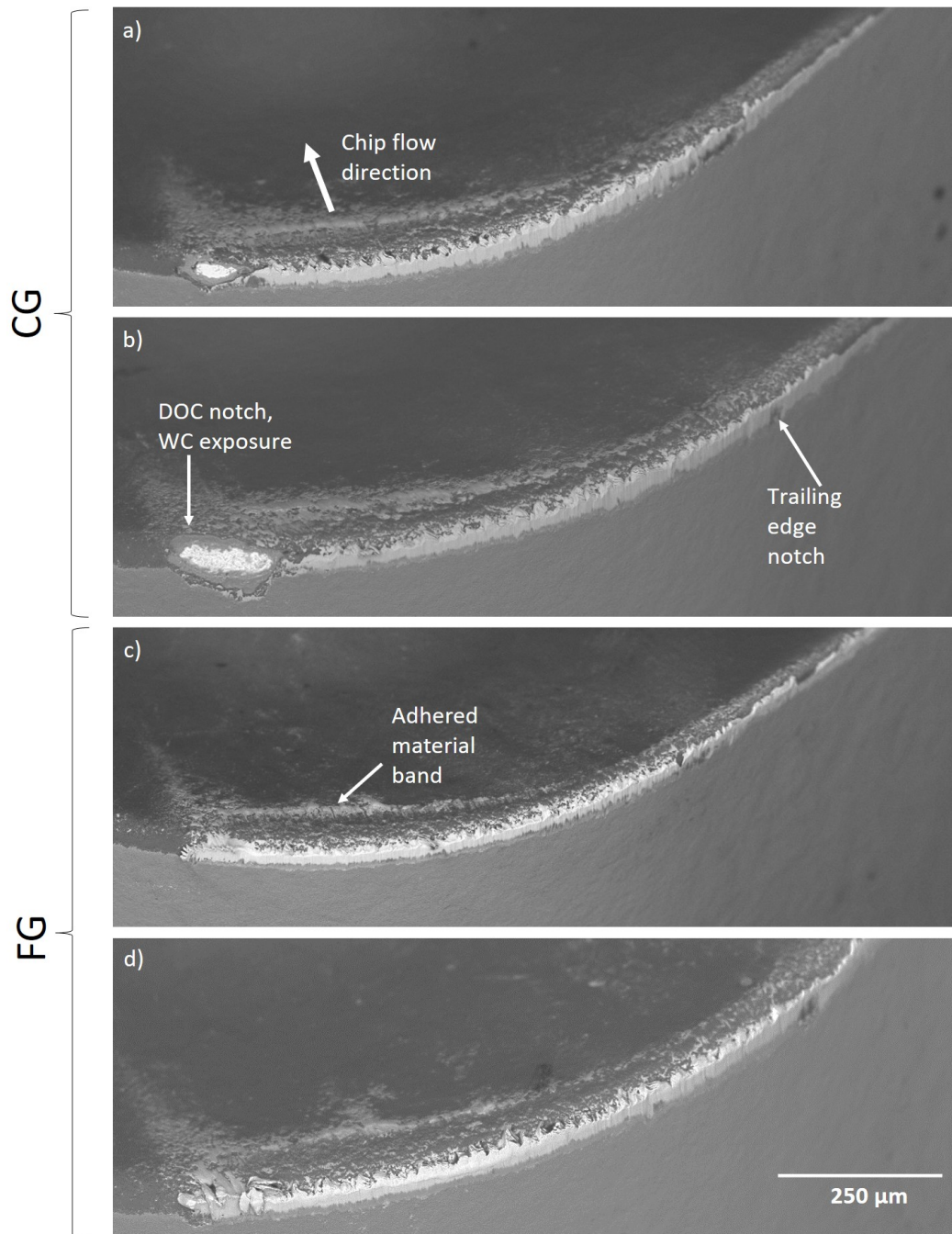


Figure 6.18: BSE SEM micrograph of tool nose after a SCL of 2 m when turning (a) CG RR1000 at $70 \text{ m} \cdot \text{min}^{-1}$ (b) CG RR1000 at $100 \text{ m} \cdot \text{min}^{-1}$ (c) FG material at $70 \text{ m} \cdot \text{min}^{-1}$ (d) FG material at $100 \text{ m} \cdot \text{min}^{-1}$.

Viewing the contact zone from above in Figure 6.19, demonstrates how the levels of adhesion of workpiece material evolves over time. After a SCL of 2 m when turning CG and FG materials, more rake face adhesion occurs at the lower cutting speed of $70 \text{ m} \cdot \text{min}^{-1}$. Overall,

higher levels of adhesion and smearing of workpiece material across the rake face occur when turning the CG material at both cutting speeds tested. This may be attributed to the different deformation mechanics of the two RR1000 conditions, since in the CG material dislocation slip is much greater compared to the FG, allowing it to "smear" across the tool surface more readily. It could also be related to increased cutting temperatures that occur when turning the CG material as a result of larger fluctuations in the machining force response.

Figure 6.19 also shows that the degree of adhesion varies considerably in different regions of the cutting tool depending on the contact conditions. In the sticking zone, the normal stress is highest, and high levels of adhesion are observed. Moving across the contact zone in the direction of chip flow, towards the sliding zone, thinner layers of adhered material are detected. Towards the end of the contact zone, adhesion increases, and a bright contrast band (BCB) is observed to form at the point the chip deflects from the workpiece. After a SCL of 2 m, the BCB appears broader, and more smeared on the cutting inserts used to turn the CG material compared to those used to turn the FG material at both speeds tested. Distinct variations in tone within the band can also be detected (bright towards the cutting edge transitioning to darker contrast moving in the direction of chip flow), indicating the presence of two distinct phases. This can be seen most clearly when machining the FG material at $100 \text{ m} \cdot \text{min}^{-1}$ after a SCL of 2 m.

Figure 6.19 demonstrates through SCLs of 32 m and 64 m, that the variation in degree of adhesion across the contact becomes more inconsistent when comparing the different conditions. Compared to 2 m SCL, adhesion within the sticking and sliding zone reduces for all conditions tested, due a transition towards thermally accelerated wear phenomena (chemical adhesion, and plastic deformation). This alters the surface topography, such that there are fewer instances of coating pull-out, and therefore, fewer sites available for mechanical adhesion to take place. Adhered material in the sliding zone is readily removed by the flowing chip. The wear rate in this region immediately behind the cutting edge is typically highest as the stresses and temperatures are at a maximum. Observing Figure 6.19 after a SCL of 64 m, total removal of alumina on the rake face occurred, as indicated by the TiCN exposure. Only partial alumina removal occurred when turning the FG material, and the wear rate was greater at the higher speed of $100 \text{ m} \cdot \text{min}^{-1}$.

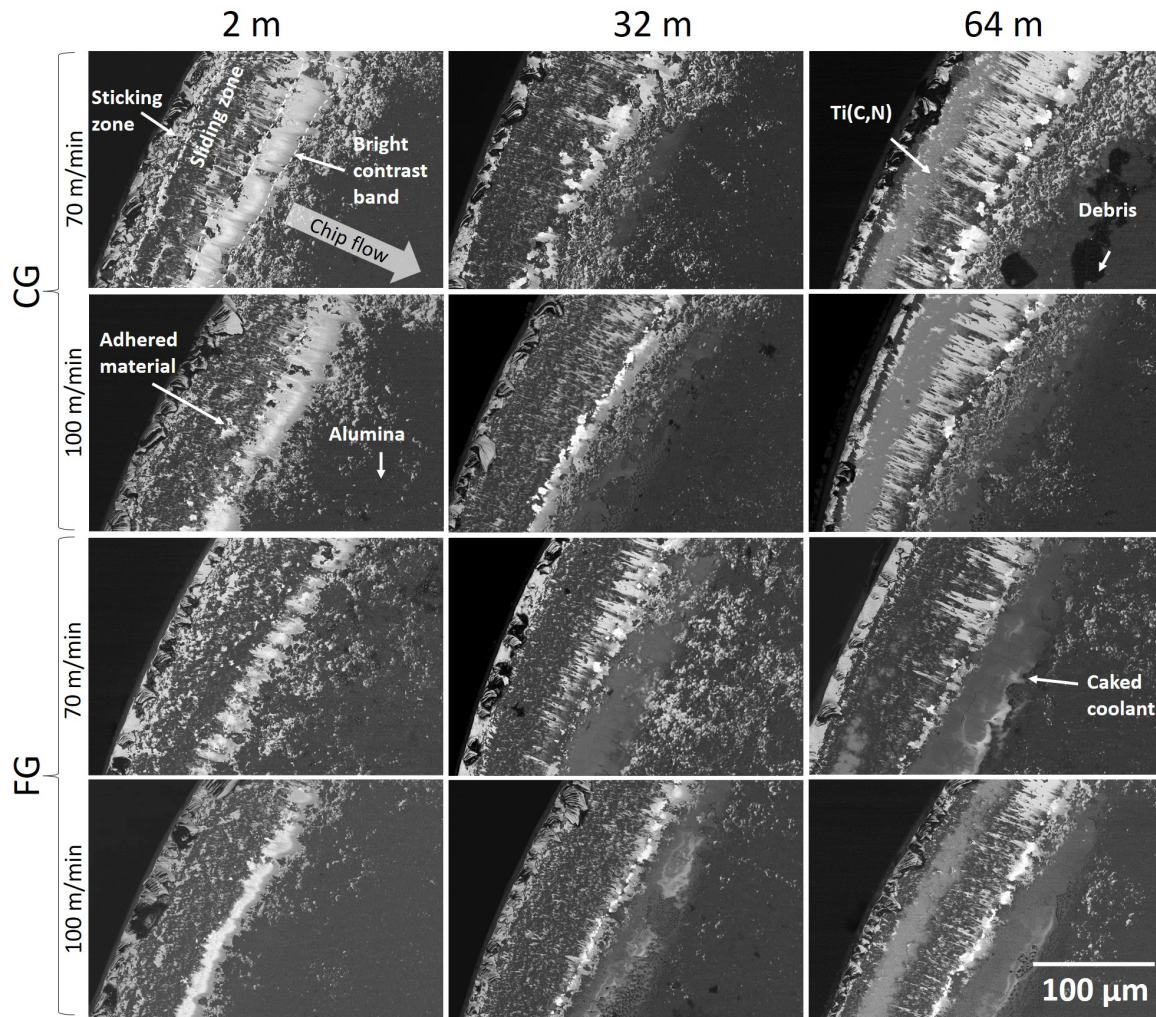


Figure 6.19: BSE SEM micrograph of rake face after a SCL of 2 m when turning (a) CG material at $70 \text{ m} \cdot \text{min}^{-1}$ (b) FG material at $70 \text{ m} \cdot \text{min}^{-1}$ for FG material (c) CG material at $100 \text{ m} \cdot \text{min}^{-1}$ (d) FG material at $100 \text{ m} \cdot \text{min}^{-1}$.

Figure 6.20 shows the BCB at higher magnification, formed when the CG material was turned at a cutting speed of $100 \text{ m} \cdot \text{min}^{-1}$. Alumina grain pull-out, indicative of adhesive wear, is observed in front of the band. The fracture of the underlying alumina in this region is likely exacerbated tensile forces due to deflection of the chip, as observed in Chapter 5. Initial inspection of the region, presented in Figure 6.20, using X-EDS analysis (Figure 6.21), reveals the brightest section of the BCB is rich in strong oxide former's such as (Hf, Zr, Ta). To the right of this region there is a darker contrast area, appearing to be rich in Al and Ti.

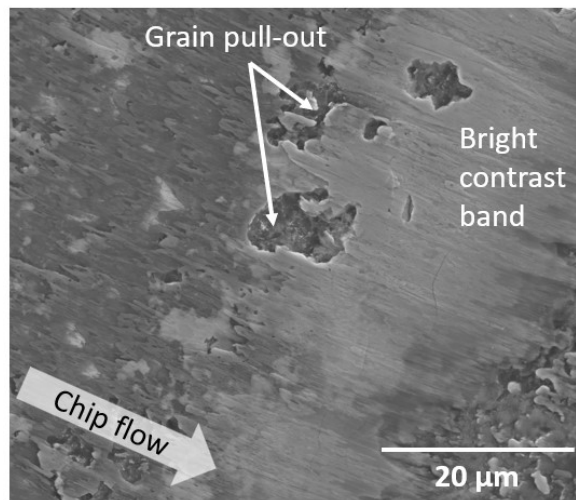


Figure 6.20: SE SEM micrograph of BCB formed on rake face after 2 m SCL, at $100 \text{ m} \cdot \text{min}^{-1}$ when turning the CG material.

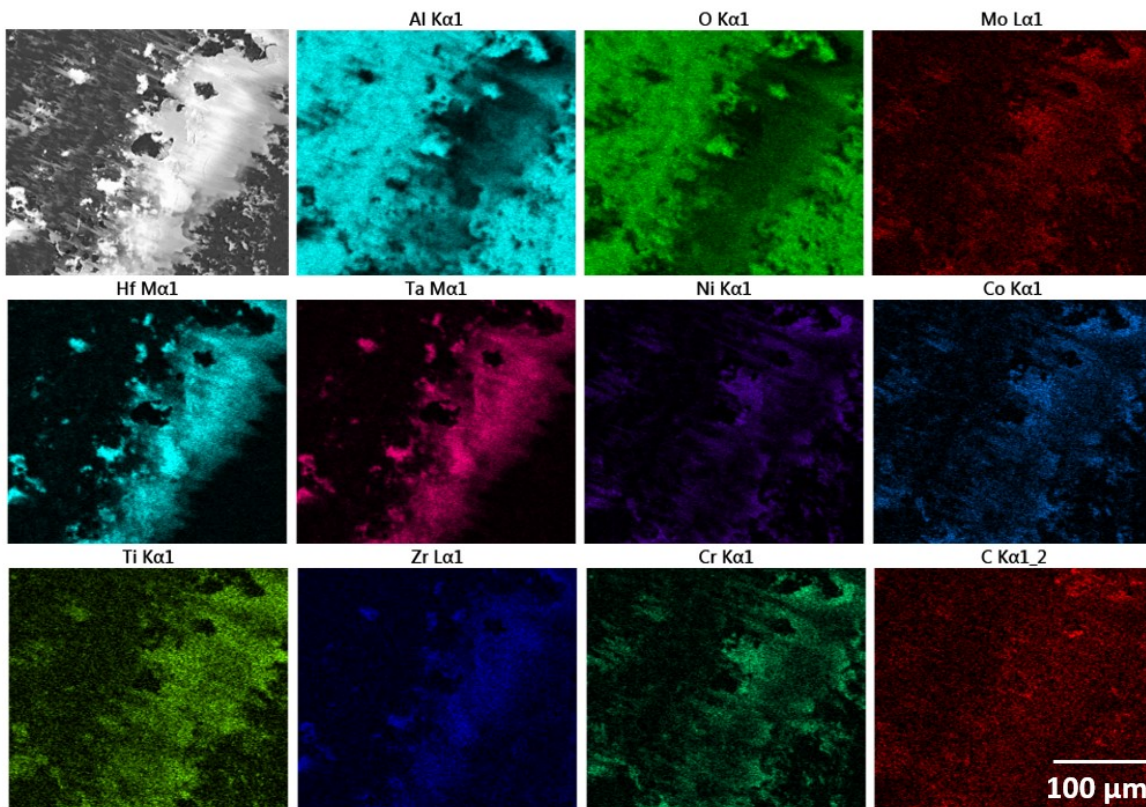


Figure 6.21: X-EDS scan of BCB to rear of rake face formed when turning CG material for 2 m SCL at $100 \text{ m} \cdot \text{min}^{-1}$.

To confirm these observations, a BCB cross-section was scanned using EPMA, fitted with a WDS detector. This method provides more accurate measurement of composition. Figure 6.22 shows a cross-section of the BCB produced after a SCL of 16 m when turning the FG material at $100 \text{ m} \cdot \text{min}^{-1}$. Three distinct phases are observed within the BCB. Table 6.3 displays compositional measurements taken for each of the distinct phases observed; C and O were not included due to high levels of noise, Zr was not included as it was only found in trace amounts.

Region 1 is located at rear of the contact, where the chip deflects, and corresponds to the dark phase seen in Figure 6.21; it was found to be rich in Al, and also some Hf. Region 2 appears to be the same phase, although it is richer in Ti. Region 3 is bright phase observed in Figure 6.21, and is rich in Hf. It appears as if these two phases are blended here; the dark Al-rich phase appears to be the matrix phase, and the bright Hf-rich phase is a swirling agglomeration of small inclusions (see Figure 6.23). Region 4 is the most similar to the bulk alloy, with a slight increment in γ forming elements, as well as Ti, that has likely dissolved from the γ' due to high temperatures and strains. The alumina coating below this exhibits adhesive wear and grain pull-out, which has occurred due to the tensile forces in this region.

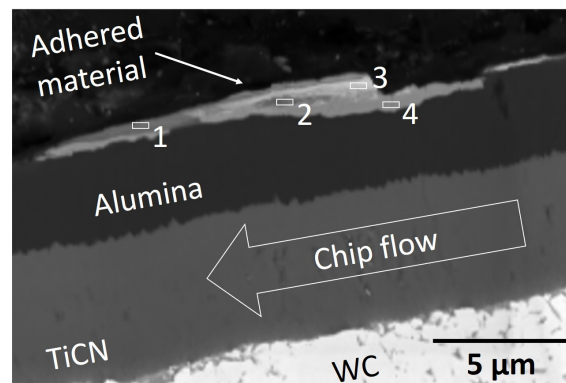


Figure 6.22: BS SEM micrograph of insert BCB formed when turning the FG material 16 m SCL at $100 \text{ m} \cdot \text{min}^{-1}$; corresponding compositions for each region is given in Table 6.3.

Table 6.3: Normalised composition in Wt.% for major elements in RR1000 found within regions of BCB (see Figure 6.22).

Element	Ref. [128]	1	2	3	4
Ni	52.3	4.7	5.2	3.9	67.3
Co	18.5	1.7	1.1	3.2	20.8
Cr	15.0	3.2	3.0	1.8	19.3
Mo	5.0	0.8	1.0	2.3	4.8
Ti	3.6	2.8	7.2	2.9	5.7
Al	3.0	47.0	45.8	14.3	3.9
Ta	2.0	1.7	3.5	2.8	1.3
Hf	0.5	20.3	28.3	59.6	0.8

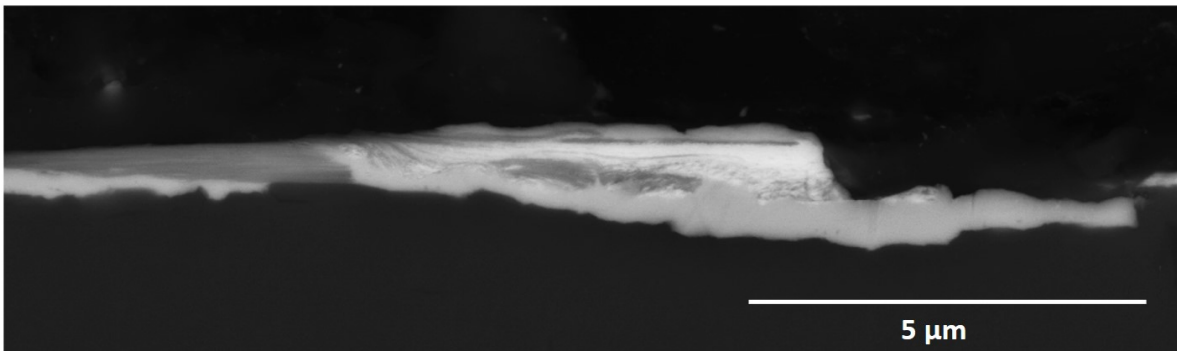


Figure 6.23: Close-up BS SEM micrograph of Figure 6.22, showing rake face BCB formed when turning the FG material 16 m SCL at $100 \text{ m} \cdot \text{min}^{-1}$.

Figure 6.24 shows the compositional variation in the form of EPMA WDS maps. The map for O appears to indicate that the dark Al-rich phase is oxide in nature. The C map is inconclusive due to contamination from the Bakelite used for mounting. As the chip deflects the adhered material will be exposed to both air and cutting fluid ingress, hence, oxide formation is highly plausible. It is unclear however whether or not the Al found in this oxide originates from a chemical reaction between tool and workpiece or if it is solely from the workpiece. The high concentration of Al would indicate the former may be plausible.

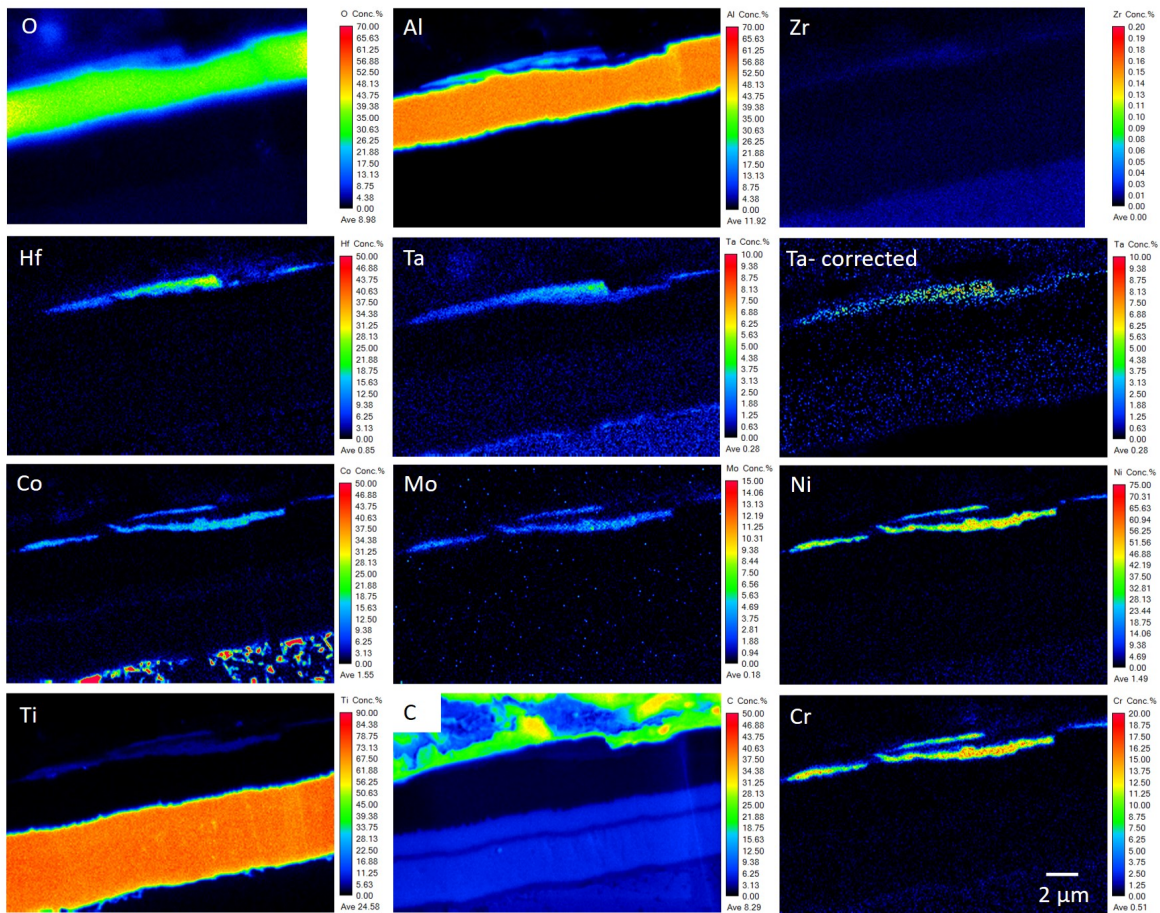


Figure 6.24: EPMA scans and accompanying BSE image of BCB on insert formed when turning the FG RR1000 16 m SCL at $100 \text{ m} \cdot \text{min}^{-1}$.

To reveal reaction products, the cutting tools were etched in Glyceregia (see Section 4.9.2). The rake faces at an SCL of 2 m and 32 m are displayed in Figure 6.25. Etching with Glyceregia removes metallurgically bonded adhered material. This suggests that the adhered material retained after etching, i.e., the brighter contrast areas, has reacted with the alumina surface. The highest concentration of reaction products are detected towards the rear of the contact zone, forming a BCB. Additional reaction products can also be observed across the sliding zone and appear to be more concentrated when machining the CG material (see Figure 6.26). These include heavily deformed Hf-rich inclusions (bright phase), which preferentially adhere to regions displaying alumina grain-out, which suggests that the higher concentration of reaction products when turning the CG is related in part to increased adhesive wear and attrition. Disruptions in the continuous BCB are observed that correspond to incidents of coating pull-out. These are most prevalent when turning the CG grain material and at the lower speed of $70 \text{ m} \cdot \text{min}^{-1}$, which may correspond to reduced levels of workpiece softening, combined with larger fluctuations in the machining force response (see Figure 6.10).

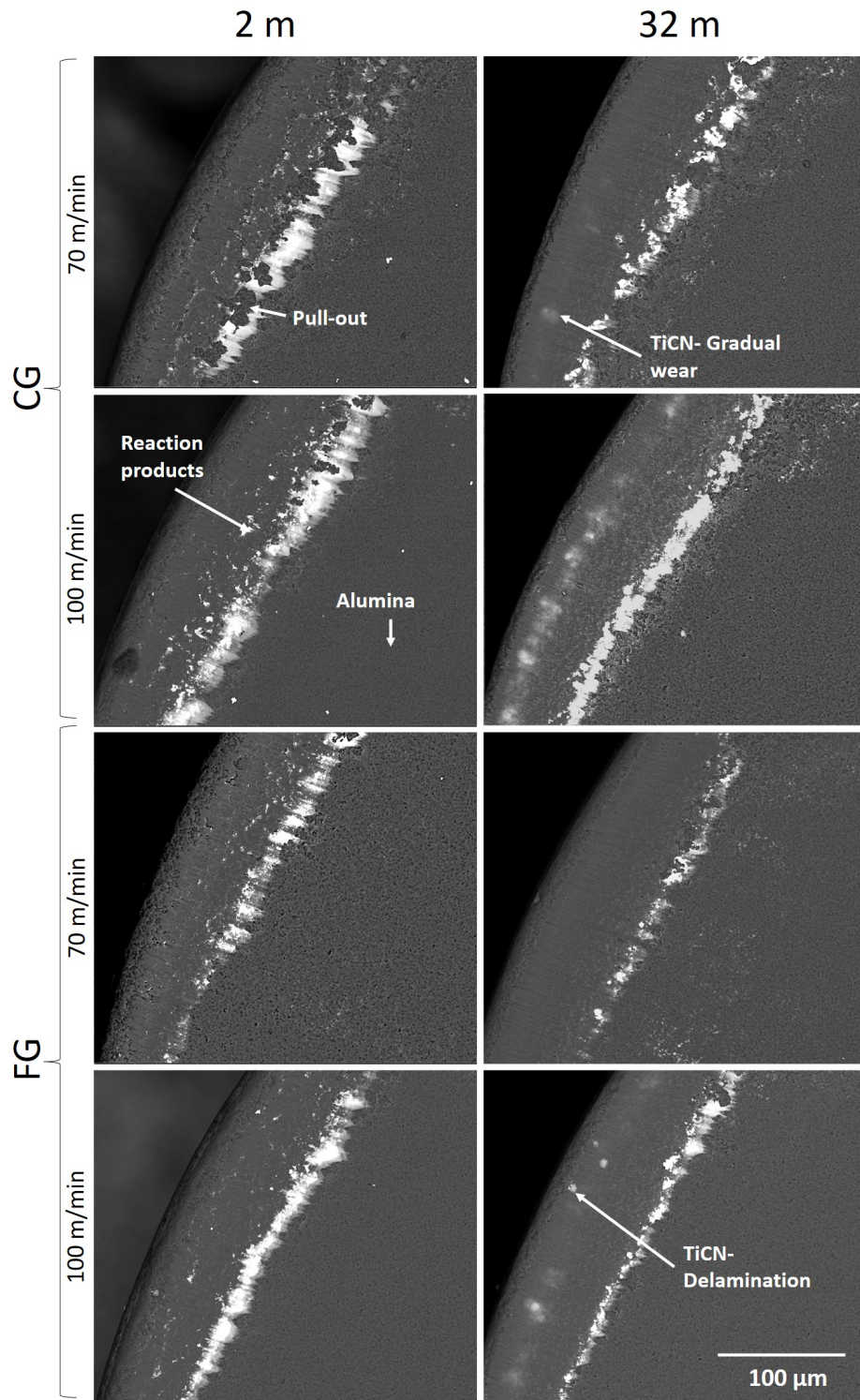


Figure 6.25: BSE SEM micrograph of etched rake face after a SCL of 2 m when turning (a) CG material at $70 \text{ m} \cdot \text{min}^{-1}$ (b) FG material at $70 \text{ m} \cdot \text{min}^{-1}$ for FG material (c) CG material at $100 \text{ m} \cdot \text{min}^{-1}$ (d) FG material at $100 \text{ m} \cdot \text{min}^{-1}$.

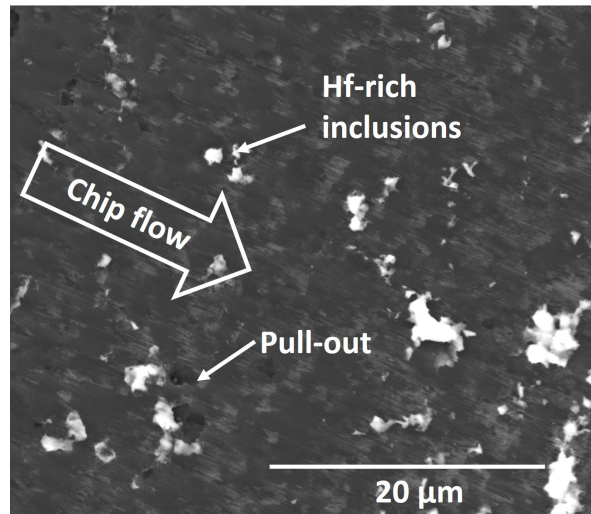


Figure 6.26: BSE SEM micrograph of tool face post etching for tool used to turn CG RR1000 for 2 m SCL at $100 \text{ m} \cdot \text{min}^{-1}$.

Inspecting the etched cutting inserts after 32 m SCL (Figure 6.25), fewer instances of adhesion in the sliding zone can be observed, as the dominant wear mechanism shifts from adhesive attrition towards thermally accelerated wear phenomena (local plastic deformation, potential chemical wear). Varying levels of alumina wear rate are indicated by the exposure of TiCN. It should be noted that due to the penetration depth of BSE electrons, visibility of TiCN does not necessarily indicate that the alumina coating has been entirely removed, although, some minor instances of complete delamination can be observed where there is a sudden change in contrast (Figure 6.25). Figure 6.25 suggests that the highest wear rate occurs at the highest speed when turning the CG material. Turning the FG material at lower speeds yielded the lowest rate of wear. Faster rates of alumina removal are observed in both materials at higher cutting speeds due to increased heat generation; this in turn leads to higher local temperatures, and a reduction in the alumina layer's strength and hardness [155].

Comparing this behaviour to IN718 turning in Chapter 5, it is clear coating pull-out via adhesive wear mechanisms is less severe when turning RR1000, since no delamination of the alumina layer occurs in the first turned metres, which would be indicated by an exposure of TiCN. Nevertheless, compared to IN718, significantly more reaction products are observed on the tool surface after etching, indicating chemical wear could occur which appears to be related to the presence of Hf. Comparing the two alloys, RR1000 has improved strength at high temperatures due to a higher γ' Vf, therefore higher temperatures will be generated during machining, facilitating thermally accelerated wear mechanisms. Figure 6.27 displays a region of the sliding zone after etching where both reaction products and ridges indicative of plastic deformation are observed. In addition, there is evidence of ploughing type abrasion, potentially caused by workpiece inclusions.

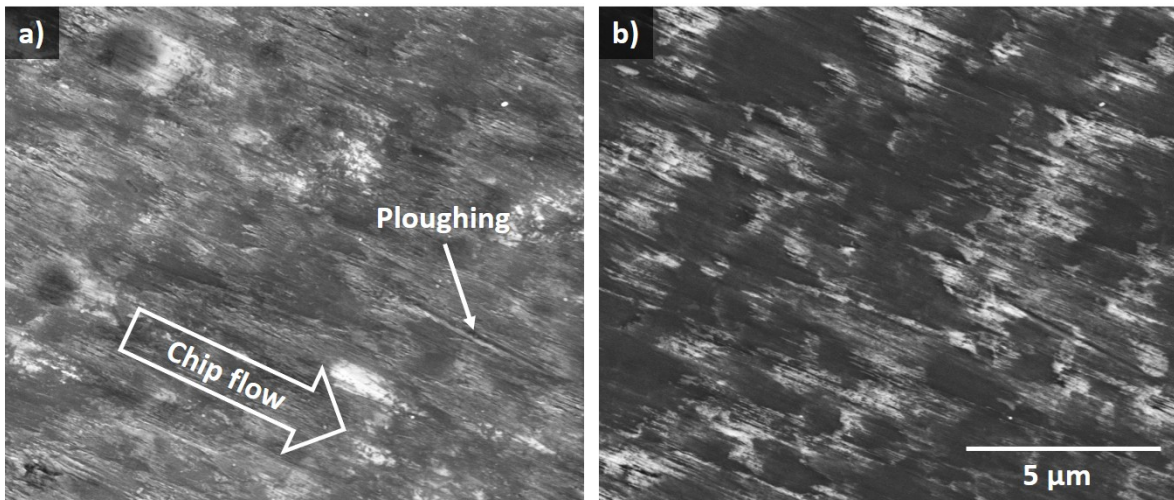


Figure 6.27: SEM micrographs of sliding region on tool rake face after turning CG material 32 m SCL at $70 \text{ m} \cdot \text{min}^{-1}$, viewed using (a) SE imaging mode (b) BSE imaging mode.

Observing Figure 6.25c, a band of alumina immediately behind the cutting edge is retained through out the wear process, since it could be protected by adhered material on the cutting edge, which redirects the chip flow. Indeed, even after an SCL of 600 m at a speed of $70 \text{ m} \cdot \text{min}^{-1}$, alumina can still be detected near to the cutting edge (Figure 6.28). In addition Figure 6.28 reveals the smooth topography of the worn TiCN, indicative of chemical wear, as TiCN will react with constituent elements of RR1000 [156, 157].

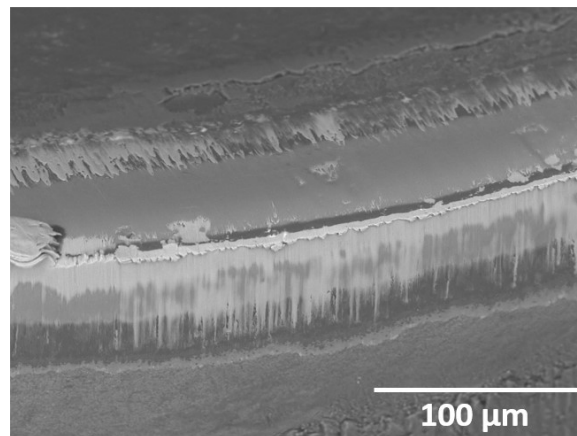


Figure 6.28: BSE SEM micrograph of rake face after turning the FG material after a SCL of 600 m, turned at a speed of $70 \text{ m} \cdot \text{min}^{-1}$.

Cross sectional micrographs were taken parallel to the direction of chip flow approximately $150 \mu\text{m}$ away from the auxiliary cutting edge (see Figure A4 of Appendix A). Inserts were

then examined for each cutting speed and material condition at 3 SCLs : 2 m, 16 m and 32 m (see Figure A5). Shorter SCLs were selected to focus the investigation onto the degradation of the alumina layer. Due to the destructive nature of obtaining cross-sectional samples, the graphs shown in Figure 6.29 and Figure 6.30 were constructed using several "sister" inserts ran to each successive SCL; this leads to some negative wear rates being observed in Figure 6.30

Figure 6.29 demonstrates how the change in alumina layer thickness varies significantly in different locations of the tool, and that this variation is affected by both speed and material condition. Under all conditions tested, the region of the rake face immediately behind the tool nose, exhibited the fastest rate of wear within the first 2 m (see Figure 6.30). It is hypothesised that the majority of the observed coating loss occurs during the tool engagement, since there will be no workpiece softening; the brittle tool coating, which will be at room temperature, will tend to fracture, as it is unable to deform plastically. During the remaining 2 m there is limited time for thermally driven wear phenomena to occur, and the majority of coating loss can be attributed to adhesive wear, which causes wear via fracture of the alumina coating. When turning the CG material at the higher cutting speed, additional rake face wear was also observed in the form of coating pull-out; it is likely related to the combination of high local temperatures, and the large fluctuation in the machining force response observed in Figure 6.12, which relates to greater chip instability, and larger cyclic mechanical loading of the coating.

An example of coating fracture on the tool nose beneath a BUE is shown in Figure 6.31. This demonstrates that cracks can preferentially form within the alumina layer instead of the coating/workpiece interface, indicating there is a strong chemical affinity between tool and workpiece; this leads to terrace formation around the nose radius of the tool. The interface between tool and workpiece also displays smooth areas indicating surface localised plastic deformation and potential chemical wear. These mechanisms occur at a slower rate than adhesive wear, which is the dominant wear type in this region. Terrace type features were observed on all inserts around the tool nose. Figure 6.32 shows diagrammatically the locations of key features and the dominant wear mechanisms in different regions.

Observing Figure 6.29, after a SCL of 16 m, the nose wear continues to develop and spread across the rake face, becoming more crater-like under all conditions tested. During this period the coating is subjected to an extended period at high temperature, promoting plastic deformation, and potentially chemical wear along the hottest regions of the tool-workpiece and tool-chip interfaces. Compared to the first 2 m of SCL, the rake face wear rate reduces under all conditions tested (Figure 6.30). For both RR1000 conditions, when comparing the two cutting speeds, a greater overall reduction in coating thickness is measured at the higher speed. It is hypothesised that this is caused by higher local temperatures, and increased strain hardening of the machined surface. After 16 m, flank wear was observed only when turning the CG material; the highest flank wear rate occurred at the higher cutting speed of $100 \text{ m} \cdot \text{min}^{-1}$.

By a SCL of 32 m, a significant amount of the alumina coating thickness on the rake has been removed under all conditions tested (see Figure 6.29), demonstrating the ineffectiveness of the coating in this region. Indeed, when turning the CG material at $100 \text{ m} \cdot \text{min}^{-1}$, only $0.5 \text{ } \mu\text{m}$ remains at the lowest point on the rake face. Nevertheless, Figure 6.30 shows that the wear rate stabilises between 16 m and 32 m SCL, which correlates with the stabilisation in the depth of workpiece subsurface damage indicated in Figure 6.9. This shows that both tool and workpiece condition evolve rapidly during the initial turned metres as cutting temperatures equilibrate.

Figure 6.29 also demonstrates that flank wear is more severe when turning the CG material. The smooth surface of the worn rake face alumina observed in Figure 6.32 suggests that plastic deformation and potential chemical wear are the dominant wear mechanisms; the inclusions observed in Figure 6.3 could also promote abrasive wear. If chemical wear does occur, then the higher flank wear rate observed when turning the CG material, may be related in part to the higher levels of damage induced in the workpiece (see Figure 6.4), since this will result in a more chemically active material.

One interesting observation from Figure 6.29 is that at the tool nose, i.e., the transition from rake to flank, the wear appears to have stabilised between SCLs of 16 m and 32 m, and almost no change in alumina thickness is observed. This suggests that the terrace formation and subsequent coating loss seen in Figure 6.31 occurs only in the early stages of the cut, after which point the BUE becomes stable and less prone to fracture. The terraces appear to assist the adhesion of the BUE by increasing the interfaces surface area.

Figure 6.33 shows how the effective wear rate varies depending on material and time in cut, and can be summarised as follows:

1. Rake face nose wear occurs during engagement leading to rapid wear via adhesive wear, this occurs most readily when turning CG material due to larger variations in machining force, which leads to irregular chip formation and increased coating fatigue.
2. Thermally accelerated wear mechanisms on both rake and flank begin to dominate as cutting temperature increases, this is accompanied by a large reduction in the wear rate.
3. Wear rate stabilises, and coating continues to be removed at continuous rate by adhesive wear, plastic deformation, and potential chemical wear.

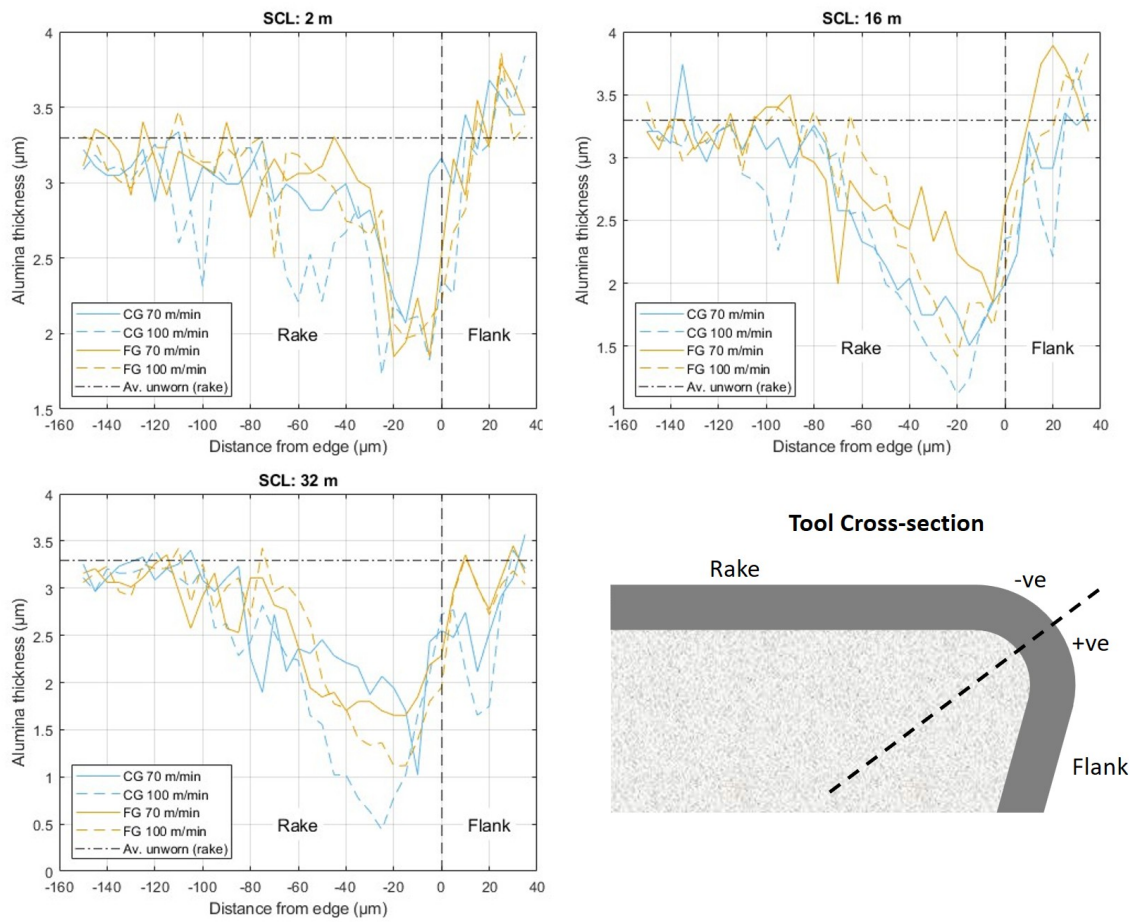


Figure 6.29: Graphs showing alumina wear across rake and flank, measured from cross-sections taken parallel to chip flow, at SCLs of 2 m, 16 m and 32 m.

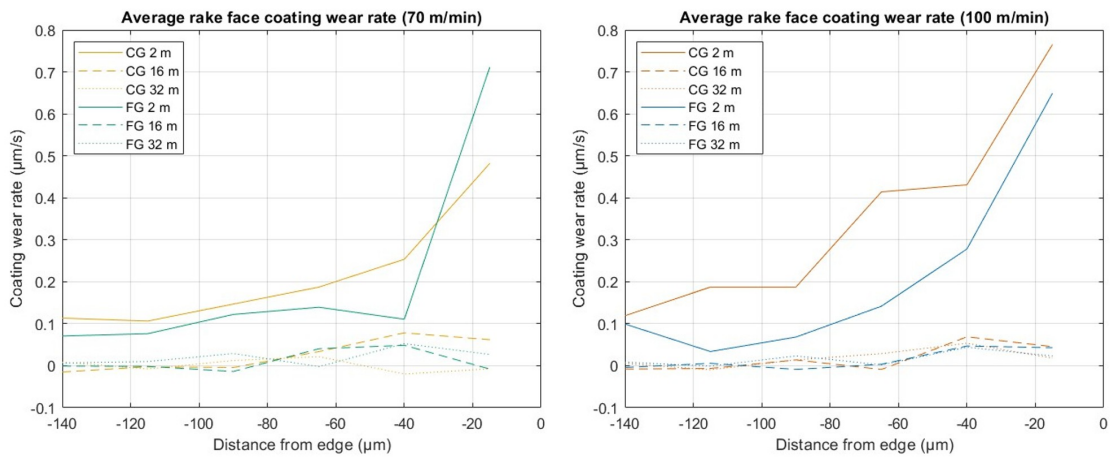


Figure 6.30: Graphs showing alumina wear rate on tool rake, measured from cross-sections taken parallel to chip flow.

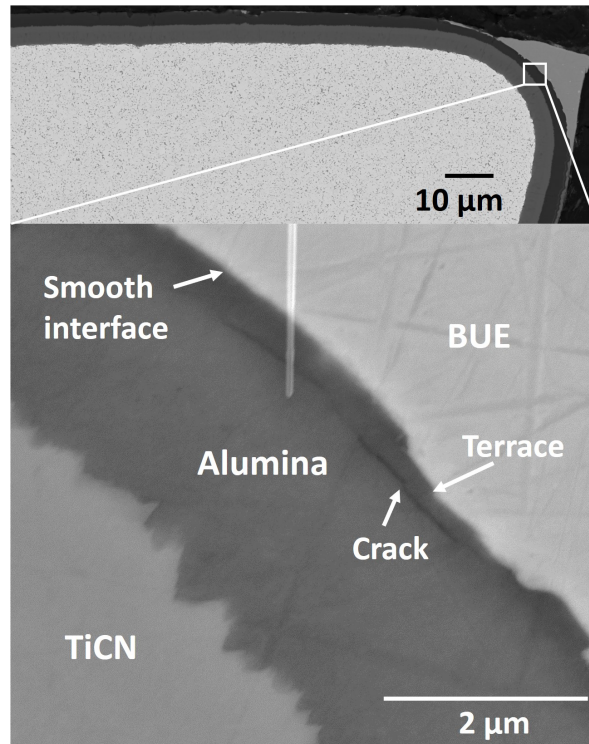


Figure 6.31: Cross-section SE SEM micrograph showing crack formation around BUE after turning FG RR1000 for 2 m.

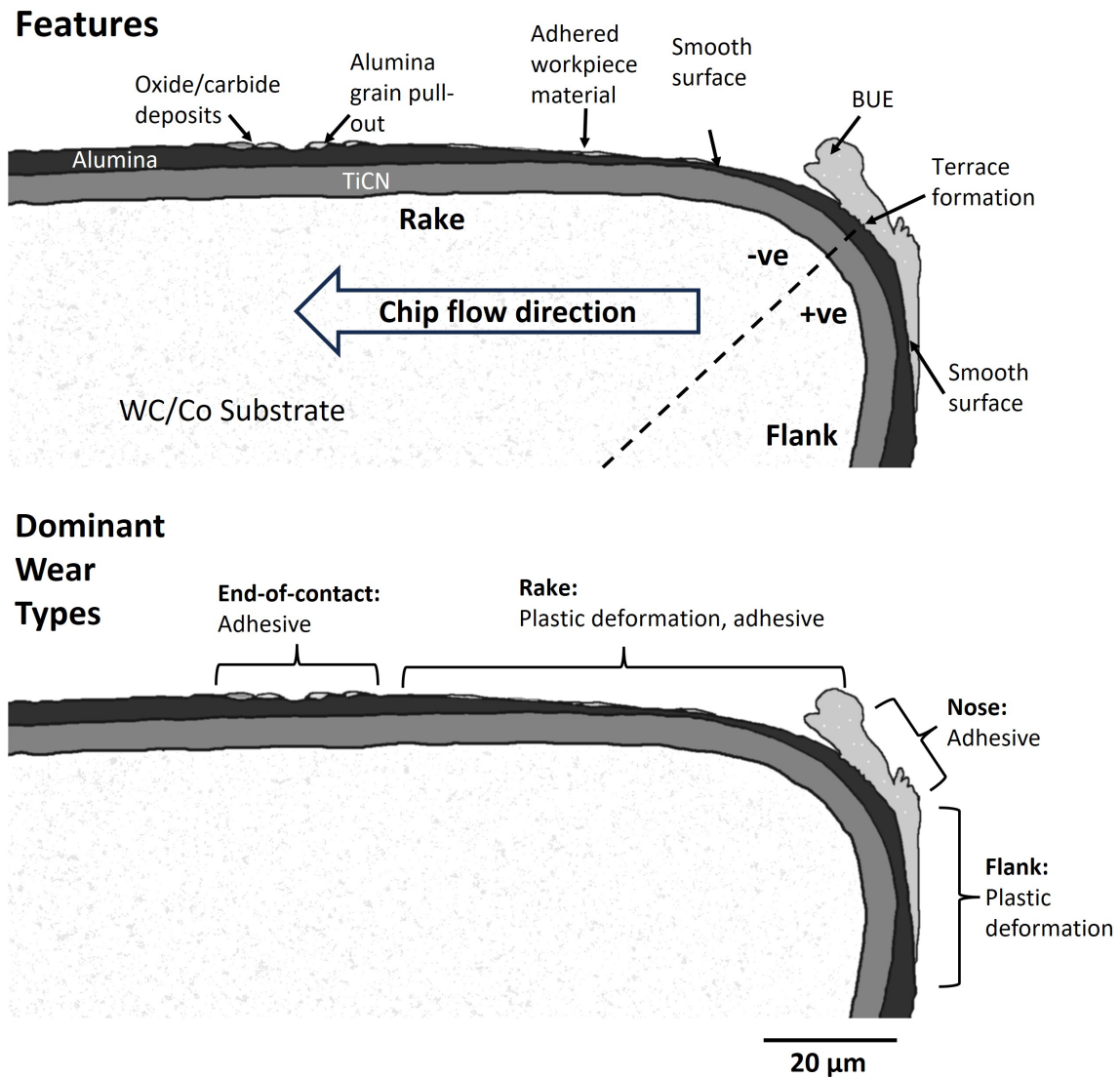


Figure 6.32: Diagram showing general features of alumina wear behaviour, adapted from SEM cross section micrograph taken after a SCL of 32 m when tuning the CG RR1000.

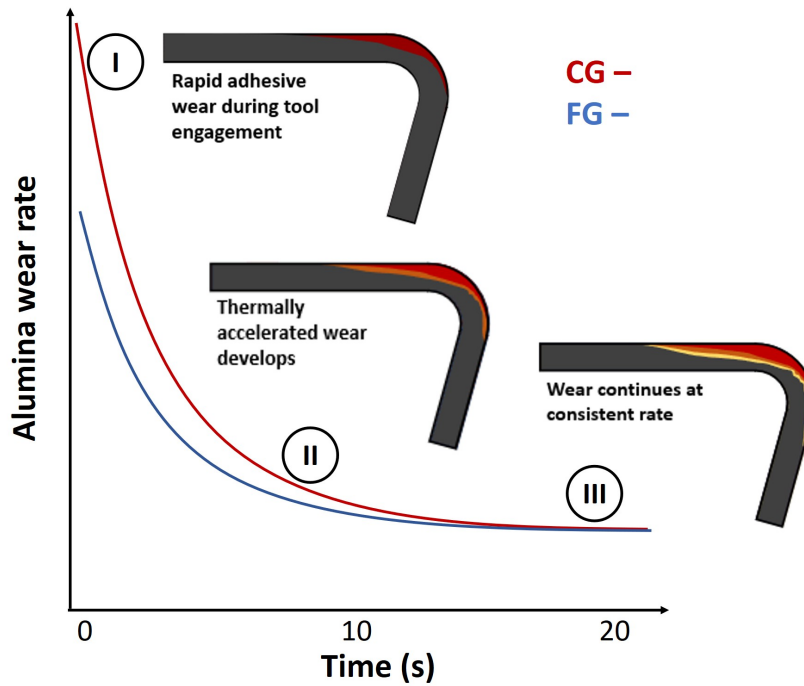


Figure 6.33: Schematic demonstrating generalised alumina wear variation against time for CG and FG RR1000.

Thermo-Calc Modelling of BCB Formation when Turning RR1000

To better understand the chemical driving force behind BCB formation, Thermo-Calc modelling was employed (see Section 4.10.1), whereby the influence of O_2 on the stable phase equilibria of RR1000 was examined by varying the partial pressure of O_2 from 1×10^{-40} to 1 (pure O_2). This was done to replicate the transition from chip seizure to the chip deflection, which occurs across the rake contact, resulting in increased O_2 ingress. Figure 6.34 and Figure 6.35 display the graphical results of the calculations performed; Figure 6.36 displays the results in tabulated form with the chemical formulas for all phases formed. It should be noted that these calculations are made for equilibrium conditions, so any phase identification is not definite.

These results demonstrate that a range of oxides can be formed depending on the partial pressure of O_2 . At O_2 partial pressures ranging from 1×10^{-40} – 1×10^{-26} , shown in Figure 6.34, there are several miscibility gaps observed, and numerous phases form. Of interest are corundum phases, as these may correlate to the Al-rich phases in regions 1 and 2 of Table 6.3. Pure Al corundum forms at the lowest O_2 partial pressure ($\approx 1 \times 10^{-34}$), followed a Ti-enriched between 1×10^{-32} – 1×10^{-27} . The enrichment of Ti in region shown in Table 6.3 combined with the high concentration of Al, suggests that this could be the phases being observed.

At O_2 partial pressures ranging from 1×10^{-28} – 1×10^{-19} Cr-enriched corundum becomes stable, which was not observed.

The calculations also demonstrate that Rutile is stable over a wide range of O_2 partial pressures (1×10^{-31} – 1×10^{-11}). Rutile remains relatively stable in composition with only little enrichment (0.1 At.%) at O_2 activities above 1×10^{-27} . However, the composition of Rutile exhibits a sharp transition at low partial pressure 1×10^{-31} , where ZrO_2 is formed instead of TiO_2 ; it can be observed in Figure 6.24 that Zr was only present in trace amounts within the BCB. Spinel phase $(Cr,Co,Al)_3O_4$ is anticipated to form at O_2 activities ranging from 1×10^{-20} –1, no overlap between the constituent elements was detected in Table 6.3 to indicate this phase has formed in the BCB, however similar Fe containing spinels have been reported as possible causes for chemical wear within the sliding zone when turning steel, since their formation would lead to a reduction in wear resistance [81].

The bright contrast phase is observed in region 3 of Table 6.3 was observed to be rich in Hf; HfC is observed to form at primarily low O_2 partial pressure ($<1 \times 10^{-28}$) environments as well as at 1×10^{-12} , and where HfC is not formed, Hf remains in the γ matrix. However, as shown in Figure 6.26, the Hf-rich inclusions present in the workpiece readily adhere to the alumina coating, it is hypothesised that they gradually accumulate at BCB as they move across the secondary shear zone. It is well known experimentally that MC carbide type precipitates can readily oxidise [158, 159], therefore, there may be a driving force for them to react with the O atoms present within the alumina layer when exposed to high temperatures and pressures in the secondary shear zone. In this region however they do not appear to be directly in contact with the coating, however they may have interacted with the coating as they moved across the secondary shear zone, culminating in chemical wear.

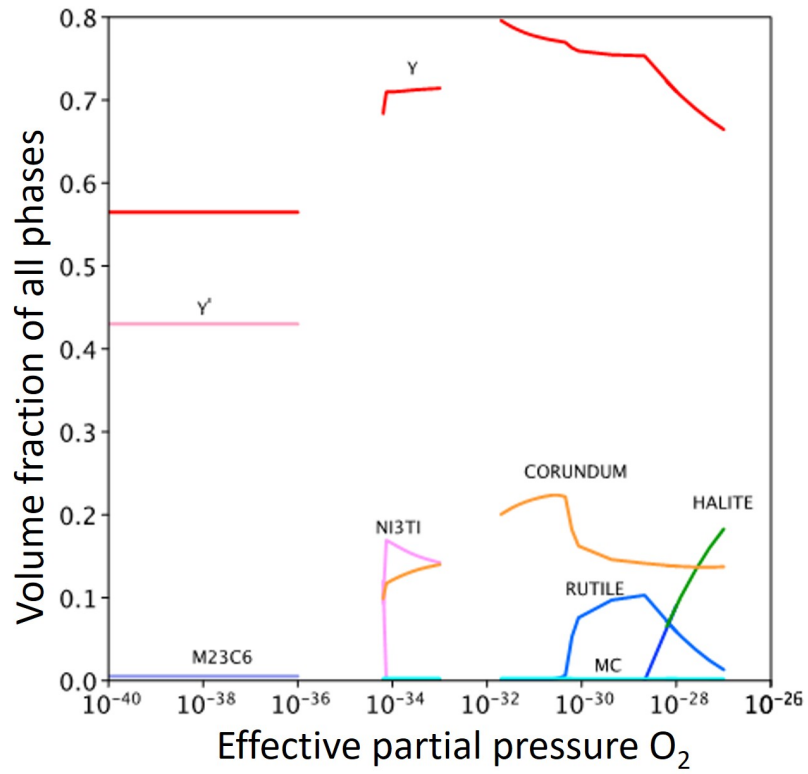


Figure 6.34: Graph showing calculated volume fraction against O₂ partial pressure for O₂ partial pressures ranging from 1 × 10⁻²⁷ to 1, corresponding phase compositions are give in Figure 6.36.

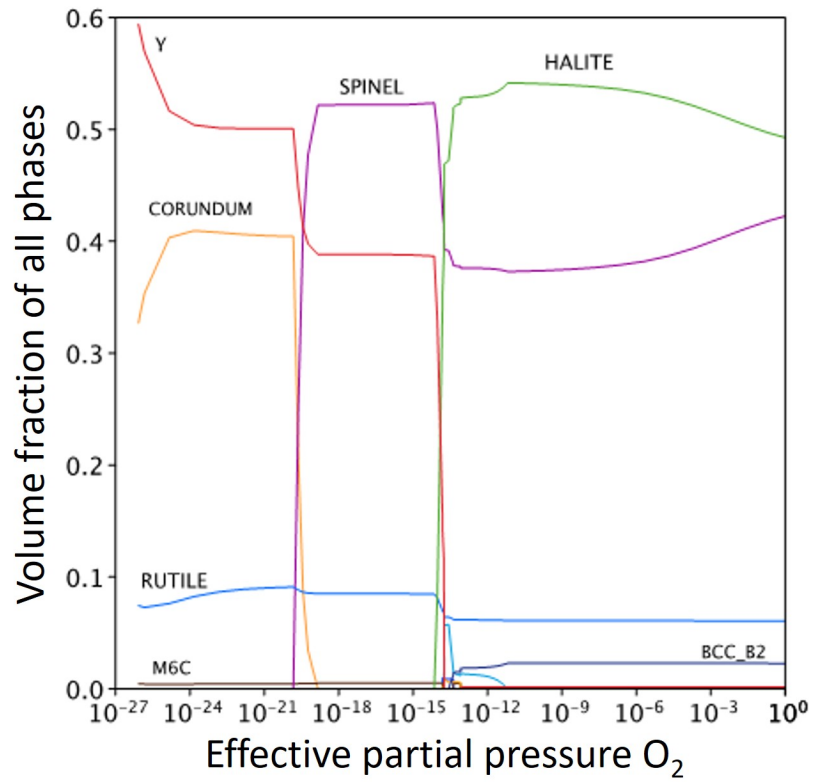


Figure 6.35: Graph showing calculated volume fraction against O₂ partial pressure for O₂ partial pressure ranging from 1×10^{-27} to 1, corresponding phase compositions are give in Figure 6.36.

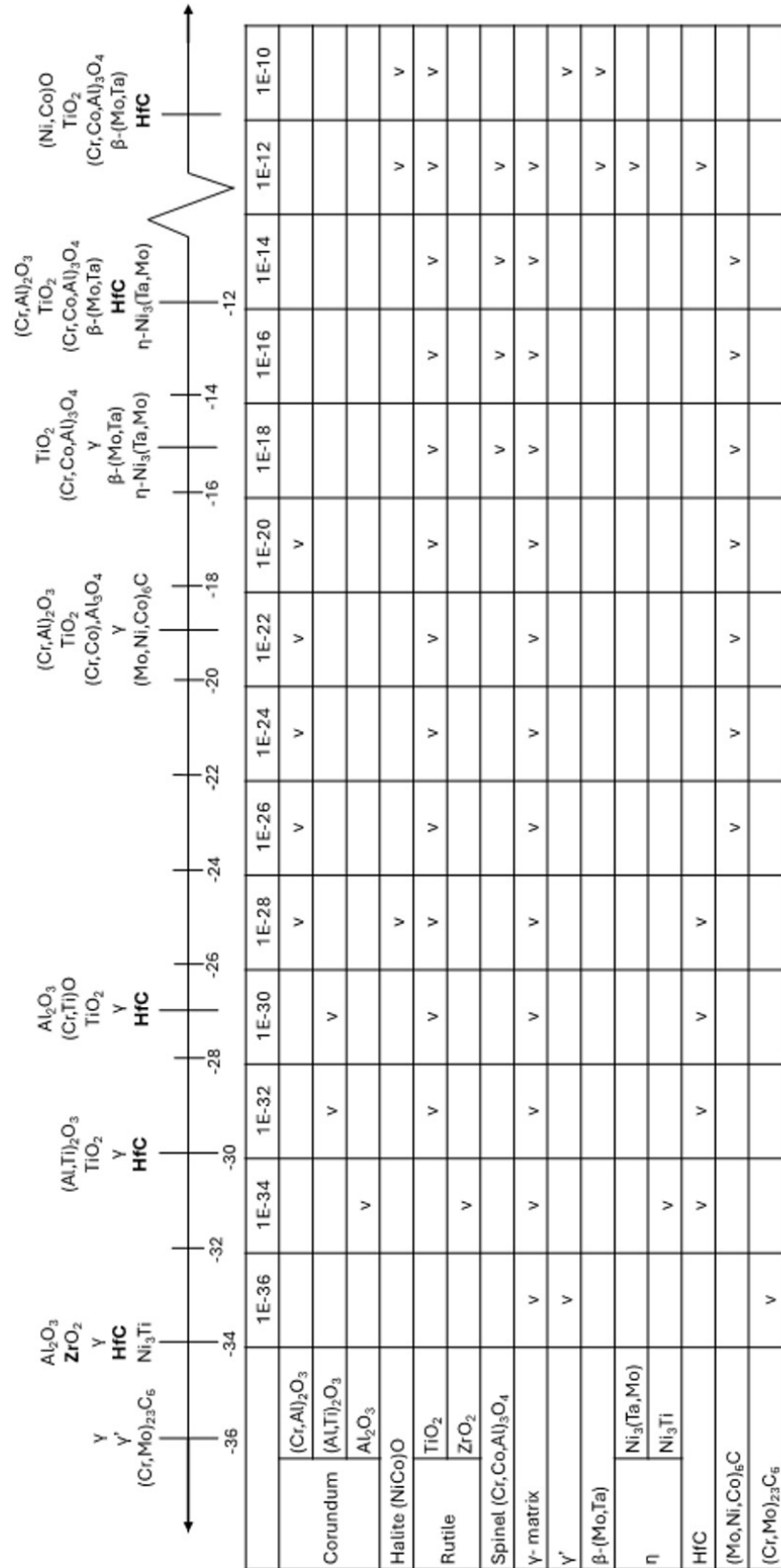


Figure 6.36: Table showing compositional variation of RR1000 as O₂ partial pressure is varied.

6.4 Conclusion

In this chapter, the relationship between workpiece material deformation and tool wear was explored for CG and FG RR1000 over a range of cutting speeds; the major findings are summarised in Figure 6.37. This included analysis of the machined surfaces, as well as analysis of the produced chips, which was supported by mean field modelling and FEM modelling. Following this, a detailed investigation of the tool wear was performed, including chemical analysis of reaction products formed on the tool surface, and accompanying Thermo-Calc modelling. These results highlight the limitations of state-of-the-art textured alumina coatings when turning advanced aeroengine high-pressure turbine materials.

Observing the machined surface, slip-band formation and γ' dissolution in an SPD layer were observed under all conditions tested. The dissolution of secondary γ' indicates high local temperatures; mean field modelling of the temperature effect on γ' dissolution revealed temperatures of at least 1100°C are required to produce significant dissolution. Reprecipitation of smaller tertiary γ' was also predicted but not observed.

Larger depths of damage were observed when machining the CG material in terms of swept grain and SPD layer thickness. Regions displaying cross-slip were detected; grain orientation was observed to heavily influence the degree of deformation. Higher cutting speeds were seen to encourage higher levels of subsurface deformation when turning the FG material. When turning the CG material, higher levels of deformation only occurred at the higher speed in the first $\approx 15 \mu\text{m}$ from the surface, and a lower total depth of deformation was detected when turning at the lower speed. This suggests that, since the FG deformation is less diffuse, it is more sensitive to the effect of increased cutting temperatures, which occur at higher cutting speeds.

The relationship between cutting speed and cutting temperature was explored using FE modelling. Overall, 9% higher temperatures were observed when turning at the higher cutting speed. Dynamometer results revealed that, although the average machining forces were comparable for the different conditions tested, the range was much higher when turning the CG material, as a result of local anisotropy, leading to irregular chip formation.

Alumina wear rates were found to be highest during tool engagement on the nose region of the tool towards the rake face. It is hypothesised that this occurs as a result of reduced workpiece softening during this period of low-temperature cutting, which leads to brittle coating failure and rapid adhesive wear, culminating in coating pull-out. This was observed to occur more readily when turning the CG material. This is attributed in part to the larger fluctuations in machining forces leading to coating fatigue.

Faster rates of flank wear were measured when turning the CG material condition. It is hypothesised that the higher levels of surface damage induced in the CG material could increase the chemical activity of the workpiece, leading to greater adhesion and accelerated potential

chemical wear. In a similar vein, significant notch wear was also detected when turning the CG material, whereas no significant notch wear was observed when turning the FG material during tool engagement. This may be related to both work hardening of the workpiece and HPC application. Terrace formation was observed below the BUE in the nose region of the tool for all conditions tested, as a result of parallel crack formation in the alumina subsurface, highlighting the strength of the bond between the alumina and RR1000.

At increased SCLs, when turning CG and FG RR1000, the wear rate was observed to stabilise as rising cutting temperatures causing thermally accelerated wear mechanisms to dominate. This is indicated by the smooth topography of worn alumina on both the flank and rake, as well as the large amount of reaction products retained after etching. Towards the rear of the contact, adhesive wear is the dominant wear mechanism, and coating pull-out occurs due to tensile forces during chip deflection. Here, the wear rate is slower than around the tool nose, since stresses and temperatures are lower.

Alumina grain pull-out towards the rear of the contact was shown to provide sites for the accumulation of the most chemically reactive oxide-forming elements in a so-called BCB. There appear to be three distinct phases: a corundum-type oxide (with some Ti enrichment), Hf-rich inclusions, and an enriched γ phase containing Ti from dissolved γ' . The Hf-rich inclusions were observed to adhere readily to the tool surface and appear to gradually accumulate at the BCB after moving across the secondary shear zone.

Compared to turning IN718 (Chapter 5), the propensity for pull-out and alumina delamination is greatly reduced when turning RR1000. However, thermally accelerated wear mechanisms appear more dominant (local plastic deformation, potential chemical wear), which may be related to higher cutting temperatures and the presence of different alloy addition, such as Hf. A recommendation from this work for material manufactures would therefore be to limit or remove Hf from the next generation alloys. Overall these findings demonstrate that whilst alumina coatings protect the underlying hardmetal substrate during the initial turned meters when turning CG and FG RR1000, the wear rate is rapid in regions of the contact where stresses and temperatures are highest. To improve multilayered textured alumina coatings for these specific applications further, the resistance to coating fracture should be enhanced to limit coating loss in the initial turned meters. Alternative machining strategies could also be explored that increase the workpiece temperature prior to tool engagement, i.e., laser-assisted machining.

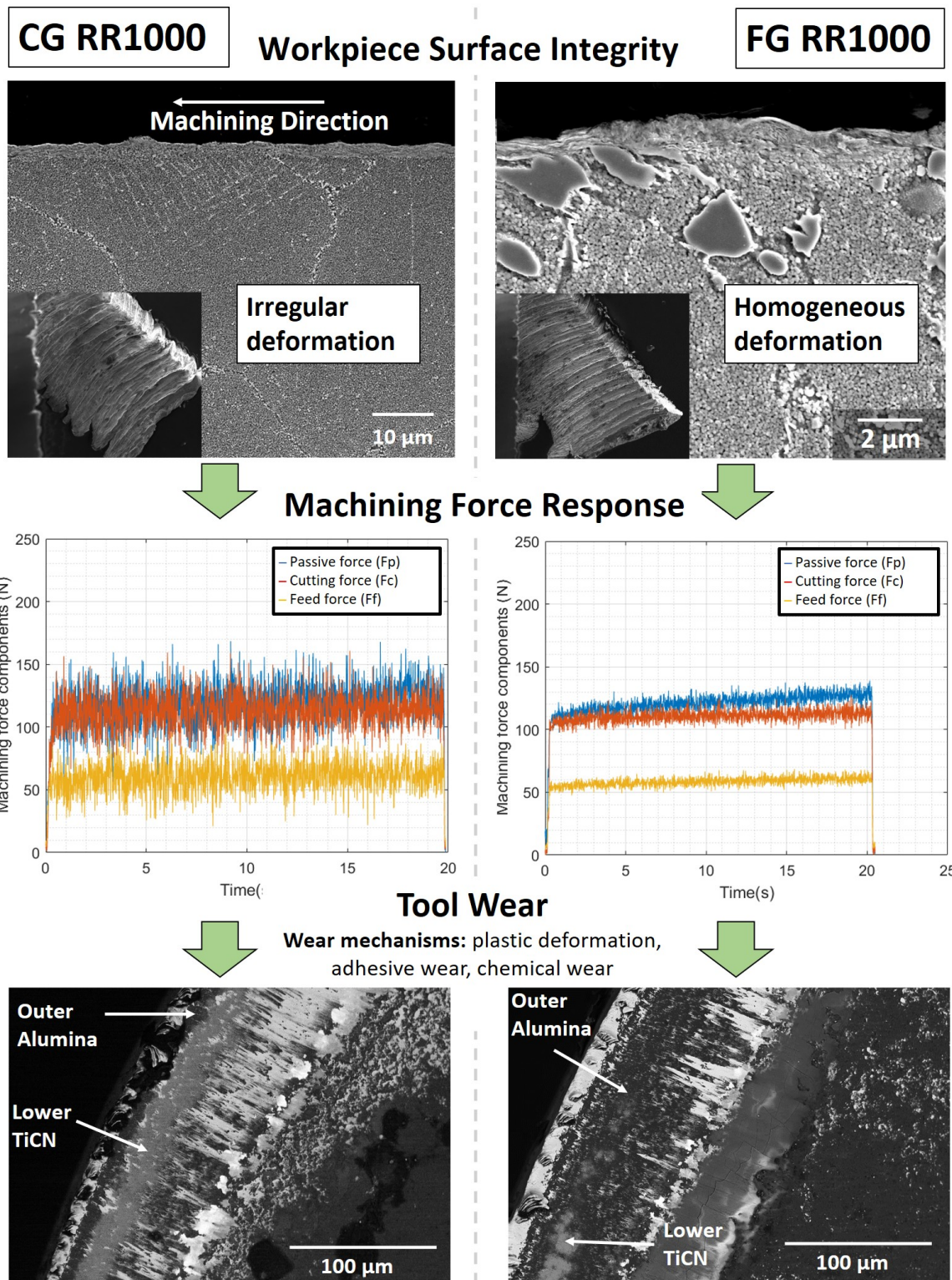


Figure 6.37: Summary schematic demonstrating relationship between workpiece surface integrity, chip formation, machining force response, and alumina wear rate for CG and FG RR1000 .

Chapter 7

Orthogonal dry turning of RR1000 in the as-HIP condition using multi-layer CVD alumina coated carbide tools

Both Chapter 5 and Chapter 6 demonstrated the effectiveness of using SCLs to examine the degradation of the outermost alumina coating layer when machining Ni-based superalloys, exploiting the rapid wear that they generate. These findings highlighted the inherent differences in terms of alumina wear behaviour for the two respective alloys, could be observed using minimal workpiece material. When turning the more heavily alloyed RR1000 in Chapter 6, suspected chemical wear was observed to be a more dominant wear mechanism. Evidence supporting this included the formation of a BCB to the rear of the contact zone containing strong oxide forming elements, such as Hf, as well as the retention of reaction products over the rake face after chemical etching. In the following chapter the chemical interaction on the rake face was further investigated by orthogonally cutting as-HIP RR1000 material.

7.1 Introduction

In the following study, RR1000 was orthogonally turned in an as-HIP condition (see Section 3.2), in order to better understand the interaction between alumina coated tools and the workpiece material. In this context, as-HIP material is hypothesised to be sufficient to capture said behaviour, since it has the same composition. The main advantage to using as-HIP material compared to HIP then forged material, is that it can be manufactured at a substantially lower cost, and with a lower overall energy consumption, which are both important considerations for experimental machining trials. Indeed it has been shown that in a fully heat treated state, as-HIP material has comparable mechanical properties to material that has also undergone the final forging step [40]. Post machining, X-EDS analysis was carried out on worn tools to observe the reaction products that accumulate on the tool rake face. In addition, SEM in the BSE imaging mode was also employed to investigate material adhesion and BUE formation. Cross-sectional samples were taken from worn tools parallel to the CFD to

observe the worn alumina topography. Finally, SEM in SE imaging mode was used to image electrolytically etched samples displaying machining induced damage in the workpiece material normal to the cutting direction.

7.2 Materials and Methods

The following section details the materials and methodology utilised in the machining experiment presented.

7.2.1 Experimental Materials

The workpiece material used in the trial was as-HIP RR1000 with a diameter of ≈ 60 mm. The composition of the material is given in Table 3.1.

Sandvik Coromant inserts with a TCMW110304 geometry were utilised for all cuts performed (see Section 3.1.2). These inserts feature an S205 multi-layer CVD coating (see Section 3.1.1). Cutting edges with an ER of $\rho = 46.9 \pm 1.2$ μm were utilised for the trial. All cuts were performed dry, using a custom-made shank. The tool was kept at a 0° rake angle.

7.2.2 Test methods

Orthogonal machining was carried out by producing grooves in the billet stock material to form fins with a fixed thickness of 2 mm (see Figure 7.1). The speed and feed rate were kept constant: $100 \text{ m} \cdot \text{min}^{-1}$ and $0.05 \text{ mm} \cdot \text{rev}^{-1}$ respectively, whilst the SCL was varied: 12 m, 17 m and 57 m.

A Kistler plate piezoelectric force dynamometer (Type 9129AA model) was attached to a C5 tool adapter to measure the machining force components: F_c , F_f , and F_p , at a sampling rate of 20,000 Hz (see Section 4.7).

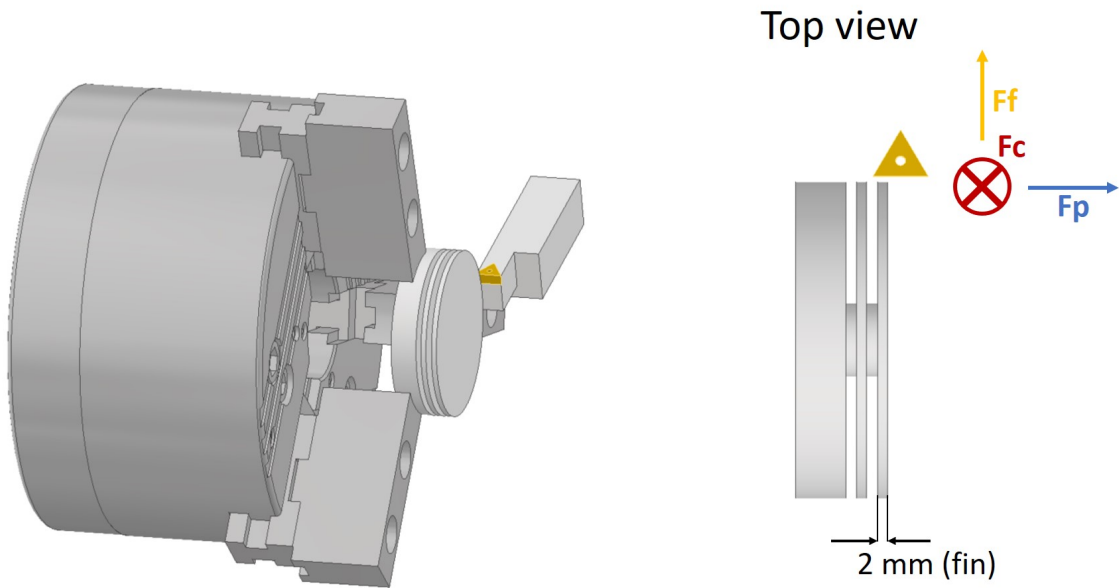


Figure 7.1: Diagram of experimental setup used in orthogonal turning trial, and relevant machining force components.

7.2.3 Characterisation Techniques

SEM was conducted using an FEI Inspect F50, utilising BSE detectors to identify compositional and topological features; an 80 mm Oxford X-EDS detector mounted on the same system was used for compositional analysis (see Section 4.1). Machined surfaces were electrolytically etched with phosphoric acid (see Section 4.9). The insert ER values were measured using an Alicona InfiniteFocus SL (see Section 4.4.2). Cutting inserts were cross-sectioned in the position shown in Figure 7.2; they were then polished using the method described in Section 4.6.

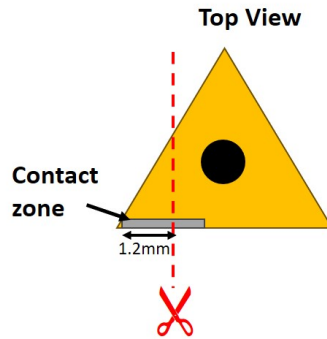


Figure 7.2: Diagram showing top down view of cutting inserts used in trial, and approximate position of sectioning line used to produce cross-sectional samples.

7.3 Results and Discussion

7.4 Machining Forces and Tool Wear

Average F_f and F_c values were found to be 358 ± 25 N and 392 ± 22 N, respectively, demonstrating good repeatability was achieved with the experimental setup employed. Due to the orthogonal nature of the cutting mechanics, average F_p values were measured to be significantly lower (13 N). Averages were taken during the first 3 seconds of tool engagement to reduce the impact of tool wear and the corresponding change of tool microgeometry. During the initial testing of the experimental setup, it was found that feed rates above $0.5 \text{ mm} \cdot \text{rev}^{-1}$ could lead to chatter at certain cutting speeds, as a result of the dynamic instability of the system. To utilise higher feed rates, a more rigid system would need to be employed, this could potentially be achieved by omitting the dynamometer from the setup or by using tools with a less aggressive geometry (e.g., a more positive rake angle or chip breaker). Similarly, attempts to increase cutting speed to $150 \text{ m} \cdot \text{min}^{-1}$, resulted in tool failure after approximately 20 s due to overheating and substrate fracture, as such, the cutting speed was limited to $100 \text{ m} \cdot \text{min}^{-1}$ for all cuts performed. Tool failure was preceded by an exponential increase in cutting force; the author would recommend that if higher cutting speeds are to be used for orthogonal turning of Ni-based superalloys using a similar setup, that some form of cooling be introduced to prevent this, i.e., flood, cryogenic, HPC, supercritical CO_2 etc., or else that the time in cut be shortened and increased incrementally.

Figure 7.3 shows the tool rake faces viewed from above for all SCLs tested. In this region of the wear scar, wear is consistent across the contact zone, and there is no significant impact from the notches that form at the edges during tool engagement. In all cases, significant adhesion is observed, and a BUE forms across the entire cutting edge of the tool. It should be

noted that the "true" adhesion will be even greater, since the thinnest layers are not observed at the operating voltage utilised in the figure (10 kV); this effect is shown clearly in Figure 7.4. The drawback of using lower operating voltages is that contamination from the cleaning process often becomes more visible, which can obscure the region of interest, in addition the BCB also becomes less visible. An operating voltage of 10 kV was therefore selected as a compromise between these conflicting effects.

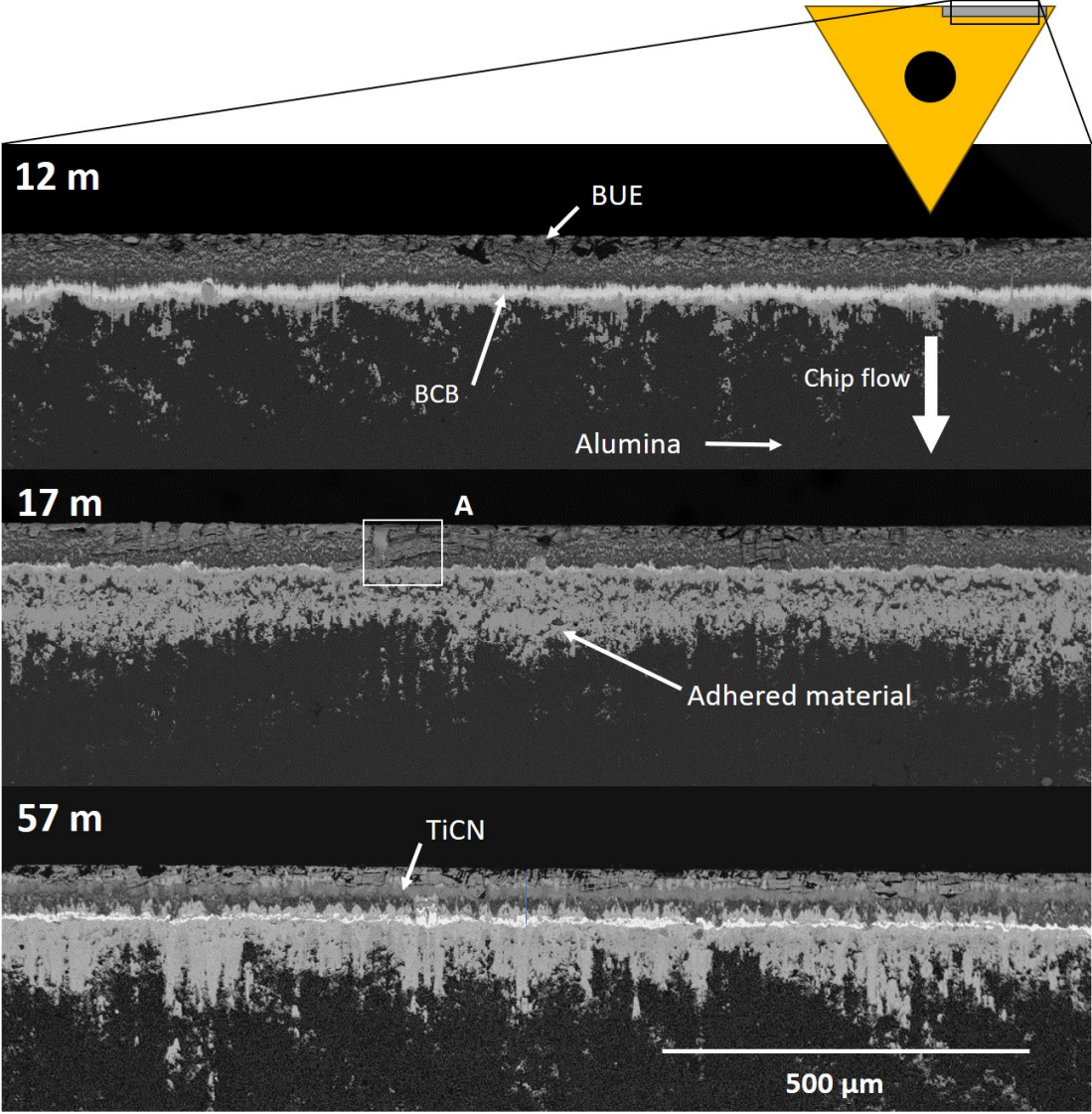


Figure 7.3: BS SEM micrographs showing rake face wear during RR1000 turning trial after varying SCLs: 12 m, 17 m and 57 m.

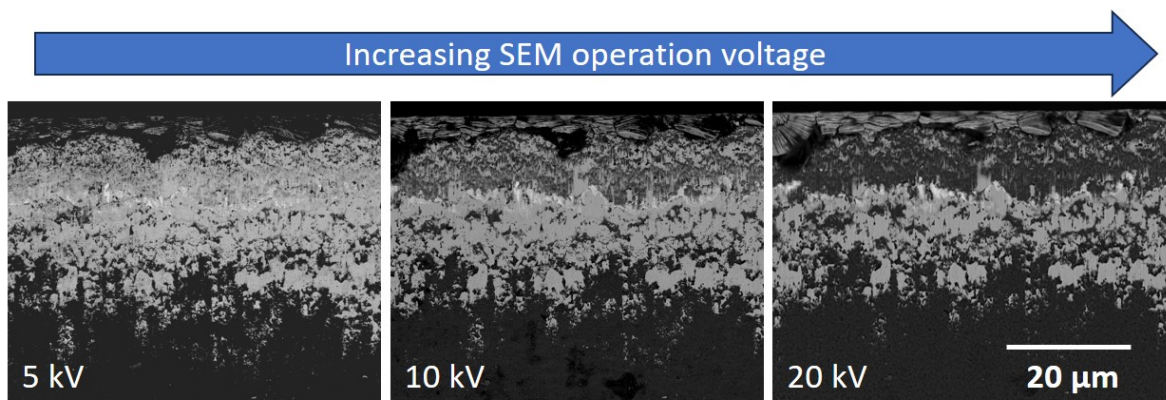


Figure 7.4: Influence of kV on the amount of adhered material observed during BS SEM imaging; micrographs show rake face adhesion on a test insert ran at surface speed of $80 \text{ m} \cdot \text{min}^{-1}$ for 11 m, at a feed rate of $0.5 \text{ mm} \cdot \text{rev}^{-1}$.

Figure 7.3 demonstrates that adhesion tends to increase as SCL increases during dry orthogonal turning of RR1000 in an as-HIP condition. Throughout SCLs of 12 m and 17 m, chips were observed to be discontinuous shards as a result of a low feed rate similar in magnitude to the tool ER. Although no temperature measurements were made, variations in chip formation were observed during the longest cut (SCL = 57 m) after a SCL of approximately 37 m, whereby chips transitioned from discontinuous shards to continuous ribbons as the cutting temperature increased; this was accompanied by a visible increase in chip incandescence. As the cut is performed, heat in the fin will accumulate rapidly, since there is no workpiece material at either side to serve as a heat sink, accelerating the temperature rise, which promotes workpiece softening, and, in this instance, continuous chip formation. It is also likely that higher cutting temperatures will have promoted adhesion on to the rake of the insert too. After a SCL of 57 m, significant TiCN exposure can be observed directly behind the BUE as a result of alumina layer wear, altering the tool microgeometry, which may have also contributed to the change in chip formation.

In all instances, a BCB was observed to form towards the rear of the contact zone as shown in Figure 7.3; it can be seen most clearly for the insert ran to a SCL of 12 m, since there is less adhesion of fresh Ni-based material on top. Figures 7.5 and 7.6 display the X-EDS scans utilised to examine the elemental composition of the species that form in this region of the rake face for inserts ran to a SCL of 12 m and 57 m, respectively. Figure 7.5 shows that bright phase contains Hf, Ta, and Zr, and the dark phase is Ti-rich

As discussed in Chapter 6, the bright Hf-rich phase is hypothesised to originate from the adhesion of inclusions that move across the secondary zone. The dark phase is hypothesised to be an oxidation product. The key difference when compared to Figure 6.21 is that the dark phase is rich in Ti and not Al. The results shown in Figure 6.35 demonstrate that several oxides can form, including corundum enriched with Ti, as well as rutile (TiO_2). Due to the

non-equilibrium nature of the conditions present within the BCB, it is uncertain how reliable these simulation results are. Nevertheless, it can be concluded from the absence of Al in the dry orthogonal case that the excess Al observed within Figure 6.21 is more likely to originate from the workpiece than the coating. Due to the large number of differences (cooling strategies, tool geometry, workpiece material condition) between the two experiments, it is unclear which factor or combination of factors has led to the variation in oxidation behaviour.

The location of alumina coating without workpiece material adhesion is shown in regions where O overlaps with Al. Since O is present in the alumina coating, it is hard to determine from the data presented whether the change in intensity seen in the BCB region is due to an increase in O concentration, or if it is caused by a reduction in thickness of the adhered material; the EPMA results presented in Chapter 6 would suggest the former to be the more likely. C also appears to overlap with all areas displaying any workpiece material adhesion, including regions rich in Hf, Ta, and Zr, which are known to be strong MC carbide formers. Indeed, Hf/Ta carbides have been observed in other microstructural studies performed on RR1000 [150]. γ forming elements Ni, Cr, Mo, Co are not found in the BCB and are distributed mainly at the rear of the contact zone. These elements are also seen to overlap with Ti, which is a γ' forming element that could be dissolved into the γ phase as a result of the high strains and temperatures present at the tool-chip interface, as observed in the TEM study performed on the machined surface shown in Figure 6.5.

Observing X-EDS maps in Figure 7.6, similar trends are seen with respect to the congregation of constituent workpiece elements across the BCB, although it now appears to be narrower, and there is no obvious segregation between Ti rich regions and regions rich in Ta, Hf, and Zr. The major difference when compared to Figure 7.5 is an additional band of Ti appears in front of the BCB, which is formed by the exposure of TiCN layer below the alumina, and is not caused by workpiece material adhesion; wearing of TiCN may provide additional Ti that could congregate in the BCB. Another obvious difference is the large amount of γ forming elements that are distributed both in front and behind the BCB due to an increased propensity for adhesion during longer cuts.

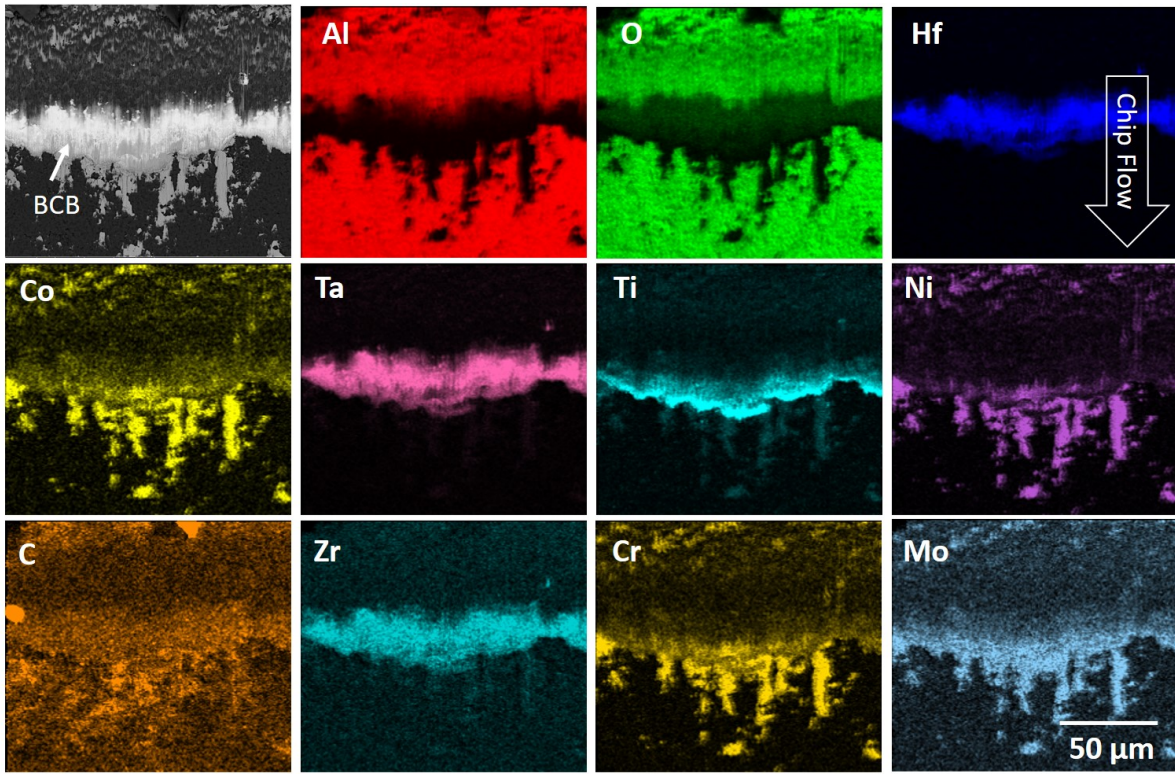


Figure 7.5: X-EDS scan and accompanying BS SEM micrograph of BCB after a turning a SCL of 12 m.

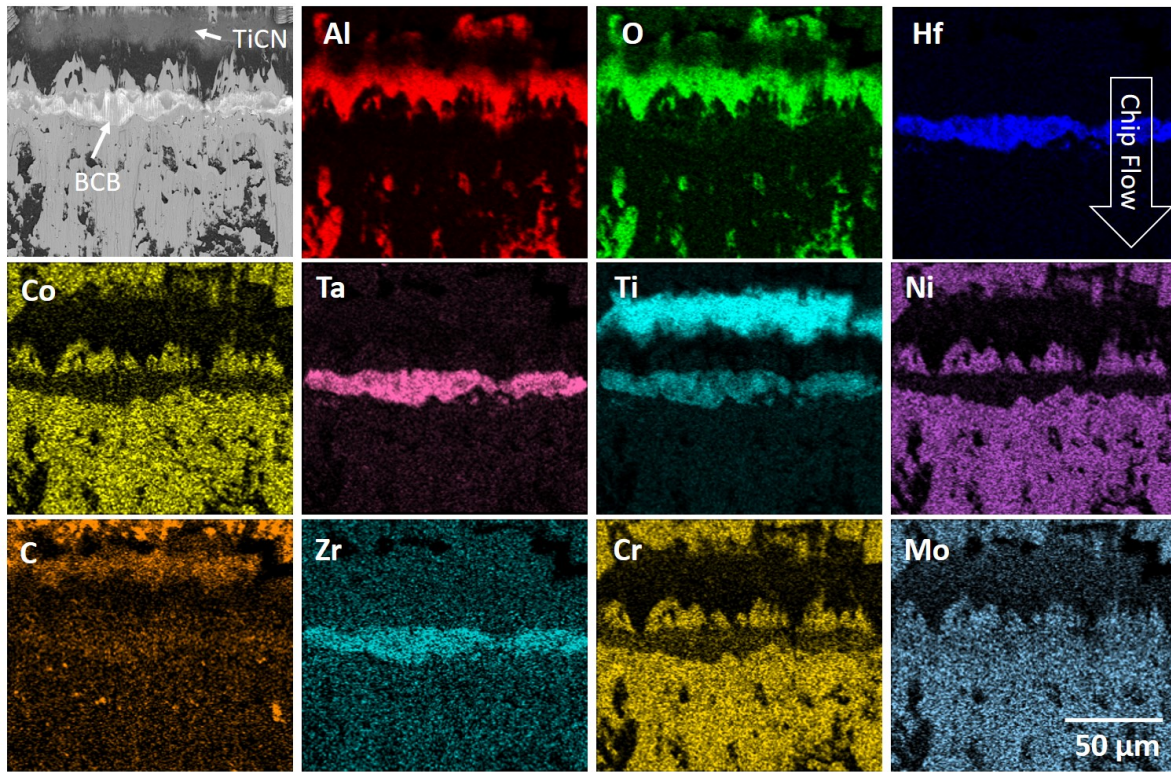


Figure 7.6: X-EDS scan and accompanying BS SEM micrograph of BCB after a turning a SCL of 57 m.

Figure 7.7 shows cross sections of the tools at each SCL. The BUE has remained intact for inserts ran to SCLs of 12 m and 57 m, but it has been dislodged during the metallographic preparation for the insert ran to an SCL of 17 m, as demonstrated in Figure 7.3, whereby the BUE has formed across the entirety of the cutting edge. Viewing the BUE from this orientation, demonstrates how the effective geometry of the tool changes upon adhesion of the BUE. It also demonstrates how the BUE prevents the alumina layer from interacting with the machined surface on the tool flank; in essence, the adhered workpiece material becomes part of the cutting tool, and Ni-based material cuts Ni-based material.

At this magnification, there is only a minor indication of adhered material across the rake face contact for the insert ran to a SCL of 12 m, however, significant adhered material is observed across the contact for the insert ran to a SCL of 17 m. Regions of the coating that have worn fastest, as a result of some adhesive wear resulting in grain pull-out, have been "filled" by adhered material, such that the tool surface has a smooth topography. By 57 m SCL, the majority of rake face coating has been removed by a combination of wear mechanisms acting in tandem (i.e., chemical, adhesive, plastic deformation). Since no coolant was employed, thermally accelerated wear phenomena, such as chemical wear, appear to have become dominant in the latter stages of wear, due to the increasing local temperatures

previously discussed. This hypothesis is supported by the smooth surface of the worn alumina layer in regions I and II (Figure 7.7), which is indicative of chemical wear.

The strong chemical affinity that exists between the Ni-based material and the alumina layer, which promotes chemical wear, is further highlighted in region I. Here the BUE has fractured along the Ni-based superalloy side of the bond, rather than along the bond itself, demonstrating that interface is in fact stronger. The nature of the chemical interaction that results in said bonding is still unknown, and must occur at a finer scale than can be detected by the methods employed in this study.

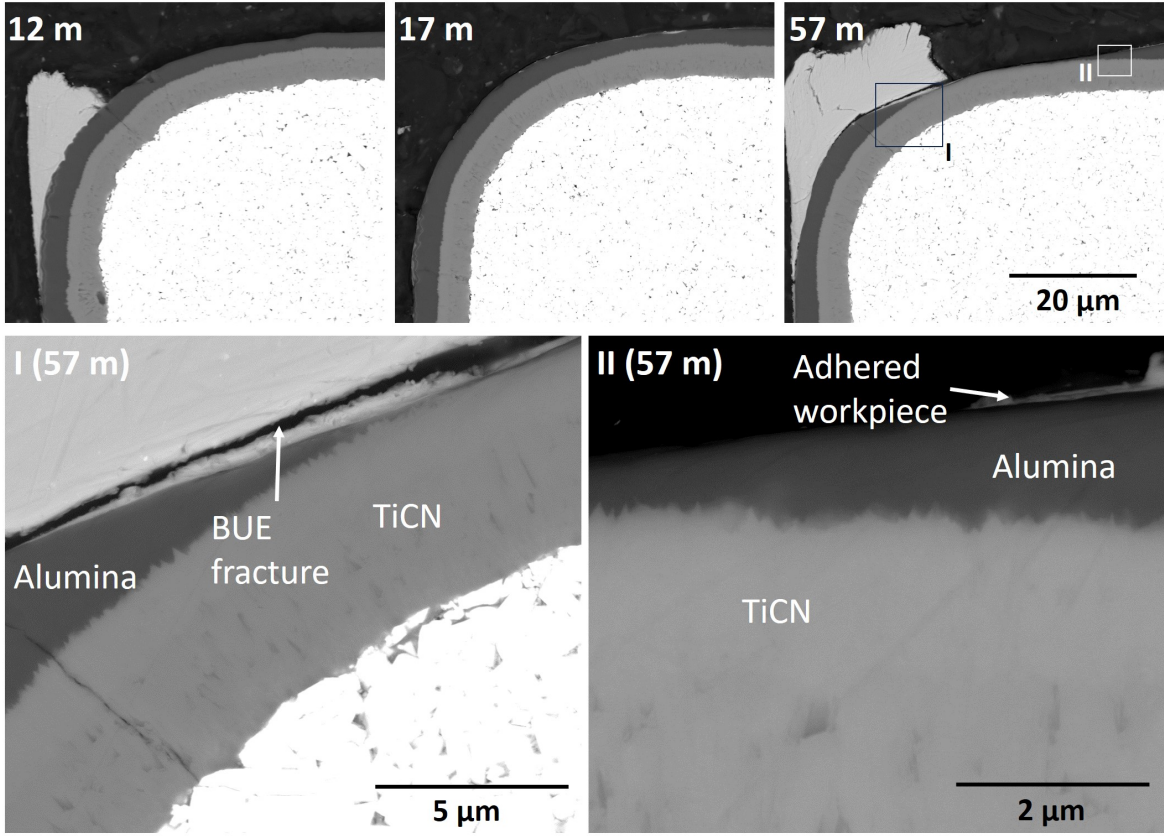


Figure 7.7: BS SEM micrographs of cross sections taken parallel to chip flow after varying SCLs: 12 m, 17 m and 57 m.

Figure 7.8 shows the cross section of the BCB formed after machining a SCL of 57 m. X-EDS was performed on this same region (see Figure 7.8), and demonstrates that the BCB contains a mixture of O rich phases, the brightest being rich in Hf, Zr, and Ta, which appears to be an agglomeration of heavily deformed inclusions. A darker Ti rich phase is observed to form surrounding this brighter phase and may also contain some Hf, Zr, and Ta, however it is hard to assess given the limited resolution of the technique employed. Figure 7.8 demonstrates that the BCB has formed in a region of the alumina coating that has undergone grain pull-out,

since the topography of the alumina layer is wavy. These findings are comparable to those seen in Figure 6.24. The most obvious difference is that in the orthogonal case is that this dark contrast matrix type phase appears to be rich in Ti instead of Al, suggesting it could be Rutile instead of metastable Corundum. It is hypothesised that this may be related absence of HPC, which slows the reaction kinetics, allowing more time for phases requiring higher O_2 activities, such as Rutile, to form.

Observing further along the contact in the direction of chip flow, γ forming elements (Ni, Co, Mo, Cr) appear to have accumulated, and the coating shows sign of significant grain pull-out as a result of adhesive wear. Due to the absence of the strong oxide forming elements, this transition represents the end of the secondary shear zone. In this end-of-contact region, temperatures are lower and adhesive wear dominates due to tensile forces caused by the adhesion of deflecting chips. Similar observations were made in both Chapter 5 and Chapter 6, suggesting this is a general wear characteristic of alumina tool when turning Ni-based Super-alloys.

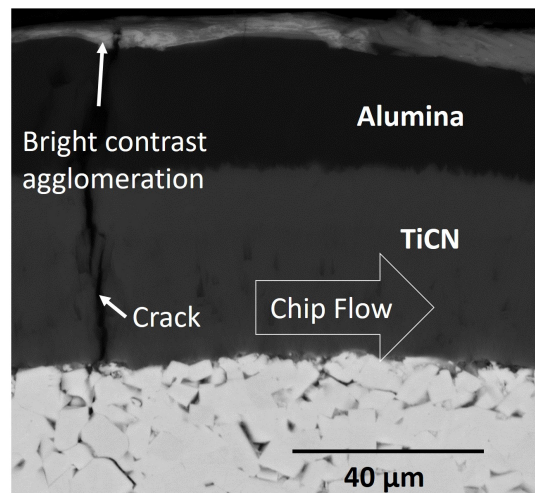


Figure 7.8: Cross sectional BS SEM micrograph of BCB formed after turning a SCL of 57 m; the crack observed was likely formed during metallographical preparation.

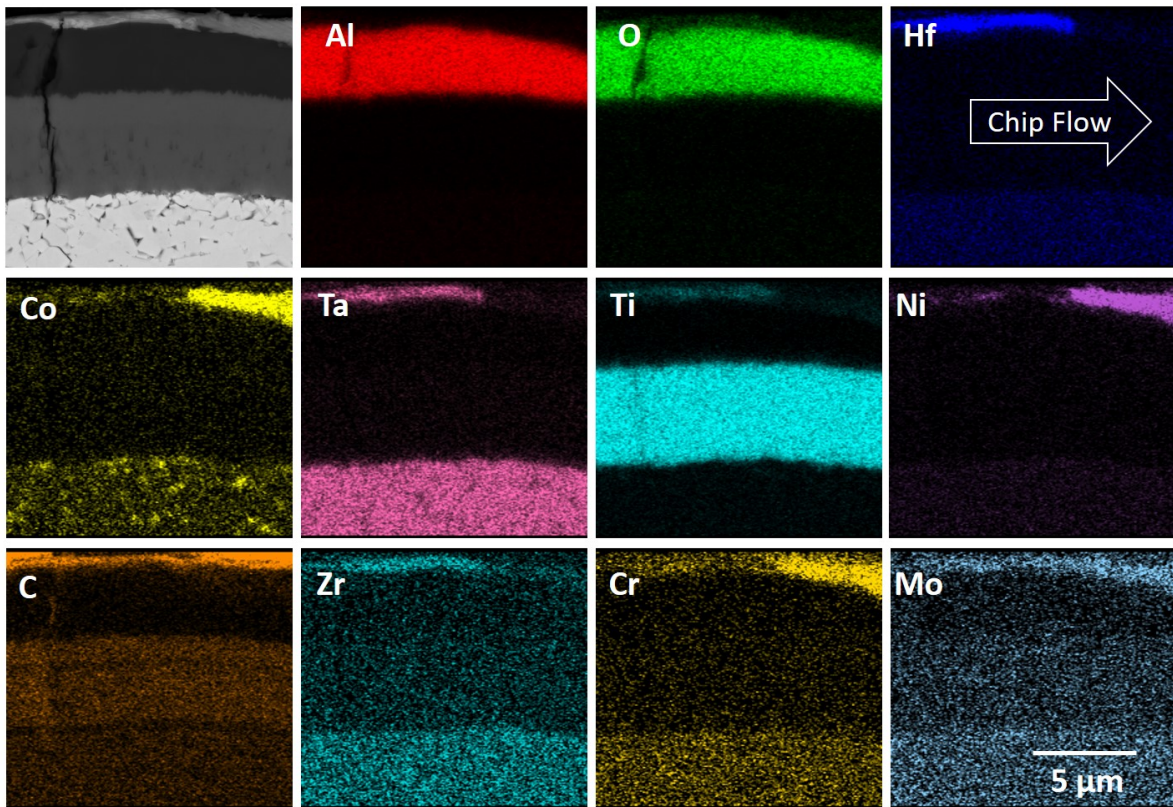


Figure 7.9: X-EDS scan and accompanying BS SEM micrograph of region displayed in Figure 7.8.

Figure 7.10 shows a diagram of the proposed wear mechanisms acting during the study presented. Regarding the BCB formation, in the machining case there is a continual renewal of fresh workpiece material. This boundary condition means that the elements with the highest propensity for adhesion to alumina become concentrated at the interface between tool and workpiece (sliding zone), and over time become concentrated in the BCB at the rear of the sliding contact. In this region as discussed in Chapter 5 and Chapter 6, tensile forces lead to alumina grain pull-out, which provides areas for workpiece material to adhere and oxidation products to accumulate. The sliding contact in the secondary shear zone is characterised by intense friction. This friction generates significant heat which accelerates chemical wear near to the interface between tool and workpiece material. The composition of the BCB gives an indication of the reactive oxide forming elements that contribute to chemical wear of alumina coatings. To the rear of BCB there is an area of intermittent contact where Ni-based material with chemistry similar to the bulk alloy adheres that has not moved across the sliding contact. The adhesion of this material occurs due to the wider thermal gradients when machining dry, which means the chip is hotter and softer in this region, and so adheres more readily; there is also no chip breaker to cause the chip to deflect, preventing further adhesion. Figure 7.11 displays an adhered chip on the insert ran to a SCL of 17 m that remained connected after

machining. This chance occurrence offers a "snapshot" of how the heavily compressed chip interacts with the BUE and the rake face surface, depositing material as it moves across the flow zone.

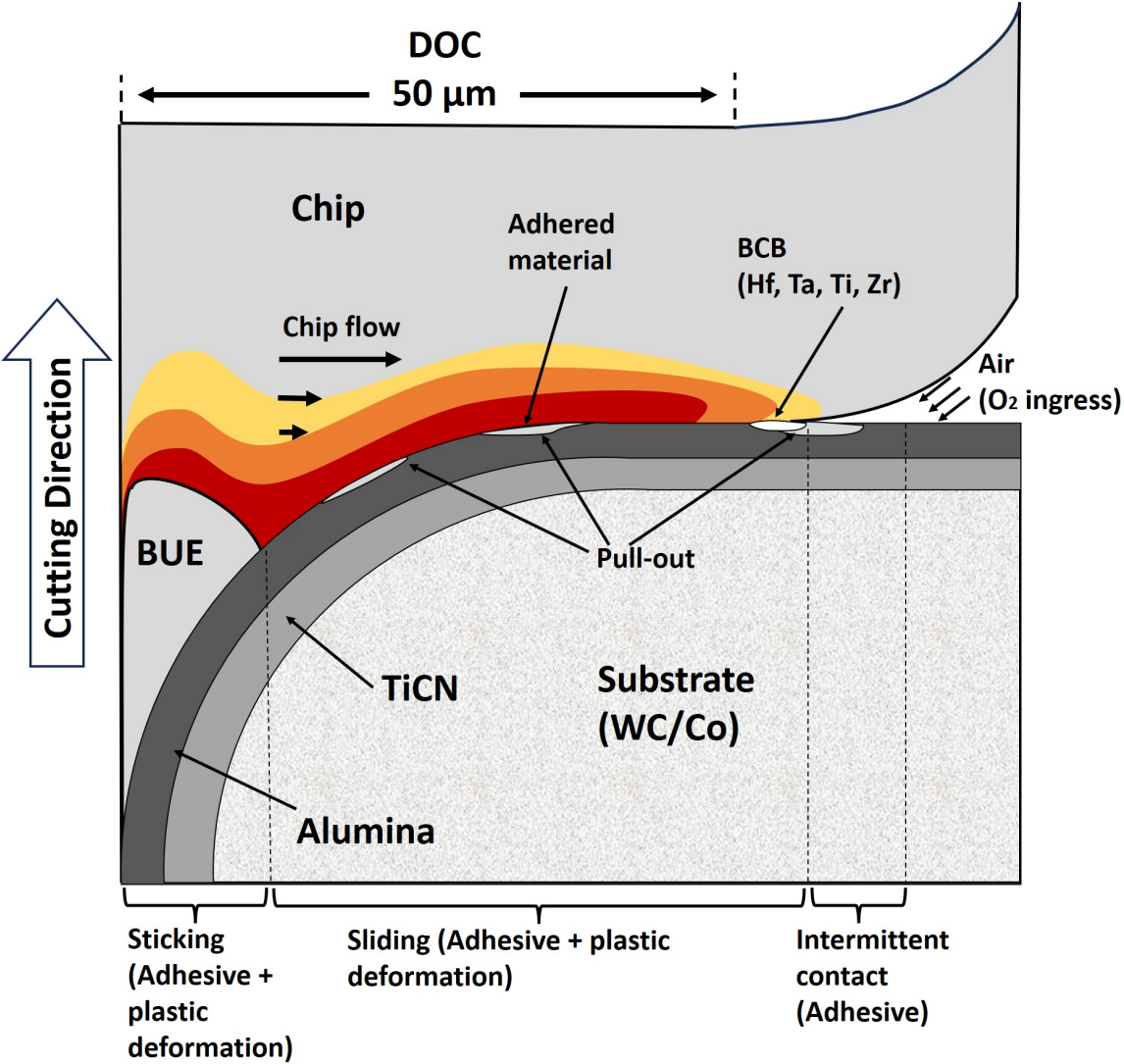


Figure 7.10: Simplified schematic showing characteristic wear behaviour during orthogonal turning in RR1000.

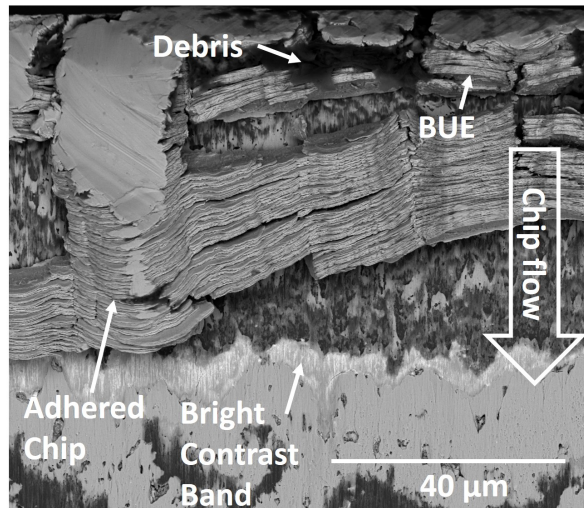


Figure 7.11: BS SEM micrograph of adhered chip on tool rake face after a SCL of 17 m.

During HIP processing, as with forged Ni-based Superalloy material, there is a variation in cooling rate when moving from the billet surface to the centre, which leads to changes in γ' morphology in the microstructure, whereby precipitates closer to the edge of the billet are finer due to faster cooling rates. As such, there is some inconsistency in material properties when comparing the shorter cuts (12 m and 17 m), which were performed at the edge of the billet, to the longest cut (57 m), which started at the edge and finished towards the centre. With as-HIP material there is also the added consideration of PPBs, that can be deleterious to mechanical properties [40, 100]. It is unclear to what extent these microstructural features influenced the results of this study, however it is apparent from Chapter 6 that equivalent wear behaviour will be observed when machining conventionally processed material, as highlighted by the formation of similar Hf-rich reaction products, and the occurrence of similar wear mechanisms.

7.5 Conclusion

In this chapter, dry orthogonal machining was employed to understand the interaction between tool and workpiece when turning as-HIP RR1000 with alumina coated carbide tools. This revealed high levels of adhesion and strong bonding at the interface formed between tool and workpiece. The amount of adhered material was observed to increase with increasing SCL, alongside a change in chip formation from discontinuous shards to continuous ribbons; this is attributed to increased cutting temperatures, leading to increased workpiece softening. Evidence of alumina grain pull-out as a result of adhesive wear was detected. In addition, worn regions with a smooth topography were also observed, at longer SCLs, indicating chem-

ical wear may be a contributing wear mechanism.

As observed in Chapter 6, a BCB was observed towards the end of the sliding zone, containing a bright Hf-rich phase that appears to be an agglomeration of highly deformed inclusions; however, unlike Chapter 6, it is surrounded by a Ti-rich phase, which is a suspected oxidation product. It is unclear whether this change in oxide is due to differences in the material condition, cutting temperatures, coolant application, or some combination of these factors. Regardless, the presence of Hf in RR1000 appears to be significant.

These results highlight the ineffectiveness of the alumina coating on the tool rake face during dry turning of highly alloyed advanced Ni-based superalloy material with alumina-coated tools. Due to the fine-scale nature of the chemical interactions between workpiece and tool, higher resolution characterization techniques (i.e., TEM) must now be employed to facilitate an improved understanding of the mechanism responsible. This, in turn, will lead to greater insight for cutting tool manufacturers as to how they must adapt the coating systems for Ni-based superalloy machining. This knowledge could also be factored into the alloy design process by material producers, such that problematic elements, like Hf, are eliminated or reduced. In certain scenarios, it may be the case that the energy savings made through improved manufacturing efficiency, outweigh the energy savings made from increased performance in-service.

Chapter 8

Conclusions and Future Work

8.1 Conclusions

The initial motivation for this thesis was to provide insights that could support the development of improved tooling solutions for the aerospace industry. Such improvements aim to reduce costs, time, and energy consumption, facilitating more sustainable manufacturing practices. Achieving this goal requires a series of incremental steps. The first step is to understand the current state of the art and its limitations. The next is to determine how these insights can inform the development of the next generation of the technology. The final step involves industrial implementation. This thesis primarily addresses the first step, offering critical observations that serve as a foundation for the next phase of product development.

In this work, the wear behaviour of state-of-the-art textured CVD alumina multilayer coatings was examined during the turning of various Ni-based superalloys, revealing the complex interplay between workpiece properties and tool wear. The findings suggest a need to target coatings towards specific material types. At present, Sandvik's S205 grade, the focus of this study, is recommended for all Ni-based materials. However, it is clear from the evidence presented that this grade is less suited to machining high- γ' PM alloys such as RR1000, particularly when grain size is larger. Although more adhesive wear was observed when turning the wrought alloy IN718, the wear rate was significantly lower directly behind the cutting edge, which is the most critical region of the rake face due to its influence on both surface generation and chip formation, as well as the high stresses that develop here, which can promote premature tool failure. In this respect, the S205 grade appears better suited to turning wrought Ni-based alloys, which operate at lower temperatures, and more generally, to turning processes with reduced levels of force fluctuations, i.e., finer grained material.

A further outcome of this research was the assessment of surface integrity when turning both CG and FG RR1000. When carried out alongside analysis of machining forces and chip formation, this provided valuable insight into how workpiece deformation influences tool wear. Coupling observations of workpiece deformation with modelling techniques provided additional validation of the hypotheses presented. This was most effectively applied when considering γ' dissolution, which offered direct evidence of the temperatures in the region

of 1100° C within the tertiary shear zone. As temperature measurement is often difficult to implement during typical industrial machining operations, this approach could be adopted by aeroengine manufacturers and tooling suppliers to estimate cutting temperatures in materials that exhibit clear and visible surface-level phase transformations during machining.

Although the surface integrity analysis was conducted primarily to understand tool wear, valuable insights regarding surface generation were also gained. In the case of the influence of cutting speed on surface integrity for CG RR1000 and FG RR1000, the FG material condition was observed to be more sensitive to changes in cutting speed, since deformation occurs closer to the surface, and was therefore more affected by the increased temperatures generated at higher cutting speeds. In contrast, turning the CG material is more influenced by mechanical effects that extend deeper into the surface, due to reduced grain boundary strengthening. This knowledge can be useful to aeroengine manufacturers when selecting appropriate processing parameters during Ni based turning of critical parts, where surface integrity is of particular importance due to their safety critical applications.

Within the thesis, chemical etching of the worn tools revealed complex chemical changes across the tool rake face. Although it could not be directly ascertained whether the apparent reaction products retained after etching indicate phases that may contribute to chemical wear, they do emphasise the clear chemical affinity that exists between Ni-based materials and alumina. In the case of Hf present within RR1000, the evidence suggests that Hf is the most likely candidate for promoting chemical wear due to the high concentrations detected across the contact zone after etching. Removing Hf from new alloys altogether may therefore be a valid way to increase tool life, which could be a consideration within the alloy design process.

In summation, the limitations of using CVD alumina coated carbides for Ni-based turning have been presented. In terms of the next steps for developing improved coatings for Ni-based turning, there appear to be two options: further optimise the CVD alumina coatings, or explore alternative coatings that exhibit reduced workpiece material adhesion. If the first option is pursued, it is suggested that, for improved performance, the interface strength with the underlying TiCN coating should be increased to prevent delamination, which occurs readily towards the rear of the contact zone when turning IN718. There should also be a focus on improving intergranular alumina strength to prevent grain pull-out. Similarly, to further enhance coating performance when turning advanced alloys such as RR1000, tooling manufacturers must also focus on understanding the chemical interactions between tool and workpiece that could lead to chemically driven wear, which will be accelerated by higher cutting temperatures. If the second option is considered preferable, then other coating technologies, such as PVD, must also be explored. From the findings of this thesis, however, it would appear that no single coating system will be optimal for all Ni-based alloys. Instead, coating systems will need to become evermore tailored in order to efficiently process the ever improving materials they are required to machine.

8.2 Future Work

It is apparent from the work presented that there remains much to be learned about the interaction between tool and workpiece at an atomic scale, the temperatures encountered during machining, and the flank face wear mechanisms. Simplified modelling was performed using Thermo-Cal to simulate alumina degradation by observing where different elements preferentially partition as temperature is increased. The results (see Figure A6 of Appendix A) appear to suggest that Ti will react with corundum at the temperatures experienced during machining. To explore this hypothesis further, higher-resolution techniques must be employed (e.g., TEM, APT, XRD) to analyse the coating/workpiece interfaces on both flank and rake faces, to investigate the chemical interactions, and whether any tool protective layers form that could limit chemical wear. This work should be supported by more in-depth thermodynamic modelling, alongside orthogonal cutting experiments, designed to accurately measure cutting temperatures.

One clear disadvantage of the methods adopted in the experimental studies presented, and indeed within much of the published literature on the subject of Ni-based superalloy machining, is that the complexity of the workpiece materials being machined limits the ability to understand fundamental mechanisms and interactions. Utilising simplified model materials, i.e., binary/ternary alloys, could allow the chemical interactions to be better understood and modelled, before moving towards more complex alloy systems such as RR1000 and IN718. Such model materials would be well suited to in-operando experiments that allow the evolution of machining related phenomena to be captured in real time, by utilising high-powered energy sources (x-ray, neutron) available at large-scale infrastructure facilities. The development of such techniques requires novel experimental methods, complex data analysis, and the ability to process and store large amounts of data. This can only be achieved through research collaborations, due to the wide variety of expertise needed.

Although turning was the focus of the work performed, there are other machining processes that involve machining Ni-based superalloys with alumina-coated carbide tools that require future research. It is currently unclear how the machinability characteristics identified within the studies presented will translate to other processes, since each process yields specific challenges in terms of tool degradation. During milling, for example, thermal cycling can lead to rapid coating failure due to the interrupted nature of the cutting mechanics, which promotes crack propagation. In a similar vein, other coating materials and methods (e.g., PVD) commonly used for Ni-based superalloy machining should also be explored.

Both the materials utilised within this thesis work (IN718, RR1000) have been, or are set to be, replaced in many aerospace applications by more advanced alloys that can operate at higher temperatures. It is not currently known how general the observations made in this thesis are, and whether they provide insight regarding the machinability of next-generation alloys. This question could readily be addressed by repeating the methods presented within

this thesis work with said alloys, however, the tight control over intellectual property by aeroengine manufacturers limits workpiece material availability. Whilst this is understandable given the significant commercial edge it gives them, it is the most significant barrier to future research within the field.

An interesting observation was made regarding the accumulation of specific elements towards the end of the contact zone when turning RR1000, in a so-called bright contrast band (BCB), which exhibited distinct variations in composition. A more robust study, using directly comparable machining conditions, is required to determine if the chemical species that accumulate on the tool surface in this region are related to the material condition (as-HIP, CG, FG), or to the application of cutting fluid. If the formed oxide composition is temperature dependant, then this could be used as a means to estimate cutting temperatures in the secondary shear zone post-machining.

A final area for proposed future work is to combine 3D FEM modelling with the mean-field modelling approach, and a crystal plasticity model, to form a digital twin of the cutting process. If the computational intensity of such a multi-scale approach could be reduced to a manageable level, it could be used within industry to predict the amount of damage present within the surface, and the degree of tool wear generated. This would enable faster optimisation of manufacturing processes, reducing the number of destructive quality control assessment required, thereby facilitating significant time and energy savings.

Bibliography

- [1] *The trusted source for air travel demand updates* | *ACI World*. Section: Advisory Bulletins. Feb. 13, 2024. URL: <https://aci.aero/2024/02/13/the-trusted-source-for-air-travel-demand-updates/> (visited on 12/15/2024).
- [2] Saurav Tiwari, Michael J. Pekris, and John J. Doherty. “A review of liquid hydrogen aircraft and propulsion technologies”. In: *International Journal of Hydrogen Energy* 57 (Feb. 29, 2024), pp. 1174–1196. ISSN: 0360-3199. DOI: 10.1016/j.ijhydene.2023.12.263. URL: <https://www.sciencedirect.com/science/article/pii/S0360319923065631> (visited on 07/19/2024).
- [3] Anthony J. B. Jackson. “Optimisation of aero and industrial gas turbine design for the environment”. Publisher: Cranfield University. PhD thesis. School of Engineering: Cranfield University, Feb. 2009. URL: <http://hdl.handle.net/1826/4316> (visited on 07/19/2024).
- [4] *Global Superalloys Market Size study & Forecast and Regional Analysis, 2022-2029*. ASDR-619631. Bizwit Research, Apr. 2023, p. 200. URL: <https://www.asdreports.com/market-research-report-619631/global-superalloys-market-size-study-forecast-regional-analysis> (visited on 06/10/2024).
- [5] *Superalloys Market Size, Share | Industry Forecast, 2031*. A01758. Allied Market Research, Dec. 2022, p. 304. URL: <https://www.alliedmarketresearch.com/superalloys-market> (visited on 06/10/2024).
- [6] Jung Bahadur Singh. “Introduction”. In: *Alloy 625 : Microstructure, Properties and Performance*. Ed. by Jung Bahadur Singh. Singapore: Springer Nature Singapore, 2022, pp. 1–27. ISBN: 978-981-19156-2-8. DOI: 10.1007/978-981-19-1562-8_1. URL: https://doi.org/10.1007/978-981-19-1562-8_1.
- [7] *75. United Kingdom - Aerospace and Defense*. Nov. 3, 2023. URL: <https://www.trade.gov/country-commercial-guides/united-kingdom-aerospace-and-defense> (visited on 06/10/2024).
- [8] *National Transportation Safety Board*. 2016. URL: <http://www.nts.gov/investigations/dms.html> (visited on 01/26/2021).
- [9] Gerd Lütjering and James Williams. *Titanium*. Engineering Materials, Processes. Berlin, Heidelberg: Springer, 2007. ISBN: 978-3-540-71397-5. DOI: 10.1007/978-3-540-73036-1. URL: <http://link.springer.com/10.1007/978-3-540-73036-1> (visited on 06/10/2024).

- [10] M. D. Barath Kumar and M. Manikandan. “Evaluation of Microstructure, Residual Stress, and Mechanical Properties in Different Planes of Wire + Arc Additive Manufactured Nickel-Based Superalloy”. In: *Metals and Materials International* 28.12 (Dec. 1, 2022), pp. 3033–3056. ISSN: 2005-4149. DOI: 10.1007/s12540-022-01185-w. URL: <https://doi.org/10.1007/s12540-022-01185-w> (visited on 06/12/2024).
- [11] R. Sasikumar et al. “Wire arc additive manufacturing of functionally graded material with SS 316L and IN625: Microstructural and mechanical perspectives”. In: *CIRP Journal of Manufacturing Science and Technology* 38 (2022), pp. 230–242. ISSN: 1755-5817. DOI: 10.1016/j.cirpj.2022.05.005.
- [12] C. Herbert et al. “Influence of Surface Anomalies Following Hole Making Operations on the Fatigue Performance for a Nickel-Based Superalloy”. In: *Journal of Manufacturing Science and Engineering* 136.51016 (Aug. 6, 2014). ISSN: 1087-1357. DOI: 10.1115/1.4027619. URL: <https://doi.org/10.1115/1.4027619> (visited on 06/11/2024).
- [13] L. A. B. Marçal et al. “Spatially resolved structural and chemical properties of the white layer in machined Inconel 718 super alloy”. In: *Materials & Design* 239 (Mar. 1, 2024), p. 112789. ISSN: 0264-1275. DOI: 10.1016/j.matdes.2024.112789. URL: <https://www.sciencedirect.com/science/article/pii/S0264127524001618> (visited on 06/11/2024).
- [14] A. M. Wusatowska-Sarnek et al. “Microstructural Characterization of the White Etching Layer in Nickel-Based Superalloy”. In: *Metallurgical and Materials Transactions A* 42.12 (Dec. 1, 2011), pp. 3813–3825. ISSN: 1543-1940. DOI: 10.1007/s11661-011-0779-8. URL: <https://doi.org/10.1007/s11661-011-0779-8> (visited on 06/11/2024).
- [15] Andrea la Monaca et al. “Towards understanding the thermal history of microstructural surface deformation when cutting a next generation powder metallurgy nickel-base superalloy”. In: *International Journal of Machine Tools and Manufacture* (June 19, 2021). Publisher: Pergamon, p. 103765. ISSN: 0890-6955. DOI: 10.1016/J.IJMACTOOLS.2021.103765. (Visited on 07/09/2021).
- [16] Zhirong Liao et al. “Grain refinement mechanism of nickel-based superalloy by severe plastic deformation - Mechanical machining case”. In: *Acta Materialia* 180 (Nov. 1, 2019). Publisher: Acta Materialia Inc, pp. 2–14. ISSN: 13596454. DOI: 10.1016/j.actamat.2019.08.059. (Visited on 01/15/2021).
- [17] Abhay Bhatt et al. “Wear mechanisms of WC coated and uncoated tools in finish turning of Inconel 718”. In: *Tribology International* 43.5 (May 1, 2010). Publisher: Elsevier, pp. 1113–1121. ISSN: 0301679X. DOI: 10.1016/j.triboint.2009.12.053. (Visited on 01/15/2021).

- [18] A. Thakur and S. Gangopadhyay. “Influence of tribological properties on the performance of uncoated, CVD and PVD coated tools in machining of Incoloy 825”. In: *Tribology International* 102 (Oct. 1, 2016). Publisher: Elsevier Ltd, pp. 198–212. ISSN: 0301679X. DOI: 10.1016/j.triboint.2016.05.027. (Visited on 05/21/2021).
- [19] D. A. Axinte et al. “Turning of advanced Ni based alloys obtained via powder metallurgy route”. In: *CIRP Annals - Manufacturing Technology* 55.1 (Jan. 1, 2006). Publisher: Elsevier USA, pp. 117–120. ISSN: 00078506. DOI: 10.1016/S0007-8506(07)60379-5. (Visited on 12/07/2020).
- [20] Xianjun Kong et al. “Cutting performance and coated tool wear mechanisms in laser-assisted milling K24 nickel-based superalloy”. In: *The International Journal of Advanced Manufacturing Technology* 2014 77:9 77.9 (Nov. 30, 2014). Publisher: Springer, pp. 2151–2163. ISSN: 1433-3015. DOI: 10.1007/S00170-014-6606-9. URL: <https://link-springer-com.sheffield.idm.oclc.org/article/10.1007/s00170-014-6606-9> (visited on 01/18/2022).
- [21] Salman Pervaiz et al. “Machinability analysis of dry and liquid nitrogen-based cryogenic cutting of Inconel 718: experimental and FE analysis”. In: *The International Journal of Advanced Manufacturing Technology* (Oct. 18, 2021). Publisher: Springer Science and Business Media LLC, pp. 1–18. ISSN: 0268-3768. DOI: 10.1007/S00170-021-08173-1/TABLES/6. URL: <https://link.springer.com/article/10.1007/s00170-021-08173-1> (visited on 11/25/2021).
- [22] E. O. Ezugwu and J. Bonney. “Effect of high-pressure coolant supply when machining nickel-base, Inconel 718, alloy with coated carbide tools”. In: *Journal of Materials Processing Technology* 153-154.1 (Nov. 10, 2004). Publisher: Elsevier, pp. 1045–1050. ISSN: 0924-0136. DOI: 10.1016/J.JMATPROTEC.2004.04.329. (Visited on 12/07/2022).
- [23] E. O. Ezugwu et al. “Machining of nickel-base, Inconel 718, alloy with ceramic tools under finishing conditions with various coolant supply pressures”. In: *Journal of Materials Processing Technology* 162-163 (SPEC. ISS. May 15, 2005). Publisher: Elsevier, pp. 609–614. ISSN: 0924-0136. DOI: 10.1016/J.JMATPROTEC.2005.02.144. (Visited on 12/14/2022).
- [24] S. Rупpi. “Enhanced performance of α -Al₂O₃ coatings by control of crystal orientation”. In: *Surface and Coatings Technology* 202.17 (2008), pp. 4257–4269. ISSN: 02578972. DOI: 10.1016/j.surfcoat.2008.03.021.
- [25] A Nowotnik. “Nickel-Based Superalloys”. In: Elsevier, 2016. ISBN: 978-0-12-803581-8. DOI: <https://doi.org/10.1016/B978-0-12-803581-8.02574-1>. URL: <http://www.sciencedirect.com/science/article/pii/B9780128035818025741>.

- [26] A P Mouritz. “Introduction to Aerospace Materials”. In: ed. by Adrian P B T - Introduction to Aerospace Materials Mouritz. Woodhead Publishing, 2012, pp. 251–267. ISBN: 978-1-85573-946-8. DOI: <https://doi.org/10.1533/9780857095152.251>. URL: <http://www.sciencedirect.com/science/article/pii/B9781855739468500121>.
- [27] B. P. Bewlay et al. “TiAl alloys in commercial aircraft engines”. In: *Materials at High Temperatures* 33.4 (June 28, 2016). Publisher: Taylor and Francis Ltd., pp. 549–559. ISSN: 09603409. DOI: 10.1080/09603409.2016.1183068. URL: <https://www.tandfonline.com/doi/abs/10.1080/09603409.2016.1183068> (visited on 01/17/2021).
- [28] R.J. Mitchell and M. Preuss. “Inter-Relationships between Composition, γ' Morphology, Hardness, and γ - γ' Mismatch in Advanced Polycrystalline Nickel-Base Superalloys during Aging at 800 °C”. In: *Metallurgical and Materials Transactions A* 38.3 (Mar. 2007), pp. 615–627. ISSN: 1073-5623, 1543-1940. DOI: 10.1007/s11661-007-9089-6. URL: <https://link.springer.com/10.1007/s11661-007-9089-6> (visited on 08/28/2024).
- [29] R. J. Mitchell et al. “Process development & microstructure & mechanical property evaluation of a dual microstructure heat treated advanced nickel disc alloy”. In: *Proceedings of the International Symposium on Superalloys* (2008). Publisher: Minerals, Metals and Materials Society, pp. 347–356. DOI: 10.7449/2008/SUPERALLOYS_2008_347_356. (Visited on 02/28/2022).
- [30] J Gayda, T Gabb, and Pete Kantzos. “The Effect of Dual Microstructure Heat Treatment on an Advanced Nickel-Base Disk Alloy”. In: *Proceedings of the International Symposium on Superalloys* (Jan. 1, 2004). DOI: 10.7449/2004/Superalloys_2004_323_329.
- [31] “The physical metallurgy of nickel and its alloys”. In: *The Superalloys: Fundamentals and Applications*. Ed. by Roger C. Reed. Cambridge: Cambridge University Press, 2006, pp. 33–120. ISBN: 978-0-521-07011-9. DOI: 10.1017/CBO9780511541285.004. URL: <https://www.cambridge.org/core/books/superalloys/physical-metallurgy-of-nickel-and-its-alloys/80C1D026682ACF8E8E4CDCDDD40EE9B3> (visited on 08/19/2024).
- [32] D. P. Pope and S. S. Ezz. “Mechanical properties of Ni3Al and nickel-base alloys with high volume fraction of γ' ”. In: <http://dx.doi.org/10.1179/imtr.1984.29.1.136> 29.1 (Jan. 1, 1984). Publisher: Taylor & Francis, pp. 136–167. ISSN: 03084590. DOI: 10.1179/IMTR.1984.29.1.136. URL: <https://www.tandfonline.com/doi/abs/10.1179/imtr.1984.29.1.136> (visited on 11/04/2022).
- [33] M P Jackson and R C Reed. “Heat treatment of UDIMET 720Li: the effect of microstructure on properties”. In: *Materials Science and Engineering: A* 259.1 (1999), pp. 85–97. ISSN: 0921-5093. DOI: <https://doi.org/10.1016/>

S0921-5093(98)00867-3. URL: <http://www.sciencedirect.com/science/article/pii/S0921509398008673>.

- [34] Michael Preuss et al. “The effect of γ' particle size on the deformation mechanism in an advanced polycrystalline nickel-base superalloy”. In: *Proceedings of the International Symposium on Superalloys* (2008), pp. 405–414. DOI: 10.7449/2008/SUPERALLOYS_2008_405_414. (Visited on 05/18/2022).
- [35] Allan Harte et al. “The effect of solid solution and gamma prime on the deformation modes in Ni-based superalloys”. In: *Acta Materialia* 194 (Aug. 1, 2020), pp. 257–275. ISSN: 1359-6454. DOI: 10.1016/j.actamat.2020.04.004. URL: <https://www.sciencedirect.com/science/article/pii/S1359645420302615> (visited on 08/27/2024).
- [36] G. B. Viswanathan et al. “Investigation of creep deformation mechanisms at intermediate temperatures in René 88 DT”. In: *Acta Materialia* 53.10 (June 1, 2005), pp. 3041–3057. ISSN: 1359-6454. DOI: 10.1016/j.actamat.2005.03.017. URL: <https://www.sciencedirect.com/science/article/pii/S1359645405001655> (visited on 10/28/2024).
- [37] Jack Telesman et al. “Microstructural Variables Controlling Time-Dependent Crack Growth in a P/M Superalloy”. In: *Proceedings of the International Symposium on Superalloys* (Jan. 1, 2004). DOI: 10.7449/2004/Superalloys_2004_215_224.
- [38] E. I. Galindo-Nava, L. D. Connor, and C. M. F. Rae. “On the prediction of the yield stress of unimodal and multimodal γ' Nickel-base superalloys”. In: *Acta Materialia* 98 (Oct. 1, 2015), pp. 377–390. ISSN: 1359-6454. DOI: 10.1016/j.actamat.2015.07.048. URL: <https://www.sciencedirect.com/science/article/pii/S1359645415005194> (visited on 10/28/2024).
- [39] Brian J McTiernan. *Powder Metallurgy Superalloys*. Ed. by P Samal and J Newkirk. Vol. 7. Publication Title: Powder Metallurgy. ASM International, Sept. 30, 2015. 0 pp. ISBN: 978-1-62708-175-7. DOI: 10.31399/asm.hb.v07.a0006094. URL: <https://doi.org/10.31399/asm.hb.v07.a0006094>.
- [40] J. R. May et al. “Microstructure and Mechanical Properties of an Advanced Nickel-Based Superalloy in the as-HIP Form”. In: *Advanced Materials Research* 278 (2011). Publisher: Trans Tech Publications Ltd, pp. 265–270. ISSN: 1662-8985. DOI: 10.4028/www.scientific.net/AMR.278.265. URL: <https://www.scientific.net/AMR.278.265> (visited on 07/11/2024).
- [41] Posinasetti Nageswara Rao. *Manufacturing Technology: Metal Cutting and Machine Tools*. Google-Books-ID: MCDZAgAAQBAJ. McGraw Hill Education (India), 2013. 540 pp. ISBN: 978-1-259-02956-1.
- [42] M. Eugene Merchant. “Mechanics of the metal cutting process. I. Orthogonal cutting and a type 2 chip”. In: *Journal of Applied Physics* 16.5 (1945), pp. 267–275. ISSN: 00218979. DOI: 10.1063/1.1707586.

- [43] Edward M. Trent and Paul K. Wright. *Metal Cutting*. Google-Books-ID: ZddI0df1EEcC. Butterworth-Heinemann, Jan. 3, 2000. 466 pp. ISBN: 978-0-7506-7069-2.
- [44] Hiroyuki Sasahara. “The effect on fatigue life of residual stress and surface hardness resulting from different cutting conditions of 0.45%C steel”. In: *International Journal of Machine Tools and Manufacture* 45.2 (Feb. 1, 2005). Publisher: Pergamon, pp. 131–136. ISSN: 08906955. DOI: 10.1016/j.ijmachtools.2004.08.002. (Visited on 12/10/2020).
- [45] A. Devillez et al. “Cutting forces and wear in dry machining of Inconel 718 with coated carbide tools”. In: *Wear* 262.7 (Mar. 15, 2007). Publisher: Elsevier, pp. 931–942. ISSN: 0043-1648. DOI: 10.1016/J.WEAR.2006.10.009. (Visited on 08/31/2023).
- [46] W. Grzesik and P. Nieslony. “A computational approach to evaluate temperature and heat partition in machining with multilayer coated tools”. In: *International Journal of Machine Tools and Manufacture* 43.13 (Oct. 1, 2003), pp. 1311–1317. ISSN: 0890-6955. DOI: 10.1016/S0890-6955(03)00160-3. URL: <https://www.sciencedirect.com/science/article/pii/S0890695503001603> (visited on 07/05/2024).
- [47] S. Rinaldi et al. “Machinability of Waspaloy under different cutting and lubri-cooling conditions”. In: *The International Journal of Advanced Manufacturing Technology* 94.9 (Feb. 1, 2018), pp. 3703–3712. ISSN: 1433-3015. DOI: 10.1007/s00170-017-1133-0. URL: <https://doi.org/10.1007/s00170-017-1133-0> (visited on 07/05/2024).
- [48] Jinfu Zhao et al. “PVD AlTiN coating effects on tool-chip heat partition coefficient and cutting temperature rise in orthogonal cutting Inconel 718”. In: *International Journal of Heat and Mass Transfer* 163 (Dec. 1, 2020), p. 120449. ISSN: 0017-9310. DOI: 10.1016/j.ijheatmasstransfer.2020.120449. URL: <https://www.sciencedirect.com/science/article/pii/S0017931020333858> (visited on 07/05/2024).
- [49] J. Gibmeier et al. “In-Situ Synchrotron X-Ray Diffraction Studies in the Chip Formation Zone During Orthogonal Metal Cutting”. In: *Residual Stresses, 11. September 2018*. Ed.: M. Seefeldt. Vol. 6. Materials Research Forum LLC, 2018, pp. 39–44. ISBN: 978-1-945291-88-3. DOI: 10.21741/9781945291890-7.
- [50] L. Rogström et al. “A custom built lathe designed for in operando high-energy x-ray studies at industrially relevant cutting parameters”. In: *Review of Scientific Instruments* 90.10 (Oct. 4, 2019), p. 103901. ISSN: 0034-6748. DOI: 10.1063/1.5091766. URL: <https://doi.org/10.1063/1.5091766> (visited on 10/06/2024).

- [51] M. Moreno et al. “Strain and phase evolution in TiAlN coatings during high-speed metal cutting: An in operando high-energy x-ray diffraction study”. In: *Acta Materialia* 263 (Jan. 15, 2024), p. 119538. ISSN: 1359-6454. DOI: 10.1016/j.actamat.2023.119538. URL: <https://www.sciencedirect.com/science/article/pii/S1359645423008674> (visited on 10/06/2024).
- [52] *Cutting Tool Materials - Technical Info / Cutting Formula*. MITSUBISHI MATERIALS CORPORATION. July 7, 2022. URL: https://www.mmc-carbide.com/sea/technical_information/tec_other_data/tec_other_data_top/tec_other_data_technical/tec_cutting_tool_materials (visited on 08/07/2024).
- [53] S. Rупpi. “Deposition, microstructure and properties of texture-controlled CVD α -Al₂O₃ coatings”. In: *International Journal of Refractory Metals and Hard Materials*. Vol. 23. Issue: 4-6 SPEC. ISS. ISSN: 02634368. Elsevier, July 1, 2005, pp. 306–316. DOI: 10.1016/j.ijrmhm.2005.05.004. (Visited on 04/01/2021).
- [54] S. Shoja et al. “Calculated and experimental Schmid factors for chip flow deformation of textured CVD α -alumina coatings”. In: *Surface and Coatings Technology* 412 (Apr. 25, 2021). Publisher: Elsevier B.V. ISSN: 02578972. DOI: 10.1016/J.SURFCOAT.2021.126991. (Visited on 02/16/2022).
- [55] R. M’Saoubi and S. Rупpi. “Wear and thermal behaviour of CVD α -Al₂O₃ and MTCVD Ti(C,N) coatings during machining”. In: *CIRP Annals - Manufacturing Technology* 58.1 (Jan. 1, 2009). Publisher: Elsevier, pp. 57–60. ISSN: 00078506. DOI: 10.1016/j.cirp.2009.03.059. (Visited on 04/01/2021).
- [56] J Rech et al. “Characterization of the friction properties of various coatings at the tool—chip—workpiece interfaces in dry machining of AISI 4140 steel”. In: *Proceedings of the Institution of Mechanical Engineers, Part J: Journal of Engineering Tribology* 222.4 (Apr. 1, 2008). Publisher: IMECHE, pp. 617–627. ISSN: 1350-6501. DOI: 10.1243/13506501JET416. URL: <https://doi.org/10.1243/13506501JET416> (visited on 08/12/2024).
- [57] Mats Larsson et al. “Deposition and microstructure of PVD TiN NbN multilayered coatings by combined reactive electron beam evaporation and DC sputtering”. In: *Surface and Coatings Technology* 86-87 (Dec. 1, 1996), pp. 351–356. ISSN: 0257-8972. DOI: 10.1016/S0257-8972(96)03026-5. URL: <https://www.sciencedirect.com/science/article/pii/S0257897296030265> (visited on 08/12/2024).
- [58] T. Leyendecker et al. “TiAlN-Al₂O₃ PVD-multilayer for metal cutting operation”. In: *Surface and Coatings Technology* 97.1 (1997), pp. 790–793. DOI: 10.1016/S0257-8972(97)00176-X.
- [59] J. Park et al. “High-Performance Zinc Tin Oxide Semiconductor Grown by Atmospheric-Pressure Mist-CVD and the Associated Thin-Film Transistor Properties”. In: *ACS Applied Materials and Interfaces* 9.24 (2017), pp. 20656–20663. DOI: 10.1021/acsami.7b04235.

- [60] F. Böke et al. “Plasma-Enhanced Chemical Vapor Deposition (PE-CVD) yields better Hydrolytical Stability of Biocompatible SiO_x Thin Films on Implant Alumina Ceramics compared to Rapid Thermal Evaporation Physical Vapor Deposition (PVD)”. In: *ACS Applied Materials and Interfaces* 8.28 (2016), pp. 17805–17816. DOI: 10.1021/acsami.6b04421.
- [61] A. Aditharajan, N. Radhika, and B. Saleh. “Recent advances and challenges associated with thin film coatings of cutting tools: a critical review”. In: *Transactions of the IMF* 101.4 (July 4, 2023). Publisher: Taylor & Francis _eprint: <https://doi.org/10.1080/00202967.2022.2082154>, pp. 205–221. ISSN: 0020-2967. DOI: 10.1080/00202967.2022.2082154. URL: <https://doi.org/10.1080/00202967.2022.2082154> (visited on 08/12/2024).
- [62] A. Larsson, M. Halvarsson, and S. Ruppri. “Microstructural changes in CVD α -Al₂O₃ coated cutting tools during turning operations”. In: *Surface and Coatings Technology* 111.2 (Jan. 29, 1999). Publisher: Elsevier, pp. 191–198. ISSN: 02578972. DOI: 10.1016/S0257-8972(98)00734-8. (Visited on 06/02/2021).
- [63] P. Souza Santos, H. Souza Santos, and S.P. Toledo. “Standard transition aluminas. Electron microscopy studies”. In: *Materials Research* 3.4 (Oct. 2000). Publisher: Fa-pUNIFESP (SciELO), pp. 104–114. ISSN: 1980-5373. DOI: 10.1590/s1516-14392000000400003. URL: http://www.scielo.br/scielo.php?script=sci_arttext&pid=S1516-14392000000400003&lng=en&nrm=iso&tlng=en (visited on 04/01/2021).
- [64] Thomas R. Johannesson and Jan N. Lindström. “Factors affecting the initial nucleation of alumina on cemented-carbide substrates in the CVD process”. In: *Journal of Vacuum Science and Technology* 12.4 (July 1, 1975), pp. 854–857. ISSN: 0022-5355. DOI: 10.1116/1.568687. URL: <https://doi.org/10.1116/1.568687> (visited on 12/08/2024).
- [65] Jae-Gon Kim, Chul-Soon Park, and John S. Chun. “Effect of partial pressure of the reactant gas on the chemical vapour deposition of Al₂O₃”. In: *Thin Solid Films* 97.1 (Nov. 5, 1982), pp. 97–106. ISSN: 0040-6090. DOI: 10.1016/0040-6090(82)90421-7. URL: <https://www.sciencedirect.com/science/article/pii/0040609082904217> (visited on 08/12/2024).
- [66] C. Chatfield, J. Lindström, and M. Sjöstrand. “MICROSTRUCTURE OF CVD - Al₂O₃”. In: *Journal de Physique Colloques* 50 (C5 1989), p. C5. DOI: 10.1051/jphyscol:1989545. URL: <https://hal.science/jpa-00229568> (visited on 08/12/2024).
- [67] Ning Fang, P. Srinivasa Pai, and S. Mosquea. “Effect of tool edge wear on the cutting forces and vibrations in high-speed finish machining of Inconel 718: an experimental study and wavelet transform analysis”. In: *The International Journal of Advanced Manufacturing Technology* 52.1 (Jan. 1, 2011), pp. 65–77. ISSN: 1433-3015. DOI: 10.1007/s00170-010-2703-6. URL: <https://doi.org/10.1007/s00170-010-2703-6> (visited on 07/29/2024).

- [68] Qi Shen et al. “Effects of Cutting Edge Microgeometry on Residual Stress in Orthogonal Cutting of Inconel 718 by FEM”. In: *Materials* 11.6 (June 2018). Number: 6 Publisher: Multidisciplinary Digital Publishing Institute, p. 1015. ISSN: 1996-1944. DOI: 10.3390/ma11061015. URL: <https://www.mdpi.com/1996-1944/11/6/1015> (visited on 07/29/2024).
- [69] Tugrul Özel. “Computational modelling of 3D turning: Influence of edge microgeometry on forces, stresses, friction and tool wear in PcBN tooling”. In: *Journal of Materials Processing Technology* 209.11 (June 21, 2009), pp. 5167–5177. ISSN: 09240136. DOI: 10.1016/j.jmatprotec.2009.03.002. (Visited on 12/13/2022).
- [70] Tuğrul Özel. “Experimental and finite element investigations on the influence of tool edge radius in machining nickel-based alloy”. In: *Proceedings of the ASME International Manufacturing Science and Engineering Conference 2009, MSEC2009*. Vol. 1. American Society of Mechanical Engineers Digital Collection, Sept. 20, 2009, pp. 493–498. ISBN: 978-0-7918-4361-1. DOI: 10.1115/MSEC2009-84362. (Visited on 12/14/2020).
- [71] Farshid Jafarian, Domenico Umbrello, and Behzad Jabbaripour. “Identification of new material model for machining simulation of Inconel 718 alloy and the effect of tool edge geometry on microstructure changes”. In: *Simulation Modelling Practice and Theory* 66 (Aug. 1, 2016). Publisher: Elsevier, pp. 273–284. ISSN: 1569-190X. DOI: 10.1016/j.simpat.2016.05.001. (Visited on 08/02/2021).
- [72] Virginia García Navas, Oscar Gonzalo, and Ion Bengoetxea. “Effect of cutting parameters in the surface residual stresses generated by turning in AISI 4340 steel”. In: *International Journal of Machine Tools and Manufacture* 61 (Oct. 1, 2012), pp. 48–57. ISSN: 0890-6955. DOI: 10.1016/j.ijmachtools.2012.05.008. URL: <https://www.sciencedirect.com/science/article/pii/S0890695512000995> (visited on 07/29/2024).
- [73] J. Taylor. “The tool wear-time relationship in metal cutting”. In: *International Journal of Machine Tool Design and Research* 2.2 (Apr. 1, 1962), pp. 119–152. ISSN: 0020-7357. DOI: 10.1016/0020-7357(62)90002-1. URL: <https://www.sciencedirect.com/science/article/pii/0020735762900021> (visited on 08/07/2024).
- [74] Viktor Astakhov and Jose C. M. Outeiro. “Importance of Temperature in Metal Cutting and Its Proper Measurement/Modeling”. In: Jan. 1, 2019, pp. 1–47. ISBN: 978-3-030-03821-2. DOI: 10.1007/978-3-030-03822-9_1.
- [75] “12 Adhesion and Adhesive Wear”. In: *Tribology Series*. Ed. by G. W. Stachowiak and A. W. Batchelor. Vol. 24. Engineering TriBology. Elsevier, Jan. 1, 1993, pp. 613–635. DOI: 10.1016/S0167-8922(08)70586-8. URL: <https://www.sciencedirect.com/science/article/pii/S0167892208705868> (visited on 08/06/2024).

- [76] Alex Graves et al. “An experimental and theoretical investigation on Ti-5553/WC-Co(6%) chemical interactions during machining and in diffusion couples”. In: *Wear* (Dec. 28, 2022). Publisher: Elsevier, p. 204604. ISSN: 0043-1648. DOI: 10.1016/J.WEAR.2022.204604. URL: <https://linkinghub.elsevier.com/retrieve/pii/S0043164822003611> (visited on 01/06/2023).
- [77] Volodymyr Bushlya et al. “Tool wear mechanisms of PcBN in machining Inconel 718: Analysis across multiple length scale”. In: *CIRP Annals* 70.1 (Jan. 1, 2021). Publisher: Elsevier, pp. 73–78. ISSN: 17260604. DOI: 10.1016/j.cirp.2021.04.008. (Visited on 12/05/2022).
- [78] Fritz Klocke and Aaron Kuchle. *Manufacturing Processes I: Cutting*. Berlin, Heidelberg, GERMANY: Springer Berlin / Heidelberg, 2011. ISBN: 978-3-642-11979-8. URL: <http://ebookcentral.proquest.com/lib/sheffield/detail.action?docID=763399> (visited on 08/05/2024).
- [79] Mikael Fallqvist. “Microstructural, Mechanical and Tribological Characterisation of CVD and PVD Coatings for Metal Cutting Applications”. PhD thesis. Uppsala University, Jan. 1, 2012. URL: <https://www.google.com/url?sa=t&source=web&rct=j&opi=89978449&url=https://www.diva-portal.org/smash/get/diva2:516909/FULLTEXT01.pdf&ved=2ahUKEwjw-omPjtaHAXULUkEAHW-7DsIQFnoECBcQAQ&usq=AOvVaw3fA8WiVGuINIC1cW1TJOxv> (visited on 08/02/2024).
- [80] Alex Graves et al. “On the mechanism of crater wear in a high strength metastable β titanium alloy”. In: *Wear* 484-485 (Nov. 15, 2021). Publisher: Elsevier, p. 203998. ISSN: 0043-1648. DOI: 10.1016/J.WEAR.2021.203998. (Visited on 02/16/2022).
- [81] S. Shoja et al. “Enhanced steel machining performance using texture-controlled CVD alpha-alumina coatings: Fundamental degradation mechanisms”. In: *International Journal of Machine Tools and Manufacture* 197 (Apr. 1, 2024), p. 104137. ISSN: 0890-6955. DOI: 10.1016/j.ijmachtools.2024.104137. URL: <https://www.sciencedirect.com/science/article/pii/S0890695524000233> (visited on 04/09/2024).
- [82] P. A. Dearnley, V. Thompson, and A. N. Grearson. “Machining ferrous materials with carbides coated by chemical vapour deposition II: Wear mechanisms”. In: *Surface and Coatings Technology* 29.3 (Nov. 1, 1986). Publisher: Elsevier, pp. 179–205. ISSN: 0257-8972. DOI: 10.1016/0257-8972(86)90012-5. (Visited on 09/19/2022).
- [83] Xiaoqi Song, Takahashi Yukio, and Ihara Tohru. “Influence of built-up layer on the wear mechanisms of uncoated and coated carbide tools during dry cutting of Inconel 718”. In: *Seimitsu Kogaku Kaishi/Journal of the Japan Society for Precision Engineering* 85.10 (2019). Publisher: Japan Society for Precision Engineering, pp. 856–865. ISSN: 09120289. DOI: 10.2493/JJSPE.85.856. (Visited on 05/23/2022).

- [84] B. Mills and A. H. Redford. *Machinability of Engineering Materials*. Publication Title: Machinability of Engineering Materials. Springer Netherlands, 1983. DOI: 10 . 1007/978-94-009-6631-4. (Visited on 12/12/2020).
- [85] R. M'Saoubi et al. "A review of surface integrity in machining and its impact on functional performance and life of machined products". In: *International Journal of Sustainable Manufacturing* 1.1 (2008). Publisher: Inderscience Publishers, pp. 203–236. ISSN: 17427231. DOI: 10 . 1504/IJSM.2008.019234. (Visited on 12/08/2020).
- [86] J. Paulo Davim. *Surface integrity in machining*. Publication Title: Surface Integrity in Machining. Springer London, 2010. 1-215. ISBN: 978-1-84882-873-5. DOI: 10 . 1007/978-1-84882-874-2. (Visited on 12/08/2020).
- [87] Jean Carlos Garcia-Gonzalez, Wilfredo Moscoso-Kingsley, and Viswanathan Madhavan. "Tool Rake Face Temperature Distribution When Machining Ti6Al4V and Inconel 718". In: *Procedia Manufacturing* 5 (Jan. 1, 2016). Publisher: Elsevier, pp. 1369–1381. ISSN: 2351-9789. DOI: 10 . 1016/J.PROMFG.2016.08.107. (Visited on 04/26/2022).
- [88] E. O. Ezugwu, Z. M. Wang, and A. R. Machado. "The machinability of nickel-based alloys: A review". In: *Journal of Materials Processing Technology* 86.1 (Feb. 15, 1999). Publisher: Elsevier BV, pp. 1–16. ISSN: 09240136. DOI: 10 . 1016/S0924-0136(98)00314-8. (Visited on 12/02/2020).
- [89] A. Jawaid, S. Koksai, and S. Sharif. "Wear behavior of pvd and cvd coated carbide tools when face milling inconel 718". In: *Tribology Transactions* 43.2 (Jan. 1, 2000), pp. 325–331. ISSN: 1547397X. DOI: 10 . 1080/10402000008982347. (Visited on 01/18/2022).
- [90] T. Kitagawa, A. Kubo, and K. Maekawa. "Temperature and wear of cutting tools in high-speed machining of Inconel 718 and Ti-6Al-6V-2Sn". In: *Wear* 202.2 (Jan. 1, 1997). Publisher: Elsevier BV, pp. 142–148. ISSN: 00431648. DOI: 10 . 1016 / S0043-1648 (96) 07255-9. (Visited on 05/20/2021).
- [91] M Anthony Xavier et al. "Tool Wear Assessment During Machining of Inconel 718". In: *Procedia Engineering* 174 (2017), pp. 1000–1008. ISSN: 1877-7058. DOI: <https://doi.org/10.1016/j.proeng.2017.01.252>. URL: <http://www.sciencedirect.com/science/article/pii/S1877705817302527>.
- [92] A. Thakur and S. Gangopadhyay. "Dry machining of nickel-based super alloy as a sustainable alternative using TiN/TiAlN coated tool". In: *Journal of Cleaner Production* 129 (Aug. 15, 2016). Publisher: Elsevier Ltd, pp. 256–268. ISSN: 09596526. DOI: 10.1016/j.jclepro.2016.04.074. (Visited on 02/18/2021).
- [93] J P Costes et al. "Tool-life and wear mechanisms of CBN tools in machining of Inconel 718". In: *International journal of machine tools & manufacture* 47.7 (2007). Place: Oxford ISBN: 0890-6955, pp. 1081–1087. DOI: 10 . 1016 / j . ijmachtools.2006.09.031.

- [94] Zhirong Liao et al. “Surface integrity in metal machining - Part I: Fundamentals of surface characteristics and formation mechanisms”. In: *International Journal of Machine Tools and Manufacture* 162 (Mar. 1, 2021). Publisher: Pergamon, p. 103687. ISSN: 0890-6955. DOI: 10.1016/J.IJMACHTOOLS.2020.103687. (Visited on 07/29/2021).
- [95] A. R. C. Sharman, J. I. Hughes, and K. Ridgway. “Workpiece Surface Integrity and Tool Life Issues When Turning Inconel 718™ Nickel Based Superalloy”. In: *Machining Science and Technology* 8.3 (Dec. 30, 2004). Publisher: Marcel Dekker Inc., pp. 399–414. ISSN: 1091-0344. DOI: 10.1081/MST-200039865. URL: <http://www.tandfonline.com/doi/abs/10.1081/MST-200039865> (visited on 12/06/2020).
- [96] Chuanyong Cui et al. “Microstructure and yield strength of UDIMET 720LI alloyed with Co-16.9 Wt Pct Ti”. In: *Metallurgical and Materials Transactions A: Physical Metallurgy and Materials Science* 36.11 (2005). Publisher: Minerals, Metals and Materials Society, pp. 2921–2927. ISSN: 10735623. DOI: 10.1007/s11661-005-0065-8. URL: <https://link.springer.com/article/10.1007/s11661-005-0065-8> (visited on 12/09/2020).
- [97] Rachid M’Saoubi et al. “Surface integrity of nickel-based alloys subjected to severe plastic deformation by abusive drilling”. In: *CIRP Annals* 63.1 (Jan. 1, 2014). Publisher: Elsevier, pp. 61–64. ISSN: 0007-8506. DOI: 10.1016/J.CIRP.2014.03.067. (Visited on 07/28/2021).
- [98] Andrea la Monaca et al. “Can higher cutting speeds and temperatures improve the microstructural surface integrity of advanced Ni-base superalloys?” In: *CIRP Annals* 71.1 (Jan. 1, 2022). Publisher: Elsevier Inc., pp. 113–116. ISSN: 17260604. DOI: 10.1016/J.CIRP.2022.04.061. (Visited on 11/03/2022).
- [99] Andrea la Monaca et al. “Temperature-dependent shear localisation and microstructural evolution in machining of nickel-base superalloys”. In: *Materials and Design* 219 (July 1, 2022). Publisher: Elsevier Ltd. ISSN: 18734197. DOI: 10.1016/J.MATDES.2022.110792. (Visited on 10/31/2022).
- [100] R. C. Buckingham et al. “The effect of strain distribution on microstructural developments during forging in a newly developed nickel base superalloy”. In: *Materials Science and Engineering: A* 654 (Jan. 27, 2016), pp. 317–328. ISSN: 0921-5093. DOI: 10.1016/j.msea.2015.12.042. URL: <https://www.sciencedirect.com/science/article/pii/S0921509315307334> (visited on 07/04/2024).
- [101] Zhirong Liao et al. “On the influence of gamma prime upon machining of advanced nickel based superalloy”. In: *CIRP Annals* 67.1 (Jan. 1, 2018). Publisher: Elsevier USA, pp. 109–112. ISSN: 17260604. DOI: 10.1016/j.cirp.2018.03.021. (Visited on 12/06/2020).

- [102] Rengen Ding et al. “Characterization of plastic deformation induced by machining in a Ni-based superalloy”. In: *Materials Science and Engineering: A* 778 (Mar. 19, 2020), p. 139104. ISSN: 0921-5093. DOI: 10.1016/j.msea.2020.139104. URL: <https://www.sciencedirect.com/science/article/pii/S0921509320301921> (visited on 04/04/2024).
- [103] S. L. Soo et al. “Machinability and surface integrity of RR1000 nickel based superalloy”. In: *CIRP Annals - Manufacturing Technology* 60.1 (Jan. 1, 2011). Publisher: Elsevier, pp. 89–92. ISSN: 00078506. DOI: 10.1016/j.cirp.2011.03.094. (Visited on 01/15/2021).
- [104] R. Hood et al. “Tool life and workpiece surface integrity when turning an RR1000 nickel-based superalloy”. In: *International Journal of Advanced Manufacturing Technology* 98.9 (Oct. 1, 2018). Publisher: Springer London, pp. 2461–2468. ISSN: 14333015. DOI: 10.1007/s00170-018-2371-5. URL: <https://doi.org/10.1007/s00170-018-2371-5> (visited on 01/15/2021).
- [105] S. Cedergren et al. “The effects of grain size and feed rate on notch wear and burr formation in wrought Alloy 718”. In: *International Journal of Advanced Manufacturing Technology* 67.5 (July 16, 2013). Publisher: Springer, pp. 1501–1507. ISSN: 02683768. DOI: 10.1007/s00170-012-4584-3/METRICS. URL: <https://link.springer.com/article/10.1007/s00170-012-4584-3> (visited on 02/15/2023).
- [106] Shashi Ranjan Singh, Rakesh Ganpat Mote, and Sushil Kumar Mishra. “The effect of microstructures and precipitates (γ' , γ'' , δ) on machinability of Inconel-718 nickel-based superalloy in turning process”. In: *Journal of Manufacturing Processes* 82 (Oct. 1, 2022). Publisher: Elsevier Ltd, pp. 374–389. ISSN: 15266125. DOI: 10.1016/J.JMAPRO.2022.08.004. (Visited on 10/25/2022).
- [107] S. Olovsjö, A. Wretland, and G. Sjöberg. “The effect of grain size and hardness of wrought Alloy 718 on the wear of cemented carbide tools”. In: *Wear* 268.9 (Mar. 25, 2010), pp. 1045–1052. ISSN: 00431648. DOI: 10.1016/J.WEAR.2010.01.017. (Visited on 10/25/2022).
- [108] S. Olovsjö and L. Nyborg. “Influence of microstructure on wear behaviour of uncoated WC tools in turning of Alloy 718 and Waspaloy”. In: *Wear* 282-283 (Apr. 5, 2012). Publisher: Elsevier, pp. 12–21. ISSN: 00431648. DOI: 10.1016/j.wear.2012.01.004. (Visited on 06/03/2021).
- [109] A. Thakur et al. “Evaluation on Effectiveness of CVD and PVD Coated Tools during Dry Machining of Incoloy 825”. In: <http://dx.doi.org/sheffield.idm.oclc.org/10.1080/10402004.2015.1131350> 59.6 (Nov. 1, 2016). Publisher: Taylor & Francis, pp. 1048–1058. ISSN: 1547397X. DOI: 10.1080/10402004.2015.1131350. URL: <https://www-tandfonline-com.sheffield.idm.oclc.org/doi/abs/10.1080/10402004.2015.1131350> (visited on 11/15/2021).

- [110] K. Kadirgama et al. “Tool life and wear mechanism when machining Hastelloy C-22HS”. In: *Wear* 270.3 (Jan. 12, 2011). Publisher: Elsevier, pp. 258–268. ISSN: 00431648. DOI: 10.1016/j.wear.2010.10.067. (Visited on 02/19/2021).
- [111] Merugu Rakesh and Saurav Datta. “Machining of Inconel 718 Using Coated WC Tool: Effects of Cutting Speed on Chip Morphology and Mechanisms of Tool Wear”. In: *Arabian Journal for Science and Engineering* 45.2 (Feb. 1, 2020). Publisher: Springer, pp. 797–816. ISSN: 21914281. DOI: 10.1007/S13369-019-04171-4. (Visited on 01/18/2022).
- [112] Berend Denkena, Alexander Krödel, and Lars Ellersiek. “Influence of metal working fluid on chip formation and mechanical loads in orthogonal cutting”. In: *International Journal of Advanced Manufacturing Technology* 118.9 (Feb. 1, 2022). Publisher: Springer Science and Business Media Deutschland GmbH, pp. 3005–3013. ISSN: 14333015. DOI: 10.1007/S00170-021-08164-2. (Visited on 12/08/2022).
- [113] Nageswaran Tamil Alagan et al. “High-pressure flank cooling and chip morphology in turning Alloy 718”. In: *CIRP Journal of Manufacturing Science and Technology* 35 (Nov. 1, 2021). Publisher: Elsevier, pp. 659–674. ISSN: 1755-5817. DOI: 10.1016/J.CIRPJ.2021.08.012. (Visited on 12/11/2022).
- [114] R. Polvorosa et al. “Tool wear on nickel alloys with different coolant pressures: Comparison of Alloy 718 and Waspaloy”. In: *Journal of Manufacturing Processes* 26 (Apr. 1, 2017). Publisher: Elsevier, pp. 44–56. ISSN: 1526-6125. DOI: 10.1016/J.JMAPRO.2017.01.012. (Visited on 12/07/2022).
- [115] A. D. Sosa et al. “Contact fatigue behavior of α -Al₂O₃-Ti(C,N) CVD coated WC-Co under dry and wet conditions”. In: *Materials Letters* 284 (Feb. 1, 2021). Publisher: North-Holland, p. 129012. ISSN: 0167-577X. DOI: 10.1016/J.MATLET.2020.129012. (Visited on 12/08/2022).
- [116] P. A. Dearnley and E. M. Trent. “Wear mechanisms of coated carbide tools”. In: *Metals Technology* 9.1 (Feb. 1, 1982), pp. 60–75. ISSN: 03071693. DOI: 10.1179/030716982803285909. URL: https://www.researchgate.net/publication/272307204_Wear_mechanisms_of_coated_carbide_tools (visited on 09/19/2022).
- [117] P. A. Dearnley, V. Thompson, and A. N. Grearson. “Machining ferrous materials with carbides coated by chemical vapour deposition I: Interfacial conditions”. In: *Surface and Coatings Technology* 29.3 (Nov. 1, 1986). Publisher: Elsevier, pp. 157–177. ISSN: 0257-8972. DOI: 10.1016/0257-8972(86)90011-3. (Visited on 11/24/2021).
- [118] Gregory K.L. Goh et al. “Transitions in wear mechanisms of alumina cutting tools”. In: *Wear* 201.1 (Dec. 15, 1996). Publisher: Elsevier, pp. 199–208. ISSN: 0043-1648. DOI: 10.1016/S0043-1648(96)07238-9. (Visited on 09/19/2022).

- [119] M Fallqvist, M Nilsson, and R M Saoubi. “Abrasive wear of CVD α -Al₂O₃ and Ti (C, N) coatings at room and elevated temperature”. In: *16th Nordic Symposium on Tribology* (2014).
- [120] R. M’Saoubi et al. “Microstructure and wear mechanisms of texture-controlled CVD A-Al₂O₃ coatings”. In: *Wear* 376-377 (Apr. 15, 2017). Publisher: Elsevier Ltd, pp. 1766–1778. ISSN: 00431648. DOI: 10.1016/j.wear.2017.01.071. (Visited on 04/01/2021).
- [121] R. Bejjani et al. “Shift of wear balance acting on CVD textured coatings and relation to workpiece materials”. In: *Proceedings of the Institution of Mechanical Engineers, Part J: Journal of Engineering Tribology* 235.1 (2021), pp. 114–128. ISSN: 2041305X. DOI: 10.1177/1350650120926781.
- [122] Axel Bjerke et al. “Onset of the degradation of CVD α -Al₂O₃ coating during turning of Ca-treated steels”. In: *Wear* (Mar. 20, 2021). Publisher: Elsevier Ltd, p. 203785. ISSN: 00431648. DOI: 10.1016/j.wear.2021.203785. (Visited on 05/20/2021).
- [123] Naoki Matsui and Koji Watari. “Wear reduction of carbide tools observed in cutting Ca-added steels for machine structural use”. In: *ISIJ International* 46.11 (2006), pp. 1720–1727. ISSN: 09151559. DOI: 10.2355/ISIJINTERNATIONAL.46.1720. URL: https://www.researchgate.net/publication/250161001_Wear_Reduction_of_Carbide_Tools_Observed_in_Cutting_Ca-added_Steels_for_Machine_Structural_Use (visited on 12/15/2022).
- [124] Axel Bjerke et al. “Understanding wear and interaction between CVD α -Al₂O₃ coated tools, steel, and non-metallic inclusions in machining”. In: *Surface and Coatings Technology* 450 (Nov. 25, 2022). Publisher: Elsevier, p. 128997. ISSN: 0257-8972. DOI: 10.1016/J.SURFCOAT.2022.128997. (Visited on 11/18/2022).
- [125] S. Shoja et al. “On the influence of varying the crystallographic texture of alumina CVD coatings on cutting performance in steel turning”. In: *International Journal of Machine Tools and Manufacture* 176 (May 1, 2022). Publisher: Elsevier Ltd. ISSN: 08906955. DOI: 10.1016/J.IJMACHTOOLS.2022.103885. (Visited on 12/10/2022).
- [126] Viktoria Prostavkova et al. “Thermodynamic optimization of the Al₂O₃–FeO–Fe₂O₃–SiO₂ oxide system”. In: *Calphad* 67 (Dec. 1, 2019), p. 101680. ISSN: 0364-5916. DOI: 10.1016/j.calphad.2019.101680. URL: <https://www.sciencedirect.com/science/article/pii/S0364591619301075> (visited on 05/01/2024).
- [127] M. C. Hardy et al. “Developing damage tolerance and creep resistance in a high strength nickel alloy for disc applications”. In: *Proceedings of the International Symposium on Superalloys* (2004). Publisher: Minerals, Metals and Materials Society, pp. 83–90. DOI: 10.7449/2004/SUPERALLOYS_2004_83_90. (Visited on 02/28/2022).

- [128] Y. Q. Chen et al. “Compositional variations for small-scale gamma prime (γ') precipitates formed at different cooling rates in an advanced Ni-based superalloy”. In: *Acta Materialia* 85 (Feb. 15, 2015), pp. 199–206. ISSN: 1359-6454. DOI: 10.1016/j.actamat.2014.11.009. URL: <https://www.sciencedirect.com/science/article/pii/S1359645414008532> (visited on 02/28/2024).
- [129] Dragos Axinte et al. “What micro-mechanical testing can reveal about machining processes”. In: *International Journal of Machine Tools and Manufacture* 183 (Dec. 1, 2022), p. 103964. ISSN: 0890-6955. DOI: 10.1016/j.ijmachtools.2022.103964. URL: <https://www.sciencedirect.com/science/article/pii/S0890695522001158> (visited on 04/04/2024).
- [130] Bentejui Medina-Clavijo et al. “In-SEM micro-machining reveals the origins of the size effect in the cutting energy”. In: *Scientific Reports* 11.1 (Jan. 22, 2021). Publisher: Nature Publishing Group, p. 2088. ISSN: 2045-2322. DOI: 10.1038/s41598-021-81125-7. URL: <https://www.nature.com/articles/s41598-021-81125-7> (visited on 08/13/2024).
- [131] *Beam/specimen interactions - SEM*. URL: https://myscope.training/SEM_Beam_specimen_interactions (visited on 08/13/2024).
- [132] *EBSD Integration with EDS*. Oxford Instruments. URL: <https://www.ebsd.com/ebsd-techniques/integration-with-eds> (visited on 08/13/2024).
- [133] *Interaction of X-rays with matter - XRD*. URL: https://myscope.training/XRD_Interaction_of_X_rays_with_matter (visited on 08/14/2024).
- [134] Matthew Brown, Pete Crawforth, and David Curtis. “Rapid non-destructive sizing of microstructural surface integrity features using x-ray diffraction”. In: *NDT & E International* 131 (Oct. 1, 2022). Publisher: Elsevier, p. 102682. ISSN: 0963-8695. DOI: 10.1016/J.NDTEINT.2022.102682. (Visited on 05/16/2023).
- [135] M. Brown et al. “Non-destructive detection of machining-induced white layers through grain size and crystallographic texture-sensitive methods”. In: *Materials & Design* 200 (Feb. 15, 2021), p. 109472. ISSN: 0264-1275. DOI: 10.1016/j.matdes.2021.109472. URL: <https://www.sciencedirect.com/science/article/pii/S0264127521000253> (visited on 08/14/2024).
- [136] Anirban Naskar and S. Paul. “Non-destructive measurement of grinding-induced deformation-depth using grazing incidence X-ray diffraction technique”. In: *NDT & E International* 126 (Mar. 1, 2022), p. 102592. ISSN: 0963-8695. DOI: 10.1016/j.ndteint.2021.102592. URL: <https://www.sciencedirect.com/science/article/pii/S0963869521001912> (visited on 08/14/2024).

- [137] Matthew Brown, Pete Crawforth, and David Curtis. “Non-destructive on-machine inspection of machining-induced deformed layers”. In: *CIRP Journal of Manufacturing Science and Technology* 52 (Sept. 1, 2024), pp. 296–306. ISSN: 1755-5817. DOI: 10.1016/j.cirpj.2024.06.006. URL: <https://www.sciencedirect.com/science/article/pii/S1755581724000920> (visited on 08/20/2024).
- [138] Andrey Zhigachev. “The effect of specimen surface curvature on X-ray diffraction peak profiles”. In: *The Review of scientific instruments* 84 (Sept. 1, 2013), p. 095105. DOI: 10.1063/1.4820444.
- [139] M. E* Fitzpatrick et al. *Determination of residual stresses by X-ray diffraction*. Report/Guide. ISSN: 1368-6550 Issue: 2 Number: 2 Place: Teddington. Sept. 2005. URL: <https://eprintspublications.npl.co.uk/2391/> (visited on 10/31/2024).
- [140] *Diffraction measurements - XRD*. URL: https://myscope.training/XRD_Diffraction_measurements (visited on 08/14/2024).
- [141] Daniel Fernandez. “An Assessment of the Effect of Machining and Forging Texture on the Fatigue Performance of Daniel Suárez Fernández”. In: (April 2020).
- [142] Daniel Suárez Fernández et al. “Using machining force feedback to quantify grain size in beta titanium”. In: *Materialia* 13 (Sept. 1, 2020). Publisher: Elsevier, p. 100856. ISSN: 2589-1529. DOI: 10.1016/J.MTLA.2020.100856. (Visited on 05/11/2022).
- [143] Samuel Lister et al. “A Machinability Assessment of the Novel Application of Field-Assisted Sintering Technology to Diffusion Bond (FAST-DB) and Functionally Grade Dissimilar Nickel-Based Superalloys”. In: *Metallurgical and Materials Transactions A* (Aug. 19, 2023). ISSN: 1543-1940. DOI: 10.1007/s11661-023-07173-y. URL: <https://doi.org/10.1007/s11661-023-07173-y> (visited on 09/20/2023).
- [144] Thomas Childerhouse et al. “Rapid acquisition of digital fingerprints of Ti-6Al-4V microtexture from machining force measurement data”. In: *Materials Characterization* 207 (Jan. 1, 2024), p. 113550. ISSN: 1044-5803. DOI: 10.1016/j.matchar.2023.113550. URL: <https://www.sciencedirect.com/science/article/pii/S1044580323009099> (visited on 04/03/2024).
- [145] M. J. Anderson et al. “On the modelling of precipitation kinetics in a turbine disc nickel based superalloy”. In: *Acta Materialia* 191 (June 1, 2020), pp. 81–100. ISSN: 1359-6454. DOI: 10.1016/j.actamat.2020.03.058. URL: <https://www.sciencedirect.com/science/article/pii/S135964542030255X> (visited on 02/15/2024).

- [146] Andrea De Bartolomeis et al. “Future research directions in the machining of Inconel 718”. In: *Journal of Materials Processing Technology* 297 (Nov. 1, 2021). Publisher: Elsevier, p. 117260. ISSN: 0924-0136. DOI: 10.1016/J.JMATPROTEC.2021.117260. (Visited on 08/02/2021).
- [147] Alexey Vereschaka et al. “Delamination and Longitudinal Cracking in Multilayered Composite Nanostructured Coatings and Their Influence on Cutting Tool Wear Mechanism and Tool Life”. In: *Novel Nanomaterials - Synthesis and Applications* (Dec. 20, 2017). Publisher: IntechOpen ISBN: 978-1-78923-089-5. DOI: 10.5772/INTECHOPEN.72257. URL: <https://www.intechopen.com/state-item.id> (visited on 12/13/2022).
- [148] J. Rech et al. “Toward a new tribological approach to predict cutting tool wear”. In: *CIRP Annals* 67.1 (Jan. 1, 2018). Publisher: Elsevier, pp. 65–68. ISSN: 0007-8506. DOI: 10.1016/J.CIRP.2018.03.014. (Visited on 12/13/2022).
- [149] Doriana M. D’Addona and Sunil J. Raykar. “Thermal modeling of tool temperature distribution during high pressure coolant assisted turning of Inconel 718”. In: *Materials* 12.3 (Jan. 28, 2019). Publisher: MDPI AG. ISSN: 19961944. DOI: 10.3390/MA12030408. URL: https://www.researchgate.net/publication/330709733_Thermal_Modeling_of_Tool_Temperature_Distribution_during_High_Pressure_Coolant_Assisted_Turning_of_Inconel_718 (visited on 12/08/2022).
- [150] P. A.J. Bagot et al. “An Atom Probe Tomography study of site preference and partitioning in a nickel-based superalloy”. In: *Acta Materialia* 125 (Feb. 15, 2017). Publisher: Pergamon, pp. 156–165. ISSN: 1359-6454. DOI: 10.1016/J.ACTAMAT.2016.11.053. (Visited on 02/28/2022).
- [151] C. R.J. Herbert et al. “Investigation into the characteristics of white layers produced in a nickel-based superalloy from drilling operations”. In: *Procedia Engineering*. Vol. 19. ISSN: 18777058. Elsevier Ltd, Jan. 1, 2011, pp. 138–143. DOI: 10.1016/j.proeng.2011.11.092. (Visited on 12/07/2020).
- [152] Henry Boyle et al. “On the surface integrity of machined aero-engine grade Ni-based superalloy billets produced by the field-assisted sintering technology (FAST) route”. In: *Procedia CIRP*. 7th CIRP Conference on Surface Integrity 123 (Jan. 1, 2024), pp. 310–315. ISSN: 2212-8271. DOI: 10.1016/j.procir.2024.05.055. URL: <https://www.sciencedirect.com/science/article/pii/S2212827124002592> (visited on 08/27/2024).
- [153] Pengfei Tian et al. “Effect of workpiece microstructure on tool wear behavior and surface quality during machining Inconel 718 alloy”. In: *Tribology International* 175 (Nov. 1, 2022), p. 107814. ISSN: 0301-679X. DOI: 10.1016/j.triboint.2022.107814. URL: <https://www.sciencedirect.com/science/article/pii/S0301679X22003875>.

- [154] Haithem Khochtali et al. “Tool wear characteristics in rough turning of Inconel 718 with coated carbide tool under conventional and high-pressure coolant supplies”. In: *International Journal of Advanced Manufacturing Technology* 114.7 (June 1, 2021). Publisher: Springer Science and Business Media Deutschland GmbH, pp. 2371–2386. ISSN: 14333015. DOI: 10.1007/s00170-021-07002-9/FIGURES/18. URL: <https://link-springer-com.sheffield.idm.oclc.org/article/10.1007/s00170-021-07002-9> (visited on 11/29/2021).
- [155] Munro Munro. “Evaluated Material Properties for a Sintered alpha-Alumina”. In: *Journal of the American Ceramic Society* 80.8 (1997). _eprint: <https://onlinelibrary.wiley.com/doi/pdf/10.1111/j.1151-2916.1997.tb03074.x>, pp. 1919–1928. ISSN: 1551-2916. DOI: 10.1111/j.1151-2916.1997.tb03074.x. URL: <https://onlinelibrary.wiley.com/doi/abs/10.1111/j.1151-2916.1997.tb03074.x> (visited on 03/19/2024).
- [156] P. Ettmayer et al. “Ti(C,N) cermets — Metallurgy and properties”. In: *International Journal of Refractory Metals and Hard Materials* 13.6 (Jan. 1, 1995), pp. 343–351. ISSN: 0263-4368. DOI: 10.1016/0263-4368(95)00027-G. URL: <https://www.sciencedirect.com/science/article/pii/S026343689500027G> (visited on 04/15/2024).
- [157] Sun-Yong Ahn and Shinhoo Kang. “Formation of Core/Rim Structures in Ti(C,N)-WC-Ni Cermets via a Dissolution and Precipitation Process”. In: *Journal of the American Ceramic Society* 83.6 (2000). _eprint: <https://onlinelibrary.wiley.com/doi/pdf/10.1111/j.1151-2916.2000.tb01415.x>, pp. 1489–1494. ISSN: 1551-2916. DOI: 10.1111/j.1151-2916.2000.tb01415.x. URL: <https://onlinelibrary.wiley.com/doi/abs/10.1111/j.1151-2916.2000.tb01415.x> (visited on 04/15/2024).
- [158] Paraskevas Kontis et al. “The Role of Oxidized Carbides on Thermal-Mechanical Performance of Polycrystalline Superalloys”. In: *Metallurgical and Materials Transactions A* 49.9 (Sept. 1, 2018), pp. 4236–4245. ISSN: 1543-1940. DOI: 10.1007/s11661-018-4709-x. URL: <https://doi.org/10.1007/s11661-018-4709-x> (visited on 12/23/2024).
- [159] J. Litz, A. Rahmel, and M. Schorr. “Selective carbide oxidation and internal nitridation of the Ni-base superalloys IN 738 LC and IN 939 in air”. In: *Oxidation of Metals* 30.1 (Aug. 1, 1988), pp. 95–105. ISSN: 1573-4889. DOI: 10.1007/BF00656646. URL: <https://doi.org/10.1007/BF00656646> (visited on 12/23/2024).

Appendices

Appendix A

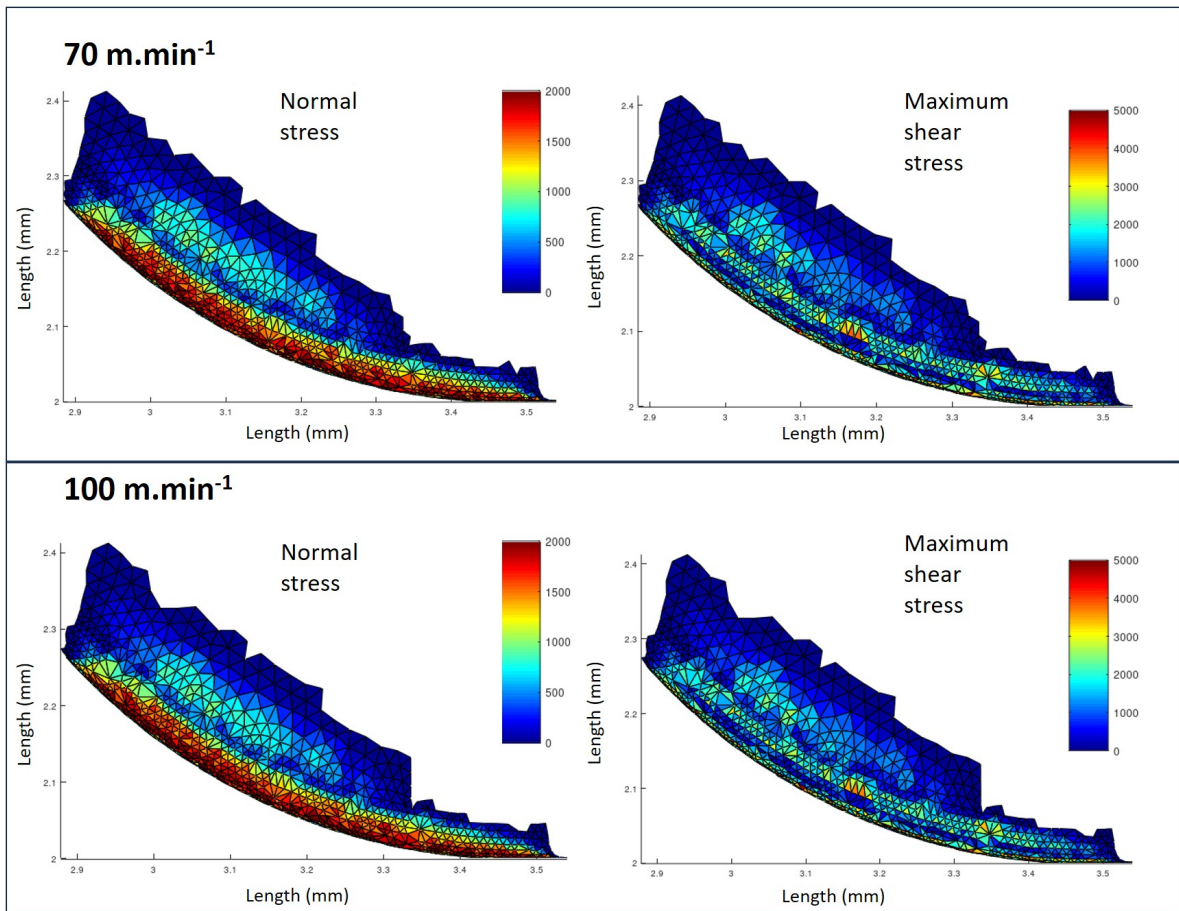


Figure A1: Modelled stresses experienced by tool during AdvantEdge FE machining simulations.

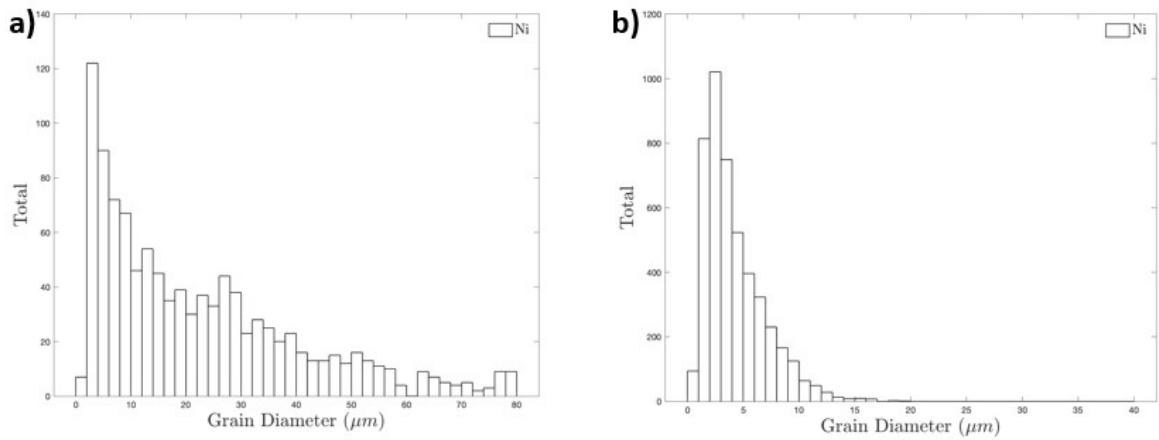


Figure A2: Average grain diameter histograms for (a) CG RR1000 (b) FG RR1000.

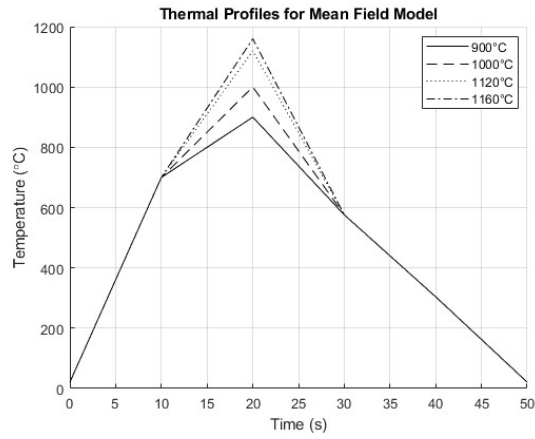


Figure A3: Thermal profiles used for mean field modelling of precipitate dissolution for FG RR1000.

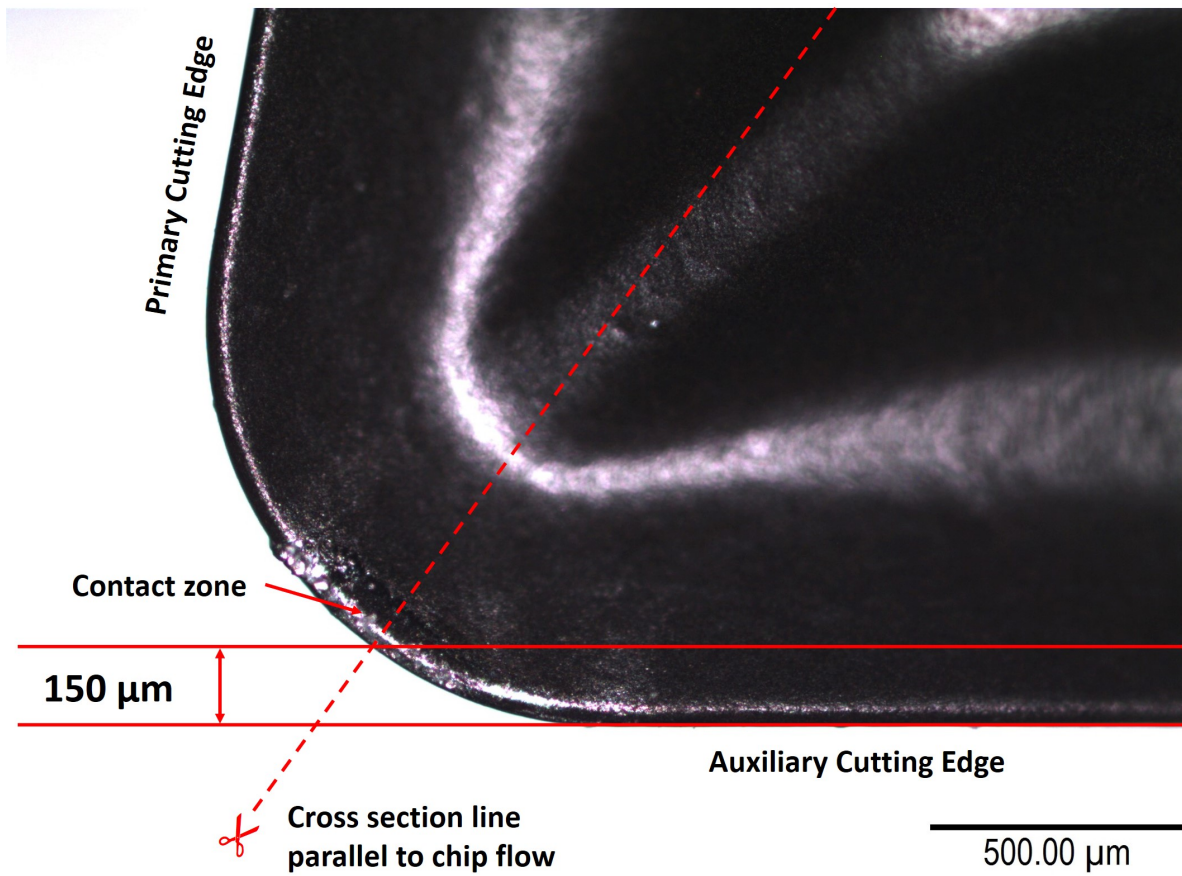


Figure A4: Approximate sectioning line taken parallel to chip flow for all inserts examined.

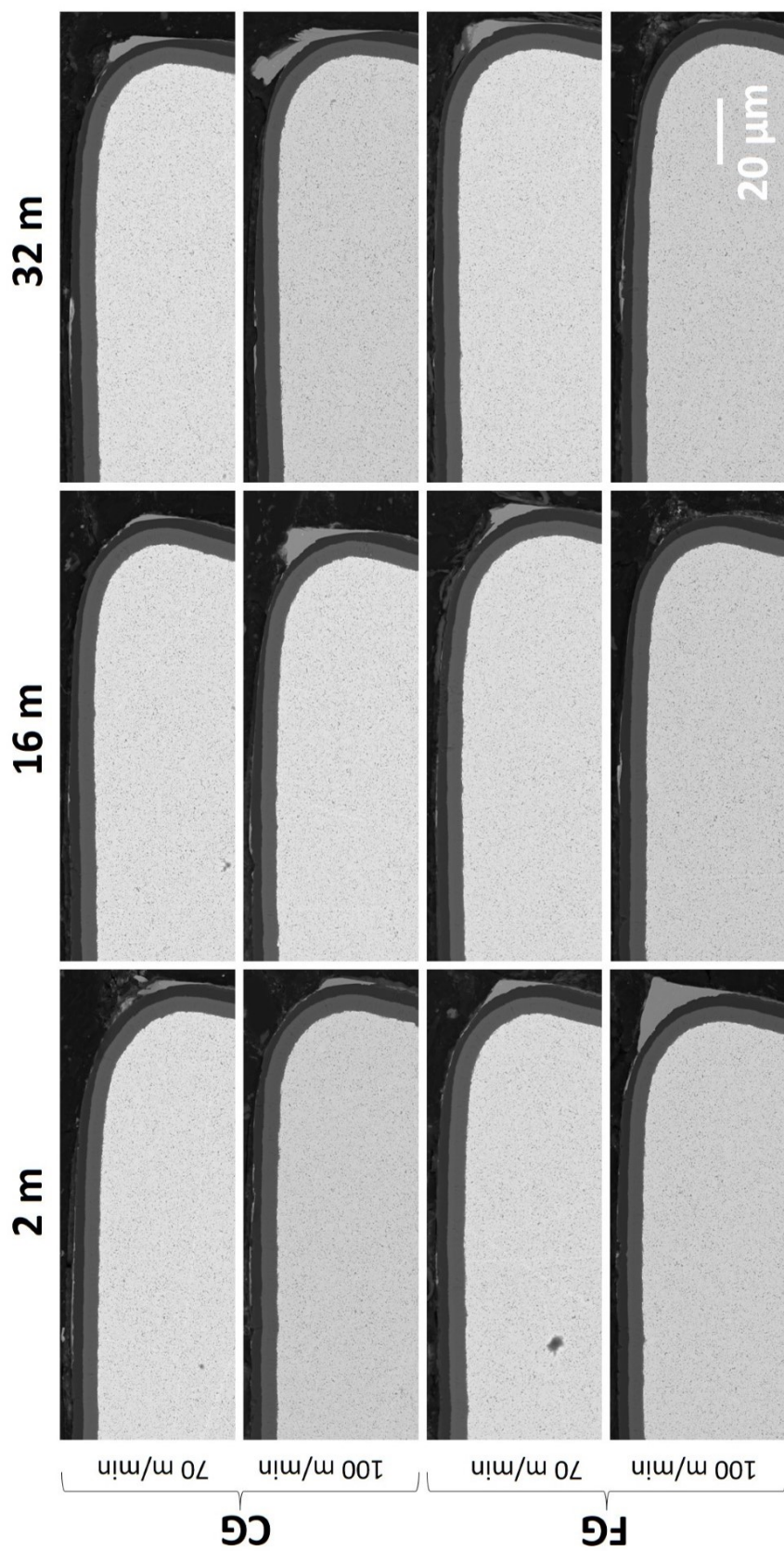


Figure A5: Cross-sections taken parallel to chip flow of cutting inserts at SCLs of 2 m, 16 m, and 32 m for both CG and FG materials.

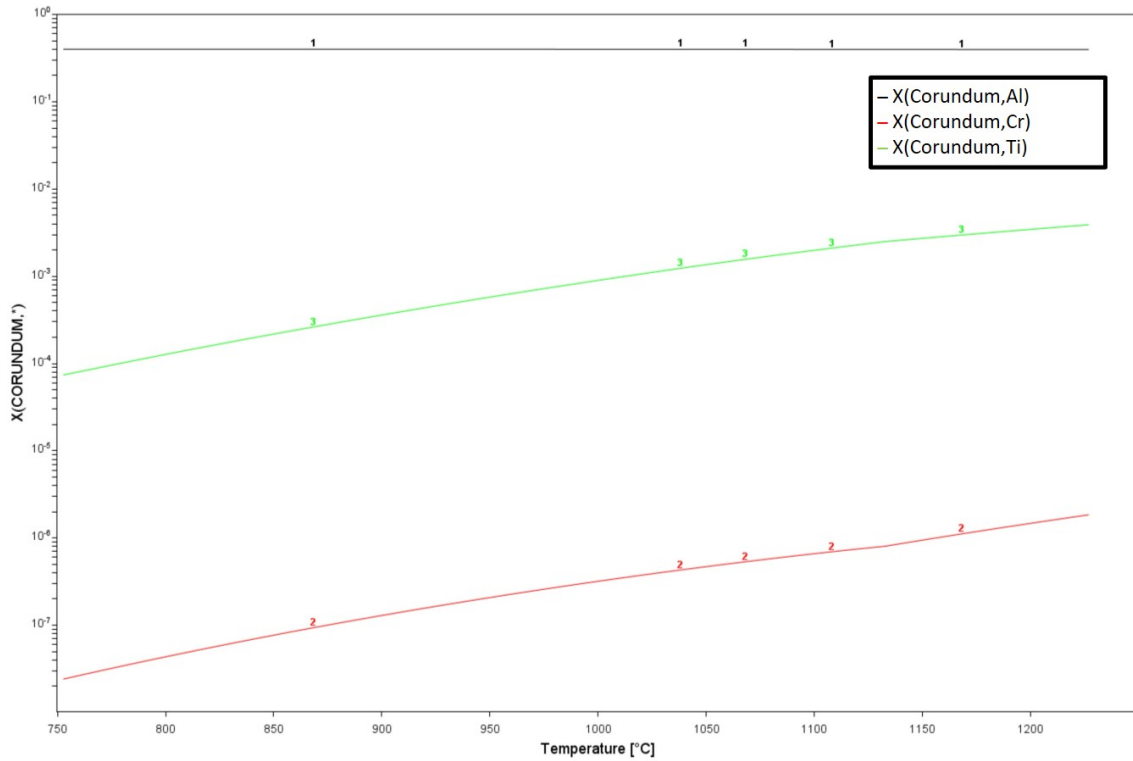


Figure A6: Variation in corundum composition in mole fraction with temperature when combined with RR1000; simulation was performed in Thermo-Calc by mixing 1 mol of RR1000 with 0.005 mol of alumina in the Poly 3 module using the TCNi12 database (all phases except corundum and L12 phases (γ , γ' , MC carbide) were suppressed).